

A deterministic approach to the modelling of electromagnetic wave propagation in urban environments

Citation for published version (APA):

Dooren, van, G. A. J. (1994). *A deterministic approach to the modelling of electromagnetic wave propagation in urban environments*. [Phd Thesis 1 (Research TU/e / Graduation TU/e), Electrical Engineering]. Technische Universiteit Eindhoven. <https://doi.org/10.6100/IR412974>

DOI:

[10.6100/IR412974](https://doi.org/10.6100/IR412974)

Document status and date:

Published: 01/01/1994

Document Version:

Publisher's PDF, also known as Version of Record (includes final page, issue and volume numbers)

Please check the document version of this publication:

- A submitted manuscript is the version of the article upon submission and before peer-review. There can be important differences between the submitted version and the official published version of record. People interested in the research are advised to contact the author for the final version of the publication, or visit the DOI to the publisher's website.
- The final author version and the galley proof are versions of the publication after peer review.
- The final published version features the final layout of the paper including the volume, issue and page numbers.

[Link to publication](#)

General rights

Copyright and moral rights for the publications made accessible in the public portal are retained by the authors and/or other copyright owners and it is a condition of accessing publications that users recognise and abide by the legal requirements associated with these rights.

- Users may download and print one copy of any publication from the public portal for the purpose of private study or research.
- You may not further distribute the material or use it for any profit-making activity or commercial gain
- You may freely distribute the URL identifying the publication in the public portal.

If the publication is distributed under the terms of Article 25fa of the Dutch Copyright Act, indicated by the "Taverne" license above, please follow below link for the End User Agreement:

www.tue.nl/taverne

Take down policy

If you believe that this document breaches copyright please contact us at:

openaccess@tue.nl

providing details and we will investigate your claim.

A Deterministic Approach to the Modelling
of Electromagnetic Wave Propagation
in Urban Environments

G.A.J. van Dooren

A Deterministic Approach to the Modelling
of Electromagnetic Wave Propagation
in Urban Environments

A Deterministic Approach to the Modelling of Electromagnetic Wave Propagation in Urban Environments

PROEFSCHRIFT

ter verkrijging van de graad van doctor aan de
Technische Universiteit Eindhoven, op gezag van
de Rector Magnificus, prof.dr. J.H. van Lint,
voor een commissie aangewezen door het College
van Dekanen in het openbaar te verdedigen op
dinsdag 29 maart 1994 te 16.00 uur

door

Gerardus Adrianus Johannes van Dooren

geboren te Roosendaal en Nispen

Dit proefschrift is goedgekeurd

door de promotoren

prof.dr.ir. G. Brussaard

en

prof.dr.ir. L.P. Ligthart

copromotor:

dr.ir. M.H.A.J. Herben.

CIP-DATA KONINKLIJKE BIBLIOTHEEK, DEN HAAG

Dooren, Gerardus Adrianus Johannes van

A deterministic approach to the modelling of
electromagnetic wave propagation in urban environments /

Gerardus Adrianus Johannes van Dooren - [S.l.: s.n.] -

Fig., foto's, tab.

Thesis Eindhoven. - With ref. - With summary in Dutch.

ISBN 90-9006889-9

NUGI 832

Subject headings: mobile telecommunications / signal interference
reduction / electromagnetic field-strength prediction.

©1994 by G.A.J. van Dooren, St. Willebrord

All rights reserved. No part of this publication may be reproduced or transmitted in any form or by any means, electronic, mechanical, including photocopy, recording, or any information storage and retrieval system, without the prior written permission of the copyright owner.

Human Behaviour

If you ever get close to a human and human behaviour, be ready to get confused.

There is definitely no logic to human behaviour, but yet so irresistible.

There is no map to human behaviour.

They are terribly moody, then all of a sudden turn happy.

But, oh, to get involved in the exchange of human emotions is ever so satisfying.

There is no map, and a compass would not help at all.

Björk Gudmundsdottir / Nellee Hooper

aan Kitty

Abstract

This thesis treats the development of a deterministic model for the electromagnetic (EM) field-strength prediction in built-up areas. The model uses Geometrical Optics (GO) together with various diffraction contributions based on the Uniform Theory of Diffraction (UTD) to determine the interaction of the EM wave with the environmental objects. Two applications of the model are discussed in this dissertation.

The first one concerns the determination of the effectiveness of placing an obstacle on the propagation path of an interfering signal in order to raise the signal-to-interference ratio of an earth-space link. Results of this intentional signal obstruction are presented for various obstacle types and positions of the observation point. Attention is also paid to the case where a receiving antenna is very close to the obstacle. In that case, a separate far-field treatment of obstacle and antenna diffraction is no longer allowed and a combined analysis should be carried out. This near-field analysis is performed for two types of parabolic reflector antennas, and results for the shielding effectiveness of obstacles are presented and compared. Also the validity of applying spatial far-field antenna weighting functions in field-strength prediction models based on ray methods is discussed.

The second application of the model described in this thesis is the prediction of the EM field strength of a Land Mobile Satellite (LMS) signal in an urban environment. Due to its deterministic character the model developed is capable of analysing effects such as specular reflection and strong shadowing. The latter are not taken into account in conventional statistical LMS field-strength prediction models. Because the GO/UTD model accepts a detailed description of the urban environment, it can be used to analyse an arbitrary environment, whereas conventional statistical models are suited for one specific geometry only. To demonstrate the capability of the model, it was used for the determination of the field strength along two trajectories at the campus of Eindhoven University of Technology. Not only the field strength, but also the Doppler spectrum, the time-delay profile and the delay-Doppler spectrogram were derived. The deterministic model is expected to be a valuable complement to existing statistical LMS field-strength prediction models, especially if detailed digital databases of towns and cities are available.

Contents

Abstract	i
1 Introduction	1
1.1 Background	1
1.2 Framework of the research	4
1.3 Scope of the thesis and survey of its contents	4
2 Review of the modelling of high-frequency EM wave propagation	7
2.1 Introduction	7
2.2 High-frequency representation of EM waves	8
2.3 Reflection of an EM wave	11
2.4 Diffraction of an EM wave	15
2.5 Higher-order diffraction contributions	23
2.5.1 Slope diffraction	23
2.5.2 Corner diffraction	24
2.5.3 Double diffraction	27
2.6 Extension of UTD for non-perfectly conducting wedges with rough faces	29
2.7 Diffraction by a rough edge	32
2.8 Reflection and diffraction by a convex obstacle	38
2.8.1 Reflection by a convex surface	40
2.8.2 Diffraction by a convex surface	41
2.9 Note on the presentation of the theory	43
3 Modelling of EM wave diffraction at obstacles with simple shapes	45
3.1 Introduction	45
3.2 Diffraction at obstacles with simple shapes	47
3.2.1 The half-plane	48
3.2.2 The finite-width screen	51
3.2.3 The metallic cylinder	55
3.2.4 The block-shaped obstacle	58
3.2.5 Finding reflection and diffraction points	62
3.3 Comparison of three field-strength prediction models	67
3.3.1 The rectangular block	67
3.3.2 UTD field-strength prediction model	68
3.3.3 FSI field-strength prediction model	69
3.3.4 PE field-strength prediction model	70
3.3.5 Comparison of results	70
3.3.6 Conclusions	71

3.3.7	Addendum: comparison of results for the half-plane and the finite-width screen	72
3.4	An engineering approach for site shielding calculations	74
3.4.1	Introduction	75
3.4.2	Average and minimum SSF	76
3.4.3	A pseudo-UTD site shielding model	79
3.4.4	Modification of the CCIR site shielding procedure	83
3.4.5	Comparison of two SSF prediction methods	84
3.4.6	A graphical method for finite-width screen shielding	86
3.4.7	Application of site shielding in a realistic situation	92
3.4.8	An engineering model for shielding by a rectangular block	92
3.4.9	Conclusions	95
4	Experimental verification	97
4.1	Introduction	97
4.2	Large-bandwidth diffraction measurements at 54 GHz using both time-domain filtering and frequency smoothing	98
4.2.1	Introduction	98
4.2.2	The measurement setup	100
4.2.3	Calibration method and measurements	103
4.2.4	SSF determination	107
4.2.5	Conclusions	110
4.3	Measurement of diffracted fields behind a thin finite-width screen	110
4.3.1	Introduction	110
4.3.2	Theoretical model and geometry	111
4.3.3	Measurement setup	112
4.3.4	Comparison of measured and theoretical results	112
4.3.5	Conclusions	114
4.4	Polarisation-dependent site shielding factor of a rectangular block	115
4.4.1	Introduction	115
4.4.2	Theoretical model, geometry and measurement setup	116
4.4.3	Comparison of measured and theoretical results	117
4.4.4	Measurement of time response	118
4.4.5	Conclusions	120
4.5	Field-strength prediction behind lossy dielectric obstacles using the UTD	120
4.5.1	Introduction	121
4.5.2	Theoretical model and geometry	121
4.5.3	Determination of complex permittivity	123
4.5.4	Comparison of measured and theoretical results	124
4.5.5	Conclusions	125
4.6	Comparison between measurements and UTD simulations of EM-wave scattering by circular cylinders	125
4.6.1	Introduction	126
4.6.2	Scattering by a circular cylinder	127
4.6.3	Numerical results	130

4.6.4	Experimental results	132
4.6.5	Conclusions	138
5	Site shielding of symmetrical parabolic reflector antennas	139
5.1	Introduction	139
5.2	Shielding of a single-reflector antenna	140
5.2.1	Description of the receiving antenna	141
5.2.2	Wide-angle reception of a parabolic reflector antenna	145
5.2.3	Reception properties of a shielded parabolic reflector antenna	153
5.2.4	Conclusions	157
5.3	On the use of antenna weight functions in field-strength prediction and interference reduction	157
5.3.1	The antenna receiving pattern	158
5.3.2	Near- and far-field simulations	159
5.3.3	Broadband analysis	162
5.3.4	Conclusions	163
5.4	Shielding of a double-reflector antenna	164
5.4.1	Description of the receiving antenna	165
5.4.2	Wide-angle reception of a Cassegrain antenna	169
5.4.3	Reception properties of a shielded Cassegrain antenna	179
5.4.4	Conclusions	180
5.5	Off-axis radiation pattern calculation of a Cassegrain antenna system with an application to site shielding	181
5.5.1	Introduction	181
5.5.2	Geometry	182
5.5.3	Radiation-pattern calculation	182
5.5.4	Shielded radiation-pattern calculation	187
5.5.5	Conclusions	190
5.6	Shielding of single- and double-reflector earth-station antennas: a near- and far-field approach	190
5.6.1	Introduction	190
5.6.2	Radiation-pattern calculation	192
5.6.3	Shielded radiation-pattern calculation	194
5.6.4	Comparison of single- and double-reflector antenna shielding	196
5.6.5	Near- and far-field antenna shielding	196
5.6.6	Conclusions	200
6	EM field-strength prediction by ray methods	201
6.1	Introduction	201
6.2	FiPre: a prediction tool for the planning of mobile and fixed satellite communication services	202
6.2.1	Introduction	203
6.2.2	Description of prediction model	204
6.2.3	Data postprocessing	207
6.2.4	Field-strength analysis	208

6.2.5	Time-delay analysis	209
6.2.6	Delay-Doppler analysis	210
6.2.7	Analysis of testcase	210
6.2.8	CPU effort	212
6.2.9	Future improvements	216
6.2.10	Conclusions	216
6.3	An efficient model for field-strength prediction	217
6.4	Discussion	219
7	Summary and conclusions	223
	References	229
	Korte samenvatting	237
	Toelichting	239
	Acknowledgments	241
	Curriculum vitae	243

Chapter 1

Introduction

1.1 Background

Due to the scarcity of available frequency spectrum, the use of the same frequency band by different users is unavoidable. This frequency reuse may introduce mutual interference between, for example, operators of an earth-space and a terrestrial radio link.

An important parameter in the frequency assignment is the coordination area, which, according to the Radio Regulations, is the area associated with an earth station outside which a terrestrial station sharing the same frequency neither causes, nor is subject to interfering emissions that exceed a permissible level. Obviously, the coordination distance, i.e. the distance beyond which a terrestrial station neither causes, nor is subject to interfering signals exceeding some threshold level, depends on the electromagnetic (EM) wave propagation mechanisms that occur in the medium in between the two terminals. Especially anomalous propagation conditions such as ducting and elevated-layer reflection are known to cause very high interfering signal levels, fortunately only for very small time percentages. In many cases where a high system reliability is needed, protective measures against inadmissible interference signal levels must be taken.

One method to reduce this interference is the placement of an object on the interfering signal propagation path, as schematically shown in Figure 1.1. This methodology is called site shielding. It can be seen in the figure that the undesired signal is obstructed by the obstacle. The signal is attenuated, but not completely removed, due to diffraction of the wave at the obstacle, and from the weaker signal it appears as if the interference source is at a larger distance. This technique can be used in operational communication systems liable to interference, to reduce the coordination distance and consequently to increase the reuse of a frequency band. So by taking into account this obstacle blockage in the planning stages of a new telecommunications link, the service planners can take advantage of the modifications introduced in this coordination parameter.

Currently available models for the prediction and analysis of the site shielding effective-

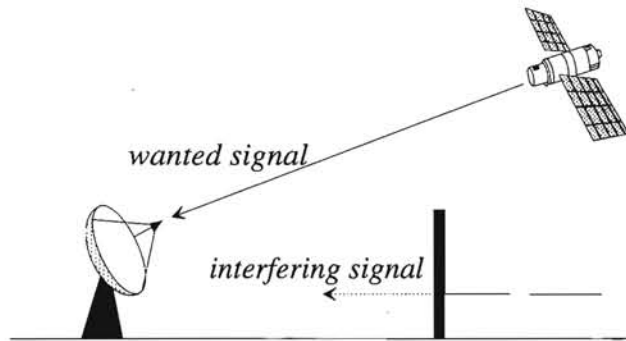


Figure 1.1: The principle of site shielding.

ness of isolated obstacles are provided by the CCIR [1, 2] and take into consideration only very simple geometries. In most of the cases the obstacle is assumed to be infinitely wide, while the antenna characteristics are extremely idealised and therefore unrealistic.

To enhance the accuracy and applicability of these site shielding models, Working Group 3 of Project 235¹ of the European organisation COST² specifically focuses on this topic with the aim of developing new, accurate site shielding models. Attention is paid to, for example, the shape of the object, the type of antenna, the obstacle-antenna distance, and the propagation mechanism responsible for the interference. Evidently, a detailed knowledge of the interaction of the interfering EM wave with the obstacle is needed. Further a thorough understanding of the spatial filtering of the receiving antenna is indispensable.

The signal blockage introduced in the site shielding method is intentional and raises the system performance, i.e. it improves the signal-to-interference ratio. In Figure 1.2 a daily situation is visualised in which the signal blockage is unintentional, and therefore undesirable. It shows a user of a Land Mobile Satellite (LMS) channel subject to 'shadowing' and multipath propagation; both effects are known to degrade system performance. This example closely resembles the previously discussed site shielding geometry since in both cases the effect of an obstacle on the signal propagation path needs to be assessed, albeit that in the latter example more objects surrounding the receiver are present. Also here a detailed knowledge concerning the interaction of the EM wave and the obstacle can be of

¹ COST 235: Radio wave propagation effects on next-generation fixed-service terrestrial telecommunications systems.

² Coopération Européenne dans le Domain de la Recherche Scientifique et Technique

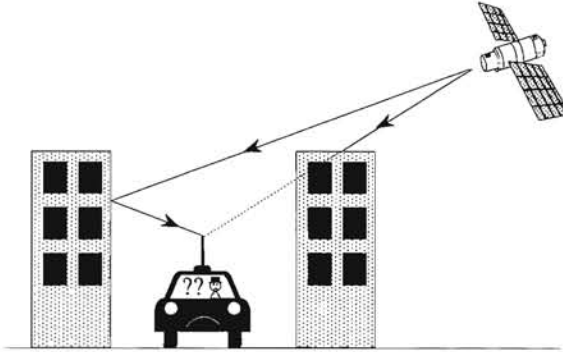


Figure 1.2: Signal blockage in an urban environment.

help in analysing this specific practical problem.

Currently available models for the planning of new LMS systems and the analysis of already installed systems are few, and most of them represent regression fits to results from measurement campaigns. Therefore they are suited for one generalised geometry only, and the strong shadowing effect as well as the specular reflection depicted in Figure 1.2 are usually not modelled adequately. Since the market for mobile telecommunications has been growing rapidly during the last few years, tools for the prediction of the field strength in an urban environment that explicit model these reflection and shadowing mechanisms have received much attention. Most of the models proposed, however, consider only a small number of propagation phenomena, such as reflection and diffraction, or are essentially two-dimensional. Obviously, a more realistic approach should involve three-dimensional geometries, and should contain a versatile, accurate and vectorial wave-propagation model. In general the model should enable the user to take into account near-field antenna effects, i.e. the case where the antenna is very close to the object, while the model should also have a deterministic character because of the desired detailed environmental input such as buildings, trees, bridges, etc. By extracting and using data from nowadays commercially available digital databases, the model itself should be applicable to nearly any scenery.

In this thesis Geometrical Optics (GO) and the Uniform Theory of Diffraction (UTD) are adopted for the composition of a ray-based field-strength prediction model matching the criteria previously mentioned. Models based on GO/UTD are well established and have been very popular ever since their introduction in the early seventies. From a theoretical point of view, they appear to be sufficiently accurate for the present application, and this will be verified in the present study. Further they permit the antenna characteristics to be

elegantly taken into account by the use of spatial antenna weight functions. The model to be developed should predict the field strength for various obstacle shapes and materials, source and observation point positions, frequencies, polarisations and types of receiving antennas.

In this study the EM wave-propagation model is applied to the site shielding as well as to the LMS geometry, although other applications such as wideband indoor radio and mobile-cellular communication services can also be thought of.

1.2 Framework of the research

As mentioned in the preceding section, two applications of the deterministic model are treated in this dissertation. For both of them a collaboration with other research institutes has been established through the years.

The site shielding problem was introduced and studied by Scheeren [3] for the case of a half-plane obstacle. These results were submitted to the European project COST 210³, which was the predecessor of COST 235. At the end of COST 210 quite a number of questions concerning site shielding remained unanswered, and it was decided to carry forward these points of attention into project COST 235. In the latter, a fruitful collaboration between the University of Glamorgan (UK), the Rutherford Appleton Laboratory (UK), Eindhoven University of Technology and some other groups was started in 1991 to combine their individual knowledge about site shielding in order to derive a better and more accurate model than presently offered by the CCIR. The author of this thesis worked in this international COST 235 project as coordinator for the subject of EM wave diffraction modelling.

A collaboration with the research centre of the European Space Agency, ESTEC, resulted in the realisation of the wave-propagation model for LMS field-strength prediction. The result of this work is also reported in this thesis.

1.3 Scope of the thesis and survey of its contents

This thesis is intended as a contribution to the development of deterministic wave-propagation models that can enhance the performance of currently available models for site shielding and field-strength prediction in urban environments. Note that it should not be con-

³ COST 210: Influence of the atmosphere on interference between radio communications systems at frequencies above 1 GHz, 1984-1991.

sidered as a replacement, but rather as a complement of current statistical models. The emphasis in the thesis will be put on the modelling of the various wave-propagation mechanisms, the practical verification of these models, the antenna spatial filtering and the use of elementary object shapes in the wave-propagation model. This is reflected in the structure of the thesis.

In Chapter 2 the high-frequency modelling of EM wave propagation as used in GO and UTD is reviewed. Theories for reflection and diffraction are discussed. Also the extension of UTD to account for surface roughness of the obstacle faces and non-perfect conductivity is examined, and a heuristic extension of UTD to account for irregular edges is proposed. Furthermore, a formal treatment of reflection and diffraction is given that can be of help in the preparation of a numerical wave-propagation model.

In Chapter 3 the site shielding models derived from GO and UTD are discussed, incorporating objects with simple shapes and an isotropic antenna at the source and observation point. For the finite-width screen with knife edges, an engineering approach for site shielding is derived, and theoretical results from three different field-strength prediction models (UTD, Fresnel surface integral and parabolic equation model) used within COST 235 are compared.

Chapter 4 concerns the practical verification of the models proposed in the previous chapter. The measurements were performed on scaled objects at a frequency of 50 GHz. During the verification a new hardware calibration scheme was developed that enables the measurements to be performed in an ordinary echoic room using a vector network analyser and signal processing techniques. Results on the relevance of diffraction by vertices, polarisation dependence of the field, and the theoretical extension of UTD to lossy material are reported and examined. Attention is also paid to scattering by cylinders.

Chapter 5 focuses on the shielding of symmetrical parabolic reflector antennas. Single- and double-reflector antennas are considered, and special attention is paid to the case where the antenna is very close to the obstacle. Results for half-plane shielding of a parabolic single- and double-reflector antenna having identical size and edge illumination are compared. Three different, but related, approaches for half-plane shielding are introduced, and results predicted by them are presented and compared. The use of the so-called far-field approach, i.e. a separate treatment of obstacle and antenna scattering as usually performed in field-strength prediction techniques, is examined. The proposed near-field models, which perform a combined analysis of obstacle and antenna diffraction, can also be of use in the determination of the optimal placement of Very-Small-Aperture Terminals (VSATs) in urban environments.

Chapter 6 covers the LMS field-strength prediction tool and the coupling of the latter

to (commercially available) digital databases using an object with a standardised shape. Results from this model are given, and derived data such as field-strength and Doppler-shift statistics are presented. Also a time-efficient computation scheme is proposed which is useful for the derivation of statistical information. Furthermore, the application of the model proposed to other types of telecommunication systems such as microcellular and terrestrial systems is discussed.

In Chapter 7 the main results of this thesis are summarised and conclusions are drawn.

Chapter 2

Review of the modelling of high-frequency EM wave propagation

2.1 Introduction

For the description of the interaction of an electromagnetic (EM) wave with objects a number of theories can be used. In general, integral representations for the EM field provide very accurate answers to scattering and diffraction problems but have the disadvantage that they are time consuming and that they do not provide a substantial insight into the problem just sketched. For this reason, and because the obstacles considered in this thesis all will be large compared to the wavelength λ , ray methods have been chosen to be used for the description of the wave interaction with obstacles.

The Geometrical Theory of Diffraction (GTD) [4] and its uniform extensions UTD [5] and UAT [6, 7] owe their popularity to the straightforward description of the edge-diffraction process and to the large number of applications that have been reported in the literature. In this thesis the UTD is used for the edge-diffraction modelling because this theory has been furthest developed, and numerous examples of its use have been reported. The fact that UAT is mathematically more rigorous is acknowledged, but from an engineering point of view the differences between the results provided by both uniform theories appear to be negligible [8, 9]. Furthermore, the uniform theories essentially reduce to GTD outside the transition regions around the shadow boundaries and therefore possible (small) differences between UTD and UAT only exist in these small regions. Therefore the UTD was adopted to model the edge-diffraction process.

A comprehensive overview between the exact solution, Kirchhoff's approximation, GTD, UTD and UAT is given in [3] for the case of a plane wave incident upon a perfectly conducting half-plane. There it is shown that, for engineering purposes, both uniform theories UTD and UAT can be used and give identical results, even if the incident wave is non-uniform with a zero amplitude at the obstacle edge.

This chapter is completely devoted to a mathematical description of the various types of wave-interaction processes such as reflection and diffraction. In Section 2.2 the high-frequency representation of EM waves is dealt with. In Sections 2.3 and 2.4 reflection and diffraction of an EM wave by an obstacle and an obstacle edge, respectively, are discussed. In some regions surrounding an object the inclusion of higher-order diffraction contributions is necessary because the first-order edge-diffracted fields vanish. For this reason, higher-order propagation mechanisms, viz. slope, corner and double diffraction, are described in Section 2.5. A heuristic extension of UTD for non-perfectly conducting wedges with rough faces is reviewed and analysed in Section 2.6. The problem of diffraction of a plane wave by a half-plane with a rough edge is addressed in Section 2.7.

In Section 2.8 attention is paid to the problem of reflection and diffraction by obstacles with convex shapes. An example of an application of this theory is the problem of the interaction of an EM wave with a street lamp post. Unless otherwise mentioned all obstacles are assumed to be perfectly conducting.

In Section 2.9 a formal description of the reflection and diffraction mechanism is presented which is quite helpful when the theory presented in this chapter is implemented in numerical algorithms.

2.2 High-frequency representation of EM waves

In this thesis we are concerned with time-harmonic EM fields propagating through free space. The time dependence adopted is $e^{j\omega t}$ with ω the radial frequency, but this exponential factor will be suppressed throughout the thesis.

To find the high-frequency asymptotic behaviour of the EM field, the electric field is expanded into an asymptotic series of the form

$$\vec{E} \propto e^{-jk\psi} \sum_{m \geq 0} \frac{\vec{E}_m}{(j\omega)^m}, \quad (2.1)$$

where $k = 2\pi/\lambda$ is the wave number for free space and ψ is the phase function. Equation (2.1) is called the *Ansatz* and is the starting point in the derivation. The electric field \vec{E} is dependent on both the position vector \vec{r} and ω , while the terms \vec{E}_m and ψ are dependent on the position vector \vec{r} only. For the magnetic field \vec{H} an identical series-representation is used.

In the subsequent part of this chapter our attention is confined to the zeroth-order terms \vec{E}_0 and \vec{H}_0 . This yields the following expressions for the ray-optical, geometrical

optics (GO) fields \vec{E} and \vec{H} ($\omega \rightarrow \infty$)

$$\vec{E} \propto e^{-jk\psi} \vec{E}_0, \quad (2.2)$$

$$\vec{H} \propto e^{-jk\psi} \vec{H}_0, \quad (2.3)$$

where the surfaces $\psi = \text{constant}$ are called equi-phase surfaces or wavefronts.

By substitution of equation (2.2) into Maxwell's curl equation for the electric field, and performing some mathematical manipulations, an explicit relation between \vec{E}_0 , \vec{H}_0 and $\nabla\psi$ is obtained. This relation is given by

$$\nabla\psi \times \vec{E}_0 = Z_0 \vec{H}_0, \quad (2.4)$$

where the direction $\nabla\psi$ is perpendicular to the wavefront, and Z_0 is the impedance of free space. Substitution of equation (2.2) into Maxwell's zero-divergence equation for the electric field results in

$$\nabla\psi \cdot \vec{E}_0 = 0. \quad (2.5)$$

Repeating the previous steps for the magnetic field \vec{H} yields

$$Z_0 (\nabla\psi \times \vec{H}_0) = -\vec{E}_0, \quad (2.6)$$

and

$$\nabla\psi \cdot \vec{H}_0 = 0. \quad (2.7)$$

After substitution of equation (2.4) into equation (2.6) we obtain the eikonal equation

$$|\nabla\psi|^2 = 1. \quad (2.8)$$

It is found that the rays in a homogeneous, isotropic medium are straight lines in space, perpendicular to the wavefronts. The ray trajectory is determined by

$$\vec{r}(s) = \vec{r}(0) + s\nabla\psi, \quad (2.9)$$

where $\vec{r}(0)$ is the position vector of the point where $s = 0$. Furthermore,

$$d\psi = |\nabla\psi| ds = ds, \quad (2.10)$$

where ds is an incremental distance along a ray path. So the phase variation along the ray trajectory is given by

$$\psi(s) = \psi(0) + s, \quad (2.11)$$

where s is the distance along $\nabla\psi$ measured positively in the direction of $\nabla\psi$, and $\psi(0)$ is the initial phase at $s = 0$.

In the subsequent part of this chapter our attention is confined to the electric field only because the magnetic field can easily be calculated from equation (2.4) once the electric field is known. The flow of energy is determined by the transport equation for \vec{E}_0 which is found by substitution of equation (2.2) into the Helmholtz equation:

$$2(\nabla\psi \cdot \nabla)\vec{E}_0 + (\nabla^2\psi)\vec{E}_0 = 0. \quad (2.12)$$

Let $\vec{E}_0(0)$ be the electric field at the reference point $s = 0$. From the transport equation (eq. (2.12)) and the use of the 'ray-tube concept' it is found that the change in amplitude of \vec{E}_0 along the ray is given by

$$\vec{E}_0(s) = \vec{E}_0(0) \sqrt{\frac{\rho_1 \rho_2}{(\rho_1 + s)(\rho_2 + s)}}, \quad (2.13)$$

where $\rho_{1,2}$ are the principal radii of curvature of the wavefront at $s = 0$ with associated principal directions $\hat{x}_{1,2}$. Here, and in the following, a caret denotes a vector with unit length. A positive (negative) radius of curvature implies that in the corresponding plane spanned by \hat{x}_i ($i = 1, 2$) and $\hat{x}_3 = \nabla\psi$ the wave is diverging (converging). It is found that at the points $s = -\rho_i$ the denominator of the radical in equation (2.13) vanishes, and hence the amplitude of the field approaches infinity. At these points the foregoing description is invalid. These points are called *caustics*, and the actual evaluation of the field at such a point should be based on another method [4, 10]. The value of s at which a caustic is located is referred to as the caustic distance. If $(s + \rho_i)$ changes sign, a phase shift of $+\pi/2$ is introduced.

The radical in equation (2.13) is called the divergence or spreading factor. Equation (2.13) reduces to the familiar $1/s$ amplitude dependence of waves with a spherical wavefront for $\rho_1 = \rho_2$ (with $\rho_{1,2} = 0$ at $s = 0$), and to the non-decaying behaviour of a plane wave for $\rho_1 = \rho_2 = \infty$. The amplitude behaviour of a wave with a cylindrical wavefront is found for $\rho_1 = \infty$ or $\rho_2 = \infty$.

For the electric field \vec{E} it is therefore found that

$$\vec{E}(s) = \vec{E}(0) \sqrt{\frac{\rho_1 \rho_2}{(\rho_1 + s)(\rho_2 + s)}} e^{-jks}, \quad (2.14)$$

with $\vec{E}(0)$ the electric field at the position $s = 0$. See Figure 2.1 for an illustration of principal radii of curvature $\rho_{1,2}$ and their associated principal directions $\hat{x}_{1,2}$, and the wavefront of an EM wave.

The expression of the electric field in equation (2.14) is valid for high-frequencies. If the electric field along a ray can be calculated using equation (2.14), then the field is said to exhibit a ray-optical behaviour.

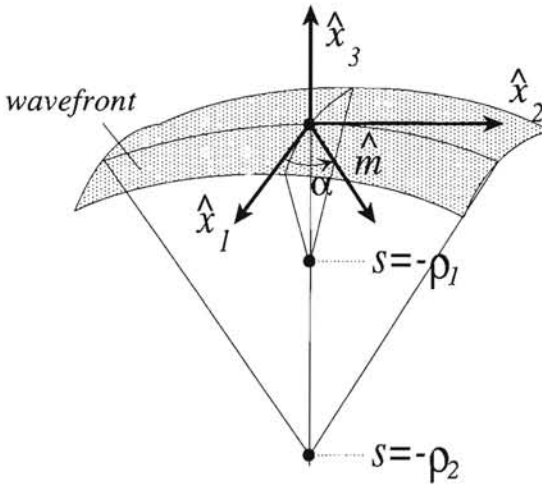


Figure 2.1: Wavefront, principal directions $\hat{x}_{1,2}$ and direction of propagation \hat{x}_3 .

From equations (2.4) and (2.6) it follows that the complex Poynting vector $\vec{E} \times \vec{H}^*$ is in the direction of $\nabla\psi$. This indicates that the power flow is in the direction \hat{x}_3 . Therefore $\hat{x}_3 = \nabla\psi$ is the direction of propagation, and $\hat{x}_{1,2,3}$ form an orthonormal system.

Notice that the propagating wave is characterised by its direction of propagation \hat{x}_3 , its principal directions $\hat{x}_{1,2}$ and its principal radii of curvature $\rho_{1,2}$, its amplitude and phase dependence as given by equation (2.14), and $\vec{E}(0)$ at the reference point $s = 0$.

Sometimes it is necessary to calculate the radius of curvature of the wavefront in a plane that is not coincident with one of the principal planes. Let this normal section be spanned by \hat{x}_3 and \hat{m} (Fig. 2.1) such that it makes an angle $\alpha = \arccos(\hat{x}_1 \cdot \hat{m})$ with the plane spanned by \hat{x}_3 and \hat{x}_1 . The radius of curvature in the plane spanned by \hat{x}_3 and \hat{m} is denoted by ρ_m and is calculated from Euler's law

$$\frac{1}{\rho_m} = \frac{\cos^2 \alpha}{\rho_1} + \frac{\sin^2 \alpha}{\rho_2}. \quad (2.15)$$

2.3 Reflection of an EM wave

If an EM wave is incident upon an obstacle, or in general an impedance boundary such as a perfect conductor, reflection occurs. To distinguish between the fields which are present before and after reflection, the superscripts i and r are introduced, referring to the *incident* and *reflected* field, respectively. The interaction of the EM wave with the obstacle will occur at the intersection R of the incident ray and the reflecting surface Σ .

At R the ray-optical reflected wave is generated and consequently its amplitude and phase dependence can be described by equation (2.14). It is characterised by a triplet $\hat{x}_{1,2,3}^r$, the radii of curvature $\rho_{1,2}^r$ of the wavefront, and \vec{E}^r . These parameters of the reflected wave are not only dependent on the parameters of the incident wave, but also on the (curvature) parameters of the reflecting surface Σ at R , and the reflection coefficients of Σ at R . The parameters of the reflecting surface Σ are described by a triplet $\hat{x}_{1,2,3}^\Sigma$ and principal radii of curvature $\rho_{1,2}^\Sigma$. These vector triplets are shown in Figure 2.2.

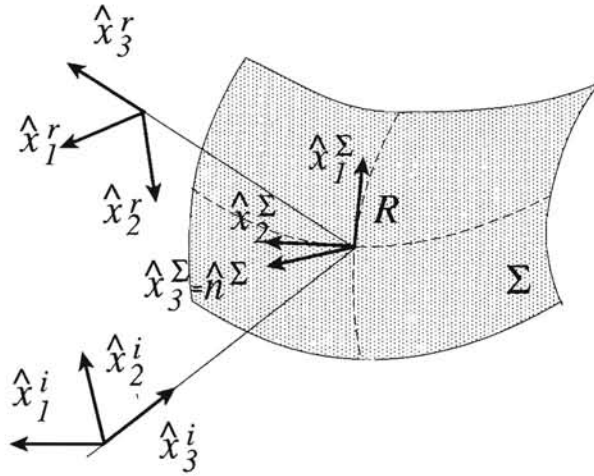


Figure 2.2: Reflection of a EM wave at R .

Let $\hat{n}^\Sigma = \hat{x}_3^\Sigma$ be the normal vector to the surface Σ at R pointing into the direction from which the wave is incident, such that $\hat{n}^\Sigma \cdot \hat{x}_3^i < 0$. The sign of the radius of curvature of a principal plane at R is positive (negative) if the corresponding normal section bends away from (towards) \hat{n}^Σ . With this sign convention a convex normal section has a positive radius of curvature, while a concave has a negative one. For a convex surface the normal vector is pointing away from both centres of curvature, while for a concave surface, the reverse is true.

The direction of propagation \hat{x}_3^r of the reflected wave depends on \hat{x}_3^i and \hat{x}_3^Σ at the reflection point R . The relation between \hat{x}_3^r , \hat{x}_3^i and \hat{x}_3^Σ is called Snell's law and is given by

$$\hat{x}_3^r = \hat{x}_3^i - 2\hat{x}_3^\Sigma(\hat{x}_3^i \cdot \hat{x}_3^\Sigma). \quad (2.16)$$

The calculation of the reflected field parameters $\hat{x}_{1,2}^r$ and $\rho_{1,2}$ is not a trivial task [5]. To

this end the (2×2) matrices \bar{Q}^i and \bar{Q}^Σ are introduced with the elements

$$Q_{11}^{i,\Sigma} = \frac{1}{\rho_1^{i,\Sigma}}, \quad (2.17)$$

$$Q_{22}^{i,\Sigma} = \frac{1}{\rho_2^{i,\Sigma}}, \quad (2.18)$$

$$Q_{12}^{i,\Sigma} = Q_{21}^{i,\Sigma} = 0. \quad (2.19)$$

Subsequently, the matrix \bar{P}^i is introduced as

$$\bar{P}^i = \begin{bmatrix} \hat{x}_1^i \cdot \hat{x}_1^\Sigma & \hat{x}_1^i \cdot \hat{x}_2^\Sigma \\ \hat{x}_2^i \cdot \hat{x}_1^\Sigma & \hat{x}_2^i \cdot \hat{x}_2^\Sigma \end{bmatrix}. \quad (2.20)$$

With these definitions, the curvature matrix \bar{Q}^r for the reflected field is given by [5]

$$\bar{Q}^r = \bar{Q}^i - 2(\hat{x}_3^i \cdot \hat{x}_3^\Sigma) \left(\bar{P}^i \right)^{-T} \bar{Q}^\Sigma \left(\bar{P}^i \right)^{-1}, \quad (2.21)$$

where the $^{-T}$ operation is the transpose of the inverse of a matrix, and the $^{-1}$ operation corresponds to the inverse of a matrix. The curvature matrix \bar{Q}^r is defined with respect to the basis vectors $\hat{x}_{1,2}^r$ given by

$$\hat{x}_{1,2}^r = \hat{x}_{1,2}^i - 2\hat{x}_3^\Sigma (\hat{x}_{1,2}^i \cdot \hat{x}_3^\Sigma). \quad (2.22)$$

These vectors are not the principal directions of the wavefront of the reflected wave. However, they are needed in the calculation of the latter.

Expressions for the elements of the matrix \bar{Q}^r can be found in [5, 3]

$$Q_{11}^r = \frac{1}{\rho_1^i} - \frac{2(\hat{x}_3^i \cdot \hat{x}_3^\Sigma)}{\det(\bar{P}^i)^2} \left(\frac{(P_{22}^i)^2}{\rho_1^\Sigma} + \frac{(P_{21}^i)^2}{\rho_2^\Sigma} \right), \quad (2.23)$$

$$Q_{12}^r = Q_{21}^r = \frac{2(\hat{x}_3^i \cdot \hat{x}_3^\Sigma)}{\det(\bar{P}^i)^2} \left(\frac{P_{22}^i P_{12}^i}{\rho_1^\Sigma} + \frac{P_{11}^i P_{21}^i}{\rho_2^\Sigma} \right), \quad (2.24)$$

$$Q_{22}^r = \frac{1}{\rho_2^i} - \frac{2(\hat{x}_3^i \cdot \hat{x}_3^\Sigma)}{\det(\bar{P}^i)^2} \left(\frac{(P_{12}^i)^2}{\rho_1^\Sigma} + \frac{(P_{11}^i)^2}{\rho_2^\Sigma} \right), \quad (2.25)$$

where $\det(\bar{P}^i)$ denotes the determinant of the matrix \bar{P}^i . Using the expressions for the elements of the matrix \bar{Q}^r , the principal radii of curvature of the wavefront of the reflected wave are found to be

$$\frac{1}{\rho_{1,2}^r} = \frac{1}{2} (Q_{11}^r + Q_{22}^r) \pm \frac{1}{2} \left[(Q_{11}^r - Q_{22}^r)^2 + 4(Q_{12}^r)^2 \right]^{1/2}, \quad (2.26)$$

whereas its principal directions are given by

$$\hat{x}_1^r = \left[\left(Q_{22}^r - \frac{1}{\rho_1^r} \right) \hat{x}_1^{r'} - Q_{12}^r \hat{x}_2^{r'} \right] \cdot \left[\left(Q_{22}^r - \frac{1}{\rho_1^r} \right)^2 + (Q_{12}^r)^2 \right]^{-1/2}, \quad (2.27)$$

$$\hat{x}_2^r = -\hat{x}_3^r \times \hat{x}_1^r. \quad (2.28)$$

The reflected field \vec{E}^r follows from the incident field \vec{E}^i and the normal vector \hat{x}_3^Σ at the reflection point R . The boundary condition for the total electric field $\vec{E}^t = \vec{E}^i + \vec{E}^r$ at R only determines the tangential parts of $\vec{E}^{i,r}$

$$\hat{x}_3^\Sigma \times \vec{E}^t(R) = \hat{x}_3^\Sigma \times \vec{E}^i(R) + \hat{x}_3^\Sigma \times \vec{E}^r(R) = 0. \quad (2.29)$$

Furthermore, the divergence relation for the total electric field at R gives that

$$\nabla \cdot \vec{E}^t(R) = \nabla \cdot \vec{E}^i(R) + \nabla \cdot \vec{E}^r(R) = 0, \quad (2.30)$$

which yields

$$\vec{E}^i(R) \cdot \hat{x}_3^\Sigma = \vec{E}^r(R) \cdot \hat{x}_3^\Sigma. \quad (2.31)$$

This leads to the relation between \vec{E}^r , \vec{E}^i and the surface normal \hat{x}_3^Σ at the reflection point R

$$\vec{E}^r(R) = -\vec{E}^i(R) + 2\hat{x}_3^\Sigma (\vec{E}^i(R) \cdot \hat{x}_3^\Sigma). \quad (2.32)$$

The relation between \vec{E}^r , \vec{E}^i and \hat{x}_3^Σ at R can compactly be written as

$$\vec{E}^r(R) = \vec{E}^i(R) \cdot \mathcal{R}^r, \quad (2.33)$$

where the dyadic reflection factor \mathcal{R}^r is given by

$$\mathcal{R}^r = \hat{e}_\perp^i \hat{e}_\perp^{r'} R_s^r + \hat{e}_\parallel^i \hat{e}_\parallel^{r'} R_h^r, \quad (2.34)$$

and, in the case of reflection by a perfect conductor, $R_{s,h}^r$ are given by

$$R_{s,h}^r = \mp 1. \quad (2.35)$$

In equation (2.35) the subscripts s and h refer to soft and hard, respectively. For soft polarisation the electric field is perpendicular to the plane of incidence, which is spanned by the vectors \hat{x}_3^i and \hat{x}_3^Σ . For hard polarisation, the electric field is parallel to the plane of incidence. For reflection by a dielectric impedance boundary, the $R_{s,h}^r$ are given by Fresnel's reflection coefficients.

The unit vectors $\hat{e}_{\perp,\parallel}^{i,r}$ used in equation (2.34) are given by

$$\hat{e}_\perp^i = \hat{e}_\perp^r = \frac{\hat{x}_3^i \times \hat{x}_3^\Sigma}{|\hat{x}_3^i \times \hat{x}_3^\Sigma|}, \quad (2.36)$$

$$\hat{e}_{\parallel}^i = \hat{e}_{\perp}^i \times \hat{x}_3^i, \quad (2.37)$$

$$\hat{e}_{\parallel}^r = \hat{e}_{\perp}^r \times \hat{x}_3^r. \quad (2.38)$$

The reflected field at an observation point P along the ray trajectory in the direction \hat{x}_3^{Σ} is thus found from

$$\vec{E}^r(P) = \vec{E}^r(R) \sqrt{\frac{\rho_1^r \rho_2^r}{(\rho_1^r + s)(\rho_2^r + s)}} e^{-jks}, \quad (2.39)$$

where s is the distance from R to P along \hat{x}_3^{Σ} . Equation (2.39) conforms to the propagation of a ray-optical field as discussed in equation (2.14). The reflected field \vec{E}^r at R is calculated using equation (2.33), while the radii of curvature of the wavefront of the reflected field $\rho_{1,2}^r$ at R can be calculated using equation (2.26).

As can be seen from equation (2.39), the reflected field is proportional to the incident field. For this case it is said that the reflected field is of order k^0 with respect to the incident field of order k^0 .

2.4 Diffraction of an EM wave

Since in GO the waves travel along straight lines, this asymptotic theory does not allow for the propagation of EM waves around edges. This means that, if at an observation point P the direct, i.e. GO, contribution for some reason is obstructed, no field would be present at all. Actually, this implies that the GO field is discontinuous in the case of ray obstruction. The location where this obstruction takes place is called a shadow boundary (SB); there is a shadow boundary associated with the incident field (ISB) and one associated with the reflected field (RSB). In geometrical optics the direct and reflection contributions are indeed discontinuous, and for this reason a diffracted field is introduced to complement the GO terms. The diffracted field is also discontinuous at the same location where the GO field, either direct or reflected, is discontinuous. The sum of the GO field and the diffracted field, however, remains continuous when .

In this section we pay attention to edge-diffracted rays. An edge is a curve where the wedge surfaces meet such that the normal vector \hat{n} for both surfaces is different, i.e. \hat{n} is discontinuous when going from one surface to the other one via the edge. The incident wave propagates along rays in the direction \hat{x}_3^i , and one of these rays intersects the obstacle edge in the diffraction point Q . At Q the edge locally is approximated by two planes that are tangential to the obstacle surfaces. These planes form a wedge geometry.

The diffraction mechanism is different from the reflection mechanism in that a whole family of diffracted rays is generated at Q . A point of similarity with the reflection mechanism is that the diffracted wave is also ray-optical, so the amplitude and phase along

a diffracted ray can be described by equation (2.14). The superscript d is introduced to indicate the diffracted wave. The diffraction point Q at the edge of the obstacle serves as a caustic of the diffracted field since all the diffracted rays seem to emanate from this point. For this reason the introduction of only one radius of curvature ρ^d suffices, i.e. after diffraction one of the radii of curvature of the diffracted wavefront $\rho_{1,2}^d$ has a zero value at Q .

At the point Q Keller's law of edge diffraction yields the directions of the edge-diffracted rays [4]

$$\hat{s}' \cdot \hat{e} = \hat{s} \cdot \hat{e}, \quad (2.40)$$

where \hat{s}' corresponds to the direction of the incident ray, \hat{s} is the direction of the diffracted ray, and \hat{e} is the unit vector tangent to the edge at Q . This law can be seen as the diffraction equivalent of Snell's law for reflection. In general, the diffracted rays form a cone with the apex at the diffraction point Q , semi-angle $\beta = \arccos(\hat{s}' \cdot \hat{e})$ and axis of symmetry \hat{e} . The diffraction cone is depicted in Figure 2.3. In case the angle $\beta = \pi/2$, the cone degenerates

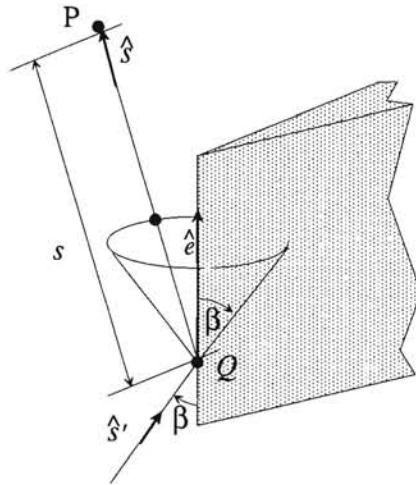


Figure 2.3: Cone of diffracted rays generated at straight edge.

into a plane through the diffraction point Q perpendicular to the edge tangent \hat{e} .

To describe the diffraction mechanism at Q , a so-called *edge-fixed coordinate system* is introduced which is shown in Figure 2.4a. The following edge-fixed unit vectors are introduced

$$\hat{\varphi} = \frac{\hat{s}' \times \hat{e}}{|\hat{s}' \times \hat{e}|}, \quad (2.41)$$

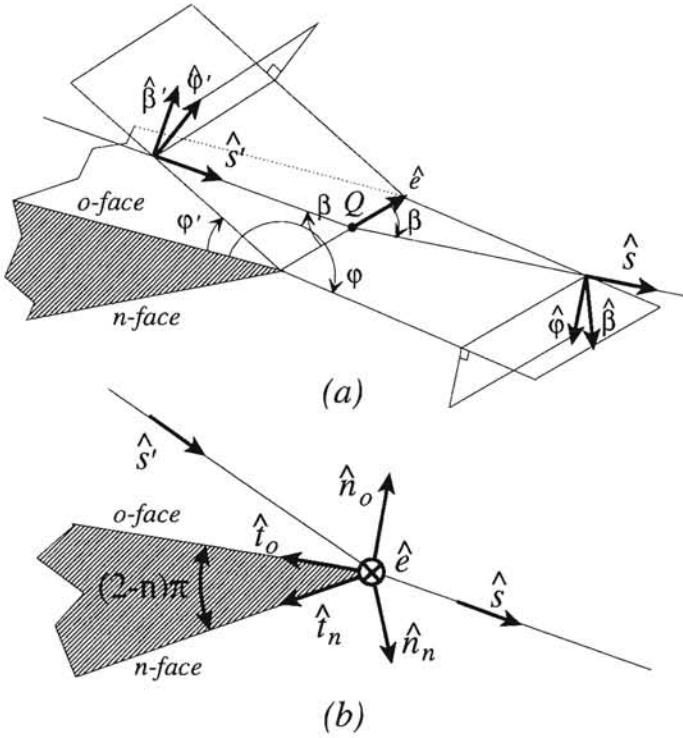


Figure 2.4: The edge-fixed coordinate system is shown in part (a), while a projection of the vectors \hat{s}' and \hat{s} on a plane perpendicular to \hat{e} through Q is depicted in part (b).

$$\hat{\beta}' = \hat{\varphi}' \times \hat{s}', \quad (2.42)$$

$$\hat{\varphi} = \frac{\hat{e} \times \hat{s}}{|\hat{e} \times \hat{s}|}, \quad (2.43)$$

$$\hat{\beta} = \hat{\varphi} \times \hat{s}. \quad (2.44)$$

The exterior wedge angle is $n\pi$. At the diffraction point Q the unit normal vector \hat{n}_o to the *o*-face, and the unit normal vector \hat{n}_n to the *n*-face are introduced (Fig. 2.4b). The unit tangent vectors \hat{t}_o and \hat{t}_n are found from $\hat{t}_o = \hat{n}_o \times \hat{e}$ and $\hat{t}_n = \hat{e} \times \hat{n}_n$.

Referring to the triplets $\hat{x}_{1,2,3}^{i,r,d}$ for the description of the ray-optical fields and the triplets $(\hat{n}, \hat{e}, \hat{t})$ and $(\hat{\beta}', \hat{\varphi}', \hat{s}')$, $(\hat{\beta}, \hat{\varphi}, \hat{s})$ for the description of the fields and the diffraction mechanism, it may seem that one of these descriptions is redundant. So why not use only one, consistent definition? The answer is that the description using $\hat{x}_{1,2,3}^{i,r,d}$ is used for a general description of GO wave propagation and it can effectively be used in ray-tracing techniques. The other coordinate systems are dependent on the orientation of the wedge and therefore

are specific for the diffraction mechanism. When implementing a numerical algorithm the various vector triplets will often be used in a mixed way.

The diffracted electric field \vec{E}^d at an observation point P on the diffracted ray can be calculated from the incident field \vec{E}^i at the diffraction point Q using [5]

$$\vec{E}^d(P) = \vec{E}^i(Q) \cdot \mathcal{D} \sqrt{\frac{\rho^d}{s(\rho^d + s)}} e^{-jks}. \quad (2.45)$$

In this equation $\vec{E}^d(P)$ is the diffracted field at an observation point P , with s the distance from Q to P along the diffracted ray, $\vec{E}^i(Q)$ is the incident field at Q , \mathcal{D} a dyadic diffraction factor and ρ^d the radius of curvature of the wavefront of the diffracted wave. In equation (2.45) the optical characteristics in terms of phase dependence and spreading factor are evident. Furthermore, only one radius of curvature ρ^d is present because s is measured from the diffraction point Q , and hence the point with coordinate $s = 0$ is a caustic. Note that due to the product $\vec{E}^i(Q) \cdot \mathcal{D}$ the wave can be depolarised by the diffraction process.

The dyadic diffraction factor \mathcal{D} in equation (2.45) is given by [5]

$$\mathcal{D} = -\hat{\beta}'\hat{\beta}D_s - \hat{\varphi}'\hat{\varphi}D_h, \quad (2.46)$$

and the factors $D_{s,h}$ are called the *three-dimensional diffraction coefficients*. The subscripts s and h correspond to the soft ($\hat{\beta}'$) and hard ($\hat{\varphi}'$) components of \vec{E}^i . The soft component of \vec{E}^i is parallel to the plane spanned by \hat{s}' and \hat{e} , while the hard component of \vec{E}^i is perpendicular to this plane. The coefficients $D_{s,h}$ are given by [5]

$$D_{s,h} = D_1 + D_2 + R_{s,h}^n D_3 + R_{s,h}^o D_4, \quad (2.47)$$

with

$$D_1 = -\frac{e^{-j\pi/4}}{2n\sqrt{2\pi k} \sin \beta} \cot\left(\frac{\pi + \varphi^-}{2n}\right) F(kL^i a^+(\varphi^-)), \quad (2.48)$$

$$D_2 = -\frac{e^{-j\pi/4}}{2n\sqrt{2\pi k} \sin \beta} \cot\left(\frac{\pi - \varphi^-}{2n}\right) F(kL^i a^-(\varphi^-)), \quad (2.49)$$

$$D_3 = -\frac{e^{-j\pi/4}}{2n\sqrt{2\pi k} \sin \beta} \cot\left(\frac{\pi + \varphi^+}{2n}\right) F(kL^r a^+(\varphi^+)), \quad (2.50)$$

$$D_4 = -\frac{e^{-j\pi/4}}{2n\sqrt{2\pi k} \sin \beta} \cot\left(\frac{\pi - \varphi^+}{2n}\right) F(kL^r a^-(\varphi^+)), \quad (2.51)$$

and $\varphi^\mp = \varphi \mp \varphi'$. The reflection coefficients $R_{s,h}^o$ and $R_{s,h}^n$ for a perfect conductor are the reflection coefficients as given in equation (2.35). In equations (2.48) to (2.51), φ' is the angle between the projection \hat{s}'_t of \hat{s}' onto a plane through Q perpendicular to \hat{e} and

the wedge surface, φ is the angle between the projection \hat{s}_t of \hat{s} onto a plane through Q perpendicular to \hat{e} and the wedge surface. Both angles are measured from the o -face, as indicated in Figure 2.4a. The projections of, respectively, \hat{s}' and \hat{s} onto the plane through Q perpendicular to \hat{e} are given by the unit vectors

$$\hat{s}'_t = \frac{-\hat{s}' + (\hat{s}' \cdot \hat{e})\hat{e}}{|-\hat{s}' + (\hat{s}' \cdot \hat{e})\hat{e}|} = \frac{-\hat{s}' + \cos \beta \hat{e}}{\sin \beta}, \quad (2.52)$$

$$\hat{s}_t = \frac{\hat{s} - (\hat{s} \cdot \hat{e})\hat{e}}{|\hat{s} - (\hat{s} \cdot \hat{e})\hat{e}|} = \frac{\hat{s} - \cos \beta \hat{e}}{\sin \beta}. \quad (2.53)$$

The angles φ' and φ can be unambiguously determined by [11]

$$\varphi' = \pi - \left[\pi - \arccos(\hat{s}'_t \cdot \hat{t}_o) \right] \text{sgn}(\hat{s}'_t \cdot \hat{n}_o), \quad (2.54)$$

$$\varphi = \pi - \left[\pi - \arccos(\hat{s}_t \cdot \hat{t}_o) \right] \text{sgn}(\hat{s}_t \cdot \hat{n}_o), \quad (2.55)$$

where the $\text{sgn}(\cdot)$ function is introduced according to

$$\text{sgn}(x) = \begin{cases} 1 & , \text{ if } x \geq 0, \\ -1 & , \text{ if } x < 0. \end{cases} \quad (2.56)$$

The transition function $F(\cdot)$ in equations (2.48) to (2.51) involves a Fresnel integral and is given by [5]

$$F(x) = 2j\sqrt{x}e^{jx} \int_{\sqrt{x}}^{\infty} e^{-ju^2} du. \quad (2.57)$$

This function may be approximated for small and large arguments by simpler expressions. For $x < 0.1$, the transition function is well approximated by

$$F(x) \approx \left[\sqrt{x\pi} - 2xe^{j\pi/4} - \frac{2x^2e^{-j\pi/4}}{3} \right] e^{j(x+\pi/4)}, \quad (2.58)$$

whereas for large arguments ($x > 10$) a series expansion for $F(x)$ is given by

$$F(x) \approx 1 + \frac{j}{2x} - \frac{3}{4x^2} - \frac{j15}{8x^3} + \frac{105}{16x^4}. \quad (2.59)$$

For small arguments the transition function $F(x)$ is of order $x^{1/2}$, as for large arguments it is of order x^0 . An approximation of the Fresnel function convenient for numerical evaluation for $0.1 \leq x \leq 10$ is given in [12]. The real and imaginary part of $F(x)$ are given in Figure 2.5.

The functions $a^\pm(\cdot)$ in equations (2.48) to (2.51) are given by [5]

$$a^\pm(x) = 2 \cos^2 \left(\frac{2n\pi N^\pm - x}{2} \right), \quad (2.60)$$

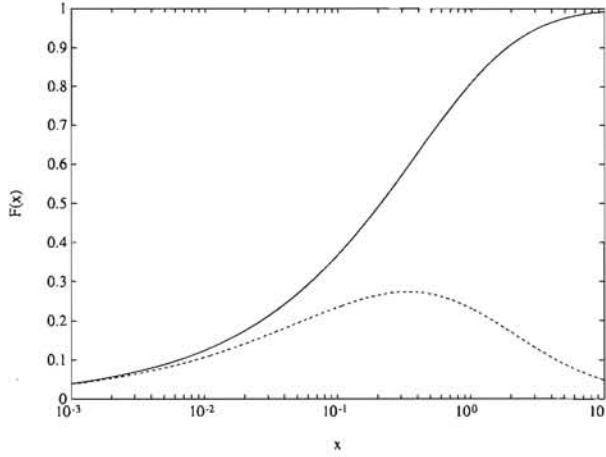


Figure 2.5: Real (————) and imaginary (-----) part of the transition function $F(x)$.

where N^\pm ($N^\pm \in \{-1, 0, 1\}$) are integers which minimise the functions f and g given by

$$f(x) = |2\pi n N^+ - x - \pi|, \quad (2.61)$$

$$g(x) = |2\pi n N^- - x + \pi|. \quad (2.62)$$

It should be noted that the superscript $+$ is associated with the n -face, whereas the superscript $-$ is associated with the o -face. More details concerning the functions a^\pm can be found in [5].

The distance parameter L^i in equations (2.48) and (2.49) is given by

$$L^i = \frac{s(\rho_e^i + s)\rho_1^i \rho_2^i}{\rho_c^i(\rho_1^i + s)(\rho_2^i + s)} \sin^2 \beta. \quad (2.63)$$

The parameter ρ_e^i is the radius of curvature of the wavefront of the incident wave in the plane spanned by \hat{s}' and \hat{e} , and can be calculated using Euler's law (eq. (2.15)). For a wave with a spherical or plane wavefront $\rho_e^i = \rho_{1,2}^i = \rho$ and the expression for L^i simplifies considerably:

$$L^i = \frac{s\rho}{s + \rho} \sin^2 \beta. \quad (2.64)$$

Also for a wave with a cylindrical wavefront some simplifications for L^i are introduced, but they will not shown here.

It is found from a theoretical investigation that the radii of curvature $\rho_{1,2}^{o,rn}$ of the wavefront of the reflected wave are also necessary to evaluate the diffraction coefficients,

viz. in the factors $L^{ro, rn}$. The distance parameters $L^{ro, rn}$ have similar expressions as that of the distance parameter L^i :

$$L^{ro, rn} = \frac{s(\rho_e^{ro, rn} + s)\rho_1^{ro, rn}\rho_2^{ro, rn}}{\rho_e^{ro, rn}(\rho_1^{ro, rn} + s)(\rho_2^{ro, rn} + s)} \sin^2 \beta, \quad (2.65)$$

where $\rho_{1,2}^{ro, rn}$ are the principal radii of curvature of the wavefront of the wave reflected from the o - or n -face, respectively. They can be found by applying the matrix transformation of incident-field parameters and surface parameters to the reflected-field parameters, viz. equation (2.21). The radius of curvature of the wavefront of the reflected wave in the plane spanned by \hat{e} and \hat{x}_3^r is denoted by $\rho_e^{ro, rn}$, where the superscripts ro and rn refer to reflection from the o -face and n -face, respectively. It can be shown that this particular choice of $L^{i, ro, rn}$ enforces continuity across the shadow boundaries for non-converging incident waves [3]. For incident converging waves, a complex correction factor should be used [13]. Notice that if the matrix \bar{P}^i in equation (2.21) is singular, the transition functions in the three-dimensional diffraction coefficients should be replaced by the value 1. This is the case if $\hat{n}_{o,n} \perp \hat{x}_3^i$, which corresponds to grazing incidence.

Until now nothing has been said about the curvature of the edge at the diffraction point Q . The radius of curvature of the wavefront of the edge-diffracted field ρ^d in equation (2.45) is found from [5]

$$\frac{1}{\rho^d} = \frac{1}{\rho_e^i} - \frac{\hat{n}_e \cdot (\hat{s}' - \hat{s})}{a_e \sin^2 \beta}, \quad (2.66)$$

with $a_e > 0$ the radius of curvature of the edge at the diffraction point Q , and \hat{n}_e is the normal vector to the edge, pointing away from the centre of curvature, as depicted in Figure 2.6. It is in this way that the curvature from an edge affects the diffracted field

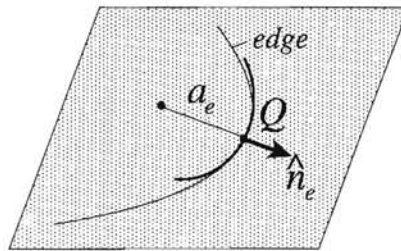


Figure 2.6: Definition of the radius of curvature a_e of the edge and the edge normal \hat{n}_e .

from the wedge. This knowledge can for instance be used to suppress the amplitude of diffracted fields in antenna systems and compact test ranges [14]. It is possible that the observation point P is located at a caustic of the diffracted field. In this case the UTD can not be applied.

Around the incident and reflection shadow boundary, respectively, a region can be distinguished in which the diffracted field exhibits a rapid spatial variation. These regions are called the *transition regions*, and are bounded by [11]

$$kLa^\pm = 2\pi. \quad (2.67)$$

For plane wave illumination this equation defines an area with a parabolic contour, with either the incident (ISB) or the reflection shadow boundary (RSB) as symmetry axis, and the edge as the focus. The higher the frequency, the smaller the transition region becomes; for $\lambda \rightarrow 0$ the width of the transition region reduces to 0. The transition regions are shown in Figure 2.7. The interpretation of the transition function $F(\cdot)$ is that it makes

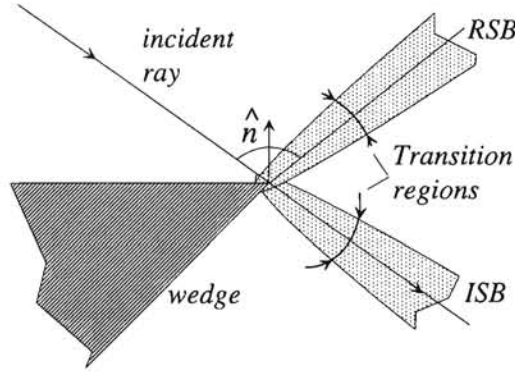


Figure 2.7: Transition regions at a wedge illuminated by a plane wave. The upper transition region is associated with the reflection shadow boundary (RSB), as the lower transition region is associated with the incident shadow boundary (ISB).

the UTD bounded at the shadow boundaries. Setting $F = 1$ results in a reduction of UTD to GTD, being singular at the shadow boundaries. The argument of F becomes zero for observation points on the shadow boundary, while the cotangent function becomes singular. The product of the transition function F with the cotangent function, however, is finite. Traversing the shadow boundary from the lit region to the shadow region results in a discontinuity of the edge-diffracted field which precisely compensates the abrupt obstruction of the GO field. The total field is therefore continuous across the shadow boundary.

Outside the transition regions the edge-diffracted field is of order $k^{-1/2}$ with respect to the incident field of order k^0 . Inside the transition regions, the edge-diffracted field is of order k^0 .

2.5 Higher-order diffraction contributions

The edge-diffraction contributions just discussed are the main contributions to the total field if the GO terms (direct, reflected) are not present. If also the first-order edge-diffraction contributions for some reason vanish, higher-order diffraction contributions should be taken into account in calculating the field strength at an observation point P . Some of these are discussed in the following. Notice that the adjective ‘higher-order’ is used for diffraction terms of order k^{-n} , where $n > 1/2$, as well as for multiple-diffraction terms. The latter are also of order k^{-n} , $n > 1/2$, but this is due to a repeated interaction with the obstacle. The higher-order terms discussed in this section do not correspond to the ‘higher-order’ terms \vec{E}_m used in equation (2.1).

2.5.1 Slope diffraction

From equation (2.45) it can be seen that the diffracted field is proportional to the amplitude of the incident field at the diffraction point Q . In the case of an incident field with a zero amplitude at the edge, the next higher-order term needs to be incorporated for an accurate computation of the diffracted field. This term is called the *slope-diffracted field*, and can be calculated using [15]

$$\vec{E}_{\beta,\varphi}^{d,slope}(P) = \frac{1}{jk \sin \beta} \frac{\partial \vec{E}_{\beta',\varphi'}^i(Q)}{\partial \hat{n}} \frac{\partial D_{s,h}}{\partial \varphi'} \sqrt{\frac{\rho^d}{s(\rho^d + s)}} e^{-jks}, \quad (2.68)$$

with $E_{\beta',\varphi'}^i$ denoting the soft ($\hat{\beta}'$) and hard ($\hat{\varphi}'$) component of the incident field at the diffraction point Q , respectively. The directional derivative of the incident field is in a direction \hat{n} that points from the shadow region into the lit region, perpendicular to both the direction of propagation \hat{s}' and the edge tangent vector \hat{e} . Apart from the first-order edge-diffracted field (eq. (2.45)), the total edge-diffracted field consists of higher-order terms of which the slope-diffracted field is one. In [16] it is shown that the total edge-diffracted field \vec{E}_{total}^d can compactly be written as

$$\vec{E}_{total}^d = \vec{E}^d + \vec{E}^{d,slope} + \vec{E}^{d*} + \dots, \quad (2.69)$$

where \vec{E}^d is the diffraction field proportional to the incident field amplitude given in equation (2.45), $\vec{E}^{d,slope}$ is the conventional slope-diffracted field proportional to the directional derivative of the incident field as given in equation (2.68), and \vec{E}^{d*} is an additional slope-diffraction term proportional to the incident-field amplitude. If the amplitude of the incident field is zero it can readily be deduced from equation (2.69) that the term $\vec{E}^{d,slope}$ is indeed the next higher-order term because the other terms \vec{E}^d and \vec{E}^{d*} vanish. If the

amplitude is not equal to zero, the \vec{E}^d term, as well as the $\vec{E}^{d,slope}$ and the \vec{E}^{d*} , should be taken into account. At present, no UTD expressions for this term have been formulated, but GTD-like expressions are given in [16].

For an incident field of order k^0 it is found that the slope-diffraction term $\vec{E}^{d,slope}$ given in equation (2.68) is of order $k^{-3/2}$ outside the transition regions, while it is of order $k^{-1/2}$ in the transition regions.

2.5.2 Corner diffraction

The geometry for corner diffraction is shown in Figure 2.8. The point source S illuminates a perfectly conducting quarter-plane, and the observation point P is in the shadow region of the obstacle as seen from S . One of the rays from the source hits the corner D_c , which is defined as an intersection of two edges. In the geometry shown, also an edge-diffraction point D_e is identified. The importance of the corner-diffraction contribution can be demonstrated by assuming that the observation point P moves into the direction specified by the edge tangent \hat{e} . The edge-diffraction point D_e will move towards D_c until they coalesce. At this point P is said to be on the diffraction shadow boundary because any further movement of P into the direction of \hat{e} will cause the edge-diffraction contribution to suddenly vanish. This discontinuity is compensated for by the corner-diffraction contribution in a similar way as the edge-diffraction contribution compensates the discontinuous GO contribution. The sum of edge-diffracted and corner-diffracted fields is continuous through the diffraction shadow boundary [17]. Since a corner is made up from at least two edges there is a corner-diffracted field for each edge.

If an incident field with a spherical wavefront is considered, the corner-diffracted field \vec{E}^c of a planar geometry (Fig. 2.8) associated with a corner and edge 1 of the obstacle is given by

$$\vec{E}^c(P) = \vec{E}^i(D_c) \cdot \mathcal{D}_c \sqrt{\frac{ss'(s+s_c)}{s''s_c(s'+s'')}} \frac{e^{-jks}}{s}, \quad (2.70)$$

where s' is the distance from S to D_e , s_c is the distance from S to D_c , s'' is the distance from D_e to P , and s is the distance from D_c to P . Notice that the corner-diffracted ray has a $1/s$ amplitude dependence, indicating that the corner acts a point source. The dyadic factor \mathcal{D}_c is given by

$$\mathcal{D}_c = -\hat{\beta}'\hat{\beta}D_s^c - \hat{\varphi}'\hat{\varphi}D_h^c, \quad (2.71)$$

and the corner diffraction coefficients $D_{s,h}^c$ are expressed as

$$D_{s,h}^c = C_{s,h}(D_e) \frac{\sqrt{\sin \beta_{0c} \sin \beta_c}}{\cos \beta_{0c} - \cos \beta_c} F[kL_c a(\pi + \beta_{0c} - \beta_c)] \frac{e^{-j\pi/4}}{\sqrt{2\pi k}}, \quad (2.72)$$

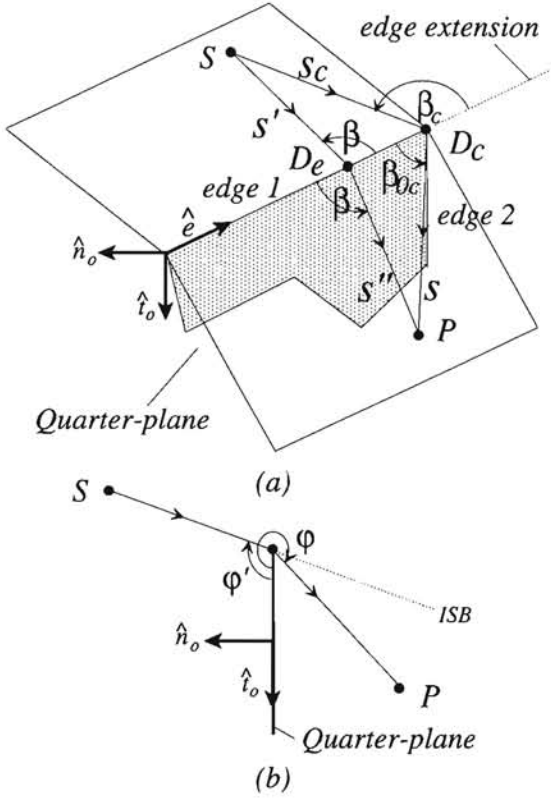


Figure 2.8: Geometry for corner diffraction at a quarter-plane (a), and definition of angles φ and φ' in a plane perpendicular to \hat{e} (b).

and

$$C_{s,h}(D_e) = \frac{-e^{-j\pi/4}}{2\sqrt{2\pi k} \sin \beta} \left[\frac{F(kLa(\varphi^-))}{\cos(\varphi^-/2)} \left| F\left(\frac{La(\varphi^-)/\lambda}{kL_c a(\pi + \beta_{0c} - \beta_c)}\right) \right| \right. \\ \left. + R_{s,h}^r \frac{F(kLa(\varphi^+))}{\cos(\varphi^+/2)} \left| F\left(\frac{La(\varphi^+)/\lambda}{kL_c a(\pi + \beta_{0c} - \beta_c)}\right) \right| \right], \quad (2.73)$$

where the reflection coefficients $R_{s,h}^r$ for a perfect conductor are given by $R_{s,h}^r = \mp 1$. The angles φ and φ' are defined in Figure 2.8b, while $a(x) = 2 \cos^2(x/2)$. The distance parameters L and L_c are given by

$$L = \frac{s's''}{s' + s''} \sin^2 \beta, \quad (2.74)$$

and

$$L_c = \frac{s_c s}{s_c + s}, \quad (2.75)$$

respectively. The angle β_c is measured from \hat{e} to the incident ray at D_c , whereas β_{0c} is the angle measured from the edge to the corner-diffracted ray. The angle β is the angle between the incident ray at D_e and \hat{e} . The transition function $F(\cdot)$ is given by equation (2.57). The modification factor

$$\left| F \left(\frac{La(\varphi^\mp)/\lambda}{kL_c a(\pi + \beta_{0c} - \beta_c)} \right) \right|, \quad (2.76)$$

is a heuristically derived function which ensures that the diffraction coefficient will not change sign abruptly when it passes through the diffraction shadow boundary of the edge [17].

The expression for the function $C_{s,h}$ as given in equation (2.73) is only valid for a geometry in which the exterior wedge angle is 2π . If the corner is part of some three-dimensional geometry then another expression for the coefficient $C_{s,h}$ should be used [18]. Every pair of edges making up a corner geometry should be treated independently, and the exterior wedge angle $n\pi$ of each geometry may be different from 2π . If a geometry is not illuminated by a source S then its contribution is neglected.

For $n \neq 2$ the proper expression for $C_{s,h}$ is given by

$$C_{s,h}(D_e) = D_1^c + D_2^c + R_{s,h}^n D_3^c + R_{s,h}^o D_4^c \quad (2.77)$$

with

$$D_1^c = -\frac{e^{-j\pi/4}}{2n\sqrt{2\pi k} \sin \beta} \cot \left(\frac{\pi + \varphi^-}{2n} \right) \Im \left(kL^i a^+(\varphi^-) \right), \quad (2.78)$$

$$D_2^c = -\frac{e^{-j\pi/4}}{2n\sqrt{2\pi k} \sin \beta} \cot \left(\frac{\pi - \varphi^-}{2n} \right) \Im \left(kL^i a^-(\varphi^-) \right), \quad (2.79)$$

$$D_3^c = -\frac{e^{-j\pi/4}}{2n\sqrt{2\pi k} \sin \beta} \cot \left(\frac{\pi + \varphi^+}{2n} \right) \Im \left(kL^r a^+(\varphi^+) \right), \quad (2.80)$$

$$D_4^c = -\frac{e^{-j\pi/4}}{2n\sqrt{2\pi k} \sin \beta} \cot \left(\frac{\pi - \varphi^+}{2n} \right) \Im \left(kL^r a^-(\varphi^+) \right), \quad (2.81)$$

and where the function $\Im(\cdot)$ has been introduced according to

$$\Im(x) = F(x) \left| F \left(\frac{x/2\pi}{kL_c a(\pi + \beta_{0c} - \beta_c)} \right) \right|, \quad (2.82)$$

and the function F has been defined in equation (2.57). It can easily be shown that for $n = 2$ equation (2.77) reduces to equation (2.73). Equation (2.77) shows some similarity with equation (2.47). The reflection coefficients $R_{s,h}^o$ and $R_{s,h}^n$ were also used in this equation; $R_{s,h}^o = \mp 1$ for a perfect conductor, while for a dielectric they are given by Fresnel's reflection coefficients.

The formulation used here is based on an approximate method which provides continuity when traversing the diffraction shadow boundary. Investigations have revealed that this formulation shows good numerical agreement with another approach [19] which is based on an approximation to the radiation integral to account for corner diffraction phenomena [20]. From the comparison of results in [20] it is concluded that, for the application considered in this thesis, the present formulation of the corner-diffraction coefficient will suffice, although the physical basis, i.e. the induced surface currents and their behaviour near the corner, may be criticised.

The corner-diffracted field is of order k^{-1} outside the transition regions, it is of order $k^{-1/2}$ inside the transition regions associated with the edge-diffracted field ($\varphi^\pm \approx \pi$) or if $\beta_{0c} \approx \beta_c$, and of order k^0 in the transition region where $\varphi^\pm \approx \pi$ and $\beta_{0c} \approx \beta_c$.

2.5.3 Double diffraction

The diffraction terms dealt with on the previous pages are called higher-order diffraction terms because they can be used in addition to the edge-diffracted field. In case none of the formerly discussed wave contributions are present it is sometimes necessary to incorporate also double-diffracted waves. The double-diffracted wave can be calculated by performing twice the procedure as outlined for the single-diffracted wave, with the diffracted field from the first diffraction point Q_1 acting as incident field for the second diffraction point Q_2 . A typical geometry for using double diffraction is depicted in Figure 2.9a. Below the diffraction shadow boundary (DSB) double diffraction is the only remaining type of contribution.

The diffracted field from the first edge is called the primary diffracted field. This field is present in the whole space, except in the region to the right of the obstacle and below the DSB. The only field in the latter region is the diffracted field from the second edge and it is called the secondary diffracted field.

The primary diffracted field, incident at grazing angle upon the second, perfectly-conducting edge, has a zero $\hat{\beta}$ component due to the boundary condition. For this component the slope-diffracted field should be used to obtain continuity of the total field if the DSB is traversed. For the $\hat{\varphi}$ component of the primary diffracted field this is not necessary. In fact, the slope-diffracted field for the $\hat{\varphi}$ component is zero. Now a consecutive application of the edge-diffraction algorithm yields a continuous total field when the DSB is traversed. In addition, a factor 1/2 is introduced for the amplitude of the secondary diffracted field because its incident and reflection shadow boundary coalesce [15].

Some caution is needed in the evaluation of the double-diffracted field because the

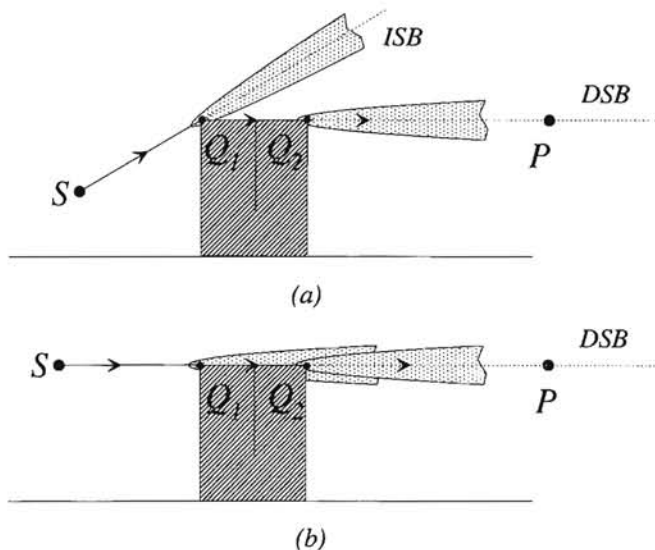


Figure 2.9: Diffraction at a pair of joined wedges; non-overlapping transition regions shown in (a), and overlapping transition regions shown in (b).

incident field should be ray-optical. In the calculation of the secondary diffracted field the distance from Q_1 to Q_2 should be large compared to λ . Furthermore, the distance from S to Q_1 and from Q_2 to P should be large compared to the wavelength [21]. If the second edge lies in the transition region of the primary diffracted field, severe errors will be introduced by mechanically applying wedge diffraction. See Figure 2.9b for an example of overlapping transition regions. To cope with this problem, closed form, double-wedge diffraction coefficients have been derived during the last decade for the case of overlapping transition regions [22, 23, 24, 25].

The double-diffracted field \vec{E}^{dd} can be thought to arise from two sequential interactions

$$\vec{E}^{dd}(P) = \mathcal{D}_{Q_2} \left(\mathcal{D}_{Q_1} \left(\vec{E}^i \right) \right), \quad (2.83)$$

where \mathcal{D}_{Q_l} corresponds to diffraction at the point Q_l ($l = 1, 2$), and \vec{E}^i is the incident field at Q_1 . The diffraction operator \mathcal{D} corresponds to the calculation of the diffracted field for the associated edge as set out in equation (2.69) and further. The operation $\mathcal{D}_{Q_1}(\vec{E}^i)$ yields the primary diffracted field at Q_2 , while $\mathcal{D}_{Q_2}(\cdot)$ gives the secondary diffracted field at P .

The incident field \vec{E}^i is of order k^0 . For non-overlapping transition regions, the double-diffracted field is of order k^{-1} outside, and of order $k^{-1/2}$ inside one of the transition regions. In case the transition regions are overlapping, the double-diffracted field is of

order k^{-1} outside the (overlapping) transition regions, and of order k^0 inside the transition regions. As already mentioned, errors will be introduced in the computation of \vec{E}^{dd} if the transition regions of the primary and secondary diffracted field overlap.

2.6 Extension of UTD for non-perfectly conducting wedges with rough faces

The reflection coefficients $R_{s,h}^{o,n}$ as used in GTD and UTD can be modified to include effects of non-perfect conductivity and roughness of the wedge faces. Notice that this extension does not satisfy Maxwell's equation in any formal sense, but encouraging results have been obtained by using this method [26, 27].

The soft and hard reflection coefficients $R_s^{o,n}$ and $R_h^{o,n}$ in the factors \mathcal{R}^r (eq. (2.34)), $D_{s,h}$ (eq. (2.47)), and $C_{s,h}$ (eq. (2.77)) are replaced by Fresnel's reflection coefficients $R_{s,h}^F$ in case the object is made of dielectric material, while also an additional attenuation factor ρ_r for the surface roughness is taken into account. This results in the following expressions for $R_{s,h}$ [26, 27, 28]

$$R_s^{o,n} = R_s^F \rho_r = \frac{\sin \theta - \sqrt{\varepsilon_r - \cos^2 \theta}}{\sin \theta + \sqrt{\varepsilon_r - \cos^2 \theta}} e^{-(\Delta\varphi)^2/2}, \quad (2.84)$$

and

$$R_h^{o,n} = R_h^F \rho_r = \frac{\varepsilon_r \sin \theta - \sqrt{\varepsilon_r - \cos^2 \theta}}{\varepsilon_r \sin \theta + \sqrt{\varepsilon_r - \cos^2 \theta}} e^{-(\Delta\varphi)^2/2}, \quad (2.85)$$

where it has been assumed that the relative permeability μ_r of the obstacle is equal to 1, and the complex relative permittivity is given by ε_r . Furthermore, the angle θ is the angle between the reflecting surface and the direction of propagation of the incident or reflected ray. For reflection by either the o - or n -face the angle θ is given by

$$\theta = \pi/2 - \arccos(-\hat{s}' \cdot \hat{n}), \quad (2.86)$$

where the unit normal vector $\hat{n} = \hat{n}_o$ for reflection by the o -face, and $\hat{n} = \hat{n}_n$ for reflection by the n -face. The normal vectors $\hat{n}_{o,n}$ have been introduced in Figure 2.4b.

The parameter $\Delta\varphi$ is related to the surface roughness and is given by

$$\Delta\varphi = 2k\Delta h \sin \theta, \quad (2.87)$$

with Δh being the standard deviation of the surface height which has a normal distribution and zero mean. The expressions for $R_{s,h}^F$ as in equations (2.84) and (2.85) automatically reduce to ∓ 1 in case the faces of the wedge are perfectly conducting ($|\varepsilon_r| \gg 1$) and their

roughness is zero ($\Delta h = 0$). In the extension of UTD for non-perfectly conducting objects several assumptions have been made that will be briefly discussed.

The reflection coefficients as given by equations (2.84) and (2.85) are the average reflection coefficients for rough surfaces. An underlying assumption is that the irregularities of the surface have a normal distribution, and that the irregularities of two adjacent surface points are uncorrelated, i.e. the correlation distance $T = 0$ [28]. Furthermore, it is assumed that the transmission of the incident wave through the object may be neglected, indicating that the complex relative permittivity has a large absolute value. If the assumption of transmittivity is not fulfilled also multiple reflections within the wedge should be taken into account. Recently this problem including internal reflections was solved for a lossless dielectric wedge, where the wave is incident under an angle of $\pi/2$ with the edge tangent \hat{e} ($\beta = \pi/2$) [29, 30]. The mathematical solution proposed, however, is very complicated and not suited for engineering purposes.

To have a continuous total field across the reflection shadow boundary, the same reflection coefficients should be used for the GO reflected ray and the edge-diffracted ray. If these reflection coefficients are also used in the calculation of the slope-diffracted field, it can be shown that a continuous total field is obtained [31]. If the derivatives are calculated taking into account the partial derivatives of the reflection coefficients with respect to θ , the slope-diffracted field for a non-perfectly conducting wedge automatically provides a continuous total field across the shadow boundary.

As can be deduced from the foregoing, the modification of the diffraction coefficient for non-perfectly conducting objects only affects the part that is proportional to the reflected field of either the σ - or n -face. For a perfectly absorbing wedge the reflected wave amplitude is zero. This implies that the part of the diffraction coefficient associated with the reflected wave vanishes. Consequently, the reflection shadow boundary disappears and the diffraction coefficient $D_{s,h}$ reduce to

$$D_s = D_h = D_1 + D_2, \quad (2.88)$$

with $D_{1,2}$ as given in equations (2.48) and (2.49). A similar result is reported in [32].

The usefulness of the heuristic extension of the UTD in the way just explained is discussed in [33], where also a comparison is made between results obtained from the extended UTD and a method based on a canonical solution for diffraction by a wedge with impedance faces [34]. Good agreement was obtained between the results calculated by both methods. A comparison of predicted results using the extended UTD and measured results for diffraction by a three-dimensional object can be found in Section 4.5.

The complex relative permittivity ϵ_r used in equations (2.84) and (2.85) is given by

$$\epsilon_r = \epsilon - j \frac{\sigma}{\omega \epsilon_0}, \quad (2.89)$$

where ϵ is the relative permittivity of the material, ϵ_0 is the permittivity of vacuum, and σ is the conductivity. Values of ϵ and σ of some common materials are given in Tables 2.1 to 2.3.

Table 2.1: Relative permittivity ϵ and conductivity σ of some materials [35]; σ in $\Omega^{-1}m^{-1}$.

Material	ϵ	$\sigma \cdot 10^{-6}$
Al	1	37
Cu	1	58
Fe	1	4.8
Zn	1	1.6
Ni	1	1.3
glass	5-10	10^{-18}
wood	3-7	10^{-18}
perspex	3	10^{-27}
porcelain	7	10^{-18}
Si	12	10^{-11}
dry ground	3	10^{-10}

Table 2.2: Relative permittivity ϵ and conductivity σ of brick as function of relative humidity at a frequency of 37.5 GHz [36]; σ in $\Omega^{-1}m^{-1}$.

Rel. Hum. [%]	ϵ	$\sigma \cdot 10^3$
0	3.1	0
2	3.6	173.2
4	3.8	577.9
6	4.2	1274.6
8	4.8	2086.2
10	5.1	3129.3
12	5.9	4172.3
14	6.4	5570.1
16	7.1	7656.3

Table 2.3: Relative permittivity ϵ and conductivity σ of brick as function of frequency and humidity [36]; $\sigma \cdot 10^3$, σ in $\Omega^{-1}m^{-1}$.

frequency [GHz]	Relative Humidity			
	0%	5%	10%	15%
0.1	$\epsilon = 3.3$	$\epsilon = 5.3$	$\epsilon = 8.7$	$\epsilon = 12.9$
	$\sigma = 0$	$\sigma = 4.4$	$\sigma = 6.6$	$\sigma = 8.9$
0.3	$\epsilon = 3.3$	$\epsilon = 5.3$	$\epsilon = 8.7$	$\epsilon = 12.9$
	$\sigma = 0$	$\sigma = 6.6$	$\sigma = 11.7$	$\sigma = 16.7$
1	$\epsilon = 3.3$	$\epsilon = 5.3$	$\epsilon = 8.7$	$\epsilon = 12.9$
	$\sigma = 0$	$\sigma = 16.7$	$\sigma = 33.4$	$\sigma = 46.2$
3	$\epsilon = 3.3$	$\epsilon = 5.3$	$\epsilon = 8.7$	$\epsilon = 12.9$
	$\sigma = 0$	$\sigma = 83.4$	$\sigma = 156.9$	$\sigma = 267.0$
10	$\epsilon = 3.3$	$\epsilon = 4.9$	$\epsilon = 7.5$	$\epsilon = 11.6$
	$\sigma = 0$	$\sigma = 389.4$	$\sigma = 1001.4$	$\sigma = 1780.2$
30	$\epsilon = 3.3$	$\epsilon = 4.4$	$\epsilon = 5.8$	$\epsilon = 7.6$
	$\sigma = 0$	$\sigma = 1168.3$	$\sigma = 3004.1$	$\sigma = 5507.0$

2.7 Diffraction by a rough edge

Up to now, the theory presented considers the edge on which the diffraction point lies to be smooth. In many cases, however, the edge is rough. A literature survey revealed that currently no theory is available to tackle the problem of diffraction by a rough edge, neither in a deterministic nor in a statistical way.

The problem of reflection of an EM wave at a rough surface was solved in [28], and this solution was used in the heuristic extension of the UTD to account for non-perfect conductivity and surface roughness (Sec. 2.6). The modified reflection coefficients $R_{s,h}$ can compactly be written as

$$R_{s,h} = R_{s,h}^F \rho_r, \quad (2.90)$$

where $R_{s,h}^F$ are the Fresnel reflection coefficients and ρ_r is the reflection attenuation factor. Expressions for $R_{s,h}^F$ and ρ_r are given in Section 2.6. It seems plausible that also for diffraction by a rough edge some modification factor for the diffraction coefficient should be introduced. To investigate the influence of edge roughness on the diffracted field, in this section a modification factor is derived for the special case of a plane incident wave and a crenated half-plane edge.

To this end, the concept of equivalent edge currents is used [37]. According to this theory, the far-zone diffracted field due to the edge C of a wedge with plane faces is given

by

$$\vec{E}^d(\vec{r}) \propto jk \int_C [Z_0 I(\vec{r}') \hat{s} \times (\hat{s} \times \hat{e}) + M(\vec{r}') \hat{s} \times \hat{e}] G(\vec{r}', \vec{r}) dl, \quad (2.91)$$

where k is the wavenumber of the incident wave, Z_0 is the impedance of free space, \vec{r} and \vec{r}' are the position vectors of the point of observation and of an integration point on the contour C , respectively. The tangent vector to C at \vec{r}' is denoted by \hat{e} and the direction of observation \hat{s} is given by

$$\hat{s} = \frac{\vec{s}}{s} = \frac{\vec{r} - \vec{r}'}{|\vec{r} - \vec{r}'|}. \quad (2.92)$$

The three-dimensional Green's function G is expressed as

$$G(\vec{r}', \vec{r}) = \frac{e^{-jks}}{4\pi s}. \quad (2.93)$$

The quantities $I(\vec{r}')$ and $M(\vec{r}')$ are the tangential parts of the electric and magnetic equivalent currents, respectively. For a perfectly-conducting half-plane edge ($n = 2$, $a_e = \infty$) these currents are given by [37]

$$I(\vec{r}') = \frac{2j\sqrt{2}Y_0 \sin(\varphi'/2)(\sin \beta' - \sin \beta \cos \varphi)^{1/2} \vec{E}(\vec{r}') \cdot \hat{e}}{k(\sin \beta')^{3/2}(\sin \beta \cos \varphi + \sin \beta' \cos \varphi')} + \frac{2j\sqrt{2} \cos \varphi \cos(\varphi'/2)(\sin^2 \beta \cos \beta' - \sin^2 \beta' \cos \beta) \vec{H}(\vec{r}') \cdot \hat{e}}{k(\sin \beta')^{3/2} \sin \beta (\sin \beta \cos \varphi + \sin \beta' \cos \varphi')(\sin \beta' - \sin \beta \cos \varphi)^{1/2}}, \quad (2.94)$$

and

$$M(\vec{r}') = \frac{2\sqrt{2}Z_0 \sin \varphi \cos(\varphi'/2) \vec{H}(\vec{r}') \cdot \hat{e}}{jk \sin \beta (\sin \beta \cos \varphi + \sin \beta' \cos \varphi')} \left(\frac{\sin \beta'}{\sin \beta' - \sin \beta \cos \varphi} \right)^{1/2}, \quad (2.95)$$

where $\vec{E}(\vec{r}')$ is the incident electric field at the integration point, $\vec{H}(\vec{r}')$ is the incident magnetic field, $Y_0 = 1/Z_0$ is the admittance of free space, φ' (φ) is the angle between the plane of incidence (diffraction) and the screen face, and β' (β) is the angle between the direction of incidence (diffraction) and the edge tangent \hat{e} . These angles are defined in Figure 2.10.

Equation (2.91) expresses that the edge-diffracted field can be found using some integration of (hypothetical) electric and magnetic currents. The (GTD) diffracted field can be found using an asymptotic evaluation of the integral in equation (2.91).

In this section we will confine ourselves to diffraction by a half-plane with a crenated edge. This obstacle is shown in Figure 2.11 and can be thought of as an infinite array of joined strips of width $2T$, placed in the yz -plane. Each strip extends infinitely into the $-y$ direction, and the end is at $y = \xi_l$. At the centre of the strip-end an origin O_l with coordinates $(0, \xi_l, \delta + 2Tl)$ is introduced, with $l = \dots, -2, -1, 0, 1, 2, \dots$, and δ an arbitrary

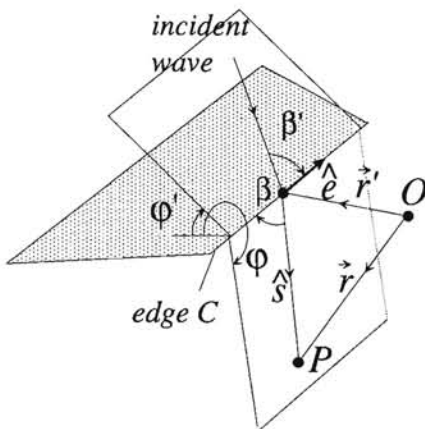


Figure 2.10: Geometry for integration of equivalent currents.

constant with $0 < \delta < 2T$. Furthermore, ξ_l has a normal distribution with zero mean and variance μ . The plane wave is incident under an angle $\beta' = \pi/2$ with the z -axis.

The unit vector from O_l to the point P with coordinates $(x_p, y_p, 0)$ is denoted by \hat{s}_l , and the distance from O_l to P is s_l . The tangent vector \hat{e} to the strip-end is $\hat{e} = \hat{z}$. Along segment l the distance $s_l(z)$ from a point on this segment to P is approximated by

$$s_l(z) \approx s_l + \xi \sin \beta_l \cos \varphi - z \cos \beta_l, \quad (2.96)$$

where z varies from $-T$ to $+T$ with respect to O_l , and β_l is the angle between \hat{s}_l and \hat{e} . For $\beta' = \pi/2$ some simplifications in the expressions for the equivalent currents I and M arise

$$I(\vec{r}')_{\beta'=\pi/2} = \frac{2j\sqrt{2}Y_0 \sin(\varphi'/2)(1 - \sin \beta \cos \varphi)^{1/2} \vec{E}(\vec{r}') \cdot \hat{e}}{k(\sin \beta \cos \varphi + \cos \varphi')} - \frac{2j\sqrt{2} \cos \varphi \cos(\varphi'/2) \cos \beta \vec{H}(\vec{r}') \cdot \hat{e}}{k \sin \beta (\sin \beta \cos \varphi + \cos \varphi')(1 - \sin \beta \cos \varphi)^{1/2}}, \quad (2.97)$$

$$M(\vec{r}')_{\beta'=\pi/2} = \frac{2\sqrt{2}Z_0 \sin \varphi \cos(\varphi'/2) \vec{H}(\vec{r}') \cdot \hat{e}}{jk \sin \beta (\sin \beta \cos \varphi + \cos \varphi')} \left(\frac{1}{1 - \sin \beta \cos \varphi} \right)^{1/2}. \quad (2.98)$$

In the subsequent analysis it will be assumed that $\xi_l \ll T$. Therefore only the strip ends oriented into the z -direction will contribute to the diffracted field at P , and consequently the field due to the connection between strip l and strip $(l+1)$ is neglected ($l = \dots, -2, -1, 0, 1, 2, \dots$).

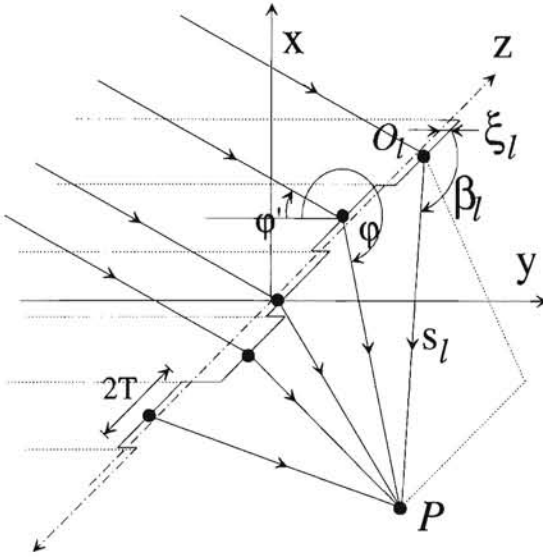


Figure 2.11: Geometry for diffraction by a crenated half-plane edge.

For an E-polarised wave, $\vec{E} = E_o \hat{z} \exp[-jk(-x \sin \varphi' + y \cos \varphi')]$, it can be readily seen that $M = 0$ and that the diffracted field is given by

$$\vec{E}^d(P) = - \int_C \frac{2\sqrt{2} \sin(\varphi'/2)(1 - \sin \beta \cos \varphi)^{1/2}}{(\sin \beta \cos \varphi + \cos \varphi')4\pi s} E_o \exp[-jks - jk\xi \cos \varphi'] \hat{s} \times (\hat{s} \times \hat{z}) dz. \quad (2.99)$$

The integral can be approximated by the sum of the contributions of the individual segments l , while also the co-polarised z -component of the field is extracted

$$E_z^d(P) = -2\sqrt{2} \sin(\varphi'/2) E_o \sum_{l=-\infty}^{l=\infty} \int_{O_l-T}^{O_l+T} \frac{(1 - \sin \beta_l \cos \varphi)^{1/2}}{4\pi s_l (\sin \beta_l \cos \varphi + \cos \varphi')} (\hat{s}_l \times (\hat{s}_l \times \hat{z})) \cdot \hat{z} \exp[-jks_l - jk\xi_l (\cos \varphi' + \sin \beta_l \cos \varphi) + jkz \cos \beta_l] dz, \quad (2.100)$$

where for every segment $\beta = \beta_l$ has been used. The integral over z can be solved analytically and gives rise to a sinc-function, while the triple product gives an additional factor $-\sin^2 \beta_l$. Also the distance s_l can be expressed as $s_l = s_0 / \sin \beta_l$, where $s_0 = \sqrt{x_p^2 + y_p^2}$ is the shortest distance from P to the z -axis. This results in

$$E_z^d(P) = \frac{\sqrt{2} \sin(\varphi'/2) E_o T}{s_0 \pi} \sum_{l=-\infty}^{l=\infty} \frac{(1 - \sin \beta_l \cos \varphi)^{1/2}}{(\sin \beta_l \cos \varphi + \cos \varphi')} \text{sinc}(kT \cos \beta_l) \sin^3 \beta_l \cdot \exp[-jks_0 / \sin \beta_l - jk\xi_l (\cos \varphi' + \sin \beta_l \cos \varphi)]. \quad (2.101)$$

The ratio E_z^d/E_0 can be compactly expressed as

$$\frac{E_z^d}{E_0} = \sum_{l=-\infty}^{l=\infty} f(\varphi', \varphi, T, \beta_l) \exp[-jk\xi_l(\cos \varphi' + \sin \beta_l \cos \varphi)], \quad (2.102)$$

with

$$f(\varphi', \varphi, T, \beta) = \frac{\sqrt{2}T \sin(\varphi'/2)(1 - \sin \beta \cos \varphi)^{1/2} \text{sinc}(kT \cos \beta) \sin^3 \beta e^{-jk s_0 / \sin \beta}}{s_0 \pi (\sin \beta \cos \varphi + \cos \varphi')}. \quad (2.103)$$

The previous procedure can also be carried out for an H-polarised wave. The incident magnetic field is given by $\vec{H} = H_0 \hat{z} \exp[-jk(-x \sin \varphi' + y \cos \varphi')]$. For this case it appears that the fields due to the electric current I are cross-polarised. Therefore only the diffracted field caused by M is considered to derive the ratio H_z^d/H_0 . Repeating the previous analysis for this incident field yields

$$\frac{H_z^d}{H_0} = \sum_{l=-\infty}^{l=\infty} g(\varphi', \varphi, T, \beta_l) \exp[-jk\xi_l(\cos \varphi' + \sin \beta_l \cos \varphi)], \quad (2.104)$$

with

$$g(\varphi', \varphi, T, \beta) = -\frac{\sqrt{2}T \sin \varphi \cos(\varphi'/2) \text{sinc}(kT \cos \beta) \sin^3 \beta e^{-jk s_0 / \sin \beta}}{s_0 \pi (\cos \varphi' + \sin \beta \cos \varphi)(1 - \sin \beta \cos \varphi)^{1/2}}. \quad (2.105)$$

The results for the ratios E_z^d/E_0 and H_z^d/H_0 can be regarded as the product of an attenuation function ρ_d with the integral representation of the GTD edge-diffracted field. In the far-field $s_0 \rightarrow \infty$ and $\beta_l \approx \pi/2$. Both results can then be expressed as

$$V_E = \sum_{l=-\infty}^{l=\infty} f(\varphi', \varphi, T, \pi/2) e^{-ja\xi_l}, \quad (2.106)$$

$$V_H = \sum_{l=-\infty}^{l=\infty} g(\varphi', \varphi, T, \pi/2) e^{-ja\xi_l}, \quad (2.107)$$

with

$$a = k(\cos \varphi' + \cos \varphi). \quad (2.108)$$

These expressions relate the amplitude and phase of the diffracted field to the incident field. The quantity $V_{E,H}$ is a complex number consisting of an infinite amount of components with a random phase $a\xi_l$. It can be shown that the average value $\overline{V_{E,H}}$ of $V_{E,H}$ is given by [28]

$$\overline{V_E} = e^{-a^2 \mu^2 / 2} \sum_{l=-\infty}^{l=\infty} f(\varphi', \varphi, T, \pi/2), \quad (2.109)$$

$$\overline{V_H} = e^{-a^2 \mu^2 / 2} \sum_{l=-\infty}^{l=\infty} g(\varphi', \varphi, T, \pi/2), \quad (2.110)$$

The series containing f and g can be written as an integral of equivalent currents along a straight edge in order to derive the GTD diffracted fields. After using a stationary phase approximation to the integral in equation (2.91), the ratio E_z^d/E_0 is expressed as

$$\frac{E_z^d}{E_0} = \exp \left[-2 \left[k\mu \cos(\varphi^+/2) \cos(\varphi^-/2) \right]^2 \right] D_s^{GTD} \frac{e^{-jk_s0}}{\sqrt{s_0}} = \rho_d D_s^{GTD} \frac{e^{-jk_s0}}{\sqrt{s_0}}, \quad (2.111)$$

while the ratio H_z^d/H_0 is given by

$$\frac{H_z^d}{H_0} = \exp \left[-2 \left[k\mu \cos(\varphi^+/2) \cos(\varphi^-/2) \right]^2 \right] D_h^{GTD} \frac{e^{-jk_s0}}{\sqrt{s_0}} = \rho_d D_h^{GTD} \frac{e^{-jk_s0}}{\sqrt{s_0}}, \quad (2.112)$$

where $\varphi^\pm = \varphi \pm \varphi'$, ρ_d is the diffraction attenuation function, and the diffraction coefficient $D_{s,h}^{GTD}$ for a half-plane with a straight edge can be deduced from equation (2.47) by substitution of $n = 2$ and $F(\cdot) = 1$ in equations (2.48) to (2.51). An explicit expression for the GTD diffraction coefficients is given in equation (3.5) where the transition functions F should be set to 1.

Equations (2.111) and (2.112) indicate that the diffraction coefficient $D_{s,h}^C$ of a crenated half-plane edge is given by the diffraction coefficient $D_{s,h}^{GTD}$ of the smooth half-plane edge multiplied by the diffraction attenuation function ρ_d . This is expressed by

$$D_{s,h}^C = D_{s,h}^{GTD} \rho_d, \quad (2.113)$$

where ρ_d is given by

$$\rho_d = \exp \left[-2 \left[k\mu \cos(\varphi^+/2) \cos(\varphi^-/2) \right]^2 \right]. \quad (2.114)$$

Notice that $\rho_d = 1$ for $\varphi^\pm = \pi$ and $\varphi^\pm = 3\pi$. This indicates that on the shadow boundaries the crenatures have no effect on the amplitude of the diffracted field. Obviously the GTD diffraction coefficients are singular here.

Also the average power at P , $\overline{V_{E,H}^2}$, was determined. This result, however, does not allow a straightforward interpretation and will not be given here.

The value of ρ_d as function of φ and $k\mu$ is given in Figure 2.12 for $\varphi' = \pi/2$.

Note that the diffraction attenuation function ρ_d can also be derived in an other way. To this end we consider the two-dimensional geometry shown in Figure 2.11, where all the strips are aligned along the z -axis ($\xi_l = 0$). The diffracted field arriving at the observation point P with coordinates $(x_p, y_p, 0)$ originates from the diffraction point Q located at the origin. Next we assume that the half-plane edge has a small deviation in its location. So the edge is not placed along the z -axis, but it is parallel to the z -axis at $x = 0$, $y = \xi$. Consequently the diffraction point Q has coordinates $(0, \xi, 0)$. The parameter ξ has a normal

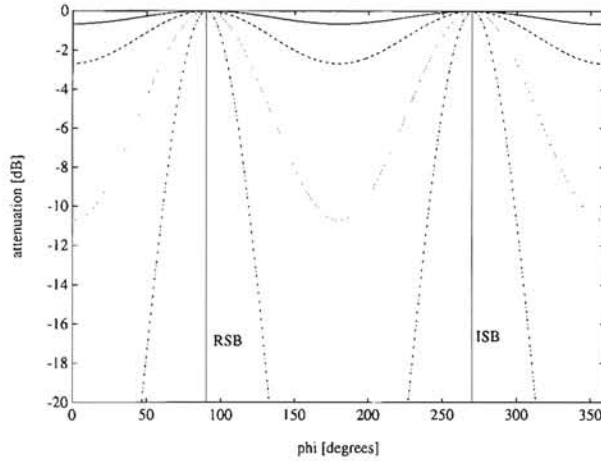


Figure 2.12: Diffraction attenuation function ρ_d for $\varphi' = \pi/2$, $k\mu = \pi/8$ (—————), $k\mu = \pi/4$ (-----), $k\mu = \pi/2$ (.....) and $k\mu = \pi$ (-·-·-·-·).

distribution with zero mean and variance μ . The change in the phase of the diffracted field at P is found to be $\Delta\phi = k\xi(\cos\varphi + \cos\varphi')$. The average value of the diffracted field at P can be found by integration over the probability distribution of ξ . In this way we arrive at the same diffraction attenuation function ρ_d .

2.8 Reflection and diffraction by a convex obstacle

The geometries considered in the previous section all had one or more edges where the diffracted wave was generated. Diffracted waves are also excited when a ray attaches to a convex surface and couples into a surface ray. Whilst propagating along the convex surface, this surface ray sheds energy into the shaded space by launching rays into a direction tangential to the convex surface.

In this section the problem of reflection and diffraction of an EM wave by a perfectly conducting convex surface is studied. Some applications of this theory are for example the scattering by lamp posts and road signs in an urban environment, and the scattering of struts in a reflector antenna system. In the following sections a general description of the reflection and diffraction problem will be given.

The geometry is depicted in Figure 2.13 which schematically shows the reflection and surface-diffraction phenomena. The field at P consists of various parts. If P is in the lit

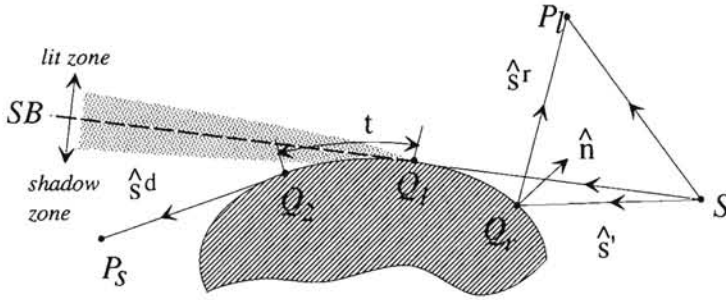


Figure 2.13: Rays associated with reflection and diffraction by a (two-dimensional) convex obstacle.

zone (P_l), the GO reflection contribution should be taken into account. One of the rays of the source S intersects the obstacle at Q_r , and reflection takes place. The GO reflection contribution can be calculated according to the theory as discussed in Section 2.3. Some of the rays originating at S are tangential to the reflecting surface and excite reflected rays which are also tangential to the reflecting surface. The latter divide the space surrounding the reflecting obstacle into two regions, as depicted in Figure 2.13. The first region is the lit zone, and the second is the shadow zone. There is a shadow boundary (SB) at the location where both regions meet. Traversing this shadow boundary results in the vanishing of two GO contributions. The first is the direct field and the second is the reflected field.

The field in the shadow zone is caused by the incident ray that is tangential to the reflector surface at Q_1 . This ray couples to a surface ray which, whilst propagating along the convex surface, continuously sheds surface-diffracted rays into the shadow zone. One of these rays reaches the point P_s after having followed the reflector surface along a distance t , as depicted in Figure 2.13. The surface-diffracted ray leaves the convex surface at the point Q_2 , where it is tangential to the surface.

Continuity of the field for P going from the lit zone, through the SB, into the shadow zone is obtained if the incident and reflected fields near SB in the lit zone match the surface-diffracted field near SB in the shadow zone. The formulation of the GO reflected field as discussed in Section 2.3 does not provide this continuity, and consequently another theory for reflection should be used.

In general the reflection point Q_r and the attachment and shedding point $Q_{1,2}$ are found using numerical procedures that make use of the specific properties of these points. At Q_r Snell's law should hold, and at $Q_{1,2}$ the direction of arrival and departure are both

perpendicular to the normal vector to the surface. Together with the fact that the ray trajectories in both cases are paths of stationary path length, i.e. the first-order variation of the path length is zero, the reflection, attachment and shedding point can be determined.

The theory to be used for the reflection and surface-diffraction process will be presented in the following sections.

2.8.1 Reflection by a convex surface

For the observation point in the lit zone the total field \vec{E}^t at P_l is given by [38]

$$\vec{E}^t(P_l) = \vec{E}^i(P_l) + \vec{E}^i(Q_r) \cdot \mathcal{R}^g \sqrt{\frac{\rho_1^r \rho_2^r}{(\rho_1^r + s^r)(\rho_2^r + s^r)}} e^{-jk_s r}, \quad (2.115)$$

where \vec{E}^i is the directly incident field at P_l and $\rho_{1,2}^r$ are the radii of curvature of the reflected wavefront. The parameter s^r is the distance from Q_r to P_l . The generalised dyadic reflection factor \mathcal{R}^g is defined by

$$\mathcal{R}^g = \hat{e}_\perp^i \hat{e}_\perp^r R_s^g + \hat{e}_\parallel^i \hat{e}_\parallel^r R_h^g. \quad (2.116)$$

This definition of the generalised dyadic reflection factor \mathcal{R}^g is similar to that of the dyadic reflection factor \mathcal{R}^r introduced in equation (2.34). The unit basis vectors $\hat{e}_{\perp,\parallel}^{i,r}$ were introduced in equations (2.36) to (2.38) and form the surface-fixed coordinate system.

The reflected field $\vec{E}^r(P)$ is generated at the reflection point Q_r and is characterised by ρ_l^r , ($l = 1, 2$), the reflected field \vec{E}^r at Q_r , and the direction of propagation \hat{x}_3^r . These parameters can be found using the procedure as outlined in equation (2.21) and further.

The generalised reflection coefficients $R_{s,h}^g$ are given by [38, 11]

$$R_{s,h}^g = -\sqrt{\frac{-4}{\xi^l}} e^{-j(\xi^l)^2/12} \left[\frac{e^{-j\pi/4}}{2\sqrt{\pi}\xi^l} (1 - F(X^l)) + \hat{P}_{s,h}(\xi^l) \right], \quad (2.117)$$

where the transition function $F(\cdot)$ is given in equation (2.57). A superscript l is introduced to emphasise that the observation point P is in the lit zone. In equation (2.117) the following parameters are used:

$$\xi^l = -2m(Q_r) \cos \theta^i < 0, \quad (2.118)$$

$$m(Q) = \left[\frac{k\rho_g(Q)}{2} \right]^{1/3} > 0, \quad (2.119)$$

$$\cos \theta^i = -\hat{n} \cdot \hat{s}', \quad (2.120)$$

$$X^l = 2kL^l \cos^2 \theta^i, \quad (2.121)$$

$$L^l = \left[\frac{\rho_1^i \rho_2^i}{(\rho_1^i + s^r)(\rho_2^i + s^r)} \frac{s^r(\rho_b^i + s^r)}{\rho_b^i} \right]_{Q_1}. \quad (2.122)$$

The parameter ρ_b^i is the radius of curvature of the wavefront of the incident ray in the normal section spanned by \hat{s}' and $\hat{b} = \hat{s}' \times \hat{n}$. The parameter ξ^l is called the Fock parameter [38], $m(Q_r)$ is a curvature parameter at the reflection point Q_r , with $\rho_g(Q_r)$ the radius of curvature of the reflecting surface at Q_r in the normal section spanned by \hat{s}' and \hat{n} . The angle θ^i is the angle between \hat{n} and \hat{s}' and L^l is a distance parameter. The curvature parameters $\rho_{1,2,b}^i$ in the expression for L^l are to be evaluated at Q_1 where the incident ray is tangential to the reflecting surface. More details about these parameters are given in [38, 11].

The functions $\hat{P}_{s,h}$ in equation (2.117) are the soft and hard Pekeris caret-function [38]. They can be expressed as

$$\hat{P}_{s,h}(x) = \left\{ \begin{array}{l} p^*(x) \\ q^*(x) \end{array} \right\} e^{-j\pi/4} - \frac{e^{-j\pi/4}}{2x\sqrt{\pi}}, \quad (2.123)$$

where $p^*(x)$ and $q^*(x)$ are the well-tabulated Fock scattering functions [11].

In the very lit region, where $|\xi^l| \gg 1$ ($\xi^l < 0$), it can easily be shown that the generalised reflection coefficients $R_{s,h}^g$ reduce to $R_{s,h}^r = \mp 1$.

Outside the transition regions ($F(\cdot) = 1$) the reflected field is of order k^0 with respect to the incident field of order k^0 . At the shadow boundary the reflected field reduces to half the incident field of order k^0 with an additional correction term of order $k^{-1/2}$.

2.8.2 Diffraction by a convex surface

In case the observation point P lies in the shadow zone of the obstacle (P_s), neither the direct field nor the GO reflected field reaches the observation point P . Therefore, the total field consists of one contribution only, namely the *surface-diffracted field* from the convex surface. This surface-diffracted field can be thought of as propagating along the convex surface in a surface ray, thereby continuously shedding energy into the shadow zone.

For P in the shadow region the total field \vec{E}^t can be calculated from [38, 11]

$$\vec{E}^t(P_s) = \vec{E}^i(Q_1) \cdot T^g \sqrt{\frac{\rho_s}{s^d(s^d + \rho_s)}} e^{-jks^d}, \quad (2.124)$$

with \vec{E}^i the incident field at the attachment point Q_1 , T^g a generalised transmission factor and s^d the distance from the shedding point Q_2 to the observation point P_s . At the attachment point Q_1 and shedding point Q_2 we introduce the surface normal vectors $\hat{n}_{1,2}$. The vector $\hat{t}_1 = \hat{x}_3^i$ is the direction of arrival at Q_1 , $\hat{t}_2 = \hat{x}_3^d$ is the direction of departure

at Q_2 to P , and $\hat{b}_{1,2} = \hat{t}_{1,2} \times \hat{n}_{1,2}$. The surface unit vectors $(\hat{t}_{1,2}, \hat{n}_{1,2}, \hat{b}_{1,2})$ are shown in Figure 2.14.

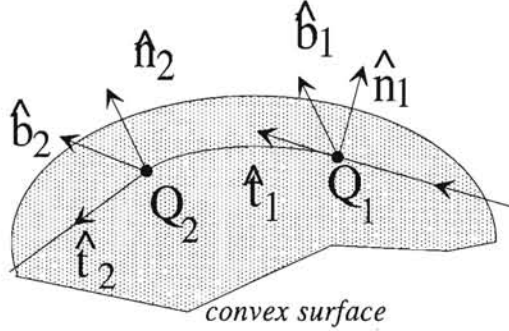


Figure 2.14: Surface-ray unit vectors \hat{t} , \hat{n} and \hat{b} at $Q_{1,2}$.

The parameter ρ_s in equation (2.124) is the radius of curvature of the wavefront of the diffracted ray in the normal section spanned by \hat{t}_2 and \hat{b}_2 , whereas the generalised transmission factor T^g is given by

$$T^g = \hat{b}_1 \hat{b}_2 T_s^g + \hat{n}_1 \hat{n}_2 T_h^g, \quad (2.125)$$

The generalised transmission coefficients $T_{s,h}^g$ are given by

$$T_{s,h}^g = -\sqrt{m(Q_1)m(Q_2)} \sqrt{\frac{2}{k}} \left[\frac{e^{-j\pi/4}}{2\sqrt{\pi}\xi^d} (1 - F(X^d)) + \hat{P}_{s,h}(\xi^d) \right] e^{-jkt}, \quad (2.126)$$

where $\hat{P}_{s,h}(x)$ are the soft and hard Pekeris caret functions (eq. (2.123)), and the transition function $F(\cdot)$ was given in equation (2.57). In addition, the following parameters are introduced, where a superscript d emphasises the surface-diffracted parameters. The Fock parameter ξ^d is given by

$$\xi^d = \int_{Q_1}^{Q_2} \frac{m(t')}{\rho_g(t')} dt', \quad (2.127)$$

where $m(t')$ and $\rho_g(t')$ both are functions of the integration variable t' along the surface-ray path. The parameter X^d is given by

$$X^d = \frac{kL^d (\xi^d)^2}{2m(Q_1)m(Q_2)}, \quad (2.128)$$

where the distance parameter L^d is expressed as

$$L^d = \left[\frac{\rho_1^i \rho_2^i}{(\rho_1^i + s^d)(\rho_2^i + s^d)} \frac{s^d(\rho_b^i + s^d)}{\rho_b^i} \right]_{Q_1}. \quad (2.129)$$

The curvature parameters $\rho_{1,2,b}^i$ should be evaluated at Q_1 . The arc length t along the convex surface is expressed as

$$t = \int_{Q_1}^{Q_2} dt'. \quad (2.130)$$

Further details can be found in [38, 11].

Outside the transition regions ($F(\cdot) = 1$) the surface-diffracted field is of order $k^{-1/2}$, where it should be noted that the Pekeris caret functions $\hat{P}_{s,h}$ play a dominant role in the determination of the amplitude of the field along the surface-diffracted ray. At the SB the surface-diffracted field is of order k^0 .

2.9 Note on the presentation of the theory

The theories as set out in this chapter are all general in the sense that simplifications in the formulae will occur as soon as additional assumptions are made concerning the type of illumination (spherical, cylindrical, plane wavefront), the radius of curvature of the edge (curved, straight edge), and the radii of curvature of the surface of the object (spherical, plane). Because it is undesirable to make these assumptions at an early stage, it is possible that well-known results from the literature cannot be recognised immediately from the general equations presented here.

In the following chapters the various propagation mechanisms discussed will be referred to as just reflection and diffraction. From a practical point of view the description of reflection and diffraction (and also line-of-sight propagation) can elegantly be seen as transformations from incident-wave parameters to reflected- and diffracted-wave parameters.

The notation is summarised for convenience. At every point M in space an EM wave is described by:

- the vectors $\hat{x}_{1,2,3}$, corresponding to the principal directions $\hat{x}_{1,2}$ of the wavefront, and the direction of propagation \hat{x}_3 ;
- the principal radii of curvature $\rho_{1,2}$ in the directions $\hat{x}_{1,2}$, respectively;
- the amplitude and phase of the electric field \vec{E} of the EM wave.

The interaction process of wave and obstacle can be seen as a transformation from incident-wave parameters at the interaction point Q to outgoing-wave parameters, usually directly calculated at an observation point P . In this transformation the parameters of the object where the interaction takes place, play an important role. The reflection process uses the surface parameters $\hat{x}_{1,2,3}^\Sigma$, $\rho_{1,2}^\Sigma$, and the information concerning the reflection and observation point for the transformation from incident- to outgoing-wave parameters. The

edge-diffraction process uses two additional parameters for the transformation: the normal \hat{n}_e to the edge Γ and the edge radius of curvature a_e . These transformations can symbolically be expressed as

$$\left[\hat{x}_{1,2,3}^i, \rho_{1,2}^i, \vec{E}^i \right] \xrightarrow{\mathcal{R}, \mathcal{D}} \left[\hat{x}_{1,2,3}^o, \rho_{1,2}^o, \vec{E}^o \right], \quad (2.131)$$

where the superscripts i and o correspond to the incoming and outgoing wave, $\vec{E}^{i,o}$ are the incident and outgoing electric field, and \mathcal{R} and \mathcal{D} denote the reflection and diffraction operators, respectively.

This symbolic presentation of wave interaction provides a convenient framework for the development of numerical algorithms, because higher-order interactions such as combinations of reflection and diffraction can easily be implemented. Because the description is a ray method, even a very complex wave-propagation model including higher-order diffraction and reflection terms will still provide a significant insight into the wave-propagation process. Furthermore, spatial-filtering functions for the simulation of the antenna receiving characteristics can readily be introduced, and typical multipath phenomena such as fading and time delay can easily be derived from the analysis.

Up to now nothing has been said about how to find the reflection and diffraction points. Actually, these points can seldom be found in an analytical way. Because the objects to be analysed will very often be specified numerically, the determination of the location of the reflection and diffraction points will usually incorporate some root-finding procedure based on Keller's law of edge diffraction or Snell's law of surface reflection. Knowledge of differential geometry will prove very useful in the determination of the reflection and diffraction points.

Chapter 3

Modelling of EM wave diffraction at obstacles with simple shapes

3.1 Introduction

In this chapter the diffraction theory discussed in Chapter 2 will be used to formulate field-strength prediction models incorporating obstacles with simple shapes. The prediction models in Section 3.2 consider simple geometries such as the half-plane and the finite-width screen, but also more complex objects such as the block-shaped obstacle.

In Section 3.3 the results from the field-strength prediction models will be compared to results predicted by other methods such as the Parabolic Equation (PE) method and the Fresnel Surface Integral (FSI) method. Simplified procedures for calculating the EM field behind two- and three-dimensional objects will be proposed in Section 3.4.

Throughout this chapter results of the calculations will be presented in the form of graphs giving parametric curves of the relative field strength or the *Site Shielding Factor* (SSF) as function of position. The SSF is a parameter that quantifies the shielding effectivity and will be introduced shortly.

Consider the case where a station operating in a satellite communication system is subject to (trans-horizon) interference from a terminal operating in a terrestrial communication system using the same frequency band ('frequency sharing'). This situation is schematically visualised in Figure 3.1, where U_w and U_i are the wanted and interfering signals for the receiver at P , respectively. The interfering signal may be caused by anomalous propagation conditions such as ducting and reflection from elevated layers. Therefore the amplitudes of these types of signals can be quite high; fortunately the probability of occurrence of these propagation phenomena is quite low.

By placing an obstacle on the propagation path of the interference signal two (main) effects are introduced. First, the interference signal is attenuated by the presence of the obstacle and this effect is intentional. Second, an unintentional multipath-propagation

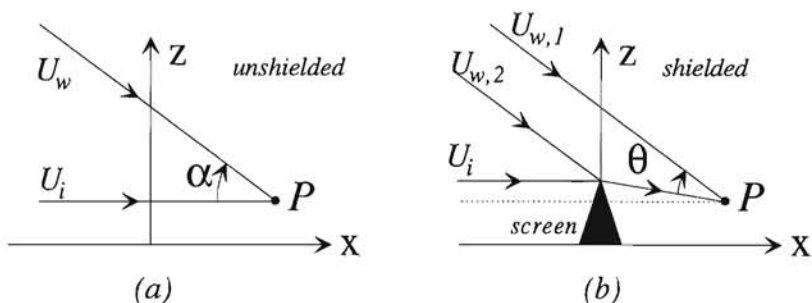


Figure 3.1: Introduction of the site shielding factor (SSF); the unshielded geometry is shown in (a), while the shielded geometry is shown in (b).

effect for the wanted signal can be introduced. In this case it is assumed that the Line-Of-Sight (LOS) component, viz. $U_{w,1}$ (Fig. 3.1b), of the wanted signal is not obstructed by the screen. The conventional definition of the SSF as used in [3], SSF_1 , is the ratio of the interference signal in the absence (I_-) and the presence (I_+) of the obstacle, respectively

$$SSF_1 = 20 \log \left[\frac{I_-}{I_+} \right] \quad [\text{dB}], \quad (3.1)$$

where it has been assumed that the placement of the obstacle has no effect on the wanted signal D . If this effect should be taken into account, the correct extension of equation (3.1) is [39]

$$SSF_2 = 20 \log \left[\frac{D_+}{I_+} \right] - 20 \log \left[\frac{D_-}{I_-} \right] \quad [\text{dB}], \quad (3.2)$$

where $D_{+,-}$ are the levels of the wanted signal in the presence (+) and absence (-) of the obstacle, respectively. Equation (3.2) expresses the change in signal-to-interference ratio that is introduced by placement of the obstacle.

The definition of the SSF as introduced in equation (3.2) is based on the ratio of the wanted and interference signal power in the absence and the presence of the obstacle. For inter-system interference problems the wanted and unwanted signals are caused by different sources, and the phase between the two can be considered to be a random variable. Consequently, only their signal powers can be used as a quantity for expressing signal-to-noise and signal-to-interference ratios.

Notice that another definition of the SSF, incorporating the effect of the placement of the screen on I as well as on D , has been reported in [40]. This definition in the present notation reads

$$SSF_3 = 20 \log \left[\frac{D_- + I_-}{D_+ + I_+} \right] \quad [\text{dB}]. \quad (3.3)$$

Here obviously the desired and interference signals are considered to be coherent, although they are caused by different sources. This linear addition of the signals is meaningless because the signals are by definition *incoherent*, and therefore the SSF given by equation (3.3) is wrong. Due to the assumption of coherence, the result in the numerator and denominator of equation (3.3) will be completely dependent on the phase *difference* between D and I at P . The result of the summation of $D + I$ is strongly frequency dependent, as is the derived SSF. It can easily be proven that this frequency dependence is completely caused by the assumption of coherence between D and I [39]. Consequently, equation (3.3), which takes into account the effect of the screen on the wanted and interfering signals, does *not* reduce to the conventional and well-accepted definition of SSF_1 , viz. equation (3.1), when it is assumed that the desired signal level remains unchanged after the obstacle has been placed. For these reasons the SSF as proposed in equation (3.1) will be used throughout the thesis, unless otherwise mentioned.

A slight rearrangement of equation (3.2) yields

$$SSF_2 = 20 \log \left[\frac{D_+}{D_-} \right] + 20 \log \left[\frac{I_-}{I_+} \right] = 20 \log \left[\frac{D_+}{D_-} \right] + SSF_1 \quad [\text{dB}]. \quad (3.4)$$

Equation (3.4) gives a direct insight in how the SSF can be raised. One can either enforce a stronger wanted signal by placing the obstacle, or one can attenuate the interfering signal. Notice that the first option for the wanted field is known as *obstacle gain* [3]. In most cases, however, both the wanted and interfering signals may be attenuated by the obstacle. As long as the attenuation for the interference signal is larger than that for the desired signal, the user will benefit from the obstacle placement because the resulting signal-to-interference ratio D/I is higher than the one before the obstacle was placed. Obviously, the level of the wanted signal needs to be higher than the noise level in order that it can still be detected.

3.2 Diffraction at obstacles with simple shapes

In this section some two-dimensional obstacles will be analysed with respect to their site shielding performance. For the simple case of the half-plane obstacle the results according to the various definitions of the SSF will be presented. For simplicity it will be assumed that all obstacles are perfectly conducting, but the analyses can be readily extended to cover non-perfectly conducting obstacles using the theory of Section 2.6.

Unless otherwise mentioned ground-plane effects like reflection will be neglected. However, these effects can be introduced if necessary.

3.2.1 The half-plane

One of the simplest obstacles that can be analysed using the UTD is the half-plane, which is shown in Figure 3.2. The half-plane is located in the yz -plane and has a height $z_{ob} > 0$.

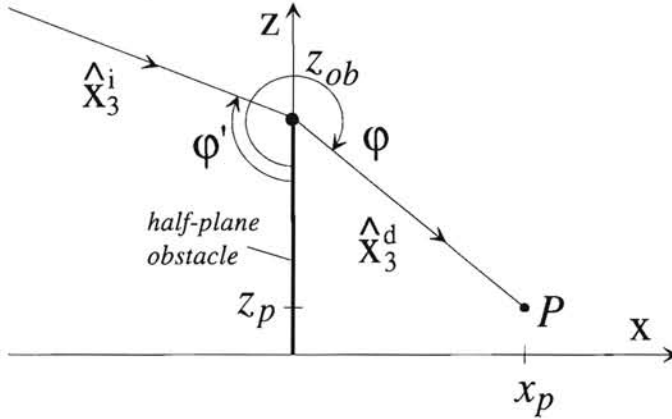


Figure 3.2: Site-shielding geometry for a half-plane obstacle.

For the case of a wave perpendicularly incident upon the edge of the half-plane, the problem is essentially two-dimensional. In the analysis the effect of the ground plane $z = 0$ will be neglected. The observation point P with Cartesian coordinates (x_p, z_p) is located behind the screen as seen from the source, which is assumed to be at a very large distance. For this reason the incident (interfering) wave has a plane wavefront. The obstacle has a height $z_{ob} = 60m$ and the frequency will be 1 GHz.

In the results to be presented, the SSF will be calculated using the definitions of $SSF_{1,2,3}$. The interfering as well as the wanted field are calculated in the same way, however, their angles of arrival (φ') and amplitude will generally be different. The wanted field arrives at an angle $\varphi' = 2\pi/3$ (satellite elevation of 30°), has a unit amplitude and is y -polarised. The interfering signal arrives at an angle $\varphi' = \pi/2$ (transhorizon propagation), has an amplitude that is ten times higher than that of the wanted signal (20 dB) and is also y -polarised. In the following figures the SSF is calculated as function of the observation-point coordinates (x_p, z_p) .

For the interference signal, the field in the lit region behind the screen ($z > z_{ob}$) consists of two parts, namely the direct field and the edge-diffracted field. In the shadow region only the edge-diffracted field is present. For the wanted signal the same is true; the shadow boundary is located somewhere else, however. The region where $\varphi > \pi + \varphi' = 5\pi/3$ is

the shadow region of the wanted signal, and for $\varphi < 5\pi/3$ P is located in the lit region. Obviously, the diffraction point Q for both signals has coordinates $(0, z_{ob})$.

For the half-plane obstacle the diffraction coefficients $D_{s,h}$ given in equation (2.47) may be simplified because the exterior wedge angle is 2π , i.e. $n = 2$. This results in

$$D_{s,h} = -\frac{e^{-j\pi/4}}{2\sqrt{2\pi k}} \left[\frac{F(kLa(\varphi^-))}{\cos(\varphi^-/2)} \mp \frac{F(kLa(\varphi^+))}{\cos(\varphi^+/2)} \right], \quad (3.5)$$

where the transition function $F(\cdot)$ is given by equation (2.57), and the angles $\varphi^\pm = \varphi \pm \varphi'$. Associated with the case $n = 2$ are some simplifications in the calculation of the radii of curvature of the wavefront of the reflected wave, the distance parameter L and caustic distance ρ^d . The distance parameter L is given by

$$L = s = \sqrt{x_p^2 + (z_{ob} - z_p)^2}, \quad (3.6)$$

while the function $a(x)$ is expressed as

$$a(x) = 2 \cos^2(x/2). \quad (3.7)$$

The caustic distance $\rho_d = \infty$, because the edge is straight ($a_e = \infty$) and the incident wave has a plane wavefront ($\rho_{1,2} = \infty$).

Figures 3.3 and 3.4 show the SSF according to the definitions in equations (3.1) to (3.3) as function of the position of P . In the first figure the value of x_p is varied while the value of z_p is fixed to $3m$. In Figure 3.4 the reverse is true. The value of z_p varies as the value of $x_p = 300m$ is kept constant. In both figures it can be clearly seen that the results for SSF_3 show very rapid fluctuations as x_p or z_p varies. This is completely due to the addition of the interfering and wanted signals on a coherent basis, and for this reason the frequency dependence reported in [40] is artificial. In Figure 3.3 the vertical line indicates the shadow boundary for the wanted field, while in Figure 3.4 the vertical line corresponds to the shadow boundary for the interference signal. It can be seen that the results predicted using the SSF_2 definition reduce to those predicted following the SSF_1 definition if the required assumption is fulfilled, i.e. $D_+ = D_-$.

Notice that this particular diffraction problem can also be solved in terms of Fresnel integrals [41, 3]. In this case the result is given by

$$SSF_2 = 20 \log \left(\frac{\mathcal{F}(\xi_D)}{\mathcal{F}(\xi_I)} \right) \quad [\text{dB}], \quad (3.8)$$

where the contribution of the reflected field to the total field has been neglected. The function \mathcal{F} contains a Fresnel integral and is related to the transition function F (eq. (2.57)). It is defined as

$$\mathcal{F}(\xi) = \frac{e^{j\pi/4}}{\sqrt{\pi}} \int_{\xi}^{\infty} e^{-ju^2} du. \quad (3.9)$$

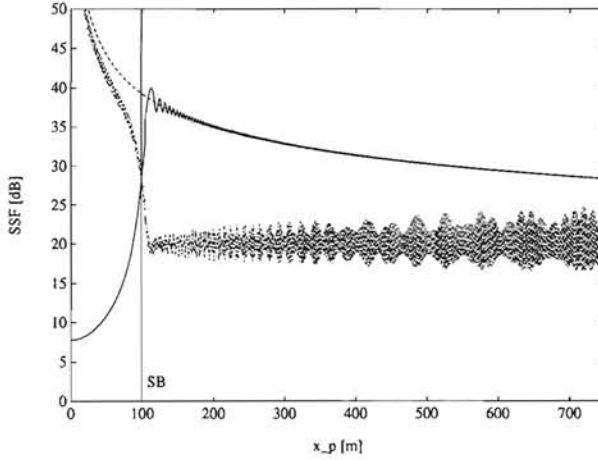


Figure 3.3: SSF of a half-plane as function of x_p : SSF_2 (—), SSF_1 (---), and SSF_3 (-·-·-·-·-·).
 Data: $z_p = 3m$, $z_{ob} = 60m$, $\lambda = 0.3m$

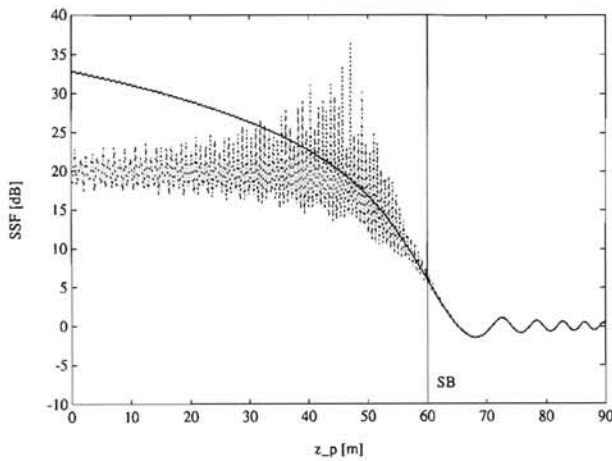


Figure 3.4: SSF of a half-plane as function of z_p : SSF_2 (—), SSF_1 (---), and SSF_3 (-·-·-·-·-·).
 Data: $x_p = 300m$, $z_{ob} = 60m$, $\lambda = 0.3m$

The parameter $\xi_{D,I}$ is the detour parameter and is given by [6, 3]

$$\xi = -\sqrt{2ks} \cos(\varphi^-/2), \quad (3.10)$$

where $\varphi^- = \varphi - \varphi'$, and $\varphi' = 2\pi/3$ for the wanted signal and $\varphi' = \pi/2$ for the interference signal. The distance s to the screen is given by

$$s = \sqrt{x_p^2 + (z_{ob} - z_p)^2}. \quad (3.11)$$

Notice that

$$\xi^2 = 2ks \cos^2(\varphi^-/2) = kLa(\varphi^-), \quad (3.12)$$

where $kLa(\varphi^-)$ is the argument of a transition function F as used in UTD, viz. equation (3.5). In case the influence of the obstacle on the desired signal is neglected ($\mathcal{F}(\xi_D) \approx 1$) equation (3.8) reduces to [3]

$$SSF_1 = -20 \log \mathcal{F}(\xi_I) \text{ [dB]}. \quad (3.13)$$

The shielding effectiveness for the half-plane has also been extensively discussed in [3] using the UTD as well as other methods (exact solution, Kirchhoff formulation, GTD and UAT).

3.2.2 The finite-width screen

Obviously, using infinitely-wide obstacles for the modelling of practical objects such as buildings is unrealistic. If a finitely-wide, perfectly-conducting obstacle is considered, additional edges are introduced, and diffraction contributions generated at these edges and corners have to be taken into account as discussed in Chapter 2. If the obstacle is very wide, the diffraction angle (φ) of both vertical side edges can become very large, and then the observation point is said to be in the deep shadow region for these edges. If this is the case, the contributions from these edges can be neglected. If the diffracting obstacle is narrow, however, diffraction by the vertical edges of the obstacle can produce diffracted fields with a substantial amplitude [42]. If practical obstacles such as buildings and fences should be modelled, it is expected that the model based on a finite-width screen is more realistic than the model incorporating a half-plane obstacle.

In this and the following sections attention will be paid to the influence of the placement of the screen on the interfering signal level only. For this reason the definition of SSF_1 according to equation (3.1) is used. In general the models proposed here can be used for the calculation of the interfering signal level as well as the desired signal level. If both calculations are performed, the SSF according to equation (3.2) can readily be determined.

For the present analysis it is assumed that the direction of propagation \hat{x}_3^i is parallel to the ground plane $z = 0$. It is given by $\hat{x}_3^i = (\sin \beta, \cos \beta, 0)$, making an angle β with the y -axis. The observation point P has coordinates (x_p, y_p, z_p) . The obstacle has a width $d_1 + d_2$ and a height z_{ob} ; it is shown in Figure 3.5. For all edges of the obstacle the UTD with diffraction coefficients for $n = 2$ (eq. (3.5)) can be used, and consequently simplifications for calculating the diffracted field can be used. The finite-width screen is defined in a Cartesian (x, y, z) coordinate system as $x = 0$, $-d_1 \leq y \leq d_2$, ($d_{1,2} \geq 0$), $0 \leq z \leq z_{ob}$. The left (right) vertical edge is denoted by Γ_1 (Γ_2), the horizontal edge is denoted by Γ_3 , and the corners are denoted by $\Gamma_{4,5}$. The coordinates of the edge-diffraction points Q_l , ($l = 1, 2, 3$) can be

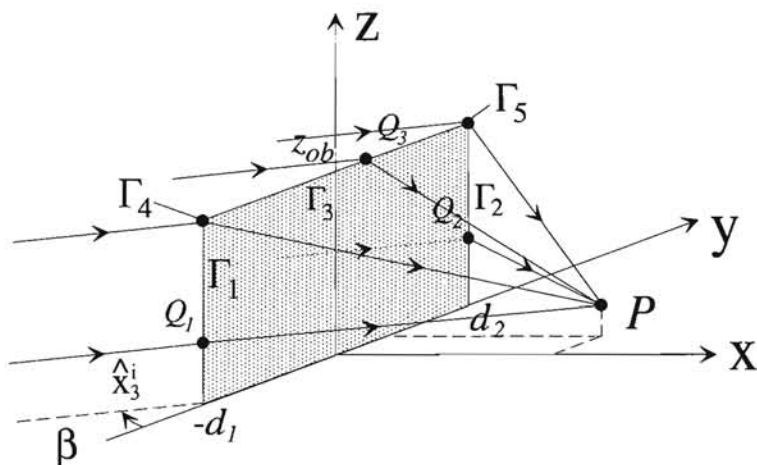


Figure 3.5: The perfectly conducting, finite-width screen

found using the projection of the observation point P along the Keller cone onto the edge Γ_l , and applying the restriction that the projection must lie on Γ_l :

$$Q_1 = (0, -d_1, z_p), \text{ if } z_p < z_{ob}, \quad (3.14)$$

$$Q_2 = (0, d_2, z_p), \text{ if } z_p < z_{ob}, \quad (3.15)$$

$$Q_3 = (0, y_q, z_{ob}), \text{ if } -d_1 < y_q < d_2, \quad (3.16)$$

where y_q is defined as

$$y_q = y_p - \frac{\sqrt{x_p^2 + (z_{ob} - z_p)^2}}{\tan \beta}. \quad (3.17)$$

The corner-diffraction points can be found at the intersections of Γ_1 with Γ_3 , and Γ_2 with Γ_3 :

$$Q_4 = \Gamma_4 = (0, -d_1, z_{ob}), \quad (3.18)$$

$$Q_5 = \Gamma_5 = (0, d_2, z_{ob}). \quad (3.19)$$

Using this information, the individual diffraction contributions can be determined. The total field at the observation point P is given by

$$\vec{E}^t = \epsilon_i \vec{E}^i + \sum_{l=1}^5 \epsilon_l \vec{E}_{Q_l}^d, \quad (3.20)$$

where \vec{E}^t is the total field at the point P , \vec{E}^i is the incident field and \vec{E}^d is the edge-diffracted or corner-diffracted field. For the sake of notational simplicity, the edge-diffracted fields are denoted by $\vec{E}_{Q_{1,2,3}}^d$, and the corner-diffracted fields by $\vec{E}_{Q_{4,5}}^d$. In equation (3.20) the shadow indicators ϵ_i and ϵ_l ($l = 1, \dots, 5$) are introduced according to

$$\epsilon = \begin{cases} 1, & \text{if the contribution exists at } P, \\ 0, & \text{if the contribution does not exist at } P. \end{cases} \quad (3.21)$$

For P in the lit zone $\epsilon_i = 1$, while if P is in the shadow zone $\epsilon_i = 0$. Furthermore, $\epsilon_{1,2} = 1$ for $z_p < z_{ob}$, $\epsilon_{1,2} = 0$ for $z_p > z_{ob}$, $\epsilon_3 = 1$ for $-d_1 < y_p < d_2$ and $\epsilon_3 = 0$ otherwise, $\epsilon_{4,5} = 1$ for all locations of P .

The width of the screen used in the results shown in Figure 3.6 is $d_1 = d_2 = 43m$. The observation point P has coordinates $x_p = 100m$, $z_p = 1.5m$, while $-50m \leq y_p \leq 150m$, and the frequency used is 1 GHz. Furthermore, the polarisation of the incident wave is vertical (z). The solid curve is for a screen with $z_{ob} = 10m$ and for $\beta = 90^\circ$. The strong fluctuations in the curve are caused by constructive and destructive interference of the wave contributions from the vertical edges and the corners, superimposed on the constant level of the horizontal-edge contribution. The horizontal line is the result of a half-plane treatment of the obstacle, i.e. $d_1 = d_2 = \infty$. In the latter case the only contribution comes from the horizontal edge Γ_3 and is constant as a function of y_p .

The dashed curve in Figure 3.6 is for an obstacle with $z_{ob} = 60m$. It is seen that the SSF for this obstacle is considerably larger than that for $z_{ob} = 10m$. Furthermore, the fluctuations of the SSF for the case $z_{ob} = 60m$ are larger than those for $z_{ob} = 10m$. This is due to the fact that the contribution from the horizontal edge is of the same order of magnitude as those from the vertical edges. For this reason total cancellation of contributions can occur, resulting in large SSF values. The importance of the corner-diffraction term can best be seen for small height differences $z_{ob} - z_p$ [43]. If the corner-diffraction term would be neglected, discontinuities in the total field would be introduced.

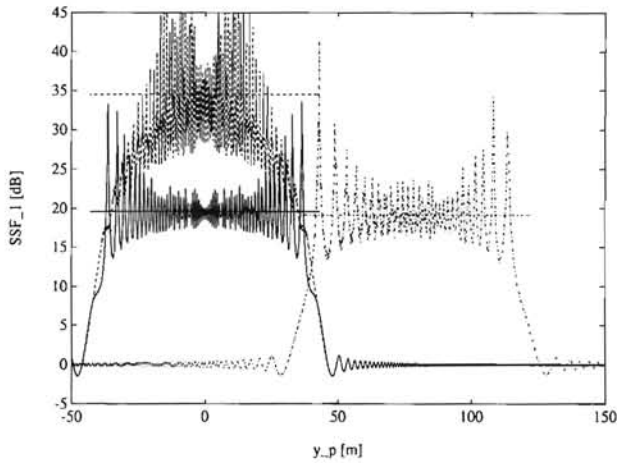


Figure 3.6: SSF of a perfectly conducting finite-width screen as function of y_p : $z_{ob} = 10m$, $\beta = 90^\circ$ (—), $z_{ob} = 60m$, $\beta = 90^\circ$ (---), and $z_{ob} = 10m$, $\beta = 52^\circ$ (-·-·-·-·-). The horizontal lines are predictions of a half-plane approximation ($d_1 = d_2 = \infty$).
Data: $x_p = 100m$, $z_p = 1.5m$, $d_1 = d_2 = 43m$, $\lambda = 0.3m$

These are caused by the step discontinuity in the contribution from the horizontal edge Γ_3 , if P moves from the shadow region behind the screen into the lit region. When P crosses the shadow boundary, two discontinuities need to be cancelled. The first one is the discontinuity in the directly incident field at P . This is cancelled by the edge-diffracted field from a vertical side. The second discontinuity is that of the contribution from Γ_3 . For small height difference $z_{ob} - z_p$ this contribution will be substantial, and consequently continuity is only obtained if the corner-diffracted contributions are taken into account.

The accuracy of this corner-diffracted field has been checked in [20] against results from another method [19]. Good agreement between the results from both methods was obtained for several geometries. This confirms the usefulness of the current formulation of corner diffraction, despite its heuristic character.

If the angle of incidence β is changed from 90° to 52° , and $z_{ob} = 10m$, the SSF given by the dash-dotted curve shown in Figure 3.6 is obtained. It can be seen that the complete SSF curve is more or less shifted laterally over a distance $\Delta y = x_p / \tan \beta = 78m$, and that the result for the half-plane approximation differs just slightly from that for the case $\beta = 90^\circ$.

If desired, some weighting function for the fields along the individual rays can be em-

ployed to simulate the directivity of a receiving antenna placed at P . It is stressed that this spatial weighting cannot always be used for the modelling of the shielding of a reflector antenna, because the obstacle may be in the near field of the antenna. Theoretically, the pattern assumed for the point receiver at the observation point P can be replaced by the receiving pattern of the antenna if the obstacle is in the far field of the antenna, i.e. if the separation of obstacle and antenna is larger than the Rayleigh distance $2D^2/\lambda$, where D is the largest physical dimension of the antenna. This matter is carefully studied and analysed in Chapter 5 for single- and double-reflector antennas.

3.2.3 The metallic cylinder

The obstacles considered thus far all had edges where the diffracted waves were generated. In this section the problem of diffraction by a circular cylinder is discussed. The cylinder is infinitely long in the y -direction, and its radius is a . The incident wave propagates into the x -direction, and the observation point P has coordinates (x_p, z_p) , where the y -coordinate is discarded because the problem is essentially two-dimensional. For P in the lit region, i.e.

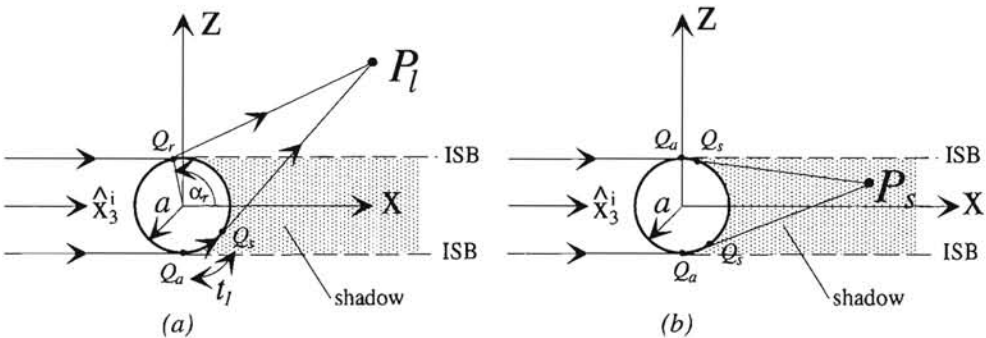


Figure 3.7: Cylinder geometry with P in the lit zone (a) and P in the shadow zone (b).

$|z_p| > a$, the total field at P_l consists of four parts: the direct incident field, the reflected field and two first-order surface-diffracted fields. The direct and reflected fields are easily calculated using the theory from Section 2.8. The main difficulty is the determination of the reflection point Q_r . Since this point lies on the cylinder surface, the location of the reflection point is determined by one coordinate only, namely the angle α_r . The value of α_r that corresponds to the reflection point Q_r can be found from Snell's law using a simple root-finding procedure. Furthermore, two surface-diffracted fields arrive at P_l ; the ray path

of one of these fields is shown in Figure 3.7a. The wave propagates around the cylinder in a counter-clockwise direction. It has its attachment point Q_a at $\alpha_r = 3\pi/2$, and the shedding point Q_s can again be found using a root-finding procedure. The second surface-diffracted field is shed by a surface wave that propagates in a clockwise direction referring to Figure 3.7a. This ray has its attachment point for $\alpha_r = \pi/2$, and a root-finding procedure needs to be used to find the associated shedding point Q_s for which $\pi/2 \leq \alpha_r \leq \pi$.

So, in the lit region the total field \vec{E}_{lit}^t at P_l is given by

$$\vec{E}_{lit}^t = \vec{E}^i + \vec{E}^r + \vec{E}_{cw,lit}^{sd} + \vec{E}_{ccw,lit}^{sd}, \quad (3.22)$$

where \vec{E}^i is the direct (GO) field reaching P_l , \vec{E}^r is the reflected field by the cylinder and $\vec{E}_{cw,lit}^{sd}$, $\vec{E}_{ccw,lit}^{sd}$ are the surface-diffracted fields shed by surface waves propagating in clockwise and counter-clockwise directions, respectively.

For P in the shadow region (Fig. 3.7b), i.e. $|z_p| < a$, the total field \vec{E}_{shadow}^t arriving at P_s consists of two first-order diffracted fields

$$\vec{E}_{shadow}^t = \vec{E}_{cw,shadow}^{sd} + \vec{E}_{ccw,shadow}^{sd}, \quad (3.23)$$

where $\vec{E}_{cw,shadow}^{sd}$ and $\vec{E}_{ccw,shadow}^{sd}$ arise from surface diffraction with attachment points at $\alpha_r = \pi/2$ and $\alpha_r = 3\pi/2$, respectively, and propagate into the shadow region behind the cylinder. The location of the shedding points can be determined by a root-finding procedure.

Comparing equations (3.22) and (3.23), it can be deduced that one surface-diffracted wave is continuous across the Incident Shadow Boundary (ISB). More specifically, at the upper ISB ($z = a$) one has $\vec{E}_{ccw,lit}^{sd} = \vec{E}_{ccw,shadow}^{sd}$, whereas at the lower ISB ($z = -a$) one has $\vec{E}_{cw,lit}^{sd} = \vec{E}_{cw,shadow}^{sd}$. Continuity of the field across, for example, the upper ISB is obtained if

$$\vec{E}^i + \vec{E}^r + \vec{E}_{cw,lit}^{sd} = \vec{E}_{cw,shadow}^{sd}. \quad (3.24)$$

Notice that $\vec{E}_{cw,lit}^{sd}$ is different from $\vec{E}_{cw,shadow}^{sd}$ in that $\vec{E}_{cw,lit}^{sd}$ travels nearly once around the cylinder, while for $\vec{E}_{cw,shadow}^{sd}$ the path along the cylindrical surface is only a short arc of the cylinder circumference. Actually, the path length t along the cylinder for $\vec{E}_{cw,lit}^{sd}$ and $\vec{E}_{cw,shadow}^{sd}$ shows a discontinuity of $t = 2\pi a$; for $z_p = a + \delta$ ($\delta \ll a$) the path length t approaches $t = 2\pi a$ for $\delta \downarrow 0$, while for $z_p = a - \delta$ the path length approaches $t = 0$ ($\delta \uparrow 0$). It can be proven that equality (3.24) holds true, so that the total field is indeed continuous across the ISB [38].

In the following examples the SSF is calculated for a circular cylinder of varying radius for $a = 0.15m$, $0.3m$, $1.5m$ and $3m$, while the observation point P has coordinates $x_p = 100m$, z_p . The frequency used is 1 GHz and vertical (\hat{y}) as well as horizontal (\hat{z}) polarisation is

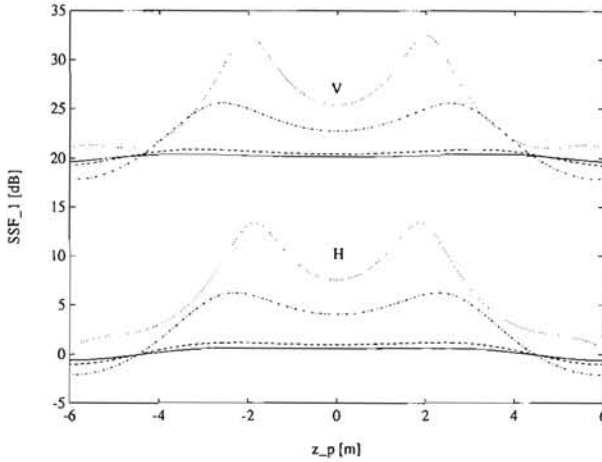


Figure 3.8: SSF of a circular cylinder of radius a as function of z_p for vertical (V) and horizontal (H) polarisation: $a = 0.15\text{m}$ (—), $a = 0.3\text{m}$ (---), $a = 1.5\text{m}$ (- · - · - · - ·) and $a = 3\text{m}$ (·····). The curves for vertical polarisation have been raised by 20 dB for legibility.

Data: $x_p = 100\text{m}$, $\lambda = 0.3\text{m}$

considered. The results of these calculations can be found in Figure 3.8 for $|z_p| \leq 6\text{m}$. From this figure it is seen that the SSF for a value of $x_p = 100\text{m}$ is quite low. An investigation for smaller x_p revealed that also for the cylinder considerable values of the SSF can be obtained if P is quite close to the obstacle and if a is large compared to λ . In practical situations, the occurrence of this type of obstacle with a large radius is low. Also, for some regions the SSF is negative, indicating that the directly incident and the obstacle-scattered field are in phase.

Numerous kinds of cylindrically-shaped obstacles with small radii are present in practical sceneries, e.g. lamp posts and road signs, and it appears that for these obstacles with small cross-sections the surface-diffracted waves are not the most important wave contributions. The reflected waves from these obstacles are more important, and can cause strong fading effects as is well known from the literature. This indicates that, for the site shielding application, cylindrically-shaped obstacles are useful only if their radius is quite large in terms of the wavelength, and if the observation point P is close to the obstacle.

If the incident wave is obliquely incident onto the cylinder axis, the SSF can also be determined using the UTD for convex obstacles. Details concerning the ray-tracing procedures and the validity of UTD for cylinders with small radii ($a \approx \lambda$) can be found in [44],

where also a comparison is made between the results predicted by UTD and those based on an exact solution in terms of Bessel functions. Some results of this study are summarised in Section 4.6.

3.2.4 The block-shaped obstacle

Obviously, the accuracy of the modelling of an obstacle can be improved by considering three-dimensional objects rather than two-dimensional ones. For this reason a versatile block-shaped obstacle is introduced in this section, which can also be used for the (numerical) modelling of diffraction by a half-plane and by a finite-width screen.

Generally speaking, the block-shaped obstacle is described by an ordered sequence of eight corner points. This ordered sequence determines 8 vertices, 12 straight edges and 6 plane faces of the solid block, some of which are indicated in Figure 3.9. Furthermore, it is allowed that corner points nearly coalesce. In this way, a suitable combination of only

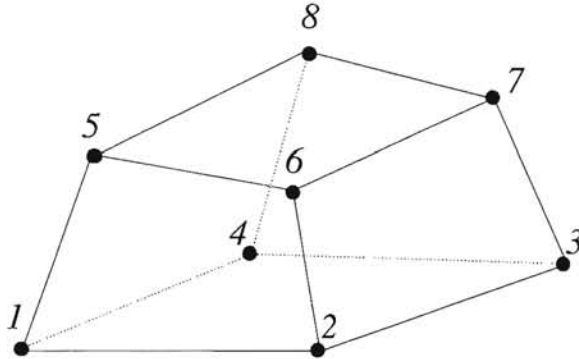


Figure 3.9: The general block obstacle consisting of 8 vertices, 6 plane surfaces and the 12 straight sides.

two block-type obstacles is an accurate model for a house, including a rooftop. The block-shaped obstacles considered in this thesis are always convex. This imposes requirements on the relations between the coordinates of the vertices. The use of the block-shaped obstacle is, among others, discussed in Chapter 6.

The rectangular block (rectangular parallelepiped) can be derived from the block-shaped obstacle. Its edges are parallel to the axes of a properly chosen Cartesian coordinate system, and it is described by $-d/2 \leq x \leq d/2$, $-h/2 \leq y \leq h/2$, $0 \leq z \leq z_{ob}$. The obstacle under consideration is placed on the ground plane (xy -plane) and the influence of the latter is neglected. It is depicted in Figure 3.10. From the geometry of this rectangular block it

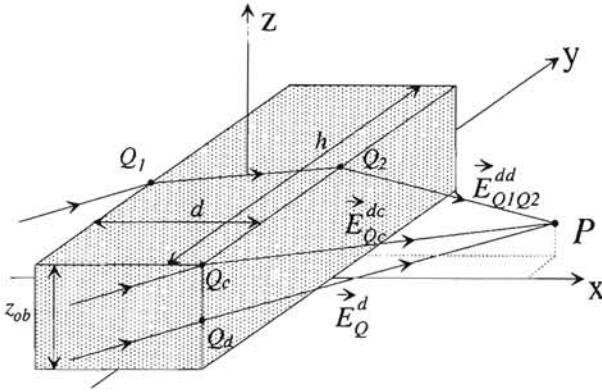


Figure 3.10: The perfectly conducting rectangular block, with some wave contributions.

is observed that there can be various kinds of wave contributions at the observation point P , some of which have already been discussed. The following types of ray-optical fields contribute to the total received field at the point P :

1. The directly incident field \vec{E}^i (not indicated in Figure 3.10). This is the geometrical optics (GO) field and it is present only if the observation point P is in lit space. Its contribution to the total field is calculated using standard GO techniques;
2. The reflected field \vec{E}^r (not indicated in Figure 3.10). This is another GO field and it is only present if one or more reflection points R exist in one or more faces of the obstacle, such that the incident ray through R and the reflected ray from R to P satisfy Snell's law;
3. The single-diffracted field \vec{E}^d . This is a diffraction field and it is present only if there exist one or more diffraction points Q_d on one or more edges of the rectangular block, such that the incident ray through Q_d and the diffracted ray from Q_d to P satisfy Keller's law of edge diffraction. Since all edges are straight, simplified expressions for diffraction parameters can be used. For the distance parameters $L^i = L^d$ because the faces are plane; the caustic distance for diffraction $\rho^d = \rho_c^i$, because the edges are straight $a_e = \infty$;
4. The double-diffracted field \vec{E}^{dd} . This is another diffraction contribution and it contributes only if a pair of diffraction points exists on different edges of the block obstacle (or on edges of different obstacles), such that Keller's law of diffraction is satisfied

at both diffraction points. The double-diffraction contribution is calculated by applying twice the diffraction operation as indicated in equation (2.83), whereby the diffracted field arising at the first diffraction point Q_1 acts as incident field at the second diffraction point Q_2 . Furthermore, a slope-diffracted field is incorporated in case the secondary incident field has a zero amplitude at Q_2 . This contribution is calculated using the theory from Section 2.5.1; see equation (2.68). In case of overlapping transition regions (Fig. 2.9), discontinuities of the double-diffracted field will occur. It is observed that for the present application, the double-diffraction contribution is only needed in case no other wave contributions are present [45];

5. The corner-diffracted field \vec{E}^{dc} . This is another diffraction term which is almost continuously present. The corresponding diffraction point is one of the vertices or corners of the obstacle and is denoted by Q_c . Mostly, corner diffraction is neglected in the analysis because it is of secondary importance. In some cases, however, corner diffraction may become important, as shown in [43].

The total field \vec{E}^t at P is found by adding the contributions from the incident, reflected, single-diffracted and double-diffracted fields. Thus

$$\vec{E}^t = \epsilon_i \vec{E}^i + \epsilon_r \vec{E}^r + \sum_l \epsilon_{d,l} \vec{E}_{Q_l}^d + \sum_m \epsilon_{dd,m} \vec{E}_m^{dd} + \dots, \quad (3.25)$$

where the ϵ -factors are introduced as shadow indicators. In general, any combination of the right-hand-side terms can occur: an edge-diffracted field can consecutively be diffracted by a corner.

As an illustration of the use of the rectangular block, the SSF behind a block with dimensions $d \times h \times z_{ob} = 20m \times 86m \times 68m$ is calculated for a frequency of 1 GHz. This corresponds approximately to the dimensions of the building of Electrical Engineering at Eindhoven University of Technology. The point source was placed on the negative x -axis in such a way that in a certain region double diffraction is needed because all other contributions are obstructed. In Figure 3.11 an identification of the areas where different ray contributions are present, can be found. Besides the ISB and RSB, also the shadow boundary of the diffracted field (DSB) is shown; across the DSB the double-diffracted field together with the single-diffracted field provides continuity of the total field.

The SSF has been calculated in points P with coordinates $x_p = 250m$, y_p , $z_p = 1.5m$, for $-150m \leq y_p \leq 150m$. The source is positioned at $(-162.5m, 0, 12.5m)$, and is modelled as having an isotropic radiation pattern. Furthermore a horizontal polarisation, i.e. parallel to the ground plane, is used.

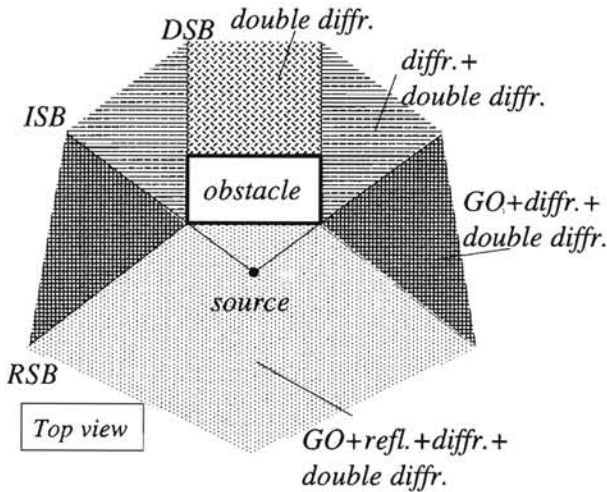


Figure 3.11: Definition of the areas where different field contributions have to be taken into account. Incident, reflection, and diffraction shadow boundaries can be distinguished.

The SSF on the observation line mentioned is shown in Figure 3.12. From the results shown here it is observed that the SSF is continuous across the shadow boundaries ISB and DSB and that strong interference exists in the region where double diffraction is the only contribution. As in the case of the finite-width screen analysis (Fig. 3.6), numerous peaks are produced by the interfering diffraction contributions. The very large SSF in the region behind the obstacle is found because there the only contribution stems from double diffraction. In most practical situations the (interfering) source will directly illuminate some edge which is also visible from the observation point, indicating that there will usually be a single-diffraction contribution. The SSF calculation for the block-type obstacle is strongly polarisation dependent as will be shown in Section 4.4.

As can be seen from the figure, the models predicts continuous fields everywhere. It should be remarked that the geometry analysed here corresponds to a worst-case analysis. In the example the source and observation point have no edge in common, i.e. no edge seen from the source is visible from the observation point and vice versa. In most practical cases they will have one or more edges in common, especially if the source is placed in such a way that the incident field arrives from a direction not parallel to the ground plane. This is, for example, the case in an earth-space link. In the latter case a less sophisticated wave-propagation model can be used, as will be demonstrated in Chapter 6.

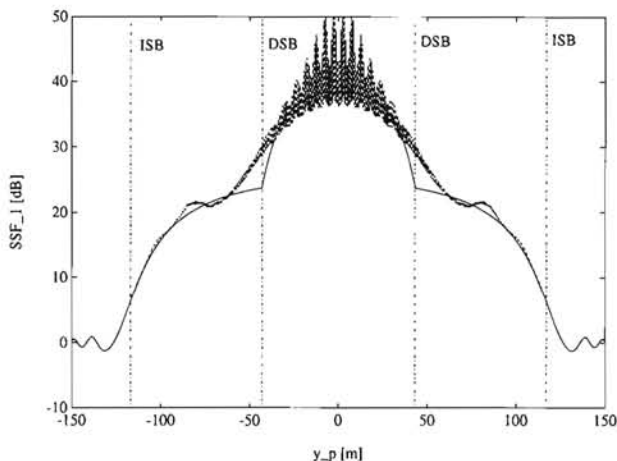


Figure 3.12: SSF behind the rectangular block as function of y_p : total field (-----) and a result from an engineering model (————) discussed in Section 3.4.8. Data: $x_p = 250\text{m}$, $z_p = 1.5\text{m}$, $d \times h \times z_{ob} = 20\text{m} \times 86\text{m} \times 68\text{m}$, $\lambda = 0.3\text{m}$

3.2.5 Finding reflection and diffraction points

In the previous sections nothing has been said about how to find the reflection and diffraction points at obstacle faces and edges, respectively. In general, this job is quite tedious, and a number of papers in the literature deal with the problem of finding reflection and diffraction points [46, 47]. Usually some kind of root-finding procedure has to be used to locate the points where the rays satisfy Snell's law, equation (2.16), or Keller's law of edge diffraction, equation (2.40). In this section alternative methods are proposed that make use of the specific properties of the block-shaped obstacle.

First we describe a very important algorithm in the determination of reflection and diffraction points and in the verification of the existence of ray paths. This algorithm has the symbolic name RAY-EXISTS, and it provides a boolean variable with the value TRUE if a ray from a point A to a point B is not obstructed. It has the value FALSE otherwise. The arbitrary points A and B should not lie inside an obstacle.

The question to be answered by RAY-EXISTS is: does the line $l = \vec{A} + \alpha(\vec{B} - \vec{A})$, $0 \leq \alpha \leq 1$, have an intersection with any face of any obstacle? If the answer to this question is affirmative, then there is ray obstruction. Otherwise, the ray path from A to B exists.

As a start, we assume that the ‘environment’ is defined by N block-shaped obstacles, as introduced in Section 3.2.4. Each obstacle definition is an ordered list of points V_i , ($i = 1, \dots, 8$) with Cartesian coordinates (x_i, y_i, z_i) . First, we determine the centre of gravity G of each obstacle, and the maximum distance r_G from G to V_i . This is easily performed:

$$\vec{G} = \sum_{i=1}^{i=8} \vec{V}_i / 8, \quad (3.26)$$

$$r_G = \max_i |\vec{G} - \vec{V}_i|, \quad (3.27)$$

where the max-function determines the maximum of $|\vec{G} - \vec{V}_i|$ for $i = 1$ to 8. Then, we perform a selection of obstacles that possibly can obstruct the ray path from A to B . For this we need the point G and r_G . If the distance from G to l is larger than r_G then this obstacle cannot obstruct the ray path. The solution for α which corresponds to the smallest distance from G to l is α_0

$$\alpha_0 = \frac{(\vec{A} - \vec{G}) \cdot (\vec{A} - \vec{B})}{|\vec{B} - \vec{A}|^2}, \quad (3.28)$$

and $0 \leq \alpha_0 \leq 1$. If $\alpha_0 < 0$ or $\alpha_0 > 1$, we set the value of α_0 to 0 or 1, respectively. If for this particular obstacle $|\vec{G} + (\alpha_0 - 1)\vec{A} - \alpha_0\vec{B}| > r_G$, it cannot obstruct the ray path. After this selection the number of obstacles M to be considered for ray obstruction is less or equal to N , i.e. $M \leq N$. In practice, only a very limited number of obstacles need to be considered for ray obstruction, so $M \ll N$.

Next, we select a face of an obstacle. Let this face be determined by the vertices V_1, V_2, V_3 , and V_4 in an infinitely-extended plane Y . If l is parallel to Y no intersection can exist, and this case will not be considered. If l is not parallel to Y then the intersection I of l and Y can easily be calculated because the face is plane.

In order to find out whether I lies in the polygon defined by the vertices V_1, V_2, V_3, V_4 , it is sufficient to calculate the vectors \vec{W}_i from V_i to I ($i = 1, \dots, 4$), and the vectors \vec{X}_i from V_i to V_{i+1} ($V_5 = V_1$). Then the vector product $\vec{Z}_i = \vec{X}_i \times \vec{W}_i$ is calculated. If the orientation of the vectors \vec{Z}_i is such that *all* of them point into the same direction, then the intersection I lies inside the polygon. This procedure should be repeated for every face of every obstacle M , i.e. $6M$ times. Of course, the algorithm can be stopped as soon as obstruction takes place. Only if none of the faces of the M obstacles give rise to ray obstruction, then RAY-EXISTS has the value TRUE. This approach is much simpler than solving a parametric equation to determine whether I lies in the polygon. Often this calculation is fairly complex because the polygon can have any (convex) shape. This ends the description of the RAY-EXISTS algorithm.

Before the calculations of the reflection and diffraction points are started, we first determine the vertices, edges and faces of the obstacles that are visible from the source S and the observation point P ; this procedure is referred to as pre-selection. In this way we consider optical blockage of vertices, edges, and faces by the obstacle itself. This is done because reflection points, edge-diffraction points, and corner-diffraction points have the property that they are visible from S as well as P . The algorithm RAY-EXISTS is used to determine whether the rays from S to V_i and from P to V_i , ($i = 1, \dots, 8$), exist. The blockage properties of the edges and faces can be derived from those of the vertices V_i . After this selection, we know which faces, edges and vertices should be considered in the determination of the reflection and diffraction points.

In the following we will consider only one particular obstacle, because other obstacles are treated in the same way. To find the reflection points it is needed to calculate the mirror image of either S or P in the face under consideration. Obviously the face should be visible, and this we know from the pre-selection. For the block-shaped obstacle the determination of the mirror-image corresponds to the calculation of a maximum of six images, and consequently the verification of the existence of six reflection points. The procedure to do this is as follows.

First the mirror image of either S or P is calculated. This is easily done because all faces of the obstacle are plane, and information regarding the normal vector \hat{n} to the face is available. From here on it will be assumed that the mirror image P' of the observation point P is available. Subsequently, the intersection R of the line from S to P' with the (infinitely extended) plane face of the obstacle is calculated. The intersection R is a true reflection point if, and only if, it is located inside the polygon formed by the four edges of the face under consideration. If it lies outside this polygon it is a virtual reflection point. This is schematically shown in Figure 3.13. To determine whether R lies inside the polygon, the approach outlined in the description of RAY-EXISTS can be used. If R proves to be a true reflection point then it has to be determined whether the rays from S to R , and from R to P are obstructed by any of the other obstacles using the algorithm RAY-EXISTS. If this is not the case, then R is a visible reflection point, and consequently its GO reflected field should be taken into account.

The location of the diffraction points can be found using approach which stems from differential geometry [48]. To find the diffraction point Q on the edge from V_1 to V_2 , we first construct the plane W which contains the source point S and the vertices V_1 and V_2 . Furthermore, we identify a rotation axis l given by the line through V_1 and V_2 . Subsequently, P is rotated around l until the rotated point P' is in W . This process is schematically shown in Figure 3.14. After this rotation, S , l and P' all lie in the plane W . The diffraction point

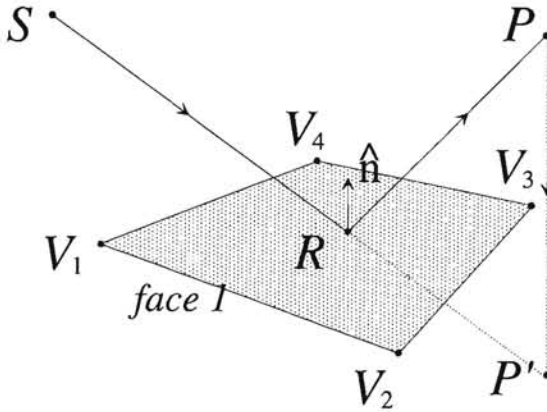


Figure 3.13: Procedure to find the reflection point R in a face of the block shaped obstacle.

Q is found as the intersection of the vector from S to P' and l , as shown in Figure 3.15. Obviously, Q should lie in between V_1 and V_2 . After the determination of Q , it should be verified whether the ray from S to Q and from Q to P is obstructed by any of the obstacles. This is performed using the algorithm RAY-EXISTS. If no obstruction is present, the diffraction point Q found is a visible diffraction point, and its diffraction contribution can be taken into account. This is determination of diffraction points is performed for all visible edges.

The approach to find the diffraction point Q can also be employed to find higher-order diffraction paths. To find the double-diffracted ray path, for example, we proceed as follows. We first construct the plane W_1 , which is uniquely determined by three of the four vertices of the two edges under consideration. A property of the block-shaped obstacle is that the fourth vertex also lies in W_1 (plane faces). Next, the observation point P is rotated around l_2 through V_3 and V_4 , until it lies in W_1 . This point is called P' . Then the source S , the first edge (V_1, V_2), and P' are treated in the same way as outlined for single diffraction. A plane W_2 is determined by S and the two vertices of the first edge (V_1, V_2). Then P' is rotated around l_1 through V_1 and V_2 until it is in W_2 . This point is called P'' . Now S , the first edge, and P'' lie in a planar geometry. The diffraction point Q_1 on the first edge is the intersection of the line from S to P'' and l_1 . The second diffraction point Q_2 is the intersection of the line from Q_1 to P' with l_2 . Of course, Q_1 should lie in between V_1 and V_2 , and Q_2 should lie in between V_3 and V_4 . The double diffraction path is from S to Q_1 , from Q_1 to Q_2 , and from Q_2 to P . Also here RAY-EXISTS is used to check whether ray obstruction arises. Notice that the two edges under consideration should be in the

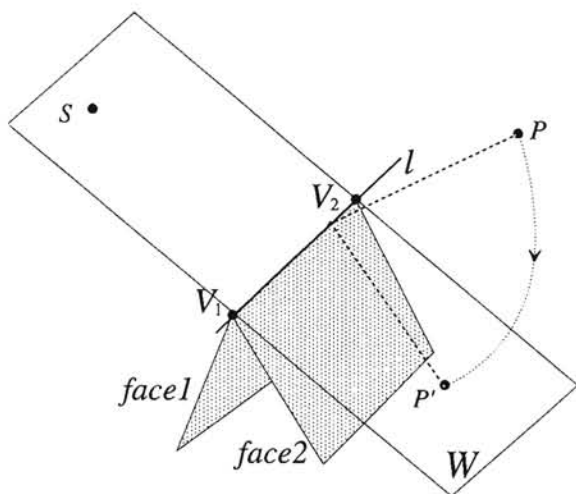


Figure 3.14: Geometry for calculation of the diffraction point Q .

same plane for the procedure to be useful. This means that the rays do not penetrate the obstacle, and consequently one edge can be combined with six other edges to make a double-diffraction geometry. These edges obviously determine the two faces of which the selected edge is part. Information from the pre-selection is used to select only those edges that are visible from S . In simulations involving a lot of obstacles (N large), an additional pre-selection to determine the vertices, edges and faces visible from P might prove worthwhile.

The simplicity of the procedures to find reflection and diffraction points is the main

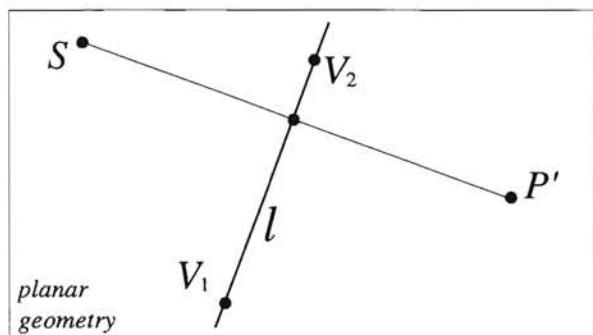


Figure 3.15: Planar diffraction geometry.

advantage of the use of the versatile block-shaped obstacle. These points need not be determined by some iterative procedure, but can be calculated in a straightforward way.

There is one possible disadvantage in using the block-shaped obstacle. Convex obstacles such as cylinders need to be approximated, and cannot be modelled accurately. This deficiency can, however, be removed by using the UTD for convex obstacles as described in Section 3.2.3. In [49] it is shown that for practical applications the circular cylinder can be replaced by a polygonal cylinder with equal height and same volume. It was found that not the diffracted, but reflected contributions from the circular-cylindrical structure are important in communications engineering. These reflections cause a multipath behaviour of the communications channel (fading). The effect of the strong reflection contributions from the cylindrical structures are modelled by the effects of reflected and diffracted waves from a *polygonal* cylinder if the block-shaped obstacle is used.

3.3 Comparison of three field-strength prediction models

In this section¹ a comparison is made between three methods to calculate the EM field diffracted by a perfectly-conducting rectangular block. The models, that are first briefly described, include a ray-based model (Uniform Theory of Diffraction) and two wave-based models (Fresnel Surface Integral and Parabolic Equation method). A test case is analysed with all methods resulting in a good agreement between the predicted results for two linear orthogonal polarisations.

3.3.1 The rectangular block

The problem of field strength prediction has gained renewed interest during the last years. Applications lie in the field of mobile and personal communications and interference reduction, and the latter is one of the research topics of the European project COST 235 [50].

Accurate field-strength predictions are required to account for diffraction of EM waves by buildings. In this section three diffraction models based on the Uniform Theory of Diffraction (UTD), the Fresnel Surface Integral (FSI) [51] and the Parabolic Equation

¹ Note: the major part of this section was already published: G.A.J. van Dooren, C.J. Haslett, and M.F. Levy: *Diffraction by a rectangular building: Comparison of three field-strength prediction techniques*, Elec. Letters, vol. 29, no. 15, pp. 1334-1335, 1993.

(PE) [52], are compared.

The geometry considered is shown in Figure 3.16. The positions of S (ource) and

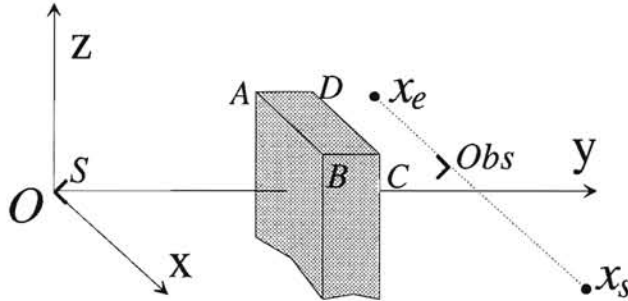


Figure 3.16: Coordinate system and obstacle geometry for field-strength prediction models.

Obs (ervation point) are given in a Cartesian (x, y, z) coordinate system. The source S is placed at the origin and emits a signal that is either horizontally (x) or vertically (z) polarised. The electric field E_{Obs} will be calculated at $Obs(x, y, z)$ for $-15m = x_e \leq x \leq x_s = 15m$, at $y = 120m$ and a frequency of 1 GHz. The obstacle has its top-face at $z_A = 1m$, while $y_A = y_B = 100m$, $y_C = y_D = 110m$, $x_A = x_D = -5m$ and $x_B = x_C = 5m$. It is further assumed that the obstacle extends indefinitely into the $-z$ -direction. The parameter Δz is defined by $\Delta z = z_A - z_{Obs}$.

3.3.2 UTD field-strength prediction model

Using UTD, the total field E_{Obs} at the observation point position is given by

$$E_{Obs} = E^{GO} + \sum_l E_l^{d,s} + \sum_m E_m^{d,d} + \sum_n E_n^{d,h}, \quad (3.29)$$

where E^{GO} is the geometrical optics field, $E^{d,s}$ is the single-diffracted field at the obstacle (eq. 2.45), $E^{d,d}$ the double-diffracted field (eq. 2.83), and $E^{d,h}$ are higher-order diffracted fields. Notice that E^{GO} is included only for observation points in the lit space. The summations in equation (3.29) extend over the number of ray paths originating from S to Obs , which contain one (single diffraction) or more (double/higher-order diffraction) points located on the edges of the rectangular block. It was found from numerical analyses that higher-order diffraction contributions should be taken into account up to order $k^{-3/2}$, where $k = 2\pi/\lambda$ with λ being the wavelength (Sec. 4.4). The contributions of order $k^{-3/2}$ correspond to waves undergoing both corner and edge diffraction.

Recently, the performance of this field-strength prediction model has been experimentally tested for scaled obstacles at a frequency of 50 GHz using a vector network analyser. Excellent agreement in great detail between theoretical and measured results was found for conducting obstacles with various geometries (Sec. 4.4).

The main advantage of the UTD model is that it provides a clear insight into the diffraction process at edges of buildings, and that diffraction at an obstacle and an antenna may be analysed in a combined way. It is very well suited for the description of diffraction phenomena if the observation point is near the obstacle.

3.3.3 FSI field-strength prediction model

In this model initially three waves are considered: one propagating over the top face of the obstacle and one around each side. Each of these paths is regarded as a two-dimensional system with a line source as the transmitter. The obstacle outline of each two-dimensional system may be likened to a flat-topped terrain obstacle [51]. It entails evaluating the relative electric field strength due to a double knife-edge system, and adding it to that for the wave undergoing a reflection in the connecting surface [51]. The diffracted field at *Obs* is found using a kind of integration, similar to Kirchhoff's theory.

When the model is extended to a three-dimensional one, parts of the two-dimensional systems are found to overlap, so that it would be incorrect to simply add the three relative field strengths together. Rather the total relative electric field is given more accurately by

$$E_{Obs} = E_1 + E_2 + E_3 - E_1 \cap E_2 - E_1 \cap E_3, \quad (3.30)$$

where E_1 is the relative electric field strength for the top face calculated by integration over the surface $y = y_D, z > z_D$ [51], E_2 for the left-hand edge of the building calculated by integration over the surface $y = y_C, x > x_C$, and E_3 for the right-hand edge of the building calculated by integration over the surface $y = y_D, x < x_D$. The terms $E_1 \cap E_2$ and $E_1 \cap E_3$ represent the field contributions due to the overlapping portions of the surfaces of integration.

In predicting the diffracted field for a vertically (z) polarised wave in the shadow of a conducting rectangular block, an effective reflection coefficient $R = 1$ is assumed for the top face diffraction component and $R = -1$ for the side-face components. These are reversed for a horizontally-polarised wave. Additionally, for a practical building, an effective reflection coefficient R must be assumed with $0 < |R| < 1$ (eq. (2.84) and (2.85)). If the electrical characteristics of the solid rectangular block are unknown, then an assumed reflection coefficient of zero may give reasonable predictions [53]. It should be noted that

only reflections in the surfaces connecting two edges are considered, i.e. surfaces parallel to the xy - and the yz -planes. Furthermore, the pattern of the antenna at Obs is not modelled.

The main advantage of this method is that it may be rapidly implemented using well-established methods.

3.3.4 PE field-strength prediction model

The PE technique provides a numerical full-wave solution to radio propagation problems. PE methods have been applied successfully to propagation over irregular terrain [52] and more recently to propagation in urban environments [54].

In three dimensions, a function $u = u(x, y, z)$ which is slowly varying with respect to the variable y , is associated with a field component $E_{Obs} = \exp(-jky)u(x, y, z)$ propagating into the y -direction. Then u satisfies approximately the outgoing wave PE [52]

$$\frac{\partial u}{\partial y} = jk \left(1 - \sqrt{1 + \frac{1}{k^2} \frac{\partial^2}{\partial x^2} + \frac{1}{k^2} \frac{\partial^2}{\partial z^2}} \right) u. \quad (3.31)$$

Notice that in equation (3.31) incoming wave solutions have been discarded [54]. The second order partial derivatives in the argument of the radical in equation (3.31) are now approximated in a numerical way. The parabolic nature of equation (3.31) allows the solution to be marched from one plane $y = \text{constant}$ to the next. It can be solved by two-dimensional FFT techniques or by finite-difference methods. FFT techniques are more efficient numerically, but currently it is not known whether arbitrary boundary conditions at the obstacle surfaces can be modelled. Finite-difference techniques require smaller integration step sizes and are hence slower, but they allow accurate modelling of boundary conditions. The results to be presented have been obtained by means of a two-dimensional split-step/FFT technique. An image model has been used to account for reflections in the obstacle faces, which can be either (perfectly) absorbing or conducting. This simple approach works well for a rectangular block with faces parallel to the Cartesian axes. The extension to an obstacle with finite conductivity, or to an obstacle of more complicated shape, is not straightforward.

The three-dimensional split-step method is straightforward to implement and can be used in the shadow region as well as the transition regions.

3.3.5 Comparison of results

Typical results obtained from the three methods discussed are shown in Figure 3.17 for both vertical (V) and horizontal (H) polarisation and for $\Delta z = 5m$. The results for vertical

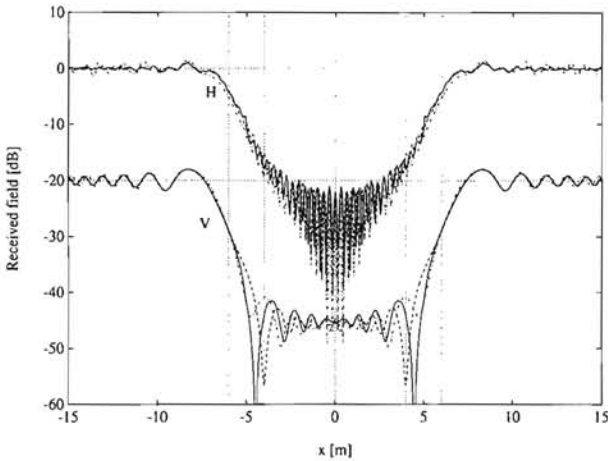


Figure 3.17: Field strength behind the rectangular block as function of x : UTD (—), FSI (---) and PE (-·-·-·-); vertical polarisation (lower curves) and horizontal polarisation (higher curves). The results for vertical polarisation have been lowered by 20 dB for legibility.
 Data: $\Delta z = 5m$, $y = 120m$, $\lambda = 0.3m$

polarisation have been lowered by 20 dB for legibility. Agreement is very good except for vertical polarisation in the interval $4 \leq |x| \leq 6$, where there are small differences. These are probably due to the treatment of corner diffraction. All models predict the same average level of the received field in the shadow region behind the building, as well as the strong polarisation dependence (Sec. 4.4). Comparisons for other values of Δz lead to similar conclusions.

3.3.6 Conclusions

Three diffraction models have been described and compared for the case of diffraction by a perfectly-conducting rectangular block at a frequency of 1 GHz and a realistic building geometry. Despite their very different nature, results of the three methods show remarkably good agreement for the predicted field strength behind the obstacle, and they confirm the strong polarisation dependence of the diffracted field.

3.3.7 Addendum: comparison of results for the half-plane and the finite-width screen

Results for the SSF predicted by the UTD, FSI and PE methods were also compared for the half-plane obstacle and the finite-width screen, depicted in Figures 3.2 and 3.5. These geometries are analysed in this section. The results for the half-plane are shown in Figure 3.18 for $z_{ob} = 60m$, $x_p = 100m$ and $0 \leq z_p \leq 90m$ and a frequency of 1 GHz. It can clearly be seen from this figure that good agreement between the result of all three methods exists, although the FSI and PE results slightly overestimate the SSF for small z_p .

The calculated SSF results for the finite-width screen shown in Figure 3.5 can be found in Figures 3.19 and 3.20. Good agreement between all results is found for both obstacle heights, although some differences between the UTD/FSI and the PE method can be found at $y_p = \pm 43m$ where corner diffraction is important. The differences between UTD and FSI would be more explicit if another polarisation would be used; the UTD results change as function of polarisation while the FSI results remain unchanged. The result from Figures 3.19 and 3.20 compare very well to the corresponding graphs given in Figure 3.6. The differences between the results shown in Figures 3.18 to 3.20 are due to the fact that FSI as well as PE neglect the part of the diffraction field caused by the reflected field, present in the UTD formulation through the coefficients $D_{3,4}$ in equation (2.47). Furthermore, PE also suffers from a paraxial approximation [52]. Other investigations have revealed that if the reflection coefficients in the UTD formulation are set to zero, the UTD results and the FSI results are identical for the half-plane and the finite-width screen analyses.

It is concluded that for simple site shielding problems incorporating single, isolated objects UTD, FSI and PE give (nearly) identical results. They can therefore all be used for site-shielding predictions, and the user can benefit from the specific advantages of the methods discussed.

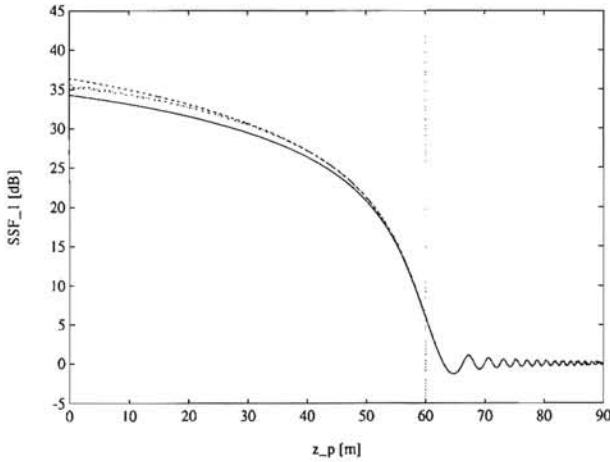


Figure 3.18: SSF of a half-plane as function of z_p : UTD (—), FSI (---) and PE (····).

Data: $x_p = 100\text{m}$, $z_{ob} = 60\text{m}$, $\lambda = 0.3\text{m}$

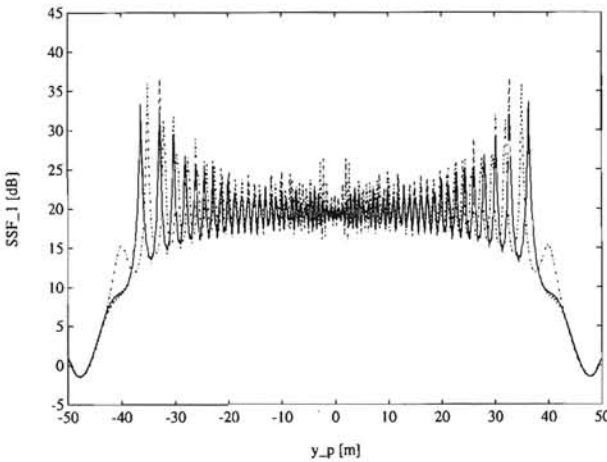


Figure 3.19: SSF of a finite-width screen as function of y_p : UTD (—), FSI (---) and PE (····).

Data: $x_p = 100\text{m}$, $z_p = 1.5\text{m}$, $z_{ob} = 10\text{m}$, $d_1 = d_2 = 43\text{m}$, $\lambda = 0.3\text{m}$

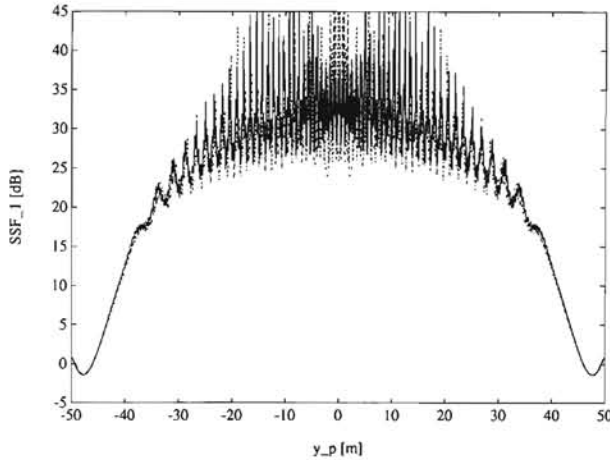


Figure 3.20: SSF of a finite-width screen as function of y_p : UTD (————), FSI (-----) and PE (· · · · ·).

Data: $x_p = 100m$, $z_p = 1.5m$, $z_{ob} = 60m$, $d_1 = d_2 = 43m$, $\lambda = 0.3m$

3.4 An engineering approach for site shielding calculations

In this section², two models for the approximate calculation of the field distribution in the vicinity of a perfectly-conducting finite-width screen are discussed. The first model is derived from the Uniform Theory of Diffraction (UTD), and is simplified such that the amplitude of the individual field contributions can be easily calculated (pseudo-UTD model). The second model is based on a graphical approach. Coefficients that are representative for the dimensions of the obstacle and for the relative position of the observation point are used together with standardised equations to calculate the field strength in the whole shadow region behind the screen. Also a modification of the current CCIR procedure for knife-edge diffraction is proposed, such that it can be applied to a finite-width screen.

Results of all models are compared with results from the more accurate model based on UTD. All models proposed are simple to apply and provide an essential extension to

² Note: the major part of this section was already published: G.A.J. van Dooren and M.H.A.J. Herben: *An engineering approach for site shielding calculations*, International Journal of Satellite Communications, vol. 11, no. 6, pp. 301–311, 1993.

currently available engineering models. It is found that the pseudo-UTD model has the best performance with respect to the reference UTD (full-UTD) approach. The graphical method, however, is more user friendly than the pseudo-UTD model, because less intermediate results need to be calculated. Moreover, the use of this method yields a field-strength distribution for the whole shadow region of the obstacle instead of the field in just a single point. It is found that also the modified CCIR approach can be used with good accuracy.

The models discussed answer some questions formulated by the CCIR concerning site shielding, and extend the currently available engineering models for this interference reduction technique.

3.4.1 Introduction

For the calculation of the scattered field in the surroundings of an obstacle several theories can be used [45, 55]. A very attractive approach from an engineering point of view is the Geometrical Theory of Diffraction (GTD) and its uniform extension (UTD), because of their ability to provide a substantial insight into the diffraction mechanisms at the obstacle edges. From a practical point of view, however, it is often necessary to even further simplify the GTD/UTD approach. As a result, approximate methods for efficiently evaluating the scattered field and/or the site shielding factor (SSF), which is a measure for the additional propagation loss along the propagation path, have been developed. Obviously, these approximate methods suffer from a number of shortcomings of which the most important are a limited range of applicability, and the fact that only scattering by infinitely wide obstacles can be accounted for [1].

Currently available engineering methods for the analysis of site shielding are provided by the International Radio Consultative Committee (CCIR, now the Radio Sector of the ITU) [56, 57, 58]. The methods offered, however, are either two-dimensional, or have a limited applicability. International cooperation projects, such as for example the project COST 235 of the European Community, focus on the development of reliable prediction procedures for site shielding and other interference reduction techniques [59]. Applications of the wave-propagation models are the analysis of the reduction of interference due to anomalous propagation, which strongly influences the coordination distance of earth stations for small time percentages.

In this section we are mainly concerned with finding approximate methods to the approaches that have been proposed in Section 3.2 for the calculation of the (scattered) field strength and/or site shielding factor of some specified finite-width screen with knife-edges. The UTD reference model presented in [55] has been extensively verified by laboratory

measurements with scaled obstacles (see also Sections 4.2, 4.3, 4.4 and 4.5). The measurements were performed at a frequency of 50 GHz in an ordinary room using a vector network analyser. A comparison of the results of the measurements and of the UTD model used can be found in Sections 4.2 and 4.3 and in [43], where also the accuracy of the measurements is discussed. In all cases considered extremely good agreement between measurements and theory was established. Since the full-UTD model is quite complex and needs a substantial amount of calculation time, and because the results show very rapid fluctuations as function of position, other parameters deduced from the field-strength distribution behind the obstacle may be of help. In this section a simplified approach for the prediction of the site shielding factor will be derived from the full-UTD model. It can be used for the calculation of the average and minimum SSF behind a finite-width screen and it is referred to as the pseudo-UTD model. Also an extension of the current CCIR method for knife-edge diffraction will be proposed such that it can be used for the analysis of an obstacle of finite extent.

3.4.2 Average and minimum SSF

In Section 3.2.2 the calculation of the field distribution in the surroundings of a perfectly-conducting finite-width screen was studied. Using UTD, the total electric field \vec{E}^t at a point P behind a screen can be calculated using

$$\vec{E}^t = \epsilon_i \vec{E}^i + \sum_{j=1}^3 \epsilon_j \vec{E}_{Q_j}^d, \quad (3.32)$$

where P is an arbitrary observation point with Cartesian coordinates (x_p, y_p, z_p) , the factors ϵ_i and ϵ_j ($j = 1, 2, 3$) are shadow indicators accounting for wave obstruction, \vec{E}^i is the directly incident field at P and $\vec{E}_{Q_j}^d$ are the individual diffraction contributions from diffraction points Q_j on the edges Γ_j . It is assumed that the projection P' of P onto the obstacle, along the diffraction cone generated at Q_j , is sufficiently removed from the corners with coordinates $(0, \pm d, z_{ob})$. If this is not the case, a corner-diffraction contribution becomes important (Sec. 3.2.2), which, for simplicity, is not included in the derivation of the engineering methods. To our opinion, these corner-diffracted field contributions are not important in the site shielding analyses as performed in this section, because site shielding is only effective in the shadow region behind an obstacle. Corner-diffraction contributions become important at shadow boundaries, where the SSF is fairly low (approximately 6 dB). However, in other applications such as mobile communications (Ch. 6), this type of field contribution may be important.

The geometry considered and the diffraction points are shown in Figure 3.5, repeated for

convenience in Figure 3.21. The obstacle is a screen in the yz -plane, of finite width $2d$. The

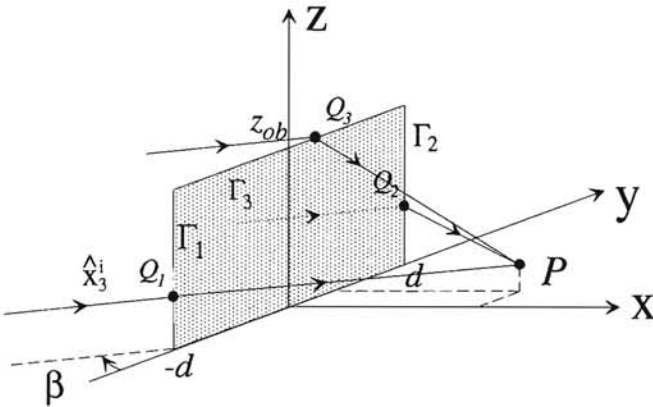


Figure 3.21: Definition of diffracting obstacle and location of diffraction points.

height of the obstacle is z_{ob} , and the xy -plane is considered to be the ground plane. The effect of the latter is neglected. The finite-width screen is described by $x = 0$, $-d \leq y \leq d$, $0 \leq z \leq z_{ob}$. The incident wave is assumed to be generated by a very distant source and therefore it can be considered as a plane wave. The direction of propagation is

$$\hat{x}_3^i = (\sin \beta, \cos \beta, 0). \quad (3.33)$$

It is obvious that \hat{x}_3^i is parallel to the ground plane, and two transverse polarisation directions are defined

$$\hat{x}_1^i = (-\cos \beta, \sin \beta, 0), \quad (3.34)$$

and

$$\hat{x}_2^i = (0, 0, 1). \quad (3.35)$$

In the following, the polarisation of the incident wave is taken as a linear combination of \hat{x}_1^i and \hat{x}_2^i . The calculation of the total field \vec{E}^t , as given by equation (3.32), is dependent on the polarisation of the incident (interference) field, and a dyadic diffraction coefficient is needed to treat the different types of polarisation (eq. (2.45)). Since, in general, the polarisation of the incident field is not exactly known, it is necessary to be able to vary the polarisation of the incident field for analysis purposes.

The locations of the diffraction points Q_j ($j = 1, 2, 3$) were already given in equations (3.14) to (3.16), where $x_p, z_p > 0$. Furthermore, the analysis will be restricted to

points P in the shadow region behind the obstacle. This means that $\epsilon_i = 0$ in equation (3.32)

In case of a plane incident wave with a unit amplitude, the SSF of the finite-width screen can be calculated from equation (3.1)

$$SSF = 20 \log \left[\frac{I_-}{I_+} \right] = -20 \log |\vec{E}^t| \quad [\text{dB}], \quad (3.36)$$

where the level of the field in the absence of the screen $I_- = 1$, and $I_+ = |\vec{E}^t|$. The SSF expresses the attenuation of the interference wave caused by the placement of the screen on the propagation path. Typical results of the calculation of the SSF for observation points behind a finite-width screen can be found in Section 3.2.

In practice, the SSF cannot be measured in exactly one point, but it will always be measured in a cluster of points. Therefore, it will be more or less an average of the SSF of the individual points. For this reason it seems more appropriate to calculate a measure for the ‘average’ value of the SSF, SSF_A , which is defined as [55]

$$SSF_A = -10 \log \left[\sum_{j=1}^3 |\vec{E}_{Q_j}^d|^2 \right] \quad [\text{dB}]. \quad (3.37)$$

Notice that SSF_A is obtained as an addition of power levels of the individual contributions $\vec{E}_{Q_j}^d$. Equation (3.37) is valid in the shadow region behind the obstacle only, and therefore $\epsilon_i = 0$ in equation (3.32), while $\epsilon_j = 1$ ($j = 1, 2, 3$). This restriction is being used because the site shielding principle is only effective in this shadow region [55, 45], and, moreover, it simplifies the calculation.

From a practical point of view also another parameter is of interest. This is the minimum attainable SSF, SSF_M , and represents some ‘worst case’ value of the site shielding factor. An expression for SSF_M is given by

$$SSF_M = -20 \log \left[\sum_{j=1}^3 |\vec{E}_{Q_j}^d| \right] \quad [\text{dB}]. \quad (3.38)$$

Notice that SSF_M is obtained as an addition of amplitude levels of the individual contributions $\vec{E}_{Q_j}^d$. Both expressions (3.37) and (3.38) can compactly be written as

$$SSF = \frac{-20}{N} \log \left[\sum_{j=1}^3 |\vec{E}_{Q_j}^d|^N \right] \quad [\text{dB}], \quad (3.39)$$

where SSF_A is obtained from equation (3.39) for $N = 2$, and SSF_M is obtained for $N = 1$. Equation (3.39) has a relation with vector calculus. Using $N = 2$ results in the calculation

of the L_2 or Euclidean norm of a vector in some three-dimensional space, while the use of $N = 1$ results in the L_1 norm. Using this analogy, it is clear that all contributions $|\vec{E}_{Q_j}^d|$ should be independent. This implies that equation (3.39) may only be used with individual contributions that have an independent phase behavior [45, 55].

In the following we are interested in finding a simple approach for the calculation of SSF_A and SSF_M of a specific finite-width screen. First, a pseudo-UTD model is presented [55]. Second, the current CCIR procedure for knife-edge diffraction is extended such that it can be used for the analysis of a finite-width screen. Finally, an even more simplified approach is presented that uses coefficients to be read from tables and graphs. All models proposed are simple to apply and give approximated results for SSF_A as well as SSF_M .

3.4.3 A pseudo-UTD site shielding model

Next we will derive the pseudo-UTD model for finite-width screen shielding. In equations (3.37) and (3.38) it can be seen that only the magnitude of the individual ray contributions is needed. A major simplification in the SSF calculation would therefore be to avoid complex arithmetic. Another simplification would be the use of some intermediate polarisation direction of the interfering incident wave. A logical choice for this polarisation direction is a polarisation constant a with the value $a = \frac{1}{2}\sqrt{2}$, corresponding to an incident polarisation \hat{e}_{pol} of

$$\hat{e}_{pol} = \left[a\hat{x}_1^i + \sqrt{1 - a^2}\hat{x}_2^i \right]_{a=\frac{1}{2}\sqrt{2}} = \frac{1}{2}\sqrt{2} \left[\hat{x}_1^i + \hat{x}_2^i \right]. \quad (3.40)$$

Throughout this section, results will be presented for this type of incident polarisation.

Since only the magnitude of the diffracted field is needed, the dyadic operation in equation (2.45) can be simplified. Because the polarisation is chosen in such a way that part of the incident field is in the $\hat{\beta}'$ direction, and the same part is in the $\hat{\varphi}'$ direction (Fig. 2.4), a typical contribution as used in equations (3.37) and (3.38) is given by [55]

$$|\vec{E}_{Q_j}^d|^2 = \frac{|D_s|^2 + |D_h|^2}{s}, \quad (3.41)$$

where s is the distance from Q_j to P , and $D_{s,h}$ are given by equation (3.5), repeated here for convenience

$$D_{s,h} = \frac{-e^{-j\pi/4}}{2\sqrt{2}\pi k} \left[\frac{F(kLa(\varphi^-))}{\cos(\varphi^-/2)} \mp \frac{F(kLa(\varphi^+))}{\cos(\varphi^+/2)} \right]. \quad (3.42)$$

For the vertical edges the distance parameter L is given by $L = s$, while for the horizontal edge $L = s \sin^2 \beta$. Furthermore it is found that

$$a(x) = 2 \cos^2(x/2), \quad (3.43)$$

and the caustic distance $\rho^d = \infty$ because the edges are straight ($a_e = \infty$). In equation (3.42), φ^\pm are given by $\varphi^\pm = \varphi \pm \varphi'$ and these angles are defined in Figure 3.22. From

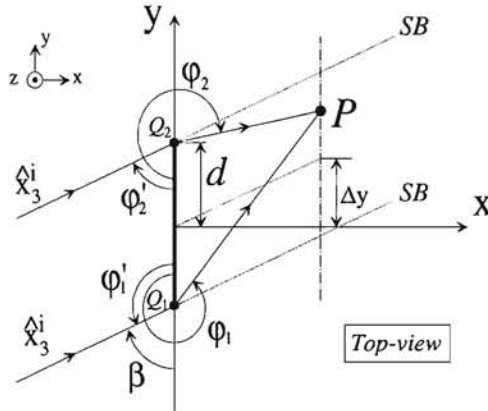


Figure 3.22: Definition of $\varphi_1, \varphi_1', \varphi_2, \varphi_2'$ and Δy .

equation (3.42) it is immediately clear that the complex character of the calculation is caused by some exponentials and the transition function F given by equation (2.57). Since the primary interest for the present application is $|\vec{E}_{Q_2}^d|$, and because only $|D_{s,h}|$ is needed, further simplifications can be made. Using equation (3.42) and equation (3.41) yields

$$|\vec{E}^d|^2 = \frac{1}{8\pi k_s} \left[\frac{|F(kLa(\varphi^-))|^2}{\cos^2(\varphi^-/2)} + \frac{1}{\cos^2(\varphi^+/2)} \right], \quad (3.44)$$

where the transition function for the reflected part of the diffracted field has been set to one because the reflection shadow boundary lies in lit space $x < 0$. In the following it will prove advantageous to approximate the magnitude of the transition function F by

$$|F(x)| = \begin{cases} \sqrt{2 \left(\sqrt{\frac{\pi x}{2}} - x - \frac{x^2}{3} \right)^2 + 2 \left(\frac{x^2}{3} - x \right)^2} & , \text{ if } 0 < x < 0.1, \\ -0.052 [\log x]^3 - 0.131 [\log x]^2 \\ + 0.329 \log x + 0.838 & , \text{ if } 0.1 \leq x \leq 10, \\ 1 & , \text{ if } x > 10. \end{cases} \quad (3.45)$$

The relative error of this approximation with respect to the exact transition function (2.57) can be found in Figure 3.23. As can be seen from this figure, the maximum relative error is always less than 1%.

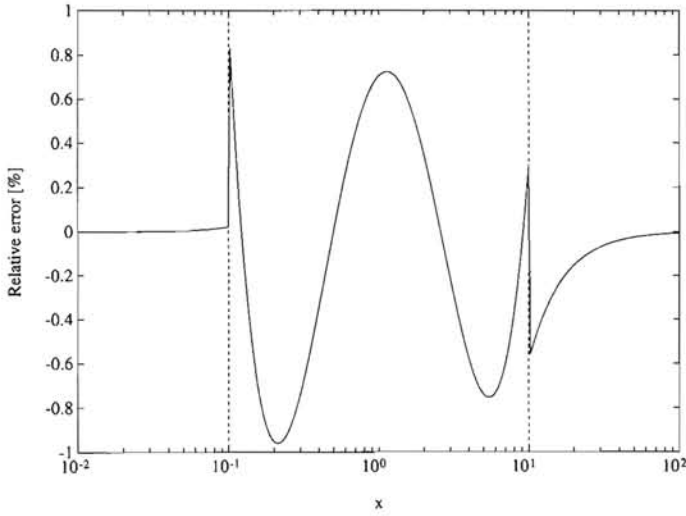


Figure 3.23: Relative error in the computation of $|F(x)|$.

Following the approach that led to equation (3.44) results in an expression for the individual field contribution $|\vec{E}_{Q_1}^d|$

$$|\vec{E}_{Q_1}^d|^2 = \frac{1}{8\pi k s_1} \left[\frac{F_1^2}{\cos^2(\varphi_1^-/2)} + \frac{1}{\cos^2(\varphi_1^+/2)} \right], \quad (3.46)$$

where s_1 is the distance from Q_1 to P

$$s_1 = \sqrt{x_p^2 + (y_p + d)^2}, \quad (3.47)$$

and

$$\varphi_1^- = \varphi_1 - \varphi_1' = \frac{\pi}{2} + \beta + \arctan\left(\frac{y_p + d}{x_p}\right), \quad (3.48)$$

$$\varphi_1^+ = \varphi_1 + \varphi_1' = \frac{5\pi}{2} - \beta + \arctan\left(\frac{y_p + d}{x_p}\right). \quad (3.49)$$

The factor F_1^2 is given by

$$F_1^2 = \left| F(2k s_1 \cos^2(\varphi_1^-/2)) \right|^2, \quad (3.50)$$

and $|F(x)|$ is given by equation (3.45).

An identical evaluation for the second contribution generated at Q_2 gives

$$|\vec{E}_{Q_2}^d|^2 = \frac{1}{8\pi k s_2} \left[\frac{F_2^2}{\cos^2(\varphi_2^-/2)} + \frac{1}{\cos^2(\varphi_2^+/2)} \right], \quad (3.51)$$

with s_2 the distance from Q_2 to P

$$s_2 = \sqrt{x_p^2 + (y_p - d)^2}, \quad (3.52)$$

and

$$\varphi_2^- = \varphi_2 - \varphi_2' = \frac{3\pi}{2} - \beta - \arctan\left(\frac{y_p - d}{x_p}\right), \quad (3.53)$$

$$\varphi_2^+ = \varphi_2 + \varphi_2' = \frac{3\pi}{2} + \beta - \arctan\left(\frac{y_p - d}{x_p}\right). \quad (3.54)$$

The factor F_2^2 is calculated using $F_2^2 = |F(x)|^2$ with $x = 2ks_2 \cos^2(\varphi_2^-/2)$.

The diffraction angles φ and φ' for the first and second diffraction point $Q_{1,2}$ can be found in Figure 3.22, where it can easily be seen that the center of the shadow region to the right of the screen at a distance x_p is located at

$$\Delta y = \frac{x_p}{\tan \beta}, \quad (3.55)$$

and that the shadow region extends from $-d + \Delta y < y_p < d + \Delta y$.

The contribution generated at Q_3 can be found in a similar way

$$|\vec{E}_{Q_3}^d|^2 = \frac{1}{8\pi k s_3 \sin^2 \beta} \left[\frac{F_3^2}{\cos^2(\varphi_3^-/2)} + \frac{1}{\cos^2(\varphi_3^+/2)} \right], \quad (3.56)$$

where s_3 is the distance from Q_3 to P

$$s_3 = \frac{\sqrt{x_p^2 + (z_p - z_{ob})^2}}{\sin \beta}, \quad (3.57)$$

and

$$\varphi_3^- = \varphi_3 - \varphi_3' = \pi - \arctan\left(\frac{z_p - z_{ob}}{x_p}\right), \quad (3.58)$$

$$\varphi_3^+ = \varphi_3 + \varphi_3' = 2\pi - \arctan\left(\frac{z_p - z_{ob}}{x_p}\right). \quad (3.59)$$

The factor F_3^2 can again be calculated using $F_3^2 = |F(x)|^2$ with $x = 2ks_3 \sin^2 \beta \cos^2(\varphi_3^-/2)$.

The definition of the angles φ_3 and φ_3' is shown in Figure 3.24. The expressions for SSF_A and SSF_M are readily obtained using equations (3.37) and (3.38), in combination with equations (3.46), (3.51) and (3.56)

$$SSF_A = -10 \log \left[|\vec{E}_{Q_1}^d|^2 + |\vec{E}_{Q_2}^d|^2 + |\vec{E}_{Q_3}^d|^2 \right] \text{ [dB]}, \quad (3.60)$$

$$SSF_M = -20 \log \left[|\vec{E}_{Q_1}^d| + |\vec{E}_{Q_2}^d| + |\vec{E}_{Q_3}^d| \right] \text{ [dB]}. \quad (3.61)$$

The pseudo-UTD model described in the foregoing can easily be implemented in a numerical model, and still offers the insight that is provided by the full-UTD model. A comparison between results obtained from the full-UTD and the pseudo-UTD model will be given in one of the following sections.

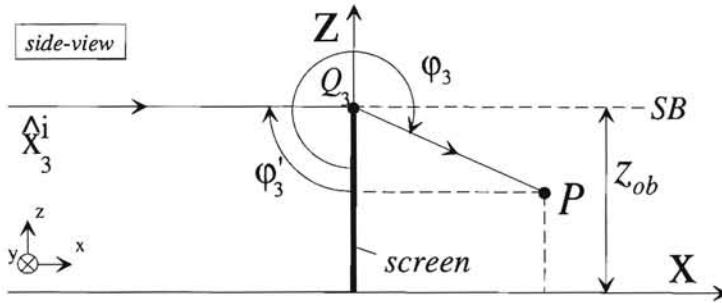


Figure 3.24: Definition of φ_3 and φ_3' ; also the projection of \hat{x}_3^i and the vector from Q_3 to P on the xz -plane are shown.

3.4.4 Modification of the CCIR site shielding procedure

The CCIR does not provide a method to calculate the SSF of a finite-width screen. For a single knife-edge an approximate model is available that is based on the Kirchhoff approximation. Introduce the parameter ν as

$$\nu = 2 \sin(\psi/2) \sqrt{\frac{2s}{\lambda}}, \quad (3.62)$$

where ψ is related to φ^- by

$$\psi = \varphi^- - \pi. \quad (3.63)$$

Notice that ν has a close relation with the detour parameter ξ as introduced in equation (3.10): $\nu = \xi \sqrt{2/\pi}$.

The site shielding factor for a single knife-edge is known to be given by [3, 1]

$$SSF = 20 \log [\mathcal{L}(\nu)] \quad [\text{dB}], \quad (3.64)$$

with

$$\mathcal{L}(\nu) = 2.1 (\sqrt{\nu^2 + 1} + \nu). \quad (3.65)$$

Notice that this version of the CCIR formula was found to be more accurate than the most recent one [1]. The CCIR formula is (theoretically) valid for small diffraction angles ψ due to approximations in the derivation of the solution for half-plane diffraction, viz. equation (3.65). In [1] an upper limit of the diffraction angle $\psi = 12^\circ$ is given as a maximum in order for equation (3.65) to be accurate, and this may restrict the use of the CCIR formula. Whether the formulation given in equation (3.65) imposes restrictions on its use and accuracy will be investigated in the following.

The CCIR model can be extended in the same way as was done for the pseudo-UTD model. In this way, the following expressions for the minimum and average SSF of the finite-width screen can be obtained

$$SSF_A = -10 \log \left[\frac{1}{\mathcal{L}^2(\nu_1)} + \frac{1}{\mathcal{L}^2(\nu_2)} + \frac{1}{\mathcal{L}^2(\nu_3)} \right] \text{ [dB]}, \quad (3.66)$$

$$SSF_M = -20 \log \left[\frac{1}{\mathcal{L}(\nu_1)} + \frac{1}{\mathcal{L}(\nu_2)} + \frac{1}{\mathcal{L}(\nu_3)} \right] \text{ [dB]}, \quad (3.67)$$

where

$$\nu_{1,2,3} = 2 \sin \left(\frac{\varphi_{1,2,3}^- - \pi}{2} \right) \sqrt{\frac{2s_{1,2,3}}{\lambda}}, \quad (3.68)$$

and the distances s_j , ($j = 1, 2, 3$), are from the diffraction points Q_j to the observation point P .

3.4.5 Comparison of two SSF prediction methods

In this section the accuracy of the pseudo-UTD and extended CCIR methods in comparison with the method of finite-width shielding as described in Section 3.2.2 will be investigated. The average and minimum SSFs derived from the full-UTD model, incorporating edge- and corner-diffraction, will act as a reference.

In the following a screen will be considered with a total width of 200λ , hence $d = 100\lambda$, and a height $z_{ob} = 200\lambda$. The SSF will be calculated at an observation point P with coordinates $x_p = 100\lambda$ or 800λ , y_p , $z_p = 5\lambda$, as a function of y_p . In practical terms this means that, at 1 GHz, the dimensions of the obstacle are $d = 30m$ and $z_{ob} = 60m$, while $x_p = 30m$ or $240m$. For simplicity $\beta = \pi/2$, such that the incident wave propagates parallel to the x -axis, perpendicular to the screen.

In Figure 3.25, $SSF_{M,A}$ based on the extended CCIR method are compared for $x_p = 100\lambda$ with results predicted by the full-UTD method. The results from the pseudo-UTD method are not shown in Figure 3.25 because they are indistinguishable from those of the full-UTD method. Despite the fact that diffraction angles much larger than 12° have been used, the modified CCIR model still predicts the average and minimum SSF quite accurately.

In Figure 3.26 the x_p coordinate has been changed to $x_p = 800\lambda = 240m$. Again, the pseudo-UTD results are identical to the results predicted by the full-UTD method and are not shown. It is seen that the results predicted by the extended CCIR model are quite accurate.

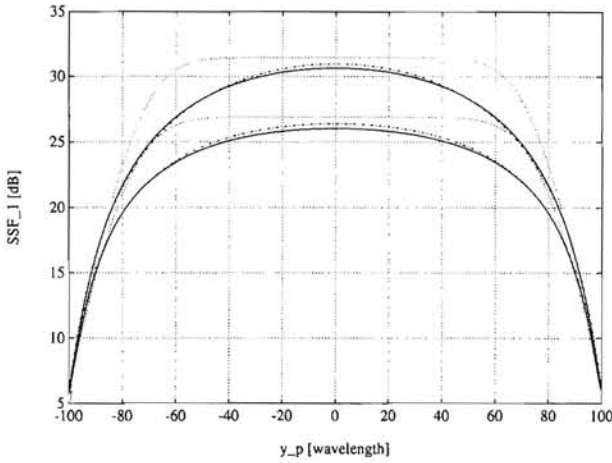


Figure 3.25: SSF of a finite-width screen as function of y_p : results from full-UTD (—) and the extended CCIR method (- - - - -), and results from the graphical approach discussed in Section 3.4.6 (· · · · ·); SSF_A (higher curves) and SSF_M (lower curves).

Data: $x_p = 30m$, $z_p = 1.5m$, $d = 30m$, $z_{ob} = 60m$, $\lambda = 0.3m$

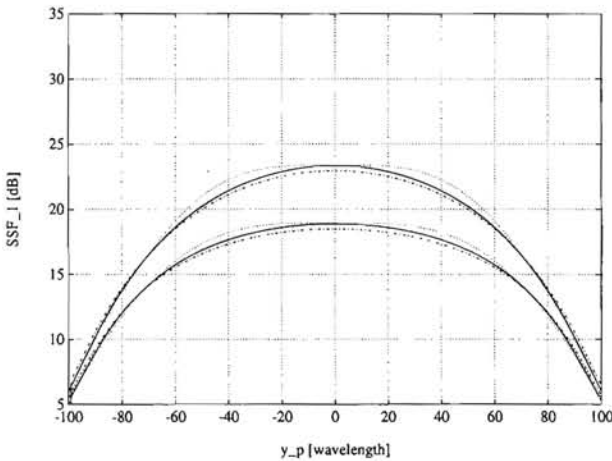


Figure 3.26: SSF of a finite-width screen as function of y_p : results from full-UTD (—) and the extended CCIR method (- - - - -), and results from the graphical approach discussed in Section 3.4.6 (· · · · ·); SSF_A (higher curves) and SSF_M (lower curves).

Data: $x_p = 240m$, $z_p = 1.5m$, $d = 30m$, $z_{ob} = 60m$, $\lambda = 0.3m$

3.4.6 A graphical method for finite-width screen shielding

In the pseudo-UTD model six angles ($\varphi_1^\pm, \varphi_2^\pm, \varphi_3^\pm$), three approximate transition functions ($F_{1,2,3}^2$), three field-strength levels ($|\vec{E}_{Q_{1,2,3}}^d|$), and SSF_A and SSF_M need to be calculated. The same is true for the extended CCIR method, although the number of intermediate calculations is somewhat less. A further simplification in the calculation of $SSF_{A,M}$ would be a graphical model, e.g. an approach using standardised equations and coefficients in graphs, expressing the field strength as a function of d , z_{ob} , and the Cartesian coordinates of P . Considering the number of degrees of freedom (d, z_{ob}, x_p, y_p, z_p), it seems unlikely that less than five coefficients will need to be tabulated for the SSF calculation.

As a first step, the contributions from the vertical and horizontal edges are separated. In this way, the two vertical edges are treated as an infinitely long, perfectly-conducting strip of width $2d$. The horizontal edge is subsequently treated as a perfectly conducting half-plane of height z_{ob} . Furthermore, it is assumed that $\beta = \pi/2$, such that the middle of the shadow region is at $y = 0$. In case $\beta \neq \pi/2$, it is assumed that the complete SSF curve for $\beta = \pi/2$ may be translated parallel to the y -axis along a distance $\Delta y = x_p / \tan \beta$ as visualised in Figure 3.6 and in [55].

A major problem in the numerical determination of the shielding properties of a finite-width screen is finding an expression which can be used to accurately approximate the y - and z -dependence of the site shielding factor. Because the field strength due to vertical and horizontal edges is calculated separately, two functions that approximate these dependencies are needed.

An expression that can be used to model the field strength behind the strip as function of the y -coordinate of P was found to be

$$E_y(y, es_y, ev_y, c) = es_y + (ev_y - es_y) \left(\frac{\exp(|y/d|^{cy}) - 1}{e - 1} \right), \quad (3.69)$$

where es_y is the field strength calculated at the centre of the shadow region behind the screen ($y = 0$), ev_y is the value of the field strength at the shadow boundary ($y = \pm d$) and cy is a coefficient. It can readily be deduced from equation (3.69) that for $y = 0$, E_y reduces to es_y , i.e. the field strength calculated at the middle of the shadow region. At the shadow boundaries, i.e. for $y = \pm d$, E_y has the value ev_y . The shape of the curve for $0 \leq |y_p| \leq d$ is determined by the exponential factor with argument $|y/d|^{cy}$. It is reminded that the SSF is only calculated in the shadow region behind the screen because in the lit region the SSF will go to zero.

The procedure to calculate the field strength behind the screen due to the vertical edges is as follows. Since the contribution from the horizontal edge is not yet taken into account,

the z_p coordinate of P is not of interest, because the strip is assumed to be infinitely long. For this reason the field strength as function of x_p , y_p and d needs to be calculated. The first parameter is the d/x_p ratio, where d is the half-width of the screen. For a given d/x_p ratio, the parameter es_y for use in the SSF_M prediction can be calculated using

$$es_{ym} = \frac{1}{2\pi\sqrt{s_y}\sin\gamma}, \quad (3.70)$$

where $\gamma = \frac{1}{2}\arctan(d/x_p)$ and $s_y = (x_p^2 + d^2)^{1/2}$. This expression is obtained if the two contributions from the edges $y = \pm d$ are calculated using the expressions for $|\vec{E}_Q^d|$. Furthermore, the factor corresponding to the diffraction field proportional to the reflected field has been neglected. The corresponding value of es_y necessary for the determination of SSF_A is given by

$$es_{ya} = \frac{1}{2\pi\sqrt{2s_y}\sin\gamma}. \quad (3.71)$$

Notice that equations (3.70) and (3.71) express the amplitude decay of a wave with a cylindrical wavefront through the factor $1/\sqrt{s_y}$.

The parameters ev_{ym} , ev_{ya} , and cy can be determined from Figures 3.27, 3.28 and 3.29, respectively. Notice that different values of ev_y should be used depending on the calculation of SSF_A or SSF_M , while identical coefficients cy can be used. The curves in Figures 3.27 to 3.29 correspond to different distances x_p by the parameter $\log x_p$. It can be seen from these figures that for large x_p , ev_{ym} and ev_{ya} approach the asymptotic value of 0.5 at the shadow boundary, corresponding to an equivalent SSF of 6 dB [45]. Coefficients es_y , ev_y and cy have been derived for d/x_p ratios of 0.1 to 3, while x_p ranges from $\log(x_p/\lambda) = 1$ to $\log(x_p/\lambda) = 3$ with steps of 0.1. If needed, the figures can be extrapolated to cover smaller and larger d/x_p ratios and larger distances x_p because all coefficients show some kind of asymptotic behaviour for small and large d/x_p , and for large x_p . At this point, the field strength caused by diffraction at the vertical edges of the strip can be calculated as function of y_p by means of equation (3.69) for $-d \leq y_p \leq d$.

The calculation from the contribution of the horizontal edge proceeds in a similar way. Obviously, this field strength is dependent on the z -coordinate of the observation point P . It was found that an expression closely resembling equation (3.69) can be used to calculate the field strength at P caused by diffraction at the horizontal edge

$$E_z(z, es_z, ev_z, c) = es_z + (ev_z - es_z) \left(\frac{\exp(|z/z_{ob}|^{cz}) - 1}{e - 1} \right), \quad (3.72)$$

where es_z is the field strength at $z = 0$, ev_z is the field strength at the shadow boundary $z = z_{ob}$, and cz is a coefficient. As can easily be seen, equation (3.72) has the same

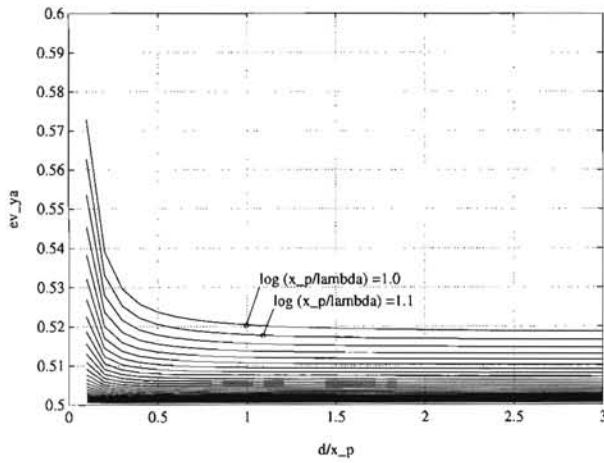


Figure 3.27: Field strength ev_{ya} at the shadow boundary $y = \pm d$ used in the calculation of SSF_{A_i} ; curves are given for $1 \leq \log(x_p/\lambda) \leq 3$, with a 0.1 step.

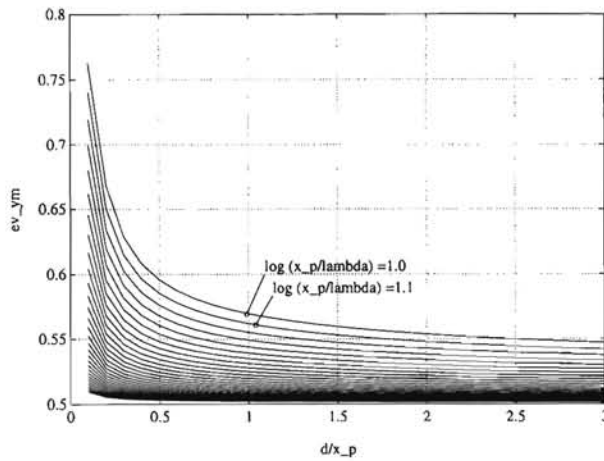


Figure 3.28: Field strength ev_{yb} at the shadow boundary $y = \pm d$ used in the calculation of SSF_{B_i} ; curves are given for $1 \leq \log(x_p/\lambda) \leq 3$, with a 0.1 step.

behaviour as equation (3.69), and it approximates the field strength behind the half-plane assumed.

For a given z_{ob}/x_p ratio the field strength es_z at $z = 0$ is calculated according to

$$es_z = \frac{1}{4\pi\sqrt{s_z}\sin\alpha}, \quad (3.73)$$

where $\alpha = \frac{1}{2} \arctan(z_{ob}/x_p)$ and $s_z = (x_p^2 + z_{ob}^2)^{1/2}$. It is seen that the expression for es_z has half the amplitude of the expression for es_{ym} given in equation (3.70). This is of course due to the fact that the strip geometry has two edges, while the half-plane has only one.

Furthermore it was found that the parameter ev_z is not dependent on z_{ob}/x_p , but only on x_p . The value of ev_z can be determined from Figure 3.30 as function of x_p . As can be seen from this figure the value of ev_z is always very close to 0.5, and for simplicity some intermediate value of ev_z can be used for all x_p , say $ev_z = 0.49$. The last parameter that is needed in the calculations is the coefficient cz . For a fixed z_{ob}/x_p ratio, the coefficient cz can be found as function of z_{ob} and x_p in Figure 3.31. These curves correspond to different distances x_p . The field strength due to the horizontal edge can be calculated with equation (3.72) for $0 \leq z_p \leq z_{ob}$. Coefficients es_y , ev_y and cz have been derived for z_{ob}/x_p ratios of 0.1 to 3, while x_p ranges from $\log(x_p/\lambda) = 1$ to $\log(x_p/\lambda) = 3$ with steps of 0.1.

The final step in this graphical method is the calculation of SSF_A and SSF_M based on the field quantities E_y and E_z . This calculation shows much similarity with equations (3.37) and (3.38); the expressions for $SSF_{A,M}$ are given by

$$SSF_A = -10 \log [E_y^2 + E_z^2] \quad [\text{dB}], \quad (3.74)$$

$$SSF_M = -20 \log [E_y + E_z] \quad [\text{dB}]. \quad (3.75)$$

Results of the use of the graphical method have been shown in Figures 3.25 and 3.26 as the dotted curves. As can be seen from these figures, the accuracy of the graphical method is reasonable, but not as good as can be achieved when using the pseudo-UTD method. Especially for small x_p (large d/x_p) the graphical method shows the tendency of overestimating the SSF results.

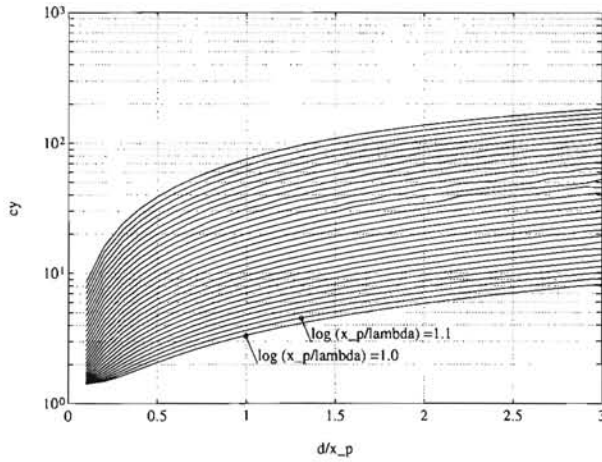


Figure 3.29: Coefficient cy of exponential in E_y used in the calculation of $SSF_{A,M}$; curves are given for $1 \leq \log(x_p/\lambda) \leq 3$, with a 0.1 step.

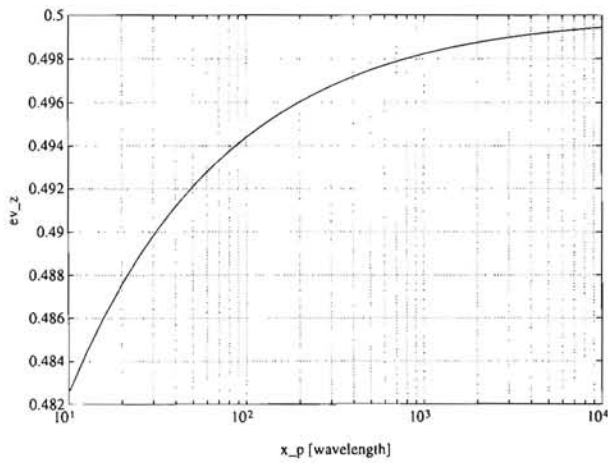


Figure 3.30: Field strength ev_z at the shadow boundary $z_p = z_{ob}$ used in the determination of E_z .

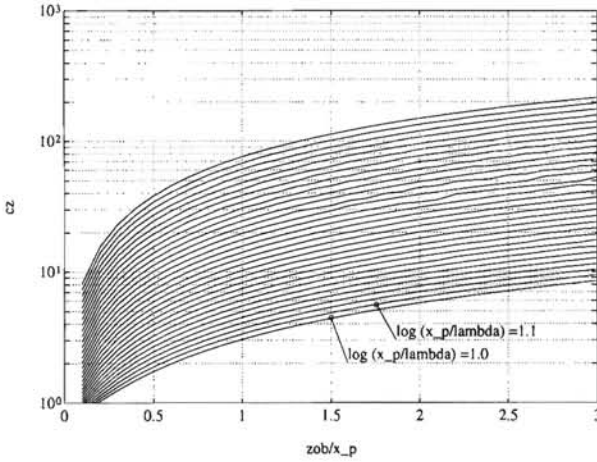


Figure 3.31: Coefficient cz of exponential in E_z used in the determination of $SSF_{A,M}$; curves are given for $1 \leq \log(x_p/\lambda) \leq 3$, with a 0.1 step.

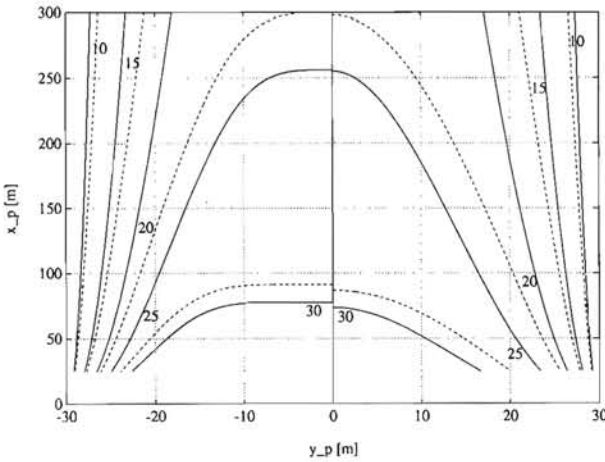


Figure 3.32: Iso-SSF lines behind the finite-width screen: SSF_A (————) and SSF_M (-----); results from graphical method are shown on the left, while pseudo-UTD results are shown on the right.

Data: $z_p = 1m$, $d = 43m$, $z_{ob} = 68m$, $\lambda = 0.3m$

3.4.7 Application of site shielding in a realistic situation

In most cases, high interference signal levels are caused by anomalous wave propagation conditions such as ducting and elevated-layer reflection. For this reason it will be assumed that the interference signal is due to a very distant source and therefore it can be considered as a plane wave. For simplicity $\beta = \pi/2$ is taken, but this is not a prerequisite for the analysis. The dimensions of the obstacle are chosen to be those of the Electrical Engineering building at Eindhoven University of Technology, namely, a total width of $86m$, hence $d = 43m$ and a height $z_{ob} = 68m$. At a frequency of 1 GHz this means $d/\lambda = 143$ and $z_{ob}/\lambda = 226$. In addition, it is assumed that the three-dimensional building may be treated as a two-dimensional one, which in fact leads to a worst-case approach. The graphical method as well as the pseudo-UTD approach will be used to determine SSF_A and SSF_M as function of the location of the observation point behind the building.

The minimum and average SSF were calculated as function of x_p and y_p for $z_p = 1m (= 3\lambda)$, where $10m (= 33\lambda) \leq x_p \leq 300m (= 1000\lambda)$ and $-30m (= -100\lambda) \leq y_p \leq 30m (= 100\lambda)$. The results are shown in Figure 3.32.

Since the plots for the minimum and average SSF are symmetrical with respect to the line $y = 0$, the results from the graphical method are shown on the left ($y_p < 0$), while the pseudo-UTD results are shown on the right ($y_p > 0$). The SSF_A corresponds to the solid line, while SSF_M is drawn as a dashed line. From this figure it can be deduced that also for very large x_p still a substantial SSF can be obtained, and that the graphical method can be used for SSF prediction behind a finite-width screen with reasonable accuracy.

3.4.8 An engineering model for shielding by a rectangular block

The types of obstacles considered thus far were two-dimensional in the sense that the thickness is zero. In this section an engineering model for the calculation of the shielding by a rectangular block will be proposed. It will be shown that this simplified approach gives a lower limit for the screening by an rectangular block. In the analysis a double finite-width screen model will be used, that is visualised in Figure 3.33. It is seen from the figure that the derived finite-width screen model essentially consists of the front- and back-side face of the rectangular block, as seen from the source position.

In the following we will calculate the SSF along an observation line parallel to the y -axis with $x > 0$. Since each finite-width screen will cause diffracted rays in the shadow regions behind and in between both screens, it is necessary to split the observation line behind the block into several parts.

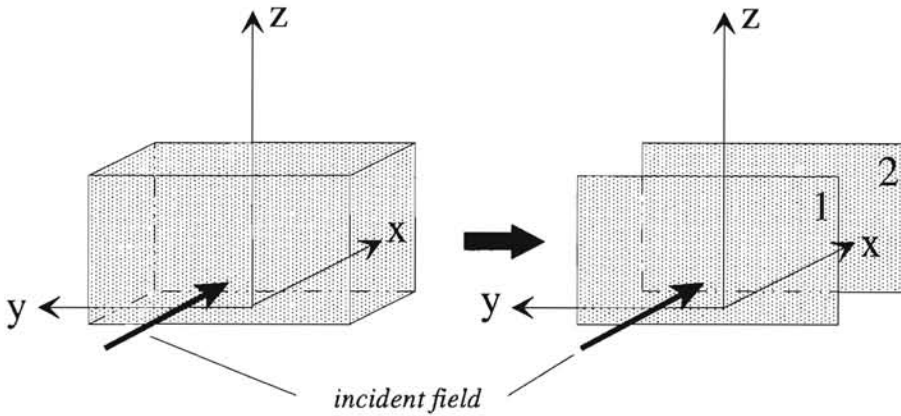


Figure 3.33: Rectangular block type geometry (left), and double finite-width screen model. The finite-width screens consist of the front- and back-faces of the rectangular block as seen from the direction of propagation of the incident wave.

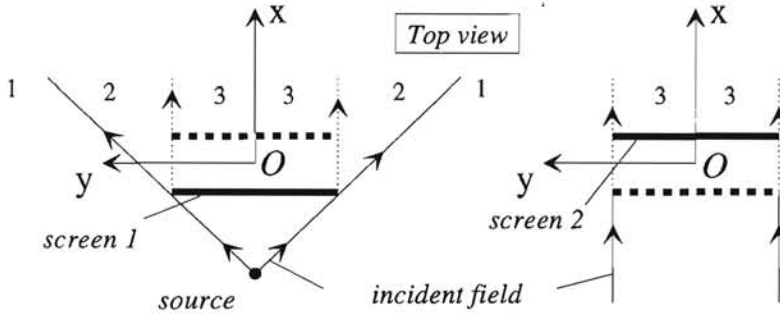


Figure 3.34: Determination of the SSF in regions 1 (lit zone), 2 (shadow zone of screen 1) and 3 (shadow zone of screen 2).

Three parts on this line can be distinguished as shown in Figure 3.34:

1. The lit region. In this region, the SSF is close to 0 dB;
2. The shadow region of the first (nearest) plate. The SSF in this region is determined by the diffraction taking place at the edges of the first screen;
3. The shadow region of the second plate. The SSF in this region is determined by the double-diffracted field.

In the following it is assumed that the polarisation of the incident wave is parallel to the xy -plane, but the other polarisation can be treated in exactly the same way.

The calculation of the SSF in regions 1 and 2 is fairly standard, and has been dealt with in Section 3.2.2. For a spherical incident wave, equations (3.37) and (3.38) can *not* be used for the calculation of the SSF. For a spherical incident wave the SSF is defined as in equation (3.1). The fact that the incident field has a spherical wavefront causes that the incident field without the obstacle is dependent on the position of the observation point P . This is not the case for an incident plane wave. The field in region 3 is calculated in a special way. The field incident upon the second screen is due to diffraction of the directly incident field at the edges of the first screen.

Since the diffracted field arising at the second screen is proportional to the incident field at the diffraction point at screen 2, the double-diffracted field can be found by assuming that the incident field at screen 2 is a plane wave having an amplitude equal to that of the diffracted field of screen 1, evaluated at screen 2. In fact the wavefront at screen 2 is cylindrical, but the assumption of plane wave illumination enables us to use the pseudo-UTD approach as discussed in the foregoing. In this way, the SSF in regions 1 and 2 is determined by screen 1, while the SSF in region 3 is determined by screen 2.

The result using the simplified approach is shown in Figure 3.12 as the solid curve. The result has been calculated using the minimum SSF for the contributions of screens 1 and 2 and may be compared with results calculated with the UTD model, also shown in Figure 3.12. It is seen from this figure that the agreement between both approaches is quite good. Obviously, the rapid variations of SSF in region 3 are absent due to the use of the minimum SSF. The result shown suggests that the results of the present engineering approach slightly overestimate the SSF for points behind the second screen, where the double diffraction contribution is most important. Furthermore, it was found that this engineering approach for the SSF calculation is much more efficient in terms of CPU time, obviously at the expense of accuracy.

In case the second screen is also directly illuminated by the source, the engineering model can be extended in a straightforward way to also include the diffracted field due to the directly incident field at screen 2. This will not be elaborated any further.

If the second screen is also illuminated by the source, an alternative for the three-dimensional engineering model would be the replacement of the rectangular block by a finite-width screen having a width equal to the diagonal cross-section of the three-dimensional obstacle. To illustrate this, the obstacle considered in Section 3.2.4 has been used; however, the source has been moved from $(-162.5m, 0, 12.5m)$ to $(-162.5m, -60m, 12.5m)$, such that also a side face is visible. The observation line still extends from

$-150\text{m} < y_p < 150\text{m}$, while $x_p = 250\text{m}$, $y_p = 1.5\text{m}$.

In Figure 3.35 a comparison between the results from the full-UTD method and the method where the obstacle is replaced by a finite-width screen, is shown. As can be seen from this figure, the result of the finite-width screen approach overestimates the SSF of the rectangular block slightly. The computational effort of the method incorporating the finite-width screen analysis is, however, only a fraction ($\approx 10\%$) of the one for the calculations with the rectangular block.

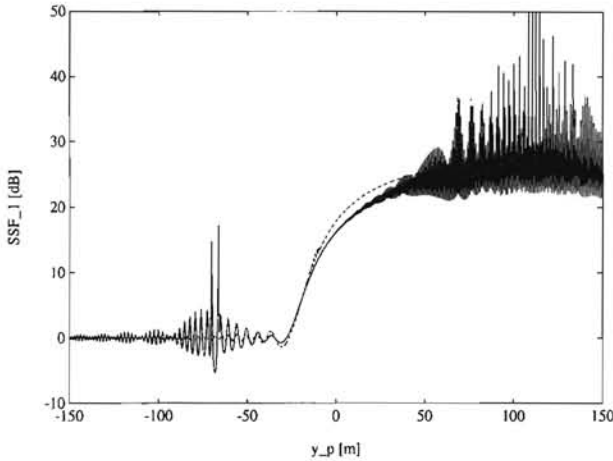


Figure 3.35: SSF behind the rectangular block as function of y_p : total field calculated using full-UTD method (—) and the result of the simplified approach (---) where the three-dimensional obstacle is replaced by a finite-width screen corresponding to its diagonal cross-section.

Data: $x_p = 250\text{m}$, $z_p = 1.5\text{m}$, $d \times h \times z_{ob} = 20\text{m} \times 86\text{m} \times 68\text{m}$, $\lambda = 0.3\text{m}$

3.4.9 Conclusions

In Section 3.4, simplified methods for the calculation of the SSF behind a finite-width screen were discussed. Emphasis is placed on a systematic simplification of the UTD models that have been described in Section 3.2.

For the calculation of the SSF behind a finite-width screen two simplified models were discussed. The first model is a pseudo-UTD model because the well-known transition function of UTD has partly been eliminated, while the field near shadow boundaries remains bounded. The graphical model for approximating the SSF of a finite-width screen is based

4.2 Large-bandwidth diffraction measurements at 54 GHz using both time-domain filtering and frequency smoothing

This section¹ describes the high-frequency measurements of the fields diffracted at the edges of an obstacle. The measurements are performed in an ordinary room by using the time-domain filtering and frequency-smoothing options of a vector network analyser.

The field distribution on a circular arc is measured without the obstacle, and with the obstacle present. The measurement approach in both cases is rather different. Without the obstacle, a modified calibration method should be used together with frequency smoothing, while in the presence of the obstacle, the same calibration set needs to be used in conjunction with time-domain filtering. In the latter case, however, the use of frequency smoothing is not allowed.

The results of the two measurements sessions can be condensed into one parametric curve expressing the additional attenuation of the radio signal, which is caused by the presence of the object on the propagation path. Practical and theoretical curves are compared for several object dimensions, and very good agreement is obtained in all cases.

4.2.1 Introduction

The topic of field-strength prediction in an urban or mobile environment has received much attention in recent years. Statistical models [60, 61, 62] and deterministic models [63, 64, 45] have been developed to predict characteristic multipath phenomena such as fading and time delay of the received signal. Obviously, these multipath phenomena degrade system performance and limit the channel capacity. For this reason, telecommunications operators can benefit from prediction models in that they can design future communication links with appropriate margins in field-strength level at the users' premises, either fixed or mobile.

The UTD field-strength prediction derived from the model developed in Section 3.2 uses the concept of site shielding. Actually, site shielding is an interference reduction technique [3] that tries to raise the signal-to-interference ratio by introducing an additional attenuation for the interfering wave, and keeping the desired (wanted) signal unaffected.

¹ Note: the major part of this section was already published: G.A.J. van Dooren, M.G.J.J. Klaassen and M.H.A.J. Herben: *Large-bandwidth diffraction measurements at 54 GHz using both time-domain filtering and frequency smoothing*, Proceedings of the 14th annual meeting and symposium A.M.T.A., Columbus, Ohio, U.S.A., pp. (13-9)-(13-14), Antenna Measurement Techniques Association, 1992.

A parameter which expresses the effectiveness of the shielding is the site shielding factor (SSF), which has been defined in Section 3.1. As can be readily deduced, it expresses the level of the received field *relative to the free-space level*.

In a practical situation, the field distribution without the obstacle is easily calculated using the radio equation, while the received field with obstacles present needs to be calculated using a more sophisticated method [45, 55]. Such a method should satisfy the requirements that the interactions of the wave and obstacles are accurately modelled, that the method is reasonably fast and that it has a vectorial character. A method satisfying all of these requirements is geometrical optics (GO), supplemented with the Geometrical Theory of Diffraction (GTD), or its uniform extension (UTD). An additional advantage of the methods mentioned is that they are ray-based methods, which provide a clear insight into the wave-propagation, reflection, and diffraction mechanisms. Furthermore, GO and GTD/UTD facilitate the calculations of channel characteristics such as the Doppler-shift and the power-delay profile. Together with the modelling of the urban environment by a standardised type of obstacle such as the block-shaped obstacle introduced in Section 3.2.4, the use of GTD/UTD is a powerful approach for both field-strength prediction and SSF calculation.

Obviously, the theoretical approaches mentioned need some practical verification in the form of measurements. These types of measurements can be performed either indoors or outdoors. The latter type of measurements closely approximates the situation encountered in practice, when installing a new telecommunications link. A major drawback of this type of measurement, however, is that the measurement setup is very vulnerable to (man-made) interference. Also external influences such as the weather can disturb the measurement results, and can largely extend the time needed to complete the measurements. For these reasons, one often carries out the measurements indoors, where they can be performed in a more controlled way.

For indoor measurements, the obstacles used for the modelling of the urban environment cannot have the dimensions of the original obstacles, so scaling of the obstacles is necessary to build a compact measurement setup, and hence high frequencies are to be used. A drawback of laboratory measurements is that reflections can disturb the results, and the high-frequency measurements are more complex than the low-frequency measurements performed outdoors. A simple, but expensive, solution to the reflection problem is to build an anechoic chamber. Another solution to suppress reflections is the use of data processing techniques such as time gating and frequency smoothing, which are present on most modern VNAs such as the Hewlett-Packard 8510C.

In this section, the measurement setup for the verification of the model for field-strength

prediction in mobile communications and site shielding is described. Also the measurements performed without and with the obstacle present, necessary to derive the SSF, will be discussed. Actually, both measurements are field-strength measurements, but it will be shown that they are quite different from a measurement-technique point of view. Subsequently, the SSF for some obstacles with a selected geometry will be derived from the measurement results, and it is compared with results obtained from a theoretical model based on GTD/UTD. Main objectives of the measurements are the verification of the theoretical prediction model mentioned, and a general verification of the high-frequency methods GO and UTD.

4.2.2 The measurement setup

As already mentioned, a major drawback of indoor measurements are the inherent reflections from walls, ceiling, floor and objects placed within the room. These reflections can roughly be classified into two groups: near and distant reflections. The distant reflections present in an anechoic chamber are suppressed by absorbing panels which are mounted against the walls, on the ceiling and the floor. In an 'echoic' chamber, the distant reflections can be suppressed using data-processing techniques such as time gating, provided the room is large enough, so that distant reflections can be distinguished in the time domain from the wanted and obstacle-diffracted field contributions. Therefore, the near reflections need to be dealt with in a separate way, depending on the actual geometry.

The measurements were performed in a standard room with dimensions $6m \times 6m \times 3m$. The choice of carrying out the measurements in this 'echoic' room has several implications for the measurements. First of all, the measurements should be performed in the swept-frequency mode of the VNA, covering a frequency span large enough to obtain the desired time-domain resolution. Actually, this gives a lower limit for the bandwidth needed. Also, a balanced frequency-point-to-frequency-span ratio is needed to eliminate aliasing in the time interval of interest. Furthermore, an upper limit for the bandwidth used is set by the frequency-dependent radiation properties of the transmitting (T) and receiving (R) antennas. In the verification measurements it is desirable that a sufficiently large portion of the obstacle is illuminated by the T-probe. Therefore the physical dimensions of the R-probe must be as small as possible, in order to be able to measure the rapid spatial field strength fluctuations behind the screen. This implies that the T- and R-probes should not have a too directive pattern.

It was found that a rectangular waveguide carrying the TE_{10} mode is very well suited to be used as transmitter and receiver probe. The directivity is reasonable, while also

the radiation properties of the WR19 waveguide are quite good in the frequency range of interest (40-60 GHz). A bandwidth of 8 GHz was found to be sufficient to perform the measurements, and within this bandwidth nearly no dispersion is present. The used bandwidth results in a time-domain pulse width of $0.24ns$, and this value will also be used in the theoretical simulations.

To guarantee the desired level of accuracy, the VNA is also used in stepped-frequency mode. This results in a measurement time of nearly 17 hours for 501 observation points. The measurement setup without and with the obstacle is shown Figures 4.1 and 4.2. In these figures, the rotating table and the VNA are shown. An arm is mounted on the table such that the obstacle, a finite-width screen with knife-edges, can be rotated. The photographs were made from a location close to the R-probe. Rotating the table results in a circular scan of the received field at the R location. The step size during this rotation is 0.1° , and usually scans are recorded from an angle of -25° to 25° , resulting in a maximum of 501 observation points per scan. Each point in this scan takes approximately 2 minutes of measurement time. In this period, the measurement data are acquired, processed and transferred to the control computer. The computer also repositions the table and initialises the VNA for the following measurement. The T- and R-probes are approximately $100cm$ apart, and the distance from T to the obstacle is $50cm$. The finite-width screen used for the verification measurements is made from aluminum with a thickness of $0.7mm$, which is small compared to the wavelength. Therefore, the rims of the obstacle can be regarded as knife-edges.

The dynamic range of the measurement setup, which is mainly limited by the signal-to-noise ratio at the input of the VNA, and its sensitivity, is approximately 45 dB. Note that some of the near reflections are suppressed by use of absorbers, however, not all reflections can be suppressed down to a sufficiently low level. Especially the wave reflected from the absorber on which the screen is mounted will be difficult to suppress.

A block diagram of the measurement setup is shown in Figure 4.3, where also the network analyser and control computer are shown. A schematic representation of the measurement setup is depicted in Figure 4.4. In the theoretical model it is assumed that the observation point moves along a circular arc of radius r parallel to the xy -plane, with the z -axis as the axis of rotation. The position of the R-probe is therefore completely determined by r and the azimuth angle φ .

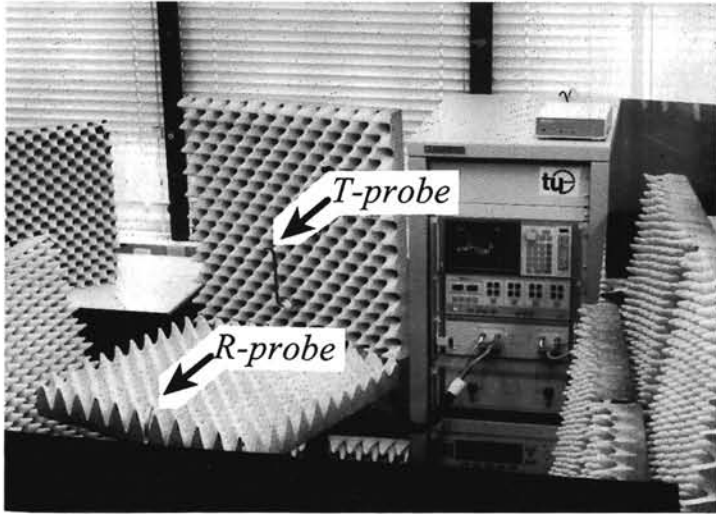


Figure 4.1: Measurement setup without obstacle.

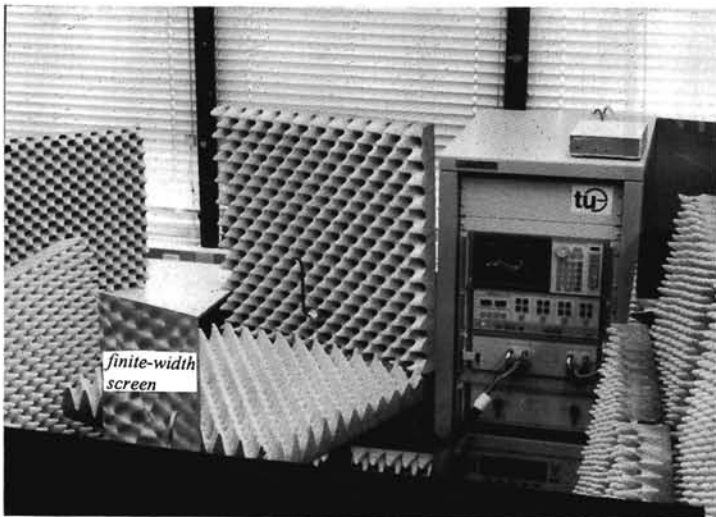


Figure 4.2: Measurement setup with obstacle.

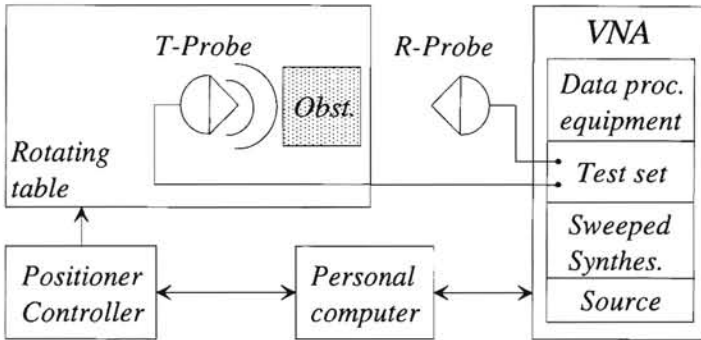


Figure 4.3: Block diagram of the measurement setup.

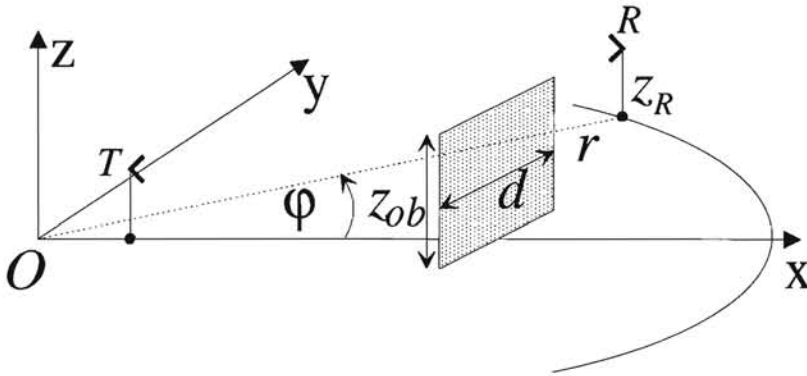


Figure 4.4: Schematic geometry for field strength measurements.

4.2.3 Calibration method and measurements

A major problem in the calibration measurement of the VNA is the presence of the wave reflected by the absorber material. The constructive and the destructive interference between the direct and the reflected wave results in a characteristic fading behaviour of the received signal as a function of frequency. A seemingly straightforward but incorrect way to eliminate this multipath propagation is to calibrate the VNA such that the presence of the reflected wave is accounted for by the analyser software. This method introduces two errors. First, an accurate compensation of the reflected wave is difficult to obtain, and after calibration a large residual error of approximately ± 0.25 dB remains in the (calibrated) frequency-domain signal. Second, a non-removable error is introduced in the measurement

with the obstacle present, if the same calibration set is used. In this case, the wave reflected by the absorber is obstructed, but its compensation in the calibration set is still present! The calibration sets for both the measurements without and with the obstacle should be identical, however. This implies that the correct solution for eliminating the absorber reflected wave is that the calibration set should be related to the direct wave only. This is accomplished by using a *gated calibration*, such that all reflections are suppressed. Using this approach, the residual error after calibration is much smaller (± 0.1 dB).

The calibration results obtained using the erroneous and the correct approach can be found in Figures 4.5 and 4.6, respectively. The measurement procedure is now as follows. The first measurement, performed without the obstacle, is an orientation measurement to figure out which time-domain signal is the pulse of interest. Subsequently, a gated calibration is performed, and the resulting calibration set is solely based upon the direct wave. The gate settings for both the measurements with and without the obstacle are determined from the calibration measurement without obstacle, and the UTD-simulations with obstacle.

The direct and reflected waves are shown in Figure 4.7, where also the (theoretically) expected diffracted wave is indicated. The gate settings should be such that the earliest arriving wave in the time domain, i.e. the direct wave, as well as the latest arriving wave, i.e. the diffracted wave with largest propagation path from T to R-probe as function of table position, fall inside the selected time gate. The settings used in the measurements are a gate start of $-0.5ns$ and a gate stop of $1.5ns$. The gate width used can be chosen somewhat smaller, but this does not affect the measurement results.

A practical implication is that, for deriving the SSF, two measurements need to be carried out. The first measurement in the SSF verification concerns the determination of the free-space level as a function of table position. Actually, this amounts more or less to the determination of the radiation pattern of the T-probe. The second measurement is for the determination of the field-strength distribution behind the screen.

Using the previously determined calibration set, we find that the characteristic two-ray frequency response is now explicitly present in the measurement without the obstacle, as shown in Figure 4.8. Although theoretically possible, time gating to suppress the reflected wave from the absorber was not used, because the gate settings should remain fixed in both measurements. To remove the interference pattern, frequency smoothing can be used, provided the smoothing factor is equal to n times ($n = 1, 2, 3, \dots$) the period of the interference pattern. The result of this smoothing operation can be found in Figure 4.8, where a smoothing factor of 17% has been used. In this figure, also the non-smoothed signal is shown. The resulting T-probe pattern with and without smoothing can be found

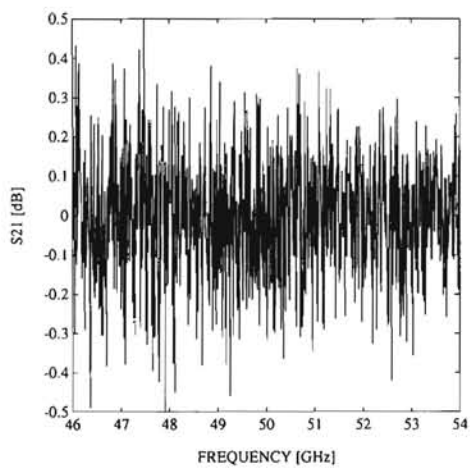


Figure 4.5: Residual error using erroneous approach.

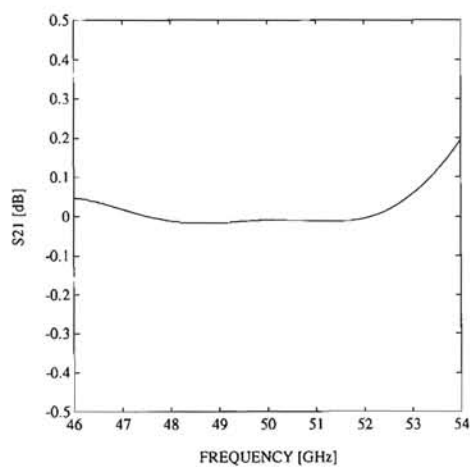


Figure 4.6: Residual error using correct approach.

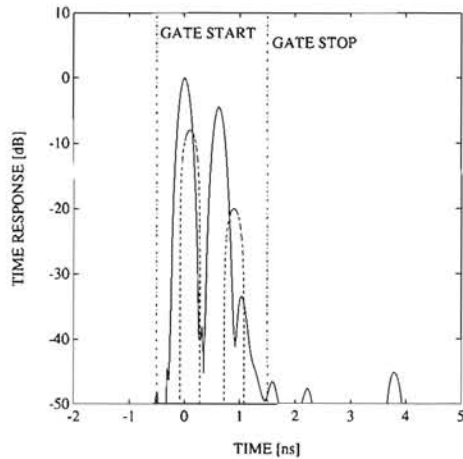


Figure 4.7: Determination of gate settings: the measured direct and reflected waves (—), and the theoretically expected diffracted wave (-----).

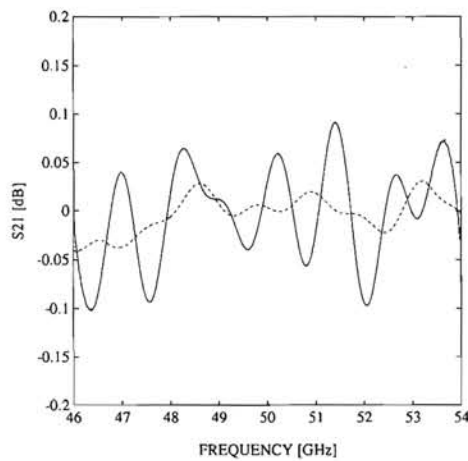


Figure 4.8: Smoothed (-----) and non-smoothed (—) frequency-domain signal from the measurement without obstacle.

in Figure 4.9, as a function of the azimuth angle. The measurements in the presence of the obstacle are performed next. In this case no frequency smoothing is employed, because the destructive and constructive interference as a function of frequency and position are of primary interest. In Figure 4.10 the field distribution along the circular arc using the correct approach is shown. The finite-width screen used has a width $d = 30\text{cm}$ and a height of $z_{ob} = 35\text{cm}$.

4.2.4 SSF determination

Using the results from both measurements described in the previous subsection, the SSF along the circular arc can be derived. In Figure 4.11, the SSF obtained from Figures 4.9 and 4.10 is shown, together with a theoretical result for the same geometry. The theoretical result is based on the UTD analysis, including corner-diffracted waves (Sec. 3.2.2). In both measurements with the obstacles present, the R-probe was positioned 4cm below the horizontal edge of the obstacle.

It can be seen from Figure 4.11 that excellent agreement exists between the measured and the theoretical results. Some discrepancies occur at the locations where sharp peaks exist in the theoretical curve. Of course, the VNA has a finite dynamic range, and precisely at the locations of the sharp peaks the signal-to-noise ratio at the receiver input reaches a minimum value. This problem can be solved by using an amplifier at the T side, such that a higher signal-to-noise ratio results at the R side, and a larger dynamic range is obtained. In Figure 4.12, an additional comparison is given for a wider screen. In this case, the screen width is $d = 35\text{cm}$, and its height z_{ob} is also 35cm . Again, excellent agreement between theory and measurements is found.

From the complete series of measurements it was found that the main sources of error are the positioning errors in the measurement setup, and the presence of a residual error after gated calibration. It was found that the geometry could be determined with an accuracy of $\pm 1\text{mm}$, while the rotating table introduced an error in azimuth of $\pm 0.05^\circ$. Using the simulations, it was observed that rather large discrepancies between theoretical and measured curves also appear in case the dimensions of the obstacle are subject to error. In general, an error in the width of the screen results in an amplification of this error at the location of the R-probe. A wider or narrower shadow region behind the screen is found, and the error in the width is multiplied by a proportionality constant > 1 . This is especially manifest around the shadow boundaries, where the SSF curve has a steep slope.

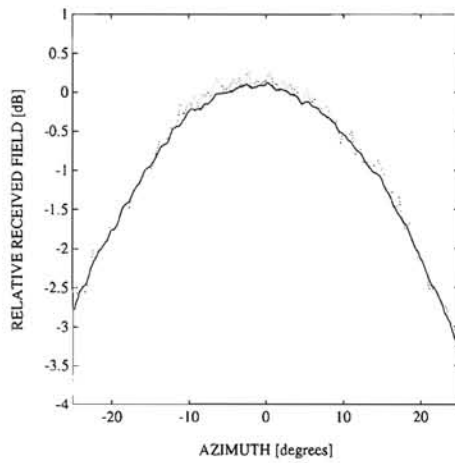


Figure 4.9: T-probe pattern with smoothing (—), and without smoothing (.....).

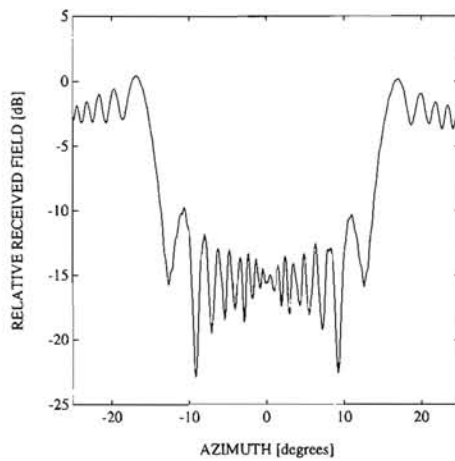


Figure 4.10: Field distribution obtained following the correct approach.

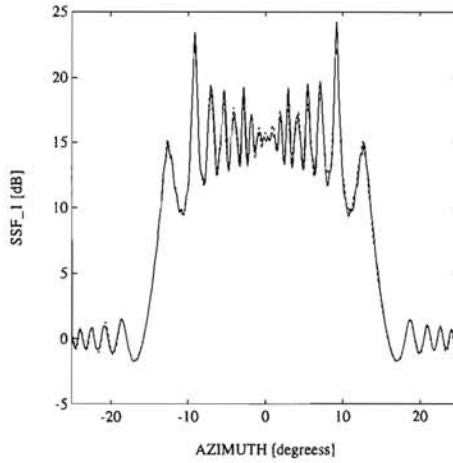


Figure 4.11: SSF of a finite-width screen: measured (————) and calculated (-----).

Data: $d = 30$ cm, $z_{ob} = 35$ cm, $z_R = 31$ cm, $\lambda = 6$ mm

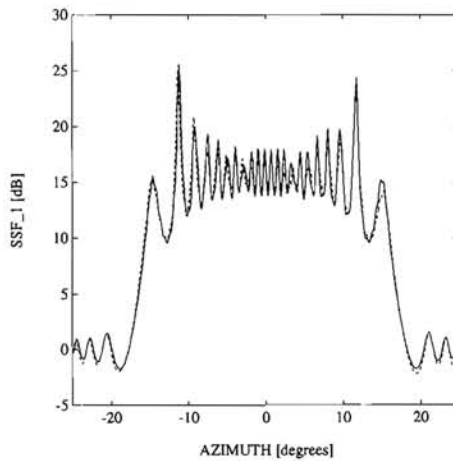


Figure 4.12: SSF of a finite-width screen: measured (————) and calculated (-----).

Data: $d = 35$ cm, $z_{ob} = 35$ cm, $z_R = 31$ cm, $\lambda = 6$ mm

4.2.5 Conclusions

The UTD model for the calculation of the SSF proves to be very accurate. The measured and theoretical results compare extremely well, and major discrepancies can be explained by the finite dynamic range of the measurement equipment, and the introduction of errors in the determination of the dimensions and relative position of the obstacle. Furthermore, it was argued that, in case of a calibration compensating for strong reflected fields, problems may arise when in a subsequent measurement these compensated reflected fields for some reason are absent. The calibration set used incorporates these reflected fields, and they will automatically be present in the measured results. It was shown that the error introduced in the measurements can be reduced by using another calibration procedure. In this procedure, the characteristic two-ray frequency response is eliminated using frequency smoothing, while the calibration set used in both measurements is based on the direct (LOS) wave only.

4.3 Measurement of diffracted fields behind a thin finite-width screen

The previous section considered the calibration procedure necessary to perform the EM diffraction measurements in an ordinary room, and details concerning the measurement setup were given. In this section² a comparison between the measured and the theoretically predicted SSF of some finite-width screens is made. The SSF is measured along a circular arc behind the screen at a frequency of 50 GHz. The measured SSF curves compare very well with those predicted by a theoretical model which uses UTD and includes corner diffraction. Good agreement is also found between the measured and the theoretically derived time-domain results. The latter clearly demonstrate the ray behaviour of the diffracted fields, in accordance with UTD.

4.3.1 Introduction

Site shielding is an interference reduction technique that tries to introduce an additional propagation loss for an interfering radio signal, while the desired radio signal remains (nearly) unaffected. The propagation loss may be caused by a natural or a man-made

² *Note:* the major part of this section was already published: G.A.J. van Dooren, M.G.J.J. Klaassen and M.H.A.J. Herben: *Measurement of diffracted electromagnetic fields behind a thin finite-width screen*, *Elec. Letters*, vol. 28, no. 19, pp. 1845-1847, 1992.

obstacle located on the propagation path, and the effectivity of the shielding is expressed by the site shielding factor (SSF) that was defined in Section 3.1.

In this section theoretically derived results for the SSF of a finite-width screen are compared with results from a measurement setup incorporating an HP8510C vector network analyser (VNA) operating at 50 GHz. The SSF at various positions behind the screen is theoretically predicted and measured, and these results are compared with each other. Also a comparison is made between the predicted time-domain response of the multipath radio channel and the measured response using the time-domain option of the VNA.

4.3.2 Theoretical model and geometry

The geometry used in the theoretical model and the measurements is shown in Figure 4.13. A Cartesian (x,y,z) coordinate system is used to describe the positions of the T(ransmit) and R(eceive) probes and the screen. The T-probe is located at the position $(x_T, 0, z_T)$ and

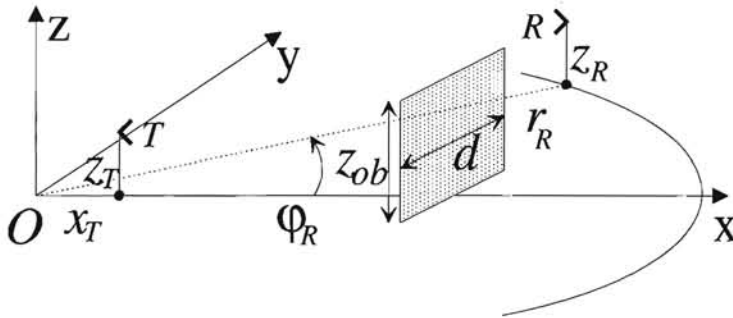


Figure 4.13: Geometry as used in the theoretical model and the measurement setup.

emits a spherical wave. The source used is a vertically polarised rectangular waveguide, with its symmetry axis pointing into the x -direction. Waveguide WR19 has been used for the T- and R-probes because of bandwidth considerations. The observation point R is located on a circular arc parallel to the xy -plane with radius r_R , and the z -axis is the axis of rotation. Its height above the xy -plane is z_R . The azimuthal angle φ_R is allowed to vary between -25° and 25° . The height of the horizontal edge above the xy -plane is z_{ob} , while the width of the screen is d . The diffraction model used in the simulations was discussed in Section 3.2 and uses a total of six field contributions. The types of field contributions included are: the direct field propagating from T to R, three edge-diffracted field contributions generated at the edges of the screen, and two corner-diffracted fields originating at the corners of the screen. The effect of the ground plane is neglected.

4.3.3 Measurement setup

Accurate, coherent measurements are needed to verify the details of the diffraction models. Since such measurements can hardly be carried out in the field with objects having realistic dimensions, e.g. houses and buildings, scaled obstacles have been used in the laboratory measurements.

The measurement setup has been built according to the geometry depicted in Figure 4.13. Using the VNA, the determination of the SSF along the circular arc amounts to performing two transmission measurements between T and R. The first measurement is performed with the screen absent. This approximately yields the radiation pattern of the T-probe, because the symmetry axis of the R-probe is always directed towards the z -axis. In the second measurement the screen is present. Now the field distribution along the circular arc is due to multipath propagation of the wave transmitted at T. Each diffracted field arriving at the R-probe is spatially weighted by the probe's receiving pattern. The SSF as a function of azimuth angle φ_R is found by relating the results of the first and second measurements, according to the definition of the SSF. Data processing techniques such as time-domain filtering and frequency smoothing have been applied in a fundamental way, together with a novel calibration scheme of the VNA. This calibration scheme was described in Section 4.2.

In the results to be presented the T-probe is located at $x_T = 18.2\text{cm}$, $y_T = 0$, $z_T = 31.6\text{cm}$ and r_R is 113.6cm . The screen has dimensions $d = 30\text{cm}$ and $z_{ob} = 50\text{cm}$; hence the screen is described by $x = 68.6\text{cm}$, $-15\text{cm} \leq y \leq 15\text{cm}$, $0 \leq z \leq 50\text{cm}$. The frequency used is 50 GHz. The screen used is thin ($< \lambda/8$), so that the edges can be treated as knife-edges. The measurement corresponds to the reduction of a signal from a terrestrial radio station which interferes with a satellite signal at a VSAT.

4.3.4 Comparison of measured and theoretical results

In Figure 4.14 two sets of SSF curves can be found, both showing measured and theoretical results. An important parameter in the measurements is the height difference $\Delta z = z_{ob} - z_R$. For the upper curves $\Delta z = 7\text{cm}$, while for the lower curves $\Delta z = 2\text{cm}$. Comparison of the theoretical and measured curves shows that excellent agreement exists in both cases, despite a small pointing error for the experiment with $\Delta z = 7\text{cm}$. Experiments with other values of the screen width d and screen height z_{ob} resulted in similar curves as shown in Figure 4.14. In Table 4.1, the average SSF, SSF_{ave} , around $\varphi_R = 0^\circ$ and the ripple ΔSSF are summarised for various values of d and Δz . It has been found that for small Δz ($\Delta z < 15 \lambda$) the contribution from the horizontal edge determines the average level of

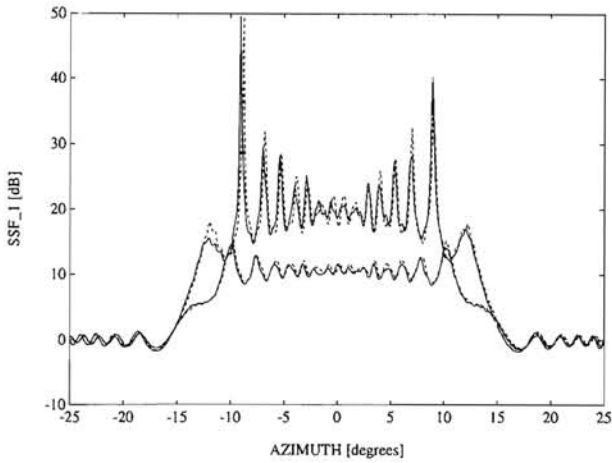


Figure 4.14: SSF of a finite-width screen: measured (—) and calculated (---) for $\Delta z = 2\text{cm}$ (lower curves) and $\Delta z = 7\text{cm}$ (upper curves).
Data: $d = 30\text{cm}$, $z_{ob} = 50\text{cm}$, $\lambda = 6\text{mm}$

Table 4.1: SSF_{ave} and ripple ΔSSF in the centre of the shadow region behind the screen ($\varphi_R = 0^\circ$).

Δz [cm]	d [cm]	SSF_{ave} [dB]	ΔSSF [dB]
2	30	10.7	± 1.0
4	25,30,35	15.7	$\pm 4.0, \pm 1.3, \pm 3.7$
7	30	19.7	± 1.5

the SSF , while the contributions from the vertical edges cause a superimposed fluctuation. Furthermore, the corner-diffraction contributions are explicitly needed to obtain a good fit of the total field across the shadow boundary at $\varphi_R = \pm 14^\circ$ [43]. Increasing the screen width d merely results in a global widening of the pattern, thereby leaving SSF_{ave} in the centre of the shadow region, $\varphi_R = 0^\circ$, nearly unaffected.

Also the arrival of the individual field contributions at R has been measured using the time-domain option of the VNA for $\varphi_R = 3^\circ$. By use of a sweep bandwidth of 18 GHz, sufficient time-domain resolution is available to distinguish the individual wave contributions. Attention is paid to the differences in individual path lengths of the field contributions, and to their amplitudes determined by the diffraction process at the edges. In this way the measured and theoretically expected time responses of the radio channel from T to

R can be compared. The results are shown in Figure 4.15, in which the horizontal line indicates the lower limit of the dynamic range of the VNA. Responses below this level are

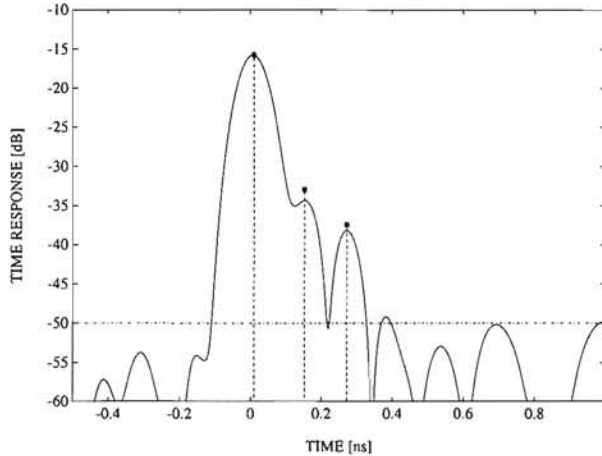


Figure 4.15: Measured (—) and calculated (---●) time response. The line-dotted horizontal line indicates the lower level of the dynamic range.

Data: $d = 30\text{cm}$, $z_{ob} = 50\text{cm}$, $\varphi_R = 3^\circ$, $\lambda = 6\text{mm}$

attributed to time-domain filtering and data processing. From Figure 4.15 it is seen that again good agreement is found in the position of the pulses as well as in their individual amplitudes. Only three pulses are measured because the direct ray from T to R is blocked. In the time domain the two corner-diffraction contributions cannot be distinguished from their associated edge-diffraction contributions.

4.3.5 Conclusions

The measured and theoretical results for the SSF of a thin finite-width screen were compared. It was found that for small values of Δz the SSF is mainly determined by the field contribution from the horizontal edge, which has the smallest diffraction angle. The fluctuations superimposed on the constant level due to diffraction at the horizontal edge are caused by constructive and destructive interference of the field contributions from vertical edges and corners. The theoretical model shows that corner-diffraction terms are explicitly needed to obtain a total field that is continuous across the shadow boundary. The use of UTD for edge diffraction and the inclusion of corner diffraction yields theoretical results which agree very well with the measured results. Also the time-domain response

of the radio channel has been calculated and measured using a Fourier transformation of the measured frequency-domain data. Also in this application, the UTD diffraction model correctly predicts the inter-arrival times and amplitudes of the individual pulses. Furthermore, the measured pulses clearly demonstrate the ray behaviour of the diffracted fields, in accordance with UTD.

So, from the presented results it can be concluded that the prediction model, which includes edge and corner diffraction, is a good description of the diffraction processes at the edges and corners of the finite-width screen. The model can therefore be used for accurate field-strength prediction to enable an optimal placement of VSATs in urban areas, and for the prediction of the coverage of land-mobile satellite systems thereby taking into account screening effects.

4.4 Polarisation-dependent site shielding factor of a rectangular block

The obstacle considered in the previous section is essentially two-dimensional, and it was found from additional measurements with a horizontal polarisation that the received field does not exhibit a considerable polarisation dependence [43]. In this section³ a comparison is made between the measured and theoretically predicted site shielding factor (SSF) of an obstacle resembling a building. The SSF is measured along a circular arc behind the obstacle at a frequency of 50 GHz. The theoretical model for the analysis uses UTD including corner, double, and edge-corner diffraction. The agreement between the measured and theoretically derived results is excellent. The strong polarisation dependence of the SSF appears to be due to slope diffraction.

4.4.1 Introduction

The tactical placement of obstacles to obstruct interfering radio waves is one method to reduce interference in radio communication systems [3]. The shielding effectiveness is called the site shielding factor and was defined in equation (3.2). A rearrangement of equa-

³ *Note:* the major part of this section was already published: G.A.J. van Dooren and M.H.A.J. Herben: *Polarisation-dependent site shielding factor of a block-shaped obstacle*, Elec. Letters, vol. 29, no. 1, pp. 15-16, 1993.

tion (3.2) yields equation (3.4), repeated here for convenience

$$SSF = 20 \log \left[\frac{D_+}{D_-} \right] + 20 \log \left[\frac{I_-}{I_+} \right] \quad [\text{dB}], \quad (4.1)$$

where D and I are the levels of the desired (wanted) and the interference (unwanted) signal, respectively. The subscripts refer to the cases that the obstacle is present (+) or absent (-).

If the placement of the obstacle has no effect on the desired signal level, then the first term in the right-hand side of equation (4.1) vanishes and this equation reduces to the conventional definition of the SSF as introduced in equation (3.1).

In this section the theoretically derived results for the shielding of an obstacle resembling a building are compared with results from a measurement setup incorporating an HP8510C vector network analyser (VNA) operating at 50 GHz. In the Section 4.3 results have been presented for the SSF of a finite-width screen, which appear to be almost independent of polarisation [43]. In this section it will be demonstrated that a rectangular block gives rise to a polarisation-dependent SSF. The measured SSF curves agree very well with those predicted by the UTD model for both orthogonal polarisations considered.

4.4.2 Theoretical model, geometry and measurement setup

The geometry used in the theoretical model and in the measurement is shown in Figure 4.16. The positions of the T(ransmit) and R(eceive) probes are given in a Cartesian

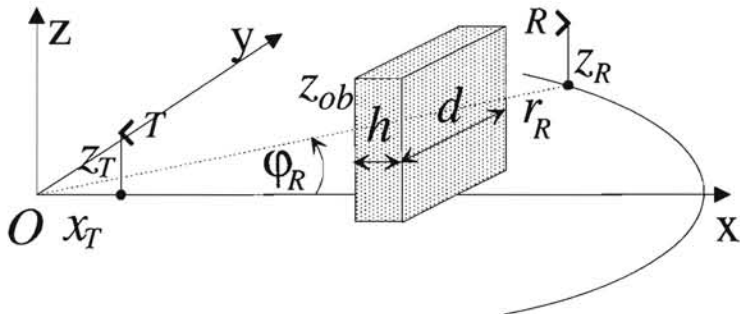


Figure 4.16: Geometry as used in the theoretical model and the measurement setup.

(x, y, z) coordinate system. The polarisation of the T-probe with position $(x_T, 0, z_T)$ is either horizontal (y) or vertical (z). Its symmetry axis points into the x -direction. The R-probe moves along a circular arc parallel to the xy -plane with radius r_R , and the z -axis

is the axis of rotation. The height of the R-probe above the xy -plane is z_R . The obstacle is a rectangular block with edges parallel to the axes of the Cartesian coordinate system. Its height is z_{ob} , its width is d , and its thickness is h . Furthermore, the rectangular block is assumed to be perfectly conducting. The SSF is measured and calculated as a function of the azimuth angle φ_R with $|\varphi_R| \leq 25^\circ$.

In the theoretical analyses (Sec. 3.2.4), the following types of field contributions are considered: the direct field propagating from T to R, edge-diffracted fields, corner-diffracted fields, and field contributions due to edge-edge and edge-corner interactions. The effect of the ground plane (xy -plane) is neglected.

The reader is referred to Section 4.2 for a detailed discussion of the measurement procedure for SSF-measurements in an 'echoic' room, and for a description of the novel VNA calibration method used.

4.4.3 Comparison of measured and theoretical results

In the results to be presented, the rectangular block has dimensions $h = 8.7\text{cm}$, $d = 30.0\text{cm}$, and $z_{ob} = 50.0\text{cm}$. Therefore the rectangular block is described by $68.8\text{cm} \leq x \leq 77.5\text{cm}$, $-15\text{cm} \leq y \leq 15\text{cm}$, and $0 \leq z \leq 50\text{cm}$. The T-probe is located at $x_T = 25.2\text{cm}$, $y_T = 0$, $z_T = 46.0\text{cm}$, while $r_R = 114.8\text{cm}$ and $z_R = 40.0\text{cm}$. The T- and R-probes are rectangular WR-19 waveguides operating at a (centre) frequency of 50 GHz. Figure 4.17 shows the theoretical and measured results for the SSF in the two cases of horizontal (H) and vertical (V) polarisation. The H-curves are raised by 15 dB so that they are separated from the V-curves. The figure shows excellent agreement between the measured and theoretical SSF curves.

The theoretical model also includes slope diffraction to account for the double-diffracted field contribution in case the polarisation is parallel to the obstacle face joining the two edges. A total of 16 diffraction contributions is taken into account.

The fluctuations of the SSF curve in the shadow region behind the screen for vertical polarisation are smaller than for horizontal polarisation. Inside the shadow region the reverse is true for the average value of the SSF. This is explained by the fact that in the case of vertical polarisation the average SSF is mainly determined by the strong double-diffraction contribution from the top face, while the fluctuations are due to constructive and destructive interference of two weak slope-diffraction contributions from the vertical edges of the side faces. This is in contrast with the result for horizontal polarisation, where the large fluctuations are due to interference between two strong double-diffraction contributions from the edges of the side faces, and the small slope-diffraction contribution

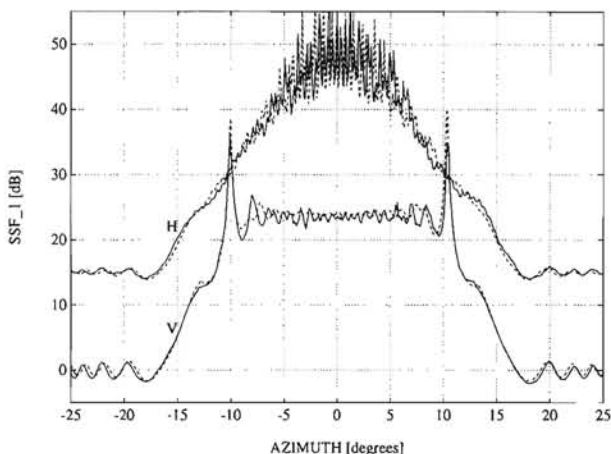


Figure 4.17: SSF of a rectangular block: measured (————) and calculated (-----) for vertical (V) and horizontal (H) polarisation. The H-curves have been raised by 15 dB for legibility.

Data: $h = 8.7\text{cm}$, $d = 30\text{cm}$, $z_{ob} = 50\text{cm}$, $\lambda = 6\text{mm}$

from the top face results in a large average SSF.

To test this polarisation dependence of the SSF curve, measurements with another type of obstacle have been performed. This obstacle consists of a pair of finite-width screens (Sec. 3.4.8), coinciding in position with the front and back face of the rectangular block. The results of these measurements are shown in Figure 4.18. Again, excellent agreement between measured and theoretical results is established. The SSF curves clearly demonstrate that the polarisation dependency indeed originates from slope diffraction at the edges of the side and top faces. For the other obstacle the polarisation dependency of the SSF curves is much weaker than that of the SSF curves of the rectangular block.

4.4.4 Measurement of time response

The arrival of the individual field contributions at the R-probe has also been measured in the time domain. By use of a sweep bandwidth of 18 GHz, the individual rays can be distinguished (Sec. 4.3). Figure 4.19 shows the results of the time-domain measurements at $\varphi_R = 3^\circ$ for both horizontal and vertical polarisations. The earliest pulse corresponds to the wave propagating along the top face of the obstacle. Now, the polarisation dependence of the diffraction process can also be inferred from the amplitudes of these pulses. It appears

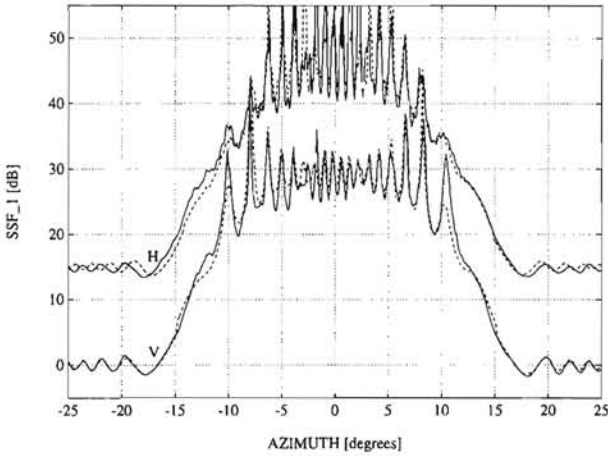


Figure 4.18: SSF of a pair of parallel, finite-width screens: measured (————) and calculated (-----) for vertical (V) and horizontal (H) polarisation. The H-curves have been raised by 15 dB for legibility.

Data: $d = 30\text{cm}$, $z_{ob} = 50\text{cm}$, screen separation of 8.7cm , $\lambda = 6\text{mm}$

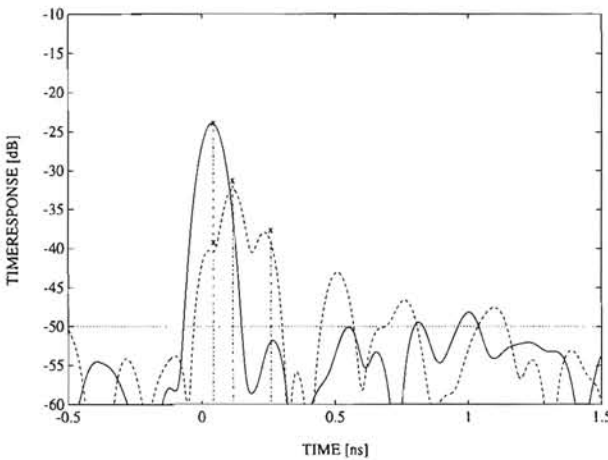


Figure 4.19: Measured time-domain results for a rectangular block for vertical (————) and horizontal (-----) polarisation. The calculated time-domain response ($\cdot\cdot\cdot\cdot\cdot\cdot x$) is also indicated. The dotted horizontal line indicates the lower level of the dynamic range.

Data: $h = 8.7\text{cm}$, $d = 30\text{cm}$, $z_{ob} = 50\text{cm}$, $\varphi_R = 3^\circ$, $\lambda = 6\text{mm}$

that the slope-diffraction mechanism for horizontal polarisation introduces an additional loss of approximately 15 dB. Note that besides the amplitudes of the individual pulses, also the inter-arrival times are correctly predicted by the theoretical model. It was found that the relatively strong pulse at $t = 0.5ns$ goes with a ray that traverses a side face three times, resulting in a quadruple-diffracted field contribution. The latter mechanism has not been implemented in the theoretical model.

4.4.5 Conclusions

Measured and theoretical SSF curves for a rectangular block show excellent agreement for both vertical and horizontal polarisations. The polarisation dependence of the measured and theoretical results has been clarified by comparing these results with the SSF curves for an obstacle consisting of two finite-width screens, and by an analysis of the time-domain measurements. It was found that slope diffraction is responsible for the polarisation dependency. From the results presented it is concluded that the UTD prediction model for building diffraction, including higher-order edge-edge and edge-corner interactions, provides an accurate and reliable description of the diffraction processes at environmental buildings. The model can therefore be used for the prediction of the shielding effectiveness of buildings, and for the prediction of the performance of land-mobile satellite systems with (strong) screening effects.

From the results presented in Section 4.3 and in this section, it is concluded that modelling of environmental objects by (any combination of) obstacles resembling a thin finite-width screen, a knife edge, or a pair of parallel screens, is not realistic. Instead, the obstacles should be modelled by the rectangular block. The latter is a particular form of the general block-shaped obstacle (Sec. 3.2.4), which numerically can also take other physical shapes such as rooftops and pyramids.

4.5 Field-strength prediction behind lossy dielectric obstacles using the UTD

Up to now the obstacles considered were perfectly conducting. In this section⁴ a comparison is made between the measured and theoretically predicted field strength in the shadow

⁴ *Note:* the major part of this section was already published: G.A.J. van Dooren and M.H.A.J. Herben: *Field strength prediction behind lossy dielectric obstacles using the UTD*, Elec. Letters, vol. 29, no. 11, pp. 1016-1017, 1993.

region of a lossy dielectric obstacle. The field strength is measured along a circular arc behind the obstacle at a frequency of 50 GHz. The theoretical model uses UTD including corner, double, and edge-corner diffraction, and is heuristically extended to include effects of non-perfect conductivity. The agreement between the measured and the theoretically derived results is excellent for both orthogonal polarisations considered. The field behind a lossy rectangular block proves to be less polarisation dependent than the field behind a perfectly-conducting obstacle.

4.5.1 Introduction

Field-strength prediction on the basis of deterministic models has gained interest during the last decade [65]. Special attention has been paid to the use of the UTD for wave-propagation modelling, because this ray method offers a clear insight into the edge-diffraction process. However, few tractable theories dealing with diffraction at non perfectly-conducting wedges are available. An extension of UTD to account for non-perfect conductivity of lossy wedges, has been proposed (Sec. 2.6) together with a slope-diffraction coefficient to be used if the incident field amplitude is zero. In Section 4.4 it has been demonstrated that this slope diffraction term causes a strong polarisation dependence of the field in the shadow region of a perfectly-conducting obstacle.

In this section the formulation of the heuristic extension of UTD is examined, and results from the theoretical model are compared to measured results. The measurements were carried out with a vector network analyser (VNA) at a frequency of 50 GHz.

4.5.2 Theoretical model and geometry

The geometry used to describe slope diffraction is depicted Figure 4.20a. Notice that the coordinates φ' and φ are defined similarly for both wedges. From this figure it is clear that the wave incident upon the second edge is at grazing incidence, and therefore $\varphi'_2 = 0$. For a vertical (z) polarisation of the incident field, UTD predicts a diffracted field from the first edge with a zero amplitude. In this case slope diffraction is the following term to be included in the analysis. For a horizontal (y) polarisation the diffracted field from the second edge is found by consecutively applying the diffraction formulas to the second edge with the non-zero diffracted field from the first edge acting as incident field.

In general, the wedge-diffracted field is proportional to a diffraction coefficient D given by

$$D \propto D_1 + D_2 + R_O D_3 + R_N D_4, \quad (4.2)$$

where D_l ($l = 1, \dots, 4$) are terms of the form $D = \cot(\pi/3 + \alpha/3) \cdot F(g(\alpha))$ (eq. (2.48)), and

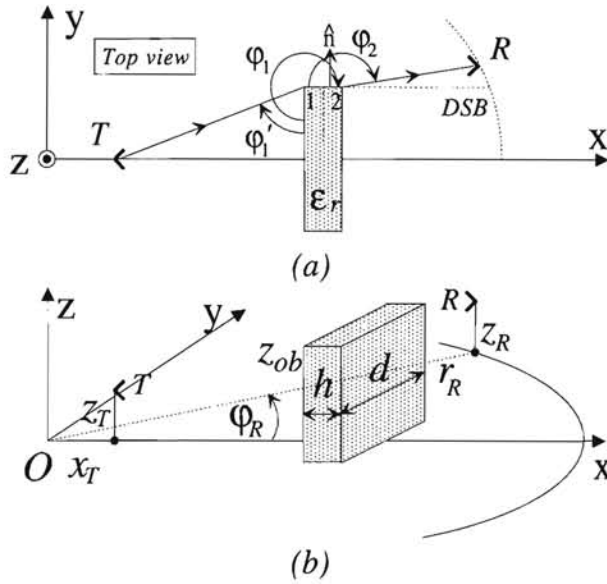


Figure 4.20: Slope-diffraction geometry (a), and geometry as used for the theoretical model and the measurement setup (b).

the transition function F is given by equation (2.57). For perfectly-conducting materials, the reflection coefficients $R_{O,N}$ take the values ∓ 1 , depending upon the polarisation of the incident wave. For grazing incidence $D_1 = D_3$ and $D_2 = D_4$ and for soft (vertical) polarisation $R_{O,N} = -1$, which explains why the first-order diffracted field has a zero amplitude. For hard (horizontal) polarisation, however, $R_{O,N} = 1$ and a non-zero diffracted field amplitude from the second edge is found.

In the heuristic extension of UTD, $R_{O,N}$ are replaced by Fresnel's reflection coefficients (eq. (2.84) and (2.85)). This implies that, for grazing incident waves, no diffracted fields from wedge 2 are present because then the Fresnel reflection coefficients have a value of -1 for both orthogonal polarisations. Hence slope diffraction fields should be taken into account.

The formulation of the amplitude of this slope-diffracted field is given by (eq. (2.68))

$$E^{slope} \propto \frac{\partial D}{\partial \phi_2'} \cdot \frac{\partial E^i}{\partial \hat{n}} \cdot A \cdot C, \quad (4.3)$$

where D is the diffraction coefficient of the second wedge in Figure 4.20, E^i is the field diffracted from edge 1 and incident upon wedge 2, $\partial/\partial \hat{n}$ is the directional derivative with

respect to the normal vector \hat{n} , A is the spreading factor and C corresponds to additional amplitude and phase constants.

Both derivatives in equation (4.3) contain Fresnel reflection coefficients as an implicit function of φ'_2 and φ_1 , respectively. It can be shown that a straightforward numerical evaluation of equation (4.3) provides a continuous total field across the diffraction-shadow boundary (DSB) indicated in Figure 4.20. Whether this heuristically extended UTD and its associated slope-diffraction term are accurate is not demonstrated in [31], but will be investigated in the following.

The geometry considered in both the theoretical model and the measurements is shown in Figure 4.20b. The positions of the T(ransmit) and R(eceive) probes are given in a Cartesian (x, y, z) coordinate system. The polarisation of the T-probe, at position $(x_T, 0, z_T)$ is either horizontal (y) or vertical (z), and its symmetry axis points into the x -direction. The R-probe moves along a circular arc parallel to the xy -plane with radius r_R , and the z -axis is the axis of rotation. Its symmetry axis is always directed towards the z -axis. The obstacle is a rectangular block with edges parallel to the axes of the Cartesian coordinate system. Its height is z_{ob} , its width is d , and its thickness is h . The complex relative permittivity of the rectangular block is given by ϵ_r . The SSF is measured and calculated as a function of the azimuth angle φ_R with $|\varphi_R| \leq 25^\circ$.

The diffraction model developed uses the extended UTD to model the diffraction of the incident spherical wave at the rectangular block. In the theoretical analyses, the following types of field contributions are considered: the direct field propagating from T to R, edge-diffracted fields, corner-diffracted fields, and field contributions due to edge-edge and edge-corner interactions. The effect of the ground plane is neglected.

4.5.3 Determination of complex permittivity

The specification of the shielding material is not very precise at the frequency used (50 GHz). For this reason the complex relative permittivity of the material was determined using the waveguide insertion method [66]. First, the VNA is calibrated in such a way that a reference plane in-between two waveguide flanges is obtained. Then a short waveguide completely filled with a sample of the material under test is inserted between the flanges. The amplitude and phase of the wave transmitted through the sample are then measured. By taking into account internal reflections, an equation for the complex relative permittivity ϵ_r can be numerically solved. Following this procedure ϵ_r at 50 GHz was found to be $1.37 - 0.99i$.

4.5.4 Comparison of measured and theoretical results

In the results to be presented, the rectangular block has dimensions $h = 7.7\text{cm}$, $d = 30.0\text{cm}$, and $z_{ob} = 50.0\text{cm}$. Therefore it is described by $68.8\text{cm} \leq x \leq 76.5\text{cm}$, $-15\text{cm} \leq y \leq 15\text{cm}$, and $0 \leq z \leq 50\text{cm}$. The T-probe is located at $x_T = 25.2\text{cm}$, $y_T = 0$, $z_T = 46.0\text{cm}$, while $r_R = 114.8\text{cm}$ and $z_R = 40.0\text{cm}$. The T- and R-probes are rectangular WR-19 waveguides operating at a (centre) frequency of 50 GHz.

The upper curves from Figure 4.21 show the measured and predicted field strength along the circular arc, for vertical polarisation. The curves for horizontal polarisation have

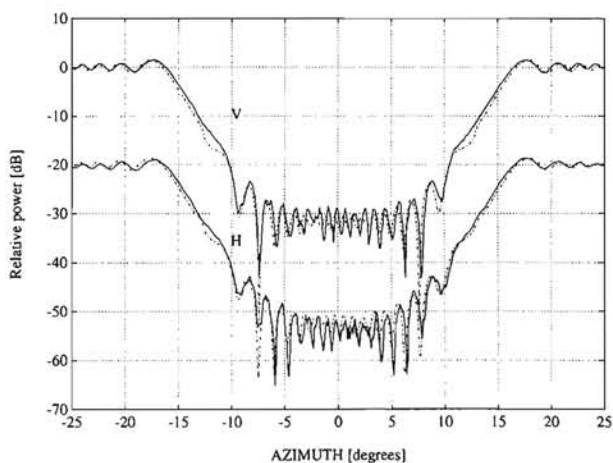


Figure 4.21: Field strength behind a rectangular block: measured (—) and calculated (---) for vertical (V) and horizontal (H) polarisation. The H-curves have been lowered by 20 dB for legibility.

Data: $h = 7.7\text{cm}$, $d = 30\text{cm}$, $z_{ob} = 50\text{cm}$, $\lambda = 6\text{mm}$

been lowered by 20 dB for legibility. As can be seen from Figure 4.21, there is excellent agreement between the measured and predicted results, and there is nearly no polarisation dependence of the field behind the obstacle. It seems as if the width of the obstacle used in the measurements is smaller than that used in the theoretical analysis. This is explained by the fact that, at the edge tip, the material is quite thin, and the EM wave is partly propagating through this thin region. That there are still (small) differences between the measured curves for vertical and horizontal polarisation can be readily explained using the formulation of the UTD. Since the diffracted field from the second edge does not exhibit any polarisation dependence due to the grazing incidence (resulting in identical

hard and soft diffraction coefficients), the differences between the results for both orthogonal polarisations are caused by the polarisation dependence of the diffraction at the *first edge*. This is confirmed by the fact that the Fresnel reflection coefficients used in the diffraction coefficient for the first edge are slightly different for vertical and horizontal polarisation. Therefore also the results for the field behind the obstacle differ for vertical and horizontal polarisation. The polarisation dependence in the measured results for the field strength behind the obstacle would be larger if the polarisation dependence in the Fresnel reflection coefficients used in the first edge geometry would be larger.

4.5.5 Conclusions

A comparison between the predicted and measured field strength behind a dielectric obstacle is made. Excellent agreement between theory and measurements is found for both orthogonal polarisations considered. In contrast with the field strength behind a perfectly conducting rectangular block (Sec. 4.4), nearly no polarisation dependence of the field strength behind the dielectric one is found. Due to transmittivity of the dielectric at the edge tips, the width of the obstacle in the measurements seems to be smaller than that used in the theoretical analysis. Despite the heuristic nature of the UTD formulation, and the assumption that the wedge may not be transparent [31] it is demonstrated that the extended UTD model is accurate and that it is useful for field-strength prediction with an application to the design and planning of land mobile satellite systems [67].

4.6 Comparison between measurements and UTD simulations of EM-wave scattering by circular cylinders

In this section⁵ the scattering of obliquely incident electromagnetic waves by a perfectly conducting circular cylinder is analysed. The applicability of a simulation model based on the Uniform Theory of Diffraction (UTD) is examined by comparisons between results obtained from the UTD and those from an exact solution. It appears that the UTD model is accurate for cylinders with radii $a \geq 0.3\lambda$, and that the far-field scattered power from cylinders with smaller radii is negligibly small.

⁵ Note: the major part of this section was already published: H.J.F.G. Govaerts, G.A.J. van Dooren and M.H.A.J. Herben: *Comparison between measurements and UTD simulations of EM-wave scattering by circular cylinders*, to appear, 1993.

Results from UTD simulations are also compared with results from experiments carried out at 50 GHz, as a function of cylinder radius and wave polarisation. In all cases considered, good agreement is obtained.

Experiments with multiple parallel cylinders indicate that the single-cylinder model can also be used to predict the field strength in situations involving a row of cylinders, by simply using superposition.

4.6.1 Introduction

In this thesis, the UTD is used in several models for field-strength prediction. The first model can be used to predict the field strength within a shielded reflector antenna system, thereby taking into account the scattering effects caused by the presence of the reflector rim(s) and the shielding obstacle on the propagation path of the EM waves involved. This application is studied in Sections 5.5 and 5.6. Its main use is the analysis of the shielding of a satellite earth-station antenna site in order to reduce the interference caused by unwanted signals from terrestrial transmitters. The second application concerns field-strength prediction in an urban environment consisting of multiple obstacles. This application is studied in Chapter 6.

Until now, all the obstacles used were modelled by (a combination of) three-dimensional (3-D) block-shaped objects having eight vertices that may coincide [49]. It can easily be coupled with digital databases that contain information of built-up areas. Although both versions are fairly complete prediction tools, they both lack the ability to accurately calculate the EM-wave scattering from cylindrical structures, the presence of which is unavoidable in man-made environments. A number of examples can be thought of, such as the analysis of scattering by feed-support struts within antenna systems, or by lamp-posts, chimneys, etc. in urban environments.

To complete the field-strength prediction tool, a 3-D algorithm based on the UTD, accounting for the computation of EM-wave scattering by a straight circular cylinder of radius a , was developed. Since the UTD is restricted in its application to obstacles having dimensions large in terms of the wavelength λ , it is investigated in this section to what cylinder radius the algorithm can be used, and whether there is a need to apply an alternative method for thin cylinders. For that purpose, a second model based on an exact solution to the boundary value problem was derived [44], which is used as a reference for the analysis of the applicability and the accuracy of the UTD model, by comparing numerical results from both models. This exact solution is also presented.

Furthermore, a number of experiments were carried out in which the EM field behind a

circular cylinder was measured, the results of which will be presented subsequently. With the measured results the accuracy of the UTD model is verified. For this purpose, six configurations involving five different cylinders are employed.

Finally, a configuration with an array of cylinders is considered, in order to get an impression of the importance of multiple-reflection and multiple-diffraction contributions to the total scattered field. Here, the emphasis is placed on practical situations, such as a number of equidistantly spaced lamp-posts within a micro-cellular environment. Measured results are compared with results from UTD simulations in which multiple-reflection and multiple-diffraction phenomena are excluded.

Note that the cylinder is assumed to be perfectly conducting, and scattering effects at its ends are excluded. The latter assumption was consciously made, because there are a large number of conceivable cylinder-top shapes, that cannot be reduced to one general model.

4.6.2 Scattering by a circular cylinder

The objective is to create an accurate model accounting for EM-wave scattering by a circular cylinder illuminated by either a plane or a spherical wave. The cylinder is arbitrarily orientated with respect to a source and an observation point. The direct incident field at the observation point P may be subject to blockage and is calculated according to Geometrical Optics (GO). The UTD is used for the calculation of the reflection and diffraction contributions to the total field in P (Sec. 2.8). In this theory, it is suggested that diffraction by a cylinder is described by the attachment of a ray to the surface at a certain point Q_a , thereupon propagating along the surface for a while, and subsequently being launched from a point Q_l in a direction tangential to the surface, as was depicted in Figure 3.7a.

The UTD solution to EM-wave scattering by a smooth convex surface has been described in Section 2.8. The main problems in developing the model are caused by the geometry involving obliquely incident rays. For computational convenience, the model was based on a fixed geometry in a Cartesian (x, y, z) coordinate system, in which the cylinder axis of symmetry coincides with the y -axis, and in which the incident ray under consideration propagates along a vector \hat{x}_3^i that lies in the xy -plane. The fixed geometry is shown in Figure 3.7 for the special case of normal plane-wave incidence, and the reflected ray and a diffracted ray are also depicted. If the initial geometry of the problem under consideration differs from the fixed geometry, translations and rotations of the whole configuration need to be carried out in order to obtain the geometry desired before the UTD calculations are started. Note that in case of spherical-wave incidence, \hat{x}_3^i depends on the position of

either the reflection point Q_r or the diffraction point Q_a , whereas in case of plane-wave illumination its direction is fixed. This implies that for spherical-wave illumination the translations and rotations are to be carried out separately for each contributing ray.

A problem in the analysis is the number of diffraction contributions that need to be taken into account to obtain accurate results. In the simple case of plane-wave illumination an infinite number of diffraction contributions exist. In the given geometry, with the cylinder stretched in y -direction and $\hat{x}_3^i = \hat{x}$, the first diffraction contribution attaches at $z = -a$ and subsequently propagates along a surface path of length $t_1 < 2\pi a$ before it is launched. Here, t_1 depends on the position of the observation point P . The second diffraction contribution attaches at $z = a$ and propagates along a surface path with length $t_2 < 2\pi a$. This contribution is also shown in Figure 3.7. The third contribution also attaches at $z = -a$, but it propagates along the entire circumference of the cylinder plus a surface path with length t_1 before being launched. In this manner, an infinite number of diffraction contributions can be found, with corresponding surface path lengths

$$t_l = \begin{cases} t_1 + (l-1)\pi a & , \text{ if } l \text{ is odd,} \\ t_2 + (l-2)\pi a & , \text{ if } l \text{ is even,} \end{cases} \quad (4.4)$$

where $l \in \{1, 2, \dots\}$. Note that with oblique incidence also an infinite number of diffraction contributions exist, provided that the cylinder is infinitely long. In that case, the ray paths are part of a helix.

A ray attaching at Q_a thus gradually sheds its energy while propagating along the surface path. As a result, the amount of energy carried by a launched contribution decreases as the length of the corresponding completed surface path increases. It is therefore obvious that the third diffraction contribution is of less influence than the first, since $t_3 > t_1$, and so on. This implies that there actually is a finite number of non-negligible diffraction contributions, which will be determined in the following section.

The total electric field \vec{E}^t at the observation point P consists of the incident field \vec{E}^i , the reflected field \vec{E}^r , and the diffracted fields \vec{E}^d . Obviously these fields are subject to blockage, as explained in previous sections. In Section 3.2.3, expressions for the total field in the lit and the shadow region have been given in equations (3.22) and (3.23), respectively.

The exact solution to EM-wave scattering by a circular cylinder is found by solving the boundary-value problem. It has been derived and presented before, although the solution is mostly given in cylindrical coordinates and only presented partially ($\beta = \pi/2$). The complete analytical solution in a Cartesian (x, y, z) coordinate system was derived assuming oblique plane-wave incidence [44], the ultimate results of which are presented here. The angle of incidence β is measured in the xy -plane, and $\beta = 90^\circ$ for normal incidence. Two orthogonal linear polarisation states are considered.

In case of parallel polarisation, the incident electric field \vec{E}^i is specified by

$$\vec{E}^i(x, y, z) = \begin{pmatrix} E_x^i \\ E_y^i \\ E_z^i \end{pmatrix} = E_0 \begin{pmatrix} -\cos \beta \\ \sin \beta \\ 0 \end{pmatrix} e^{-jk(x \sin \beta + y \cos \beta)}, \quad (4.5)$$

in which k is the wavenumber ($k = 2\pi/\lambda$). By the presence of the cylinder, a scattered field \vec{E}^s is generated according to

$$\vec{E}^s = E_0 \begin{pmatrix} \cos \beta \sum_{n=-\infty}^{\infty} p_n \left[\frac{n \sin \varphi}{u} H_n^{(2)}(u) + j \cos \varphi H_n^{(2)'}(u) \right] \\ -\sin \beta \sum_{n=-\infty}^{\infty} p_n H_n^{(2)}(u) \\ \cos \beta \sum_{n=-\infty}^{\infty} p_n \left[\frac{-n \cos \varphi}{u} H_n^{(2)}(u) + j \sin \varphi H_n^{(2)'}(u) \right] \end{pmatrix} e^{-jky \cos \beta}, \quad (4.6)$$

in which

$$\varphi = \arctan \left(\frac{z}{x} \right), \quad (4.7)$$

$$u = k\sqrt{x^2 + z^2} \sin \beta = k\rho \sin \beta, \quad (4.8)$$

and

$$p_n = j^{-n} \frac{J_n(ka \sin \beta)}{H_n^{(2)}(ka \sin \beta)} e^{jn\varphi}. \quad (4.9)$$

Here, J_n is the Bessel function of the first kind of order n , $H_n^{(2)}$ is the Hankel function of the second kind of order n , and the prime denotes a partial derivative with respect to ρ .

In case of perpendicular polarisation, the cylinder is illuminated by

$$\vec{E}^i = \begin{pmatrix} 0 \\ 0 \\ E_0 \end{pmatrix} e^{-jk(x \sin \beta + y \cos \beta)}, \quad (4.10)$$

which yields the following scattered field \vec{E}^s

$$\vec{E}^s = E_0 \begin{pmatrix} \sum_{n=-\infty}^{\infty} q_n \left[\frac{-n \cos \varphi}{u} H_n^{(2)}(u) + j \sin \varphi H_n^{(2)'}(u) \right] \\ 0 \\ \sum_{n=-\infty}^{\infty} q_n \left[\frac{-n \sin \varphi}{u} H_n^{(2)}(u) - j \cos \varphi H_n^{(2)'}(u) \right] \end{pmatrix} e^{-jky \cos \beta}, \quad (4.11)$$

with

$$q_n = j^{-n} \frac{J_n'(ka \sin \beta)}{H_n^{(2)'}(ka \sin \beta)} e^{jn\varphi}. \quad (4.12)$$

In the implementation of the numerical model the infinite sum was truncated with $|n| \leq N = 10$, including only those terms that have a relative contribution larger than $\delta_{rel} =$

10^{-6} , which is the maximum error allowed, specified by the user. If the infinite series in equations (4.6) and (4.11) are truncated to a finite sum of the first $2N + 1$ terms, the following term has a relative magnitude smaller than δ_{rel} . In the following section the results from this ‘exact’ solution are compared with the UTD results in order to validate our UTD model with respect to its accuracy.

4.6.3 Numerical results

In this section a test case involving a cylinder of radius $a = 10\lambda$ and infinite extent is analysed. The cylinder axis coincides with the y -axis. A plane wave of unit amplitude ($E_0 = 1$), propagating parallel to the xy -plane, is incident upon the cylinder at an angle $\beta = 45^\circ$. The observation points P are located on a semi-circle of radius $r = 10000\lambda$ in the space $z \geq 0$, with $P = (10000\lambda \cos \varphi, 0, 10000\lambda \sin \varphi)$. The scattered field is calculated as a function of φ . Results are presented in Figure 4.22 for vertical polarisation only; it was found that comparable results are obtained for horizontal polarisation [44]. The result from

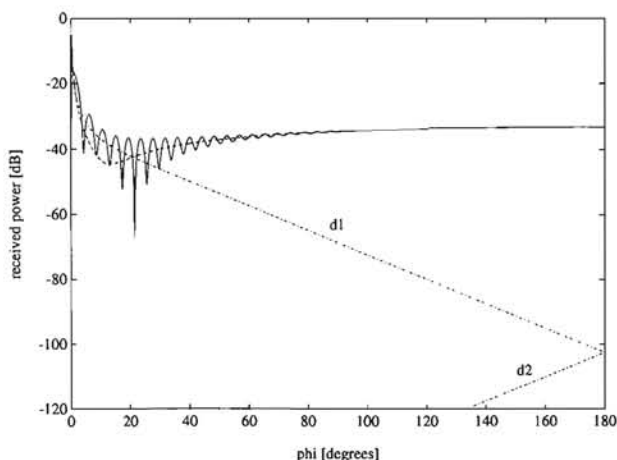


Figure 4.22: Field scattered by a cylinder with $a/\lambda = 10$ and $\beta = 45^\circ$: scattered (—), reflected (---), and diffracted (·-·-·-·).
Data: $r = 10000\lambda$, vertical polarisation

the exact solution is represented by the solid curve in the figure. The maximum relative error δ_{rel} for this computation is less than 10^{-6} . Initially, a total number of only two diffraction contributions were taken into account in the UTD calculation of the scattered field, i.e. one attaching at $z = -a$, having a surface path length $t_1 < t_\beta = 2\pi a/\sin \beta$,

and the other attaching at $z = a$, with corresponding surface path length $t_2 < t_\beta$. These are represented by the line-dotted curves. The optical shadow boundary is determined by $|\varphi| < 0.06^\circ$, and since it is very small, it can hardly be distinguished from the figure. At $\varphi = 0^\circ$ and $\varphi = 180^\circ$, both diffraction curves intersect, since they have identical path lengths at these angles. Since t_1 increases along the entire φ interval, the first diffraction curve ('d1') consequently falls as a function of φ . At the optical shadow boundary $\varphi = 0.06^\circ$, the path length t_2 shifts from 0 to $2\pi a / \sin \beta$, which yields a downward shift in the second diffraction curve ('d2'). A further increase of φ corresponds to a decrease of t_2 , so that the second diffraction curve rises as a function of φ .

At the optical-shadow boundaries, discontinuities are introduced by the diffraction contributions. On the one hand these are cancelled by the GO contribution and the reflection contribution, but owing to the abrupt shift in surface path length, the inclusion of a third and fourth diffraction contribution is required for continuity, and these contributions in their turn require fifth and sixth diffraction contributions, and so on. The maximum power level of the third and fourth diffraction contributions proved to be -168 dB in this particular case and it equals the minimum power level of the first and second contributions. This level is extremely low, and therefore these contributions have negligible influence on the total scattered field. The latter is demonstrated by the continuity of the total field, which includes the GO contribution [44]. From a large number of simulations it was found that third and higher diffraction contributions may be excluded without affecting the accuracy of the (far-field) UTD result, regardless of cylinder radius a , angle of incidence β , and polarisation direction [44].

The reflection contribution is represented by the dashed curve in Figure 4.22, and it is clearly visible that it mainly determines the 'average' of the scattered-power result, which is represented by the dotted curve. This curve coincides with the result obtained using the exact solution (solid curve), which implies that the UTD model was constructed correctly.

As mentioned before, it is expected that the UTD fails for cylinders with very small normalised radius a/λ . Keller found that his GTD solution is 'quite good' for $ka > 2$, with normal incidence [4]. These findings were confirmed by a large number of comparisons between the UTD and the exact solution for different configurations [44], and it is suggested not to use the UTD with cylinders of radius $ka < 2$ ($a < 0.3\lambda$), regardless of angle of incidence β and polarisation direction, in order to avoid unreliable results.

The exact solution is an alternative method for calculating the scattering by wire-like structures. The processing time needed by this method for $\delta_{rel} = 10^{-6}$ depends on the value of $ka \sin \beta$. It exceeds the time needed for the calculation with UTD when $ka \sin \beta > 1.3$, which reasonably well meets the requirement of $ka > 2$ for the UTD calculations [44]. This

implies that there is only a small region $0.21/\sin\beta < a/\lambda < 0.3$ in which the exact solution should be used and more processing time is needed by the UTD method than required. This region does not exist when $\beta < 43.6^\circ$.

In some practical cases the presence of cylinders with radii $a < 0.3\lambda$ can simply be neglected, because the total power scattered by these small cylinders has a maximum amplitude fluctuation of less than -50 dB in the far-field [44]. Because of the latter, and the fact that the extension of the exact solution for spherical-wave illumination introduces integral equations which cannot be solved analytically, the exact solution for spherical-wave illumination was not derived.

4.6.4 Experimental results

At EUT, indoor bi-static scattering measurements for the determination of the shielding properties of various obstacles were carried out. The HP8510C Vector Network Analyser (VNA) is used in this setup, together with a set of rectangular-waveguide probes of the WR19 type (with apertures of 4.775×2.338 mm²), between which an obstacle can be placed. A schematic diagram and the complete description of the setup can be found in Section 4.2. Here the Device Under Test (DUT) is a brass circular cylinder that is mounted on a rotating table, together with the transmitter probe. The receiver probe is in a fixed position. In the simulation model, the rotation of transmitter and DUT is modelled by the rotation of the receiver around the same axis of rotation.

The setup and its corresponding model are schematically shown in Figure 4.23. The upper part, Figure 4.23a, is a side view of the plane $\psi = 0^\circ$, and the lower part, Figure 4.23b, shows a top view of the setup. The four-cylinder array depicted in Figure 4.23b will be discussed later. The observation point is assumed to be at the receiver aperture center, and it is denoted by R . At $\psi = 0$, $R = R'$. The horizontal distance between the axis of rotation and the transmitter aperture center T is denoted by d_T . The points T and R' are horizontally separated by d_{TR} , and the vertical separation between T and R is $(h_T - h_R)$. The DUT can be tilted in the vertical plane containing T and R' by an angle χ . The horizontal distance between the cylinder axis and T is denoted by d_c .

The spherical wave emanating from the transmitter is slightly obliquely incident upon the cylinder in general, since a height difference $(h_T - h_R)$ exists. The radiation patterns of the probes are taken into account in the UTD simulations of the test cases. The measurements were performed in an ordinary office room, using a frequency range $f \in [46, 54]$ GHz, in order to enable FFTs. For that purpose, 801 samples per observation point were taken. A time gate was carefully set in order to suppress spurious reflections in the vicinity of the

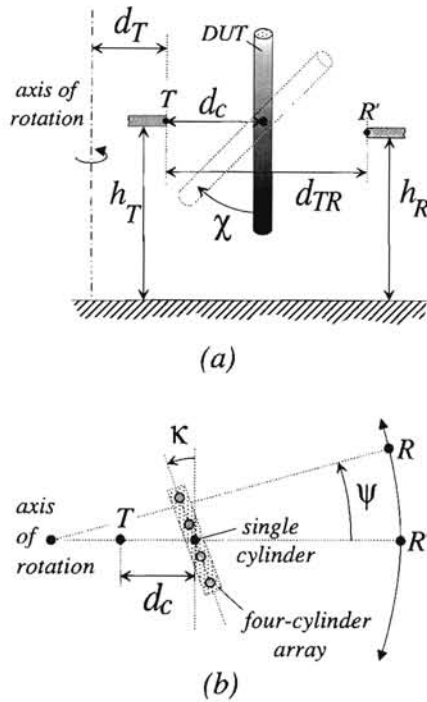


Figure 4.23: Side view of the measurement setup (a), and top view of the setup (b).

DUT and at the walls of the room. The data were extracted and stored for $f = 50$ GHz only, corresponding to a wavelength $\lambda = 6$ mm. The following non-variable parameters were measured with an accuracy of ± 0.5 mm: $d_T = 452$ mm, $d_{TR} = 699$ mm, $h_T = 1498$ mm, and $h_R = 1443$ mm. The angle span of the observation point range was taken $\psi \in [-12^\circ, 12^\circ]$, with a step of 0.1° and an accuracy of $\pm 0.05^\circ$. Five cylinders with different radii were used as a DUT, with $\chi = 0 \pm 2^\circ$. One of these cylinders was also used in tilted orientation ($\chi = 22 \pm 2^\circ$). The distance d_c depends on a and χ , as shown in Table 4.2, and it was measured with an accuracy of ± 0.5 mm. The measurements were carried out for two orthogonal linear polarisation states. With parallel polarisation, the polarisation vector is perpendicular to the earth's surface.

The solid curves in the Figures 4.24a through Figures 4.24e represent the measured results for the five different cylinders at $\chi = 0^\circ$. The upper curves show the results for perpendicular polarisation, and the results for parallel polarisation are shown in the lower part of the figures with a 10 dB offset to enhance legibility. The UTD simulation results

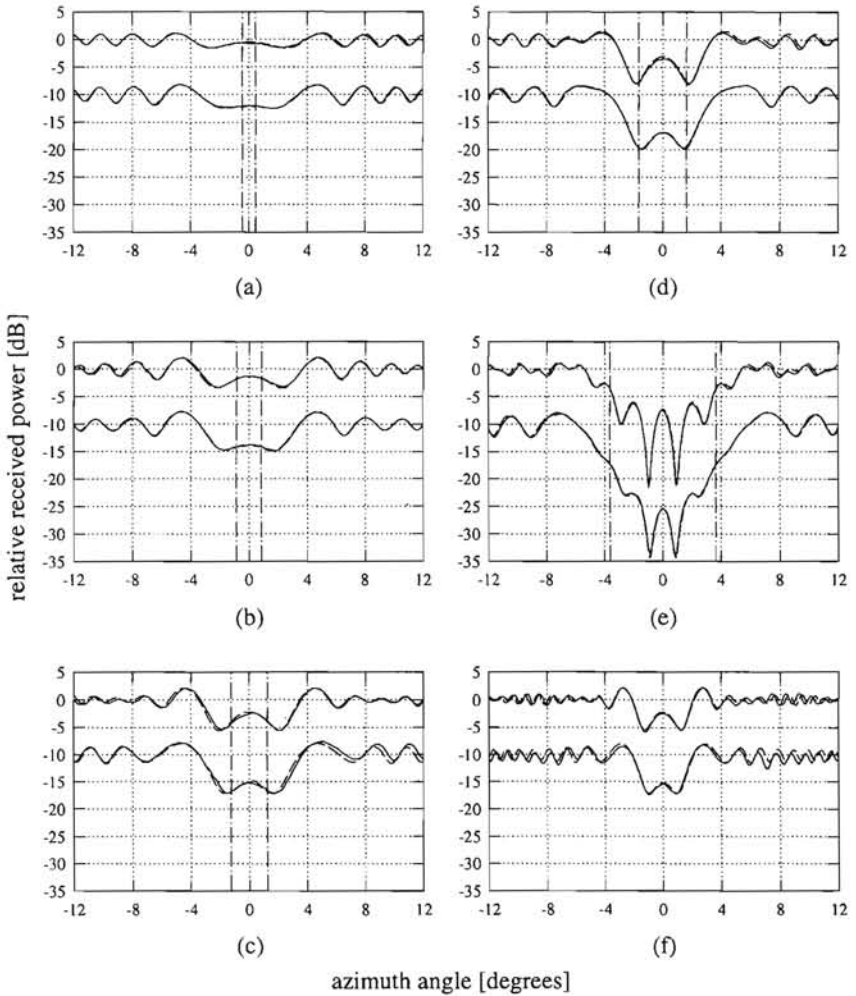


Figure 4.24: Relative received power as a function of azimuth angle: measured (—) and calculated (---) for $\chi = 0^\circ$, $a/\lambda = 0.5$ (a), $a/\lambda = 1$ (b), $a/\lambda = 1.5$ (c), $a/\lambda = 2$ (d), $a/\lambda = 5$ (e), and $\chi = 22^\circ$ and $a/\lambda = 1.5$ (f). The upper curves are for perpendicular polarisation, and the lower curves for parallel polarisation. The results for parallel polarisation have been lowered by 10 dB for legibility.

Table 4.2: Variable parameters in the measurement setup.

χ [°]	a		d_c
	[mm]	[λ]	[mm]
0	3	0.50	248
	6	1.00	253
	9	1.50	256
	12	2.00	259
	30	5.00	285
22	9	1.50	435

are represented by dashed curves. The optical-shadow (OS) regions are in between the vertical line-dotted lines. In these regions, the received power is owing to the diffraction contributions only.

From the figures it is observed that good agreement exists between measured and simulation results. The differences that occur between them are probably caused by the inaccuracies in the determination of the lengths and angles within the setup. Furthermore, it can be concluded that the total field is lowest if the polarisation vector is parallel to the cylinder axis. Another striking conclusion that can be drawn from the figures is that for cylinders with relatively small radii the minimum field strength is found outside the OS region, which may contravene intuitive expectations. This phenomenon is of course caused by the constructive and destructive interference of the different contributions to the total field.

The relative-power results shown are obtained by normalising the ‘received’ power in the presence of the cylinder to the free-space power received in the absence of the DUT. For the tilted cylinder the relative-power results are shown in Figure 4.24f. Although the agreement between the measured and the simulation results is acceptable, it is slightly worse than with $\chi = 0^\circ$. The most probable cause for this is the poor accuracy in determining χ if the cylinder is in a slanted position.

The presence of multiple cylinders on the propagation path of an EM wave gives rise to multiple reflection and diffraction contributions to the field in an arbitrary observation point. In the following, these contributions will be referred to as ‘interaction terms’. The amplitude of these terms depends on the separation of the cylinders, since the waves have a diverging character after being reflected or diffracted by a convex surface. It is likely that the influence of these terms vanishes if the separation is sufficiently large.

Elsherbeni and Kishk presented a method by which the scattered field from multiple

parallel cylinders can be calculated, which includes the interaction terms [68]. It is based on the boundary value method with plane-wave illumination, and they proved that for small separation the interaction terms cannot be neglected. In this section the aim is to get an impression of the applicability of the single-cylinder UTD model described in the foregoing in realistic multiple-cylinder configurations, such as an industrialised district with multiple chimneys, or a road along which lamp posts are placed. The latter situation could occur in a micro-cellular environment in which a communication link between a fixed transmitter antenna and a receiver antenna on a moving vehicle suffers from the scattering by a row of lamp posts. This practical problem is usually tackled by statistical analyses.

This situation was modelled within the EUT measurement setup by taking four equidistantly spaced, parallel cylinders as a DUT. The ratio $a/\lambda = 0.415$ at 1.5 GHz was used to scale the cylinder radii to the frequency of 50 GHz as used in the experimental setup. The cylinders are made of brass and all have identical radii $a = 2.5\text{mm}$, corresponding to 8.3cm at 1.5 GHz, which is representative of the radius of commonly used lamp posts. The separation between the cylinder axes of symmetry was chosen to be 40mm , which corresponds to 1.3m at 1.5 GHz. Note that this is much worse than in practical situations, since the separation of lamp posts in urban environments is generally much larger ($\approx 50\text{m}$). The measurements were carried out for different orientations of the array with respect to the antennas, as a function of the angle κ , which is indicated in Figure 4.23b. The array is symmetrical with respect to its axis of rotation, which is at a horizontal distance $d_c = 178 \pm 0.5\text{mm}$ from T . The observation points span an angle interval $\psi \in [-15^\circ, 15^\circ]$ with a step of 0.1° and an accuracy of $\pm 0.05^\circ$. The remaining parameters are identical to those used in the single-cylinder setup.

The relative-power results are depicted in Figure 4.25, for different values of κ , and parallel polarisation. The solid curves represent the measured results. The dashed curves are obtained with UTD by simply using superposition, and thus excluding the interaction terms. Except for the symmetric situation with $\kappa = 0^\circ$, the asymmetry of the curves is clearly visible. For angles κ up to 60° , the UTD simulation curves correspond quite well to the measured curves. At $\kappa = 80^\circ$, the curves also follow similar courses with coinciding minima and maxima, but large differences in power level are present. These are readily explained by the fact that the interaction terms become more significant as the angle between the incident wave and the longitudinal direction of the linear array decreases. To test the measurement repeatability, the experiment for $\kappa = 80^\circ$ was repeated once, without touching any part of the measurement setup. The second measured result is represented by the dash-dotted curve in Figure 4.25e. It slightly differs from the first measurement, and this is a good indication for the accuracy of the measured results.

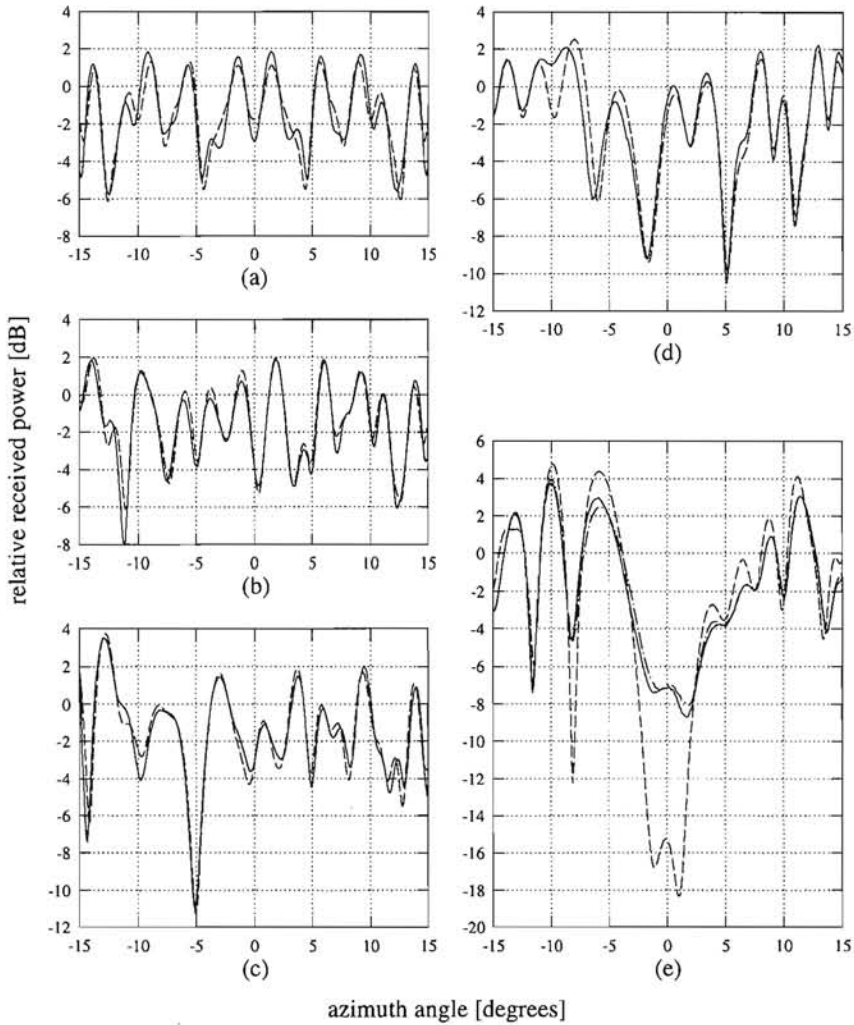


Figure 4.25: Relative received power as a function of azimuth angle for four parallel cylinders: measured (—) and calculated (---) for $\kappa = 0^\circ$ (a), $\kappa = 20^\circ$ (b), $\kappa = 40^\circ$ (c), $\kappa = 60^\circ$ (d), $\kappa = 80^\circ$ (e). In (e) also a result of a repeatability measurement is shown (-·-·-·-·).

4.6.5 Conclusions

A UTD model for calculating the EM-wave scattering by a circular cylinder of arbitrary radius was successfully implemented and tested. The number of diffraction contributions that need to be taken into account can be reduced to two, providing accurate results for cylinders with normalised radii $a/\lambda \geq 0.3$. In a mobile-communication environment it is suggested to simply neglect the presence of cylinders with radii $a < 0.3\lambda$, since the use of UTD is not justified, and the influence of the presence of the cylinders on the total field in their environment is negligible anyway.

For plane-wave illumination, an alternative method which is based on an exact solution of the boundary-value problem is presented. The application of this method is not hindered by restrictions to the normalised cylinder radius, and it appears to perform quite well on a PC, regarding runtime and accuracy [44].

In case of spherical-wave incidence, the geometrical aspects of the UTD model are more complicated. It is shown that the model provides accurate results which agree well with the measured results from experiments performed at EUT.

The single-cylinder model may also be applied in configurations involving multiple cylinders, provided that the separation between the cylinders is sufficiently large. It is expected that most practical multiple-cylinder arrays (and other configurations) can be modelled by applying the single-cylinder model repeatedly. Situations where the field is incident from a longitudinal direction with respect to the cylinder array should be considered very carefully.

The model can also be applied to tackle a variety of strut scattering problems within a reflector antenna, since the UTD can handle both plane- and spherical-wave scattering. With this application, the model may be a helpful design tool in order to meet the reference curves imposed by the CCIR concerning the envelope of the radiation pattern of reflector antennas. It can be used to determine a strut configuration such that the sidelobe envelope meets these CCIR requirements.

Chapter 5

Site shielding of symmetrical parabolic reflector antennas

5.1 Introduction

The geometries considered thus far did not incorporate any spatial filtering by the antenna located in the vicinity of the object. Instead the infinitely small antenna was assumed to have an isotropic radiation pattern. Obviously, the modelling of an antenna by a point receiver is not realistic, and therefore the combined problem of obstacle and antenna diffraction is analysed in this chapter. The attention will be restricted to reflector antennas of the parabolic type. These antennas are frequently used in satellite communications, which is the field where site shielding is often employed. Furthermore, the receiving properties of these antennas can also be analysed using the UTD.

The common procedure for taking into account the antenna receiving properties is the replacement of the antenna by a point receiver with some spatial weight function. This approach is referred to as the *far-field* approach, because the weight function employed corresponds to the antenna far-field radiation pattern. In this method the obstacle and antenna scattering are treated in an independent way, and therefore its main advantage is its simplicity.

To separate the far-field region from the near-field region of an antenna with a circular aperture, the Rayleigh distance $R = 2D_p^2/\lambda$ is commonly used, with D_p the aperture diameter and λ the wavelength. If the obstacle is in the near field of the antenna, the far-field approach cannot be applied and another method should be invoked. This other method is referred to as the *near-field* approach, and consequently the antenna and obstacle diffraction are analysed in a combined way. This implies that, in the near-field approach, the introduction of the reflector rim amounts to the analysis of diffraction at an additional obstacle edge on the propagation path.

In this chapter the analysis of a parabolic reflector antenna shielded by a finite-width

screen is dealt with. The analysis is merely an extension to the analysis reported in [3], where the obstacle used for shielding is a half-plane. The model discussed in Section 5.2 reduces to that used in [3] if the screen is infinitely wide.

A comparison between results predicted by a near-field and a far-field approach for the analysis of a parabolic reflector antenna shielded by a finite-width screen is given in Section 5.3. In this section the field strength at the terminal of a reflector antenna is calculated in a frequency band rather than for a continuous wave (CW) signal. In this way possible averaging effects as encountered in radio-receiver front-ends can be studied. Implications of using the far-field instead of the near-field approach in ray-based field strength prediction models are given.

To study the dependence of the SSF on the type of reflector antenna, the problem of half-plane shielding of a double-reflector antenna is analysed in Section 5.5. Although the Cassegrain antenna has been widely used in telecommunications, few results concerning its wide-angle receiving properties have been reported in the literature. Since these receiving properties are needed in the site shielding analysis, also results on the receiving properties of this type of antenna are given. The SSF as function of antenna orientation and other geometrical parameters is determined. A comparison between the results of half-plane shielding of single- and double-reflector antennas based on the near- and far-field approach will be given in Section 5.6.

5.2 Shielding of a single-reflector antenna

The general site shielding problem is three dimensional in nature, and can apply to various geometries. In this section a model for the shielding of a parabolic reflector antenna located behind a perfectly conducting finite-width screen is described. It is assumed that the incident (interfering) field is due to a distant source and therefore it is modelled as a uniform plane wave. Throughout this chapter, we suppose that the earth's surface between obstacle and antenna is flat, and that the influence of the atmosphere in the region in between the antenna and the obstacle is negligible. Consequently, ground reflections are not considered in the analysis. The antenna under consideration is a parabolic reflector antenna with a circular aperture, and the aperture cylinder of the antenna system is assumed not to be obstructed by the obstacle. Therefore the SSF as defined in equation (3.1) will be used in the following. The configuration is shown in Figure 5.1. It is described in a Cartesian (x, y, z) coordinate system, and the earth's surface is given by the plane $z = 0$. The finite-width screen is defined by $x = 0$, $-d_1 \leq y \leq d_2$, $0 \leq z \leq z_{ob}$, where z_{ob} is the obstacle height and $d_{1,2} > 0$. The same geometry, but then with a point receiver, was considered in

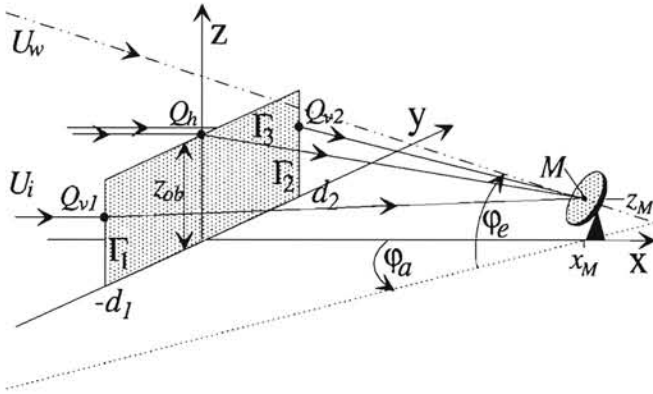


Figure 5.1: Geometry for shielding of a single reflector antenna by a finite-width screen.

Section 3.2.2.

The unwanted wave U_i , caused by some distant source, is incident upon the obstacle from a direction parallel to the xy -plane, and propagates into the x -direction. The wanted wave U_w is coming from a satellite, and is assumed to be unaffected by the obstacle [3]. Since U_w is received via the main lobe of the receiving terminal, the satellite position determines the azimuth angle (φ_a) and the elevation angle (φ_e), as depicted in Figure 5.1. It should be noted that the angles φ_a and φ_e refer to the antenna aperture centre M with Cartesian coordinates $(x_M, 0, z_M)$, $(x_M, z_M > 0)$. The height difference $\Delta z = z_{ob} - z_M > D_p/2$, such that the whole antenna is in the shadow cast by the obstacle in the half-space $x > 0$. In this way, no specific point on the reflector edge is illuminated directly by the interfering field. If required, this simplification can be removed, as shown in [69]. The site shielding problem amounts to the estimation of the influence of the obstacle on the receiving properties of the reflector antenna.

5.2.1 Description of the receiving antenna

The antenna under consideration is a parabolic reflector antenna with a feed system located at the focus F and focal distance f_p . For simplicity, the influence of the feed struts is neglected in the present analysis, although scattering from these supports may cause some high sidelobes in the radiation pattern of the antenna. Also, blockage by the feed is not considered. As in most practical cases, the reflector is assumed to be in the far field of

the feed, such that the radiation pattern of the feed at F can be described by the far-field radiation pattern G_f , which is rotationally symmetric. The main-beam axis of the feed coincides with the symmetry axis of the antenna. The antenna configuration is depicted in Figure 5.2. For the description of the geometry of the parabolic reflector antenna, a

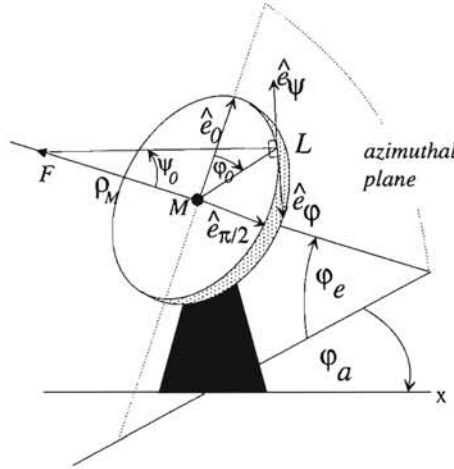


Figure 5.2: Geometry for the parabolic reflector antenna.

spherical (ρ, ψ, φ) coordinate system is employed, with the origin at F . The polar axis of the spherical coordinate system coincides with the symmetry axis of the paraboloid; the direction $\psi = \pi$ is the forward direction of the reflector antenna. The aperture centre M can be described either by its Cartesian coordinates $(x_M, 0, z_M)$ or by its spherical coordinates $(\rho_M, 0, \varphi)$. The edge of the reflector is given by $(\rho_0, \psi_0, \varphi)$ with $0 \leq \varphi \leq 2\pi$. The following geometrical relations are found

$$\rho_M = f_p - \frac{D_p^2}{16f_p}, \quad (5.1)$$

$$\rho_0 = f_p + \frac{D_p^2}{16f_p}, \quad (5.2)$$

$$\psi_0 = 2 \arctan \frac{D_p}{4f_p}, \quad (5.3)$$

where ρ_M is the distance from F to M , ρ_0 is the distance from F to a point on the reflector edge, and ψ_0 is the subtended angle of the reflector.

The far-field radiation pattern G_f of the feed is also described in the spherical coordinate system. A frequently employed feed is the corrugated horn, of which the far-field radiation pattern can well be described by a power of a cosine in the forward direction, and by a constant in the rear-angle region for which $\pi/2 < \psi < \pi$ [70]. The (voltage) feed radiation pattern is assumed to be independent of φ , and is defined as

$$G_f(\psi) = \begin{cases} G_0(a + \cos^m \psi) & , \text{ for } 0 \leq \psi \leq \pi/2, \\ G_0 a & , \text{ for } \pi/2 \leq \psi \leq \pi. \end{cases} \quad (5.4)$$

In equation (5.4), a is a dimensionless constant which determines the relative backward radiation level for $\pi/2 \leq \psi \leq \pi$, and the exponent m determines the amplitude taper over the reflector. This taper is given by $[G_f(\psi_0)f_p]/[G_f(0)\rho_0]$. The factor G_0 is dependent on a and m and is given by [3]

$$G_0 = \left[a^2 + \frac{a}{m+1} + \frac{1}{2(2m+1)} \right]^{-1/2}. \quad (5.5)$$

The forward voltage gain of the feed is $G_f(0) = G_0(a+1)$. The value of the exponent m as function of ψ and the desired relative edge illumination is shown in Figure 5.3 for $a=0.00316$, corresponding to a relative rear-radiation level of -50 dB.

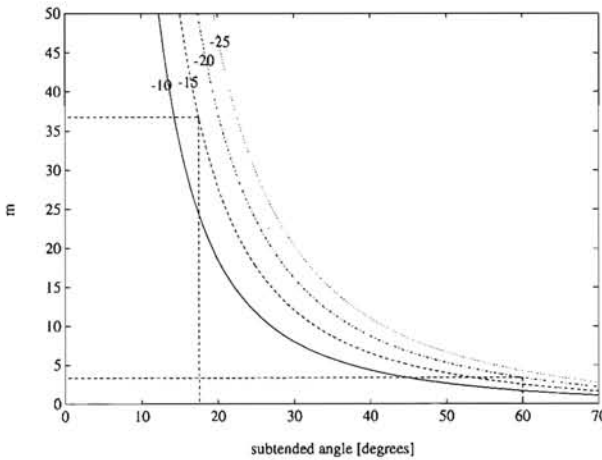


Figure 5.3: Value of m as function of ψ for a relative edge illumination of -10 dB (—), -15 dB (---), -20 dB (-·-·-·) and -25 dB (·····).
 Data: $a = 0.00316$

A Huygens-source polarisation of the feed is used. Vertical and horizontal polarisation are distinguished, corresponding to a reflected field in the aperture plane parallel and perpendicular to the azimuthal plane, respectively. The unit vector in the direction of the electric field radiated by the feed, $\hat{e}_{polV,polH}$, is found to be given by

$$\begin{aligned}\hat{e}_{polV} &= \cos \varphi \hat{e}_\psi - \sin \varphi \hat{e}_\varphi, & \text{for vertical antenna polarisation,} \\ \hat{e}_{polH} &= \sin \varphi \hat{e}_\psi + \cos \varphi \hat{e}_\varphi, & \text{for horizontal antenna polarisation.}\end{aligned}\quad (5.6)$$

For the antenna operating in receive mode, the polarisation properties apply to the field received by the feed by reciprocity. Note that in [3] two signs should be reversed in the definition of $\hat{e}_{polV,polH}$ to have the correct polarisation vector.

In the description of the antenna geometry, the vector triplet $(\hat{e}_0, \hat{e}_{\pi/2}, \hat{e}_0 \times \hat{e}_{\pi/2})$ depicted in Figure 5.2 can conveniently be used. The unit aperture vectors are dependent on the orientation of the antenna in terms of the azimuth (φ_a) and elevation (φ_e) angles and are defined as

$$\begin{aligned}\hat{e}_0 &= \sin \varphi_e \cos \varphi_a \hat{x} + \sin \varphi_e \sin \varphi_a \hat{y} + \cos \varphi_e \hat{z}, \\ \hat{e}_{\pi/2} &= \sin \varphi_a \hat{x} - \cos \varphi_a \hat{y}.\end{aligned}\quad (5.7)$$

At an arbitrary edge point L , with spherical coordinates $(\rho_0, \psi_0, \varphi_0)$, the surface triplet $\hat{x}_{1,2,3}^\Sigma$ and principal radii of curvature $\rho_{1,2}^\Sigma$ are given by [3]

$$\begin{aligned}\hat{x}_1^\Sigma &= \sin \varphi_0 \hat{e}_0 - \cos \varphi_0 \hat{e}_{\pi/2}, \\ \hat{x}_2^\Sigma &= \cos \frac{\psi_0}{2} (\cos \varphi_0 \hat{e}_0 + \sin \varphi_0 \hat{e}_{\pi/2}) - \sin \frac{\psi_0}{2} (\hat{e}_0 \times \hat{e}_{\pi/2}), \\ \hat{x}_3^\Sigma &= \hat{n}^\Sigma = \sin \frac{\psi_0}{2} (\cos \varphi_0 \hat{e}_0 + \sin \varphi_0 \hat{e}_{\pi/2}) + \cos \frac{\psi_0}{2} (\hat{e}_0 \times \hat{e}_{\pi/2}), \\ \rho_1^\Sigma &= 2f_p \cos^{-1} \left(\frac{\psi_0}{2} \right), \\ \rho_2^\Sigma &= 2f_p \cos^{-3} \left(\frac{\psi_0}{2} \right).\end{aligned}\quad (5.8)$$

where $\rho_{1,2}^\Sigma$ correspond to $\hat{x}_{1,2}^\Sigma$, respectively.

In terms of the aperture unit vectors $(\hat{e}_0, \hat{e}_{\pi/2}, \hat{e}_0 \times \hat{e}_{\pi/2})$, the location of the feed position F and the edge point L are simply found to be given by

$$\vec{F} = \vec{M} - \rho_M (\hat{e}_0 \times \hat{e}_{\pi/2}), \quad (5.9)$$

and

$$\vec{L} = \vec{M} + \frac{D_p}{2} \cos \varphi_0 \hat{e}_0 + \frac{D_p}{2} \sin \varphi_0 \hat{e}_{\pi/2}. \quad (5.10)$$

Also the vector \hat{n}_e normal to the edge in the aperture plane is required in the analysis. This vector is given by

$$\hat{n}_e = \cos \varphi_0 \hat{e}_0 + \sin \varphi_0 \hat{e}_{\pi/2}. \quad (5.11)$$

The curvature of the edge a_e in the aperture plane is equal to the radius of the circular aperture rim $a_e = D_p/2$. It should be noted that the description of the edge and unit vectors

in terms of the aperture vectors \hat{e}_0 , $\hat{e}_{\pi/2}$, $\hat{e}_0 \times \hat{e}_{\pi/2}$, is dependent on the azimuth angle (φ_a) and elevation angle (φ_e). For constant φ_a and φ_e , the edge point L and the surface triplets at this point are completely defined by the aperture angle φ and the geometrical antenna parameters.

Since the interfering signal will usually be received by some sidelobe of the antenna pattern, first the off-axis receiving properties of a single parabolic reflector antenna will be discussed, i.e. the case where the antenna is *not* shielded by an obstacle.

5.2.2 Wide-angle reception of a parabolic reflector antenna

The antenna rim can be treated as an obstacle for which the exterior wedge angle is 2π , i.e. $n = 2$. Therefore the analysis of the reflector edge diffraction is straightforward. The diffraction points Q_i ($i = 1, 2$) are located on the reflector edge, and Keller's law of edge diffraction should be satisfied at Q_i . The direction of propagation of the incident wave is $\hat{s}' = \hat{x}_3^i = \hat{x}$ (Fig. 5.1). The unit vector tangent to the edge is $\hat{e} = \hat{x}_1^\Sigma$, and it is defined at the candidate diffraction point Q_i . Note that the point Q_i and its associated surface parameters $\hat{x}_{1,2,3}^\Sigma$ are completely determined by the aperture angle φ_i corresponding to Q_i .

The direction of propagation of the diffracted wave is denoted by \hat{s} and is given by

$$\hat{s} = \frac{\vec{F} - \vec{Q}_i}{\rho_0}. \quad (5.12)$$

The coordinates of the diffraction points Q_i are found by applying Keller's law of edge diffraction (eq. (2.40)) to \hat{s}' , \hat{s} , and \hat{e} at Q_i . Equation (2.40) can be numerically solved for the variable φ_i with a one dimensional root-finding procedure. Two angles φ_i ($i = 1, 2$) are found, which specify two diffraction points Q_i with $0 \leq \varphi_1 \leq \pi$ and $\pi \leq \varphi_2 \leq 2\pi$. These values of φ_i correspond to diffraction points $Q_{1,2}$ on the left and right part on the reflector edge, respectively.

For an incident plane wave, the E- and H-pattern of the antenna configuration can easily be calculated. In the following $\varphi_e = 0$, and the incident field has a vertical (\hat{z}) polarisation. Note that the wave parameters $\hat{x}_{1,2,3}^\Sigma$ and $\rho_{1,2}$ in this case reduce to

$$\begin{aligned} \hat{x}_1^i &= \hat{y}, \\ \hat{x}_2^i &= \hat{z}, \\ \hat{x}_3^i &= \hat{s}' = \hat{x}, \\ \rho_{1,2}^i &= \infty. \end{aligned} \quad (5.13)$$

The interaction of the incident wave with the reflector edge can be described by the theory as set out in Chapter 2. In the present case the reflector edge is curved, which is in contrast

with the situations encountered in the former chapters. To first order, only a finite number of (diffraction) waves contribute to the received field at the focal point F . In the calculation of the E- and H-plane only two diffraction points are of interest, and it is found that the two solutions for φ_i differ precisely a factor π . This indicates that the diffraction points Q_i ($i = 1, 2$) are located exactly diametrically opposite. The coordinates of the points Q_i are given by $(\rho_0, \psi_0, \varphi_0)$ and $(\rho_0, \psi_0, \varphi_0 + \pi)$. For $\varphi_e = 0$ it is found that $\varphi_0 = \pi/2$.

The location of the points Q_i ($i = 1, 2$) can also be found using Fermat's principle of stationary optical path length. The points $Q_{1,2}$ correspond to a maximum and minimum path length, respectively. For $\varphi_e = 0$ and $\varphi_a = (0, \pi)$, an infinite number of diffraction points are found, because there is no minimum or maximum path length. In fact, there is only one path length. This implies that the directions $\varphi_e = 0, \varphi_a = (0, \pi)$ are caustic directions, and therefore the UTD description of the diffraction process is invalid in these regions. To calculate the received field at the feed in the forward (caustic) region ($\varphi_a \approx 0, \varphi_e = 0$), another method such as aperture integration can be used. For the backward (caustic) region ($\varphi_a \approx \pi, \varphi_e = 0$) equivalent edge currents [71, 72] can be used to calculate the received field.

In the following we will restrict our attention to $0 \leq \varphi_a \leq \pi$ for reasons of symmetry, and $\varphi_e = 0$. If only the single-diffracted fields are considered, at maximum three waves arrive at the feed (Fig. 5.5):

1. The directly incident wave. It is blocked by the reflector for $\pi - \psi_0 \leq \varphi_a \leq \pi$. To simplify the notation, it is denoted by \vec{E}_0^d , although this wave encounters no diffraction at all. Since this contribution corresponds to the incident field, it is of k^0 ;
2. The wave diffracted at Q_1 . It is obstructed by the reflector for $\pi/2 \leq \varphi_a \leq (\pi + \psi_0)/2$. The parameters of the reflected field $\hat{x}_{1,2,3}^r$ and $\rho_{1,2}^r$, needed in the calculation of the diffraction coefficients, can be determined using equation (2.21). Simplifications occur in the expressions for the diffraction coefficients $D_{s,h}$ ($n = 2$), the distance parameter $L = \rho_0$ (plane incident wave) and the expression for the function $a(x) = 2 \cos^2(x/2)$. The caustic distance ρ^d is found using equation (2.66), which reduces to

$$\rho^d = -\frac{D_p/2}{\hat{n}_e \cdot (\hat{x} - \hat{s})}, \quad (5.14)$$

where \hat{n}_e is the normal vector to the reflector rim at Q_1 . The direction of propagation of the diffracted wave is $\hat{s} = (\vec{F} - \vec{Q}_1)/\rho_0$. This contribution is denoted by \vec{E}_1^d and it is of order $k^{-1/2}$ outside the transition regions, and of order k^0 inside the transition regions with respect to the incident wave of order k^0 .

3. The wave diffracted at Q_2 . This contribution is never obstructed, and also here the simplifications arise in various diffraction parameters. The direction of propagation of the diffracted wave is $\hat{s} = (\vec{F} - \vec{Q}_2)/\rho_0$, and the diffraction contribution is denoted by \vec{E}_2^d . Also this contribution is of order $k^{-1/2}$ outside the transition regions, and of order k^0 inside the transition regions.

The resulting field at F is found as a summation of these three field contributions, each weighted by a polarisation vector \hat{e}_{pol} and multiplied by the feed (voltage) gain for the angles of incidence ψ_{Q_i} and φ_{Q_i} ($i = 0, 1, 2$). It is easily derived that

$$\begin{aligned}\psi_{Q_0} &= \arccos(-\hat{x} \cdot (\hat{e}_0 \times \hat{e}_{\pi/2})), \\ \psi_{Q_1} &= \psi_{Q_2} = \psi_0, \\ \varphi_{Q_0} &= \arccos(-\hat{x} \cdot \hat{e}_0 / \sin \psi_{Q_0}), \\ \varphi_{Q_1} &= \pi/2, \\ \varphi_{Q_2} &= 3\pi/2.\end{aligned}\tag{5.15}$$

The total field $E_{V,H}^t$ at the feed position is given by

$$E_{V,H}^t(F) = \sum_{i=0}^{i=2} \epsilon_i G_f(\psi_{Q_i}) \vec{E}_i^d(F) \cdot \hat{e}_{polV,polH}(\psi_{Q_i}, \varphi_{Q_i}),\tag{5.16}$$

where ϵ_i is a shadow indicator accounting for blockage effects and $\hat{e}_{polV,polH}$ is the polarisation vector for either vertical or horizontal polarisation corresponding to the direction of incidence of contribution i .

For the shadow indicators ϵ_i the following relations are found

$$\epsilon_0 = \begin{cases} 0, & \text{for } \pi - \psi_0 \leq \varphi_a \leq \pi, \\ 1, & \text{elsewhere,} \end{cases}\tag{5.17}$$

$$\epsilon_1 = \begin{cases} 0, & \text{for } \pi/2 \leq \varphi_a \leq (\pi + \psi_0)/2, \\ 1, & \text{elsewhere,} \end{cases}\tag{5.18}$$

and

$$\epsilon_2 = 1.\tag{5.19}$$

The regions for φ_a where shadowing exists are shown in Figure 5.4.

In order to check the results obtained via the aforementioned model, the E- and H-plane receiving pattern of a parabolic reflector antenna with parameters $D_p = 15\lambda$, $f_p/D_p = 0.433$ ($\psi_0 = \pi/3$), $m = 1$, $a = 0$, $\varphi_e = 0$ and $1^\circ \leq \varphi_a \leq 179^\circ$ were calculated. This value of m corresponds to a relative edge illumination of -8.5 dB, and the result of this calculation is shown in Figure 5.6. A comparison of this result with a pattern in [73], where the

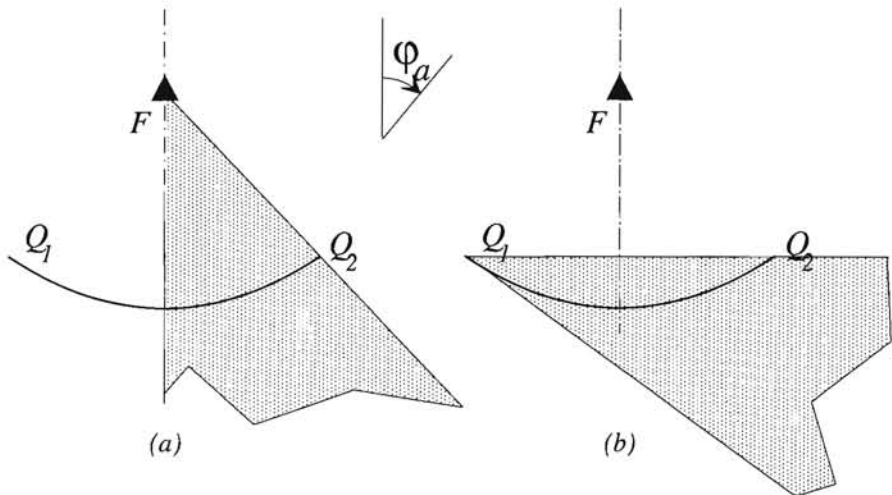


Figure 5.4: Shadow regions for field contributions: shadow region for the direct ray (a), and for the first diffraction point Q_1 (b).

same configuration was analysed in *transmit mode*, reveals that the results are identical. The pattern in Figure 5.6 near forward and rear directions was not calculated due to the presence of a caustic of the diffracted field in this region. In [73] other techniques have been used to cope with this problem.

The step discontinuity at $\varphi_a = \pi/2$, present only in the E-plane pattern, is caused by shadowing of the diffraction point Q_1 by the paraboloidal reflector. In [73] this shadowing problem is solved by introducing a heuristic factor R_{se} , independent of polarisation, which should account for the effects of surface-diffracted rays. These couple to the backside of the reflector surface and then arrive at diffraction point Q_1 , as indicated in Figure 5.5. From there on, the wave propagates to the feed F . In Section 2.8 it was described that the model for surface-diffracted waves includes a dyadic transmission factor \mathcal{T} . Since R_{se} does not possess any polarisation dependence, it is concluded that the factor R_{se} used in [73], to account for surface-diffracted waves, does not have any physical meaning.

Another method for solving the step discontinuity in the E-plane is the introduction of multiple-diffracted fields within the antenna system. These are depicted in Figure 5.5. Up to now, only the single-diffracted waves $SC \rightarrow Q_1 \rightarrow F$ and $SC \rightarrow Q_2 \rightarrow F$ were taken into account. It can be seen from Figure 5.5, that also the rays $SC \rightarrow Q_1 \rightarrow Q_2 \rightarrow F$ and $SC \rightarrow Q_2 \rightarrow Q_1 \rightarrow F$ may contribute to the received field at the feed. In general, an incident

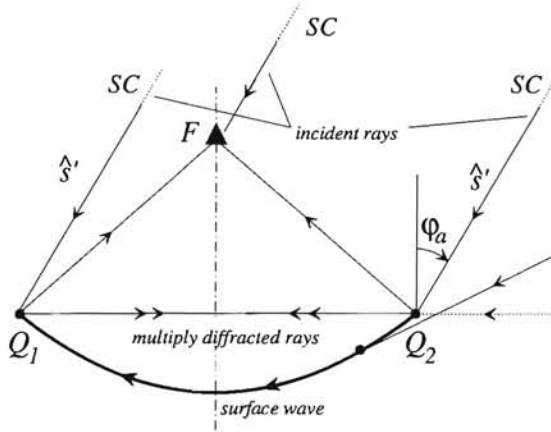


Figure 5.5: Introduction of multiple-diffracted rays within the antenna system. SC indicates the source position.

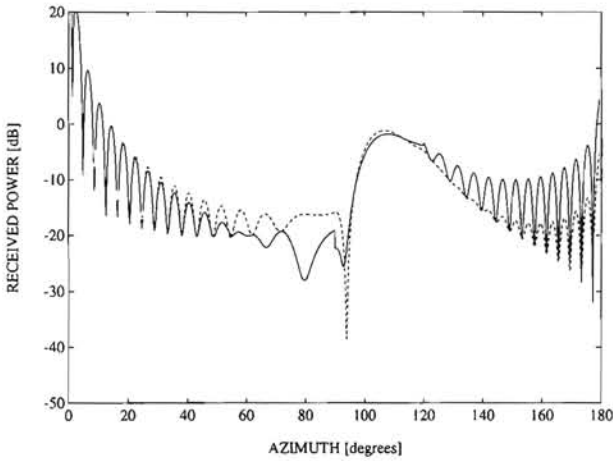


Figure 5.6: Receiving pattern of a parabolic reflector antenna as function of the azimuth angle φ_a ; shown are the E-plane pattern (—) and the H-plane pattern (---).

Data: $D_p = 15\lambda$, $f_p/D_p = 0.433$, $a = 0$, $m = 1$, $\varphi_e = 0$

ray excites a circular disk of diffracted rays at the diffraction point Q_i . One of these diffracted rays reaches F , while another diffracted ray reaches a point on the reflector rim, exactly diametrically opposite to the diffraction point Q_1 . In the present case ($\varphi_e=0$), this opposite point happens to be the second diffraction point Q_2 . The same is true for diffraction at Q_2 , where one of the diffracted rays reaches Q_1 .

The double-diffraction contribution is calculated by applying the procedure outlined in Section 2.5.3. Note that, unlike the inclusion of multiple-diffracted rays in the discussion concerning the rectangular block, the diffracted ray is not at grazing with any face of the reflector surface. Therefore there is no need for the inclusion of slope-diffracted fields. However, the incident field may be at grazing with the reflector surface, causing the procedure to find the reflected field parameters using equation (2.21) to be invalid.

If the double-diffraction contributions are included in the calculation of the receiving pattern of a parabolic reflector antenna, the step discontinuity at $\varphi_a = \pi/2$ in the E-plane disappears. Note that the H-plane pattern is unchanged by the inclusion of multiple-diffracted rays, as shown in Figure 5.7. This result can be compared with a result given in [73, Fig. 4-12], reprinted in this thesis in Figure 5.8. It is found that, despite the lack of physical basis, the factor R_{se} introduced in [73] gives reasonable results as compared to those obtained using the inclusion of multiple-diffracted rays. One major difference between both approaches is that the surface diffraction factor used in [73] modifies the E-plane pattern as well as the H-plane pattern. This is not the case if double-diffracted contributions are used; these only solve the step discontinuity in the E-plane receiving pattern, and leave the H-plane result unaffected.

To have more or less an average of the received field at the feed, the power sum of the received ray contributions is introduced (eq. (3.37)). Let the double-diffracted fields from $Q_{1,2}$ be denoted by $\vec{E}_{3,4}^d$, respectively. The total field at the feed is consequently given by

$$E_{V,H}^t(F) = \sum_{i=0}^{i=4} \epsilon_i G_f(\psi_{Q_i}) \vec{E}_i^d(F) \cdot \hat{e}_{polV,polH}(\psi_{Q_i}, \varphi_{Q_i}), \quad (5.20)$$

where co- and cross-polarisation components can be separated by choosing vertical (V) or horizontal (H) polarisation, respectively. It is found that $\epsilon_1 = \epsilon_3$, and $\epsilon_2 = \epsilon_4$.

The power sum $E_{V,H}^P$ is defined according to

$$\begin{aligned} E_{V,H}^P(F) = & \left[\epsilon_0 G_f(\psi_{Q_0}) \vec{E}_0^d(F) \cdot \hat{e}_{polV,polH}(\psi_{Q_0}, \varphi_{Q_0}) \right]^2 \\ & + \sum_{i=1}^2 \epsilon_i \left| G_f(\psi_{Q_i}) \vec{E}_i^d(F) \cdot \hat{e}_{polV,polH}(\psi_{Q_i}, \varphi_{Q_i}) \right. \\ & \left. + G_f(\psi_{Q_{i+2}}) \vec{E}_{i+2}^d(F) \cdot \hat{e}_{polV,polH}(\psi_{Q_{i+2}}, \varphi_{Q_{i+2}}) \right|^2 \Big]^{1/2}. \end{aligned} \quad (5.21)$$

A remark is that only the contributions with an independent phase behaviour may be added

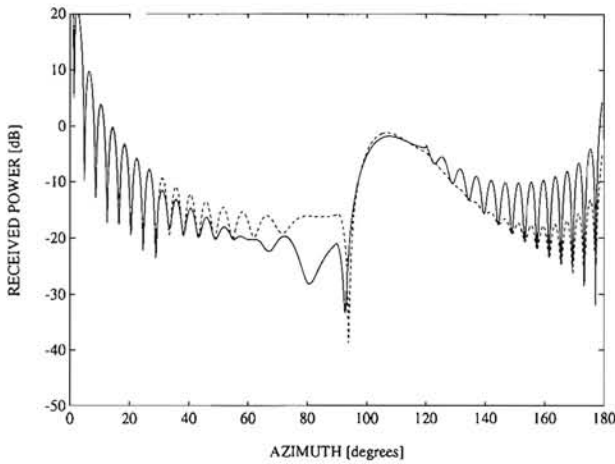


Figure 5.7: Receiving pattern of a parabolic reflector antenna as function of the azimuth angle φ_a , with double-diffraction contributions included; shown are the E-plane pattern (—) and the H-plane pattern (----).

Data: $D_p = 15\lambda$, $f_p/D_p = 0.433$, $a = 0$, $m = 1$, $\varphi_e = 0$

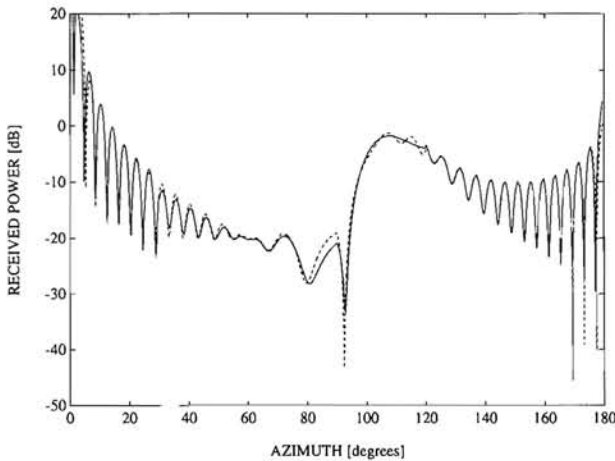


Figure 5.8: Comparison of the E-plane pattern of a parabolic reflector antenna as function of the azimuth angle φ_a ; shown are the result including double diffraction in receive mode (—), and the result using the factor R_{se} [73] in transmit mode (----).

Data: $D_p = 15\lambda$, $f_p/D_p = 0.433$, $a = 0$, $m = 1$, $\varphi_e = 0$

on a power basis. This means that single- and double-diffraction contributions which both enter the antenna system at Q_i may not be added on a power basis, because their phases do not vary independently. These two parts have a fixed phase dependence which is determined by the distance from the source to the diffraction point Q_i . In other words: *once inside the antenna system, the waves which enter the system at the same diffraction point need to be added on a (complex) vectorial basis.*

The polarisation-independent sum E^{PP} is the polarisation average of the power-sum as introduced in equation (5.21). It is given by

$$E^{PP}(F) = \left[|E_V^P(F)|^2 + |E_H^P(F)|^2 \right]^{1/2}. \quad (5.22)$$

Figure 5.9 is obtained for the received power at the feed due to an incident plane wave if the polarisation independent sum is used. The same parameters as in Figure 5.7 were employed.

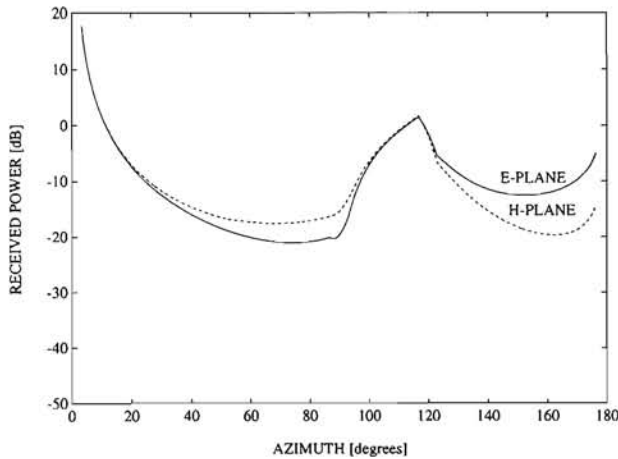


Figure 5.9: Receiving pattern of a parabolic reflector antenna as function of the azimuth angle φ_a , based on the power sum; shown are the E-plane (—) and the H-plane (---).

Data: $D_p = 15\lambda$, $f_p/D_p = 0.433$, $a = 0$, $m = 1$, $\varphi_e = 0$

5.2.3 Reception properties of a shielded parabolic reflector antenna

If the obstacle is present, the analysis of the receiving properties of the single reflector antenna changes slightly. The wave incident upon the receiving antenna is first diffracted at the obstacle edges. This diffraction causes that the diffraction points Q_i ($i = 1, 2$) at the reflector edge will not be diametrically opposite anymore.

To simplify the procedure to find the diffraction points, we make use of the $(\hat{e}_0, \hat{e}_{\pi/2}, \hat{e}_0 \times \hat{e}_{\pi/2})$ coordinate system to describe the edge of the reflector antenna. Attention will be paid only to the *left vertical edge* Γ_1 of the finite-width screen (Fig. 5.1), because the other vertical edge can be treated in the same way, and the procedure to treat the horizontal edge has been described in [3].

Because the incident field arrives from a direction parallel to the xy -plane, the diffraction point Q_{v1} on the edge Γ_1 is the projection from a (candidate) diffraction point L on the reflector edge. The point L is completely determined by φ . This means that Q_{v1} is determined by

$$\vec{Q}_{v1} = -d_1 \hat{y} + (\vec{L} \cdot \hat{z}) \hat{z}. \quad (5.23)$$

The term in braces is a function of φ_1 , φ_a and φ_e . The projection point Q_{v1} is a diffraction point if, and only if, Keller's law of edge diffraction is satisfied at the point L . At the vertical edge Keller's law is satisfied automatically. The location of the diffraction point on the reflector edge is determined by one coordinate only, i.e. φ , because φ_a and φ_e remain fixed. In general two solutions for the aperture angle φ_i are found from Keller's law, corresponding to diffraction points on either side of the reflector.

Note that, in the present geometry, the ray reaching the feed directly is also diffracted at Γ_1 at the point Q ,

$$\vec{Q} = -d_1 \hat{y} + (\vec{F} \cdot \hat{z}) \hat{z}. \quad (5.24)$$

A similar procedure involving projections can also be used to determine the diffraction points on the other edges $\Gamma_{2,3}$ of the finite-width screen. If only single-diffracted rays at the reflector edge are considered, this results in three diffracted rays for each obstacle edge, amounting to a nine-ray model for finite-width screen shielding. It is obvious that attention should be paid to blockage by the reflector. This is performed in exactly the same way as in the analysis of the unshielded geometry, and will not be repeated here. Note that for this case the elevation angle is not equal to zero; this causes that the expressions for the shadow indicators become more complex.

If the diffraction points on the reflector edge and their associated projections onto the edges $\Gamma_{1,2,3}$ are determined, the field strength calculation is nearly identical to the un-

shielded case. For the present geometry, however, attention has to be paid to the fact that the waves incident upon the antenna geometry do not have plane wavefronts, but rather cylindrical ones. This means that the changes in wave parameters $\hat{x}_{1,2,3}$ and $\rho_{1,2}$ have to be taken into account as the waves propagate from the diffraction points at the screen, towards the antenna, and into the feed at F . Obviously, the incident field at the diffraction points Q_i on the reflector edge is a diffracted field itself.

Paying attention to edge Γ_1 only, five contributions within the antenna system are incorporated in the analysis:

1. The 'direct' wave. This wave is diffracted at the edge of the finite-width screen, and reaches the feed directly. It may be obstructed by the reflector and is denoted by $\vec{E}_{0,1}^d$;
2. The 'single-diffracted' waves. These waves are diffracted at the obstacle edge, and subsequently diffracted at the reflector edge. The diffraction contribution incident at Q_1 may be obstructed by the reflector. These contributions are denoted by $\vec{E}_{1,2}^d$;
3. The 'double-diffracted' waves. These waves are diffracted at the obstacle edge, and are subsequently diffracted twice within the antenna system. The contribution of the wave which is inserted into the antenna system via diffraction point Q_1 has the same obstruction properties as the single-diffracted contribution which enters the antenna system via the same point. These double-diffracted contributions are denoted by $\vec{E}_{3,4}^d$.

It is obvious that 'direct', 'single-' and 'double-'diffracted primarily refer to the receiving antenna.

At the feed, the waves are weighted with the polarisation vector $\hat{e}_{polV,polH}$ and the radiation pattern G_f of the feed, as in the unshielded case. The total field arriving at F in the shielded case is found by addition of the weighted field contributions as defined in equation (5.20). The angles of incidence ($\psi_{Q_i}, \varphi_{Q_i}$) ($i = 0, 1, 2, 3, 4$) have to be determined from the parameters of the configuration under consideration, and will not be derived explicitly.

The following configuration for the calculation of the receiving pattern of a shielded reflector antenna is considered. The diameter $D_p = 100\lambda$, $f_p/D_p = 0.433$, $\varphi_e = \pi/9$, $x_M = 1000\lambda$, $z_M = 50\lambda$, and $z_{ob} = 200\lambda$. The feed parameters are $a=0.00316$ and $m=3.368$ corresponding to a relative edge illumination of -20 dB (Fig. 5.3). The incident field is a horizontally-polarised plane wave propagating into the x -direction. For a start, only the contributions from the *horizontal* edge Γ_3 are taken into account, i.e. $d_1 = d_2 = \infty$ [3]. In Figure 5.10 the result of this calculation is shown. It was found that some differences occur between a result in [3] and our results, only in the cross-polar pattern at an azimuth $\varphi_a = \pi/12$ and $\varphi_a = 7\pi/8$. Further investigations revealed that this is entirely due to the

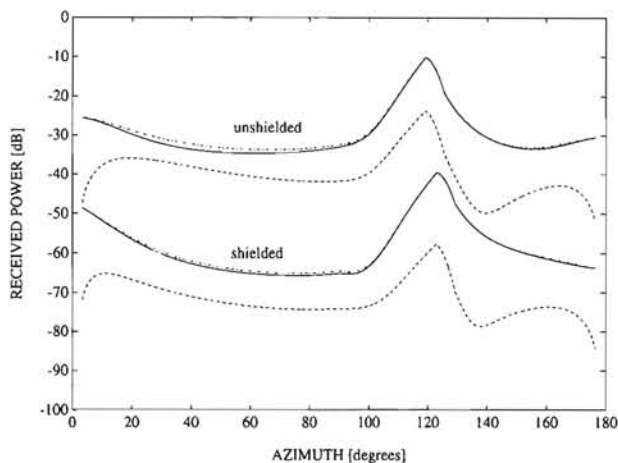


Figure 5.10: Receiving pattern of a large parabolic reflector antenna shielded by a half-plane, as function of the azimuth angle φ_a for horizontal polarisation; shown are the co- (—) and cross-polarised signal (---), based on the power sum, and a result of the polarisation independent sum (·-·-·-·).
 Data: $D_p = 100\lambda$, $f_p/D_p = 0.433$, $a = 0.00316$, $m = 3.368$, $\varphi_e = \pi/9$, $x_M = 1000\lambda$, $z_M = 50\lambda$, $z_{ob} = 200\lambda$, $d_1 = d_2 = \infty$

error in sign in the definition of $\hat{e}_{polV,polH}$ used in [3]. If in our algorithms the definition of [3] for $\hat{e}_{polV,polH}$ is used, identical results are obtained.

An SSF result that does include the contributions from the vertical edges is given in Figure 5.11, together with a result of half-plane shielding of the same antenna geometry. Again the polarisation independent sum has been used and the width of the obstacle is 150λ ($d_1 = d_2 = 75\lambda$).

If the calculations are based on the power sum, it is seen from Figure 5.11 that both results look very similar, apart from a major difference in SSF level. This is explained by the fact that for the finite-width screen geometry more energy ‘flows’ around the obstacle, hence the SSF is lower.

The SSF as function of the distance x_M and the azimuth angle φ_a is given in Figure 5.12. It is seen from this figure that the SSF curves become lower with increasing distance. Furthermore, they become more smooth as function of φ_a . The last phenomenon can readily be explained by the fact that the variations in gain for the individual contributions become lower with increasing distance, and so the fluctuations of the individual signals become less.

5.2.4 Conclusions

In this section attention was paid to the receiving properties of a parabolic reflector antenna with prescribed diameter, f_p/D_p ratio, and feed parameters. It was found that the inclusion of multiple-diffracted rays within the antenna system gives more or less the same results as obtained by application of the factor R_{se} as proposed in [73]. Multiple-diffraction contributions, however, have a more rigorous basis.

Also a model for the finite-width screen shielding of a parabolic reflector antenna was presented. If diffraction of the incident wave at the vertical edges $\Gamma_{1,2}$ is neglected, the configuration used in [3] can also be analysed. It was found that the signal level received behind the finite-width screen is higher compared to that received behind the half-plane. The derived SSF consequently is lower. Furthermore, it was found that the SSF curves as function of φ_a for the half-plane as well as the finite-width screen geometry have more or less the same shape. The SSF for the half-plane geometry is roughly 10 dB higher, however. Also SSF curves as function of φ_a at various distances x_M were presented for a reflector antenna shielded by a finite-width screen. These show that with increasing distance x_M the SSF curves become lower and more smooth as function of φ_a .

5.3 On the use of antenna weight functions in field-strength prediction and interference reduction

In most ray-based field-strength prediction models the spatial filtering at the antenna is introduced using the far-field method, i.e. a separate treatment of obstacle and reflector-edge diffraction. In this section¹ the near- and far-field approach are used to calculate the received EM field by a parabolic reflector antenna behind a finite-width screen to study explicitly the differences that can occur between the results from both methods. The effect of the atmosphere and ground in between the obstacle and antenna is neglected. It is shown that considerable differences between the results of both methods may exist, even for an obstacle-antenna separation large compared to the Rayleigh distance of the antenna, and both for a continuous wave (CW) and broadband analysis of the communications channel. It is concluded that the near-field method gives the best results and can be applied to many practical problems such as for interference reduction, and for searching the optimal position of VSATs in urban environments. Also for other types of antennas, results from

¹ Note: the major part of this section was already published: M.A.J. van de Griendt and G.A.J. van Dooren: *On the use of antenna weight functions in field strength prediction and interference reduction*, International Journal of Infrared and Millimeter Waves, vol. 14, no. 10, pp. 2233–2242, 1993.

the far-field approach may deviate considerably from those obtained using the near-field approach.

5.3.1 The antenna receiving pattern

The antenna used in both analyses is a parabolic reflector antenna with a circular aperture. The geometry of this antenna is illustrated in Figure 5.13. The reflector is described by

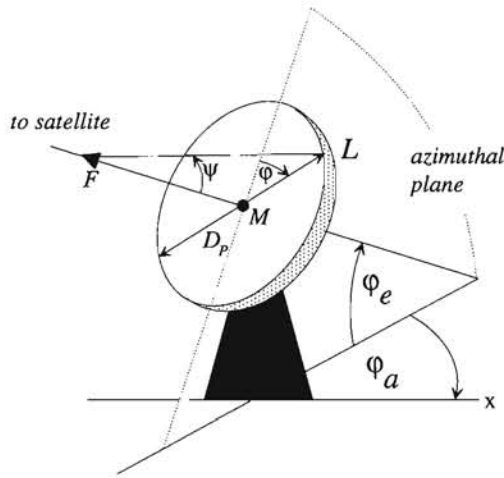


Figure 5.13: Geometry of the parabolic reflector antenna.

its diameter D_p and the focal distance f_p . The antenna orientation is determined by the azimuth and elevation angle φ_a and φ_e , respectively. A Huygens-source polarisation is used for the field radiated by the feed. Vertical and horizontal polarisation are distinguished, corresponding to a reflected field vector in the antenna aperture being parallel and perpendicular to the azimuthal plane, respectively. The far-field amplitude pattern G_f of the feed illuminating the reflector was defined in equation (5.4).

For a parabolic reflector antenna, the reception of radiation entering the system at large angles from boresight is determined mainly by feed spillover and reflector-edge diffraction. Besides a ray reaching the feed directly, it can be shown that only two points on the reflector edge give a first-order diffraction contribution to the received field for each off-axis incident wave. So, a three-ray model is adequate to describe the wide-angle reception of the parabolic antenna (Sec. 5.2). This three-ray model is used in the simulations, and reflector-blockage effects have also been taken into account. To describe the interaction of the incident wave with obstacle and reflector edges the UTD was employed [69].

The antenna geometry discussed was used to calculate the receiving antenna pattern, which equals the radiation pattern by reciprocity. The incident plane wave is assumed to travel into the x -direction. The E- and H-plane pattern of an antenna with diameter $D_p = 25\lambda$, focal distance to diameter ratio $f_p/D_p = 0.4$, and feed parameters $m = 2.415$ and $a = 0.00316$, is shown in Figure 5.14. These parameters correspond to a relative edge illumination of -20 dB and a forward gain of 10.6 dBi. The received field can be calculated

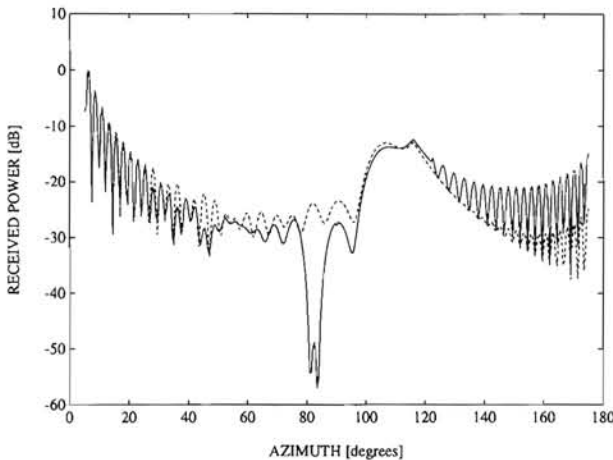


Figure 5.14: Receiving pattern of a parabolic reflector antenna as function of the azimuth angle φ_a ; shown are the E-plane pattern (—) and the H-plane pattern (---).

Data: $D_p = 25\lambda$, $f_p/D_p = 0.4$, $a = 0.00316$, $m = 2.415$, $\varphi_e = 0$

at any antenna orientation given by $0 < \varphi_a < \pi$ and $0 \leq \varphi_e \leq \pi/2$. The direction $\varphi_a = \varphi_e = 0$ and $\varphi_a = \pi$, $\varphi_e = 0$ are caustic directions, and consequently the model can not be used.

5.3.2 Near- and far-field simulations

By placing an obstacle in the signal propagation path, the amplitude of the interfering wave is attenuated. The shielded geometry used in the simulations is illustrated in Figure 5.1. It shows the antenna positioned behind a finite-width screen with its aperture centre M at $(x_M, 0, z_M)$. The finite-width screen has a height z_{ob} , and the vertical sides are at $y = -d_1$ and $y = d_2$. The screen is described by $x = 0$, $-d_1 \leq y \leq d_2$, $0 \leq z \leq z_{ob}$. The incident wave propagates parallel to the surface of the earth ($z = 0$) into the x -direction.

For interference reduction the placement of the obstacle is intentional. This is in contrast with the case where the incident wave is a desired signal. Then the obstacle obstruction is unintentional, and signal degradation will result. The latter situation can be found in urban areas with strong shadowing effects, where the user can not control the erection of new buildings and structures.

In the following, the antenna is assumed to be completely obstructed by the screen, but this is not strictly necessary. In the near-field approach each screen edge generates all of the rays used in the three-ray model, resulting in a total of nine rays reaching the feed.

In the far-field approach, however, each screen edge generates only one ray resulting in a total of three rays. These rays arrive at the aperture centre M and are then spatially weighted by the far-field antenna receiving pattern. A summation of the field contributions from the screen edges yields the total received field in both methods [69].

First, the results of the near- and far-field method for a half-plane obstacle ($d_1 = d_2 = \infty$) are examined. In this case only the horizontal edge Γ_3 contributes to the received field. This result is illustrated in Figure 5.15 as a function of antenna-obstacle distance x_M . The antenna used has the same geometry as the one used in Figure 5.14, and the position of the aperture centre M is given by $(x_M, 0, z_M)$, with $z_M = 25\lambda$. The screen has a height $z_{ob} = 300\lambda$. For a half-plane obstacle it can be seen from Figure 5.15 that the received fields in the near- and far-field approach do not differ much. A caustic is found at $x = 0.6R$; the antenna is then pointing directly towards the horizontal screen edge and UTD predicts infinitely strong fields.

The same simulation has been performed for a finite-width screen. In this case all three screen edges contribute to the total received field and $d_1 = d_2 = 100\lambda$ is used. The results of the near- and far-field method are illustrated in Figure 5.16. It is noted that the received field in the analysis using the finite-width screen is considerably higher than in the case of the half-plane obstacle. This is due to the fact that for a finite-width screen the incident wave 'flows' more easily around the obstacle, and hence the field strength is larger. Furthermore, the fluctuations of the received field behind the finite-width screen are more rapid than those behind the half-plane. This is mainly caused by the constructive and destructive interference of the edge contributions.

As is illustrated in Figure 5.16, differences of several dBs between the near- and far-field approach even occur at distances x_M much larger than the Rayleigh distance. Note that for practical applications using an antenna with a diameter of 50cm and a frequency of 10 GHz, a distance of $4R$ corresponds to about 65m. In urban environments, some obstacles will surely be located within this distance. A field-strength prediction method based on the representation of antennas by point receivers should be used with caution, not only in static

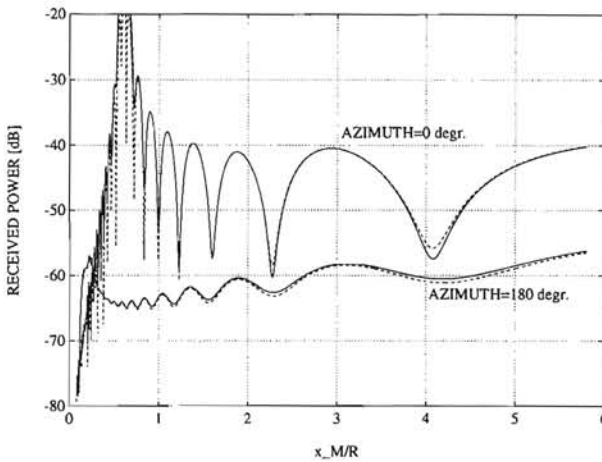


Figure 5.15: Received signal at a parabolic reflector antenna shielded by a half-plane as function of x_M ; shown are the results of the near-field method (—) and the far-field method (----).

Data: $D_p = 25\lambda$, $f_p/D_p = 0.4$, $a = 0.00316$, $m = 2.415$, $\varphi_e = \pi/9$, $z_M = 25\lambda$, $z_{ob} = 300\lambda$

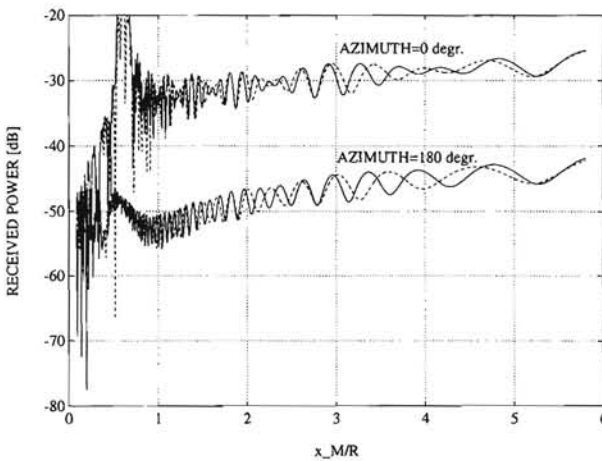


Figure 5.16: Received signal at a parabolic reflector antenna shielded by a finite-width screen as function of x_M ; shown are the results of the near-field method (—) and the far-field method (----).

Data: $D_p = 25\lambda$, $f_p/D_p = 0.4$, $a = 0.00316$, $m = 2.415$, $\varphi_e = \pi/9$, $z_M = 25\lambda$, $d_1 = d_2 = 100\lambda$, $z_{ob} = 300\lambda$

configurations (VSATs) but also in case of mobile terminals. It should be noted, however, that for mobile communications low frequencies are used (1.5 GHz), and the effect is not as explicit as in the examples shown here.

5.3.3 Broadband analysis

The analysis performed in the previous section is essentially a continuous wave (CW) analysis for one single frequency f_0 . In practice, the signal at the terminals of the receiving antenna will contain a large number of spectral components within the bandwidth B of the communications channel used. The average signal power \bar{P} at the antenna terminals is proportional to the average of the spectral power \bar{E}^2

$$\bar{P} \propto 10 \log \bar{E}^2, \quad (5.25)$$

where

$$\bar{E}^2 = \frac{1}{B} \int_{-\frac{B}{2}}^{+\frac{B}{2}} G_{filt}(f_0 + f) E(f_0 + f) E^*(f_0 + f) df, \quad (5.26)$$

and E is computed using either the near- or far-field method. The filter characteristic G_{filt} of the receiver front-end in this case was assumed to be given by $G_{filt} = 1$, and the carrier frequency f_0 was 10 GHz. The screen dimensions were $z_{ob} = 9m = 300\lambda$ and $d_1 = d_2 = 3m = 100\lambda$. The location of the aperture centre M was given by $(x_M, 0, z_M)$, with $z_M = 0.75m = 25\lambda$. The bandwidth B was 0.5 GHz, which is a typical value for satellite communications. The geometry and parameters used were identical to those as used for Figure 5.16. The result of the calculations is shown in Figure 5.17. A comparison of Figures 5.16 and 5.17 reveals that the average received power shows slower variations than the received power. This is completely due to the averaging effect in the calculation of \bar{E}^2 . The caustic at a distance of $x_M = 0.6R$ is still present. The differences between the near- and far-field method remain when performing a broadband analysis of the communication channel. The fact that both approaches predict results that still show variation even for very large distances x_M can be explained by the fact that the obstacle is in the far field of the antenna, but the *antenna* is *not* in the far field of the obstacle.

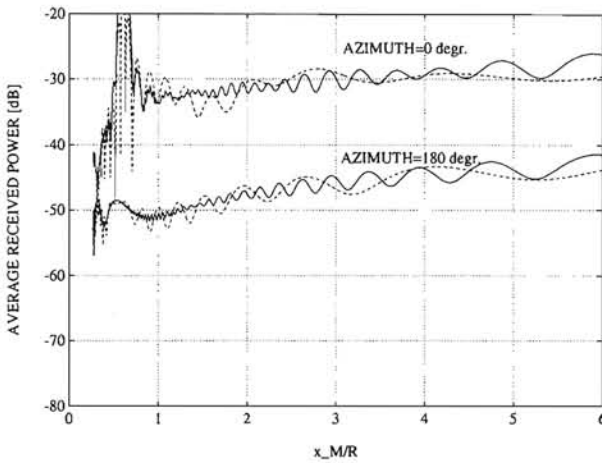


Figure 5.17: Average received signal at a parabolic reflector antenna shielded by a finite-width screen as function of x_M ; shown are the results of the near-field method (—) and the far-field method (-----).

Data: $D_p = 25\lambda$, $f_p/D_p = 0.4$, $a = 0.00316$, $m = 2.415$, $\varphi_e = \pi/9$, $z_M = 25\lambda$, $d_1 = d_2 = 100\lambda$, $z_{ob} = 300\lambda$, $f_0 = 10 \text{ GHz}$, $B = 0.5 \text{ GHz}$

5.3.4 Conclusions

It was shown that for the shielding of a parabolic reflector antenna by a finite-width screen considerable differences appear in the received field calculated by the near- and far-field approach at distances much larger than the Rayleigh distance R . From a theoretical point of view, the near-field approach as discussed in Section 5.2 is always correct, independent of the number of obstacle edges and the obstacle-antenna separation. The far-field method is only accurate, however, if one strong edge contribution is present, or if x_M is very large ($x_M \gg R$).

If limited accuracy and a speed-up of the calculations are of interest, the use of a one-dimensional table containing the spatial antenna weight factors of a symmetric far-field antenna pattern could make the far-field approach much faster than the near-field approach. This simplified far-field approach and the near-field approach will give considerable differences, especially if multiple obstacle edges are considered. The exact calculation of the weight factors of the non-symmetrical antenna receiving pattern in the far-field approach increases the accuracy as well as the calculation time. The CPU time needed for the far-field approach then becomes comparable to that of the near-field approach. To obtain best

accuracy the near-field method should be used.

If the number of obstacles is very large then the use of the near-field approach is impractical because of the huge amount of CPU time needed. The far-field approach is then the only method tractable for implementation. The results obtained must, however, be evaluated bearing in mind the possible inaccuracies introduced by the considerable simplifications present in the far-field approach.

The model proposed can effectively be used for site shielding analyses, but also for the prediction of the receiving performance of VSAT terminals in built-up areas. Note that the near-field problem itself does not only arise for a reflector antenna, but also in mobile communications, for example, where antennas are mounted on a conducting ground plane such as the roof of a car. In this case the ground plane will influence the receiving properties of the antenna, and consequently differences between a far- and near-field analysis may arise in predicting the coverage of the mobile communications system.

5.4 Shielding of a double-reflector antenna

In this section the positions of the diffraction points on the reflector edges of a Cassegrain antenna system are calculated. Therefore, this section merely supports Sections 5.5 and 5.6, because there this information is omitted.

The site shielding geometry for the Cassegrain antenna system is shown in Figure 5.18. The geometry is described in a Cartesian (x, y, z) coordinate system, and the earth's surface

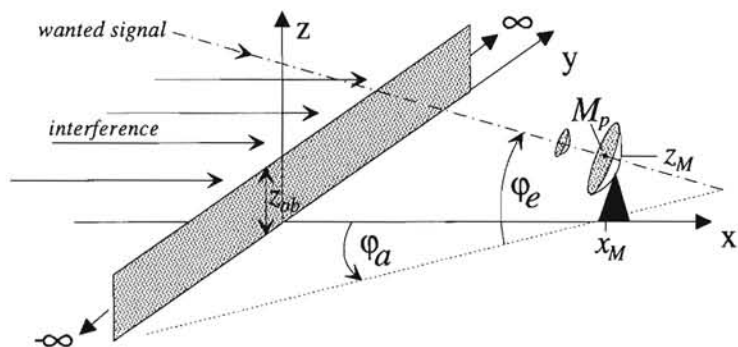


Figure 5.18: Cassegrain antenna geometry and half-plane obstacle; $z = 0$ is the ground plane.

is given by the plane $z = 0$. The obstacle is defined by $x = 0$, $0 \leq z \leq z_{ob}$, where z_{ob} is the obstacle height.

The unwanted wave, caused by some distant source, is incident upon the obstacle from a direction parallel to the xy -plane, and propagates into the x -direction. The wanted wave is coming from a satellite, and is assumed to be unaffected by the obstacle. Since this signal is received via the main lobe of the receiving terminal, the satellite position determines the azimuth (φ_a) and the elevation angle (φ_e). Note that the angles φ_a and φ_e refer to the antenna aperture centre M_p with Cartesian coordinates $(x_M, 0, z_M)$, $(x_M, z_M > 0)$. The height difference $\Delta z = z_{ob} - z_M$ is such that the whole antenna is in the shadow of the obstacle in the half-space $x > 0$. In this way, no specific point on the reflector edge is illuminated directly by the interfering wave.

First, we focus on the receiving properties of the double-reflector system in the absence of the shielding obstacle. To this end, we will outline an approach to find the diffraction points on the reflector edges. This approach is used in Sections 5.5 and 5.6 to calculate the E- and H-plane radiation (receiving) pattern of a Cassegrain reflector antenna. Subsequently, we will treat the case where the obstacle is present. This requires a modification of the ray-tracing procedure, but the analysis is more or less unchanged. Nearly the same geometry was analysed in Section 5.2 for the shielding of a parabolic reflector antenna.

5.4.1 Description of the receiving antenna

The Cassegrain antenna consists of a paraboloidal main-reflector and a hyperboloidal sub-reflector; a cross-section through the antenna system is shown in Figure 5.19. The symmetry axes of both bodies of revolution coincide, and the second focus $F_{h,2}$ of the hyperboloid coincides with the focus F_p of the paraboloid. The antenna system makes use of the focusing properties of the paraboloid in combination with a hyperboloid. A source placed at the first focus of the hyperboloid $F_{h,1}$ illuminates the sub-reflector and the reflected wave seems to emanate from $F_{h,2}$. The spherical wavefront of the incident wave is transformed into the spherical wavefront of the reflected wave. This reflected wave illuminates the paraboloidal main-reflector. The latter transforms the spherical incident wavefront into a plane wavefront in the main-reflector aperture via reflection. The point M_p is a centre of rotation for changes in the azimuth φ_a and elevation φ_e angle. The antenna feed is located at $F_{h,1}$.

Both the main- and sub-reflector are described in a spherical (ρ, ψ, φ) coordinate system with the origin at F_p . It is seen from Figure 5.19 that three angles determine the contours of the antenna system. These angles are α_0 , which is the subtended angle of the sub-reflector

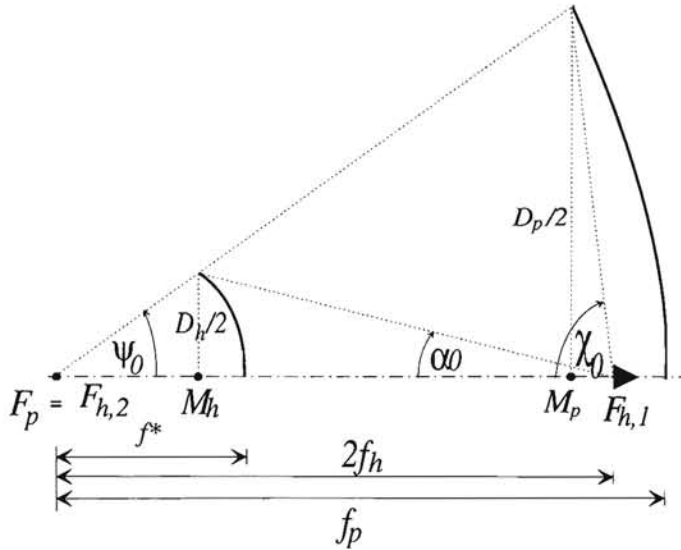


Figure 5.19: Cross-section through the Cassegrain antenna geometry; only the upper half is shown.

as seen from $F_{h,1}$, χ_0 , which is the subtended angle of the main-reflector as with respect to $F_{h,1}$, and ψ_0 , which is the subtended angle from the main-reflector with respect to $F_{h,2} = F_p$. For the configurations considered in this thesis the angle ψ_0 is also the subtended angle of the sub-reflector with respect to F_p .

Since both the paraboloid and the hyperboloid are quadric surfaces, we can define them with by a single expression. This expression is given by

$$\rho = \frac{(1+e)C}{1+e \cos \psi}, \quad (5.27)$$

where $e = 1$ for the paraboloid and $1 < e < \infty$ for the hyperboloid; C is the distance from F_p to the intersection of the body of revolution with its symmetry axis. For the paraboloid $C = f_p$. For the hyperboloid we refer to this distance as the effective focal length f^* , so $C = f^*$. The focal distance of the hyperboloid is given by $2f_h$. We denote the diameter of the main-reflector with D_p and the diameter of the sub-reflector with D_h .

We find the subtended angle ψ_0 of the main-reflector according to

$$\psi_0 = 2 \arctan \frac{D_p}{4f_p}. \quad (5.28)$$

The distance between the focus F_p and the aperture centre M_p is denoted by fm and is

given by

$$fm = f_p - \frac{D_p^2}{16f_p}. \quad (5.29)$$

The relation between the subtended angle of the sub-reflector α_0 and the angle ψ_0 is given by

$$(e + 1) \tan \frac{\alpha_0}{2} = (e - 1) \tan \frac{\psi_0}{2}, \quad (5.30)$$

where e is the eccentricity of the hyperboloid. The distance of the sub-reflector aperture centre M_h to F_p is denoted by $m_h f$ and is given by

$$m_h f = \frac{D_h}{2 \tan \psi_0}, \quad (5.31)$$

whereas the separation between both aperture planes is denoted by mm_h , which is given by

$$mm_h = |\vec{M}_p - \vec{M}_h| = fm - m_h f, \quad (5.32)$$

where \vec{M}_h and \vec{M}_p are the position vectors of the aperture centres of the sub- and main-reflector, respectively. An expression for the angle α_0 as a function of D_h and e is given by

$$\alpha_0 = 2 \arctan \left(\frac{(e - 1)}{(e + 1)} \tan \frac{\psi_0}{2} \right) = \arctan \frac{D_h}{2(2f_h - m_h f)}. \quad (5.33)$$

A relation between f_p , α_0 and D_p is

$$e = \frac{D_p + 4f_p \tan(\alpha_0/2)}{D_p - 4f_p \tan(\alpha_0/2)}, \quad (5.34)$$

whereas an expression for the effective focal length f^* is given by [74]

$$f^* = \frac{D_h(1 + e \cos \psi_0)}{2(1 + e) \sin \psi_0}. \quad (5.35)$$

The angle χ_0 is easily found as

$$\chi_0 = \arctan \frac{D_p}{2(2f_h - fm)}. \quad (5.36)$$

An important parameter in the antenna model is the amplitude taper across the sub-reflector. This taper is determined by the power of the cosine m in the feed model, as discussed in equation (5.4). Note that, in practice, the subtended angle of the sub-reflector is much smaller than that of the main-reflector ($\alpha_0 \ll \psi_0$). To have a reasonable taper across the sub-reflector (10-15 dB) a much higher value of m is needed (Fig. 5.3). Commonly used values of m in a Cassegrain geometry are 30-50. The feed placed at $F_{h,1}$ has a Huygens

source polarisation denoted by $\hat{e}_{polV,polH}$, which is either horizontal or vertical. It will be defined shortly.

To describe the antenna rim, we make use of the aperture unit vectors $(\hat{e}_0, \hat{e}_{\pi/2}, \hat{e}_0 \times \hat{e}_{\pi/2})$. These vectors are defined in equation (5.7). The equation for the sub- and main-reflector rim are given by

$$\vec{L}_h = \vec{M}_h + \hat{n}_e D_h/2 = \vec{M}_h + (\cos \varphi \hat{e}_0 + \sin \varphi \hat{e}_{\pi/2}) D_h/2, \quad (5.37)$$

and

$$\vec{L}_p = \vec{M}_p + \hat{n}_e D_p/2 = \vec{M}_p + (\cos \varphi \hat{e}_0 + \sin \varphi \hat{e}_{\pi/2}) D_p/2, \quad (5.38)$$

respectively, and $0 \leq \varphi \leq 2\pi$. The unit vector \hat{n}_e in the aperture plane and normal to the antenna rim is given by

$$\hat{n}_e = \cos \varphi \hat{e}_0 + \sin \varphi \hat{e}_{\pi/2}. \quad (5.39)$$

The radius of curvature of the antenna edge in the aperture plane $a_{eh,ep}$ is equal to the radius of the circular aperture rim $a_{eh} = D_h/2$ and $a_{ep} = D_p/2$.

A point L on the main- or sub-reflector edge is completely determined by its aperture angle φ and the azimuth and elevation angle. Since the latter are defined by the orientation of the antenna, a point on a reflector rim is a function of one variable only, namely the aperture angle φ . At L we introduce the surface triplet $\hat{x}_{1,2,3}^\Sigma$ and corresponding radii of curvature $\rho_{1,2}^\Sigma$. For points L on the main-reflector, these parameters were already defined in equation (5.8). For points L on the sub-reflector, these parameters are given by

$$\begin{aligned} \hat{x}_1^\Sigma &= \sin \varphi \hat{e}_0 - \cos \varphi \hat{e}_{\pi/2}, \\ \hat{x}_2^\Sigma &= \cos \left(\frac{\psi - \alpha_0}{2} \right) \hat{n}_e - \sin \left(\frac{\psi - \alpha_0}{2} \right) (\hat{e}_0 \times \hat{e}_{\pi/2}), \\ \hat{x}_3^\Sigma &= \sin \left(\frac{\psi - \alpha_0}{2} \right) \hat{n}_e + \cos \left(\frac{\psi - \alpha_0}{2} \right) (\hat{e}_0 \times \hat{e}_{\pi/2}), \\ \rho_1^\Sigma &= f^*(1+e) \left[1 + \frac{e^2 \sin^2 \psi}{(1+e \cos \psi)^2} \right]^{1/2}, \\ \rho_2^\Sigma &= f^*(1+e) \left[1 + \frac{e^2 \sin^2 \psi}{(1+e \cos \psi)^2} \right]^{3/2}. \end{aligned} \quad (5.40)$$

For convenience, we introduce the concept of the *equivalent parabola*. This concept expresses that for each double-reflector system there exists an equivalent single-reflector system with an identical aperture-field distribution. An important parameter in the definition of the equivalent parabola is the eccentricity e of the sub-reflector. Given a double-reflector system with prescribed D_h , D_p , f_p and e , we can define the equivalent parabola as having a diameter D_p and a focal distance f_e of

$$f_e = \left(\frac{e+1}{e-1} \right) f_p. \quad (5.41)$$

Since the interfering signal will usually be received by some sidelobe of the antenna receiving pattern, we will first focus on the determination of the diffraction points on the reflector edges. This information is used in Sections 5.5 and 5.6 to calculate the E- and H-plane receiving patterns of the Cassegrain antenna.

5.4.2 Wide-angle reception of a Cassegrain antenna

Before we are able to calculate the individual field contributions at the feed, we need to know which points on the reflector edges give rise to the main contributions at the feed point $F_{h,1}$. These points are called diffraction points, and their location can be found by applying Keller's law of edge diffraction (eq. (2.40)). Since a Cassegrain antenna has two reflectors, we will focus on these reflectors separately.

The procedure to find the diffraction points on the sub-reflector is quite simple, and shows much similarity with that used to find the diffraction points on the edge of the single-reflector antenna (Sec. 5.2). First, we need the direction of propagation of the incident wave. We denote this direction by \hat{s}' and consider the case where $\hat{s}' = \hat{x}$ (Fig. 5.18). Further we need the unit vector \hat{e}_h tangent to the sub-reflector edge. Since the orientation of \hat{e}_h is not important, we take $\hat{e}_h = \hat{x}_1^\Sigma$, defined at some candidate diffraction point $Q_{sub,i}$ ($i = 1, 2, 3, \dots$) on the sub-reflector edge. This point $Q_{sub,i}$ is completely defined by its aperture angle $\varphi_{sub,i}$. The direction of propagation of the diffracted wave is denoted by $\hat{s}_{h,i}$ and is given by

$$\hat{s}_{h,i} = \frac{\vec{F}_{h,1} - \vec{Q}_{sub,i}}{|\vec{F}_{h,1} - \vec{Q}_{sub,i}|}. \quad (5.42)$$

The coordinates of the diffraction points $Q_{sub,i}$ are found by applying Keller's law of edge diffraction at the point $Q_{sub,i}$ to \hat{s}' , $\hat{s}_{h,i}$ and \hat{e}_h . Equation (2.40), i.e. Keller's law of edge diffraction, can be numerically solved with a one dimensional root-finding procedure. We find two solutions $\varphi_{sub,i}$ ($i = 1, 2$), which specify two diffraction points $Q_{sub,i}$. It is found that $0 \leq \varphi_{sub,1} \leq \pi$ and $\pi \leq \varphi_{sub,2} \leq 2\pi$, which correspond to diffraction points $Q_{sub,i}$ on the left and right part of the sub-reflector edge, respectively. For $\varphi_e = 0$, the diffraction points $Q_{sub,i}$ are exactly diametrically opposite, so $\varphi_{sub,2} = \varphi_{sub,1} + \pi$. At both points we introduce the surface parameters $\hat{x}_{1,2,3}^\Sigma$ and $\rho_{1,2}^\Sigma$ as introduced in equation (5.40). These surface parameters are needed in the calculation of the diffraction contributions at the feed point $F_{h,1}$.

The locations of the diffraction points on the main-reflector are found in a similar way. Now we use unit vector \hat{e}_p tangent to the main-reflector edge. Since the orientation of \hat{e}_p is not important, we take $\hat{e}_p = \hat{x}_1^\Sigma$, defined at some (candidate) diffraction point $Q_{main,i}$ ($i = 1, 2, 3, \dots$) on the main-reflector edge. This point $Q_{main,i}$ is completely defined by its

aperture angle $\varphi_{main,i}$. The direction of propagation of the diffracted wave is denoted by $\hat{s}_{p,i}$ and is given by

$$\hat{s}_{p,i} = \frac{\vec{F}_{h,1} - \vec{Q}_{main,i}}{|\vec{F}_{h,1} - \vec{Q}_{main,i}|}. \quad (5.43)$$

The angles $\varphi_{main,i}$ that correspond to the diffraction points $Q_{main,i}$ are found by applying Keller's law of edge diffraction at the point $Q_{main,i}$ to \hat{s}' , $\hat{s}_{p,i}$ and \hat{e}_p . We find two solutions $\varphi_{main,i}$ ($i = 1, 2$), which specify two diffraction points $Q_{main,i}$. Furthermore, $0 \leq \varphi_{main,1} \leq \pi$ and $\pi \leq \varphi_{main,2} \leq 2\pi$, which correspond to diffraction points $Q_{main,i}$ on the left and right part of the main-reflector edge, respectively. At both of these points we introduce the surface parameters $\hat{x}_{1,2,3}^\Sigma$ and $\rho_{1,2}^\Sigma$ as introduced in equation (5.8). We will need these surface parameters in the calculation of the diffraction contributions at the feed point $F_{h,1}$. Also here the diffraction points are diametrically opposite, so $\varphi_{main,2} = \varphi_{main,1} + \pi$ ($\varphi_e = 0$). Diffraction points that are diametrically opposite are found only for incident plane waves.

It may seem that this completes the ray tracing needed to determine the diffraction points. This is not true, however, because the Cassegrain antenna system requires a higher-order diffraction analysis. This means that also higher-order diffraction contributions need to be taken into account. The reason for this is that the feed model used is such that there can be a trade-off between diffraction loss and feed gain. An example of this is that a wave may be subject to double diffraction, but its angle of incidence with respect to the symmetry axis is very small. Because the feed is quite directive, the difference in feed gain for a ray arriving at, for example, α_0 and a smaller angle can be quite substantial. So, despite the fact that the wave is subject to double diffraction, part of its diffraction loss at the reflector edges is compensated for by a high gain of the feed.

Since higher-order diffraction contributions are incorporated in the analysis, we first make an ordered list of these types of diffraction contributions. We find the following field contributions within the antenna system, ordered with a descending importance with respect to the incident wave of order k^0 :

1. The single-diffracted ray of order $k^{-1/2}$;
2. The ray that is single diffracted and single reflected of order $k^{-1/2}$;
3. The ray that is single diffracted and double reflected of order $k^{-1/2}$;
4. The ray that is double diffracted of order k^{-1} ;
5. The ray that is double diffracted and single reflected of order k^{-1} ;
6. The ray that is double diffracted and double reflected of order k^{-1} .

For notational simplicity, the orders of the diffracted waves are given only for positions of the observation point outside the transition regions. Inside this region the order is lowered, as discussed in Chapter 2.

To simplify the ray-tracing procedure, we define four points on the sub- and main-reflector edge, as indicated in Figure 5.20. In this figure we have introduced the points

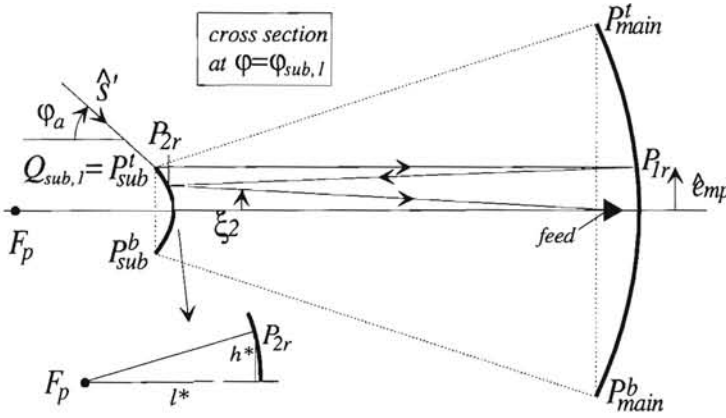


Figure 5.20: Introduction of diffraction and reflection points in the Cassegrain reflector antenna; a cross-section through the antenna system at $\varphi = \varphi_{sub,1}$. A detail from the sub-reflector is also shown.

$P_{sub}^{t,b}$ and $P_{main}^{t,b}$ that are part of a trapeze. This trapeze is found by making a cross-section through the Cassegrain reflector antenna at the angle $\varphi = \varphi_{main,i}$ or $\varphi = \varphi_{sub,i}$ ($i = 1, 2$), and connecting the points on the reflector edges. This implies that four cross-sections can be made to find the points of interest $P_{sub}^{t,b}$ and $P_{main}^{t,b}$. Also reflection points $P_{1r,2r}$ on the main- and sub-reflector are indicated in Figure 5.20.

Each wave that enters the antenna system via $Q_{sub,1} = P_{sub}^t$ excites a number of diffracted waves. The points on the sub- and main-reflector of importance for the ray-tracing procedure are given by

$$\begin{aligned}\vec{P}_{sub}^t &= \vec{Q}_{sub,1} = \vec{M}_h + \hat{e}_{mp} D_h / 2, \\ \vec{P}_{sub}^b &= \vec{M}_h - \hat{e}_{mp} D_h / 2, \\ \vec{P}_{main}^t &= \vec{M}_p + \hat{e}_{mp} D_p / 2, \\ \vec{P}_{main}^b &= \vec{M}_p - \hat{e}_{mp} D_p / 2,\end{aligned}\quad (5.44)$$

where we have introduced

$$\hat{e}_{mp} = \cos \varphi_{sub,1} \hat{e}_0 + \sin \varphi_{sub,1} \hat{e}_{\pi/2}. \quad (5.45)$$

The reflection points $P_{1r,2r}$ are given by

$$\begin{aligned}\vec{P}_{1r} &= \vec{M}_p + \left(fm - \frac{D_h}{2 \tan \xi_1} \right) (\hat{e}_0 \times \hat{e}_{\pi/2}) + \frac{D_h}{2} \hat{e}_{mp}, \\ \vec{P}_{2r} &= \vec{M}_h + (fm - l^*) (\hat{e}_0 \times \hat{e}_{\pi/2}) + h^* \hat{e}_{mp},\end{aligned}\quad (5.46)$$

Here

$$h^* = \frac{\sin \xi_1 (1 + e) f^*}{1 + e \cos \xi_1}, \quad (5.47)$$

and

$$l^* = \frac{\cos \xi_1 (1 + e) f^*}{1 + e \cos \xi_1}. \quad (5.48)$$

where

$$\xi_1 = 2 \arctan \frac{D_h}{4f_p}. \quad (5.49)$$

The angle ξ_2 is found from

$$\xi_2 = 2 \arctan \left[\frac{(e - 1) D_h}{4(e + 1) f_p} \right]. \quad (5.50)$$

We can distinguish the following types of diffracted waves within the antenna system:

1. the single-diffracted wave: this wave is diffracted at P_{sub}^t . This diffraction contribution is denoted by \vec{E}_1^S , and it is of order $k^{-1/2}$;
2. the single-diffracted and double-reflected wave: this wave is diffracted at P_{sub}^t , reflected at P_{1r} and reflected at P_{2r} . Note that this contribution arrives at a very small angle ξ_2 with the symmetry axis of the antenna. Therefore the feed gain for this contribution will be large. The diffraction contribution is denoted by \vec{E}_1^{SRR} , and it is of order $k^{-1/2}$;
3. the double-diffracted wave: this wave is diffracted at P_{sub}^t and P_{sub}^b , or at P_{sub}^t and P_{main}^t . These diffraction contributions are denoted by \vec{E}_1^{SS} and \vec{E}_1^{SM} , respectively, and they are of order k^{-1} ;
4. the double-diffracted and double-reflected wave: this wave is diffracted at P_{sub}^t and P_{sub}^b , and is subsequently reflected at P_{1r} and P_{2r} . Its diffraction contribution is denoted by \vec{E}_1^{SSRR} . Also for this contribution the angle of arrival ξ_2 is very small. It is of order k^{-1} .

For notational simplicity, the orders of the diffracted waves are given only for positions of the observation point outside the transition regions. Inside this region the order is lowered, as discussed in Chapter 2. Furthermore, some simplifications occur in the calculations of the diffraction coefficients at the points $Q_{sub,i}$ ($i = 1, 2$) because the exterior wedge angle

is 2π , and the incident wave has a plane wavefront. These simplifications were already discussed in Section 5.2, and will not be repeated here.

Note that similar diffraction contributions are found that enter the antenna system at $Q_{sub,2}$. These have a subscript 2, and are found in a similar way as those for the case of $Q_{sub,1}$. Therefore they will not be given here.

Now that we have found the positions of the diffraction points on the sub-reflector edge, the analysis proceeds as follows. We make a cross-section through the antenna at an angle $\varphi = \varphi_{main,1}$, as shown in Figure 5.21. The points that are of importance for the ray-tracing

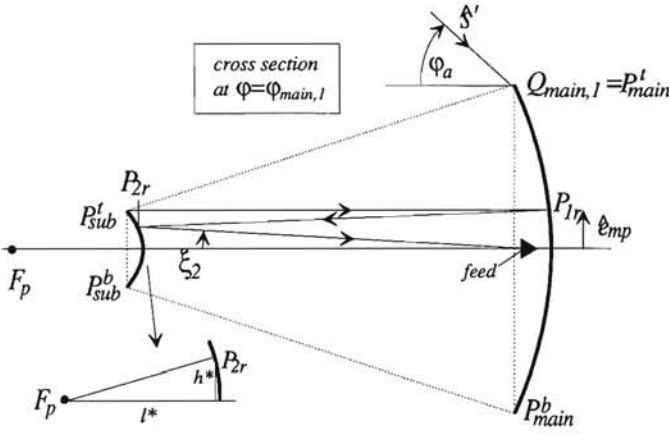


Figure 5.21: Introduction of diffraction and reflection points in the double-reflector antenna. Cross section through antenna system at $\varphi = \varphi_{main,1}$.

procedure are given by

$$\begin{aligned}\vec{P}_{sub}^t &= \vec{M}_h + \hat{e}_{mp} D_h / 2, \\ \vec{P}_{sub}^b &= \vec{M}_h - \hat{e}_{mp} D_h / 2, \\ \vec{P}_{main}^t &= \vec{Q}_{main,1} = \vec{M}_p + \hat{e}_{mp} D_p / 2, \\ \vec{P}_{main}^b &= \vec{M}_p - \hat{e}_{mp} D_p / 2,\end{aligned}\quad (5.51)$$

where we have introduced

$$\hat{e}_{mp} = \cos \varphi_{main,1} \hat{e}_0 + \sin \varphi_{main,1} \hat{e}_{\pi/2}. \quad (5.52)$$

The reflection points $P_{1r,2r}$ given by

$$\begin{aligned}\vec{P}_{1r} &= \vec{M}_p + \left(fm - \frac{D_h}{2 \tan \xi_1} \right) (\hat{e}_0 \times \hat{e}_{\pi/2}) + \frac{D_h}{2} \hat{e}_{mp}, \\ \vec{P}_{2r} &= \vec{M}_h + (fm - l^*) (\hat{e}_0 \times \hat{e}_{\pi/2}) + h^* \hat{e}_{mp}.\end{aligned}\quad (5.53)$$

Now that the diffraction paths within the antenna system are known, we can identify the diffraction contributions that enter the antenna system via P_{main}^t :

1. the single-diffracted wave: this wave is diffracted at the point P_{main}^t and is denoted by \vec{E}_1^M . It is of order $k^{-1/2}$;
2. the single-diffracted and single-reflected wave: this wave is diffracted at the point P_{main}^t and is reflected at the point P_{sub}^t . The diffraction contribution of this wave is denoted by \vec{E}_1^{MR} , and it is of order $k^{-1/2}$;
3. the double-diffracted wave: this wave is diffracted at P_{main}^t and P_{main}^b , or at the points P_{main}^t and P_{sub}^t . The diffraction contributions of these waves are denoted by \vec{E}_1^{MM} and \vec{E}_1^{MS} , respectively, and they are of order k^{-1} ;
4. the double-diffracted and double-reflected wave: this wave is diffracted at P_{main}^t and P_{sub}^t , reflected at P_{1r} and reflected at P_{2r} . Note that this contribution arrives at a very small angle ξ_2 with the symmetry axis of the antenna. Therefore, the feed gain for this contribution will be large. The diffraction contributions are denoted by \vec{E}_1^{MSRR} , and it is of order k^{-1} .

Again, the orders of the diffracted waves are given only for positions of the observation point outside the transition regions. Inside this region the order is lowered, as discussed in Chapter 2. Also for these contributions some simplifications occur in the calculations of the diffraction coefficients; the exterior wedge angle is 2π , and the incident wave at the points $Q_{main,i}$ has a plane wavefront. These simplifications were already discussed in Section 5.2, and will not be repeated here.

This concludes the description of the diffracted wave contributions which are excited at the diffraction point $Q_{main,1}$. Similar contributions are excited at $Q_{main,2}$. These will have a subscript 2, but will not be given here.

In addition to the diffracted rays within the antenna system, there is also a ray that reaches the feed directly. Its contribution is calculated using standard GO techniques, and it is denoted by \vec{E}^{DIR} . Because the direct wave is the same as the incident wave, it is of order k^0 , with respect to the incident wave of order k^0 . Adding up the rays within the antenna system we find a total of $1 + (4 \cdot 5) = 21$ field contributions. These contributions are weighted in amplitude and polarisation by the feed radiation (receiving) pattern.

Before we come to an expression of the total field $E_{V,H}^t$ at the feed, we first discuss the obstruction properties of the Cassegrain system. For particular orientations of the antenna system, it is possible that ray obstruction takes place. Since we have four diffraction points ($Q_{sub,i}, Q_{main,i}, i = 1, 2$) where higher-order diffraction contributions are excited, and one

direct ray, five shadow indicators $\epsilon_{dir}, \epsilon_{sub,i}, \epsilon_{main,i}$ ($i = 1, 2$) are used to account for blockage effects. In the following we restrict our attention to the special case $\varphi_e = 0$, which is the value used for the calculation of the E- and H-plane receiving pattern. Now the angle ψ corresponds to the azimuth angle φ_a . For arbitrary positions of the Cassegrain antenna another analysis should be carried out [74].

It is obvious that diffraction contributions that are excited at a certain diffraction point $Q_{sub,i}$ or $Q_{main,i}$ automatically inherit the blockage properties of these diffraction points. The feed and its properties are defined in spherical (r, Ψ, Φ) coordinate system with the origin at $F_{h,1}$ and the direction $\Psi = 0$ corresponds to the forward direction of the antenna. The polar axis coincides with the symmetry axis of the antenna system. For points on the sub-reflector $\Psi = \alpha_0$, while for points on the main-reflector $\Psi = \chi_0$. For $\varphi_e = 0$, as used in the calculation of the E- and H-plane receiving pattern, it is found that

$$\varphi_{sub,1} = \varphi_{main,1} = \Phi_{sub,2} = \Phi_{main,2} = \pi/2, \quad (5.54)$$

and

$$\varphi_{sub,2} = \varphi_{main,2} = \Phi_{sub,1} = \Phi_{main,1} = 3\pi/2. \quad (5.55)$$

We will restrict our attention to $0 \leq \varphi_a = \Psi \leq \pi$ for reasons of symmetry. The regions of obstruction for the diffraction points $Q_{sub,i}$ and $Q_{main,i}$ are shown in Figure 5.22. We find the following definitions of the shadow indicators ϵ for the feed position and the diffraction points $Q_{sub,i}$ and $Q_{main,i}$ ($i = 1, 2$):

1. The direct ray is obstructed for $0 < \varphi_a < \alpha_0$ and $\chi_0 < \varphi_a < \pi$. This is expressed by

$$\epsilon_{dir} = \begin{cases} 1, & \text{for } \alpha_0 < \varphi_a < \chi_0, \\ 0, & \text{elsewhere.} \end{cases} \quad (5.56)$$

2. The first diffraction point $Q_{sub,1}$ on the sub-reflector is obstructed by the sub-reflector for $\pi/2 < \varphi_a < (\pi + \psi_0 - \alpha_0)/2$. It is also blocked by the main-reflector for $\varphi_a > \Psi_1 = \arctan((D_p + D_h)/(2mm_h))$. It is well possible that $\Psi_1 < (\pi + \psi_0 - \alpha_0)/2$, indicating that for $\varphi_a > \pi/2$ the first diffraction point $Q_{sub,1}$ is always blocked. This is expressed by

$$\epsilon_{sub,1} = \begin{cases} 1, & \text{for } 0 < \varphi_a < \pi/2, \\ 0, & \text{for } \pi/2 < \varphi_a < (\pi + \psi_0 - \alpha_0)/2, \\ 1, & \text{for } (\pi + \psi_0 - \alpha_0)/2 < \varphi_a < \Psi_1, \\ 0, & \text{for } \Psi_1 < \varphi_a < \pi. \end{cases} \quad (5.57)$$

If $\Psi_1 < (\pi + \psi_0 - \alpha_0)/2$ then the second unobstructed region disappears.

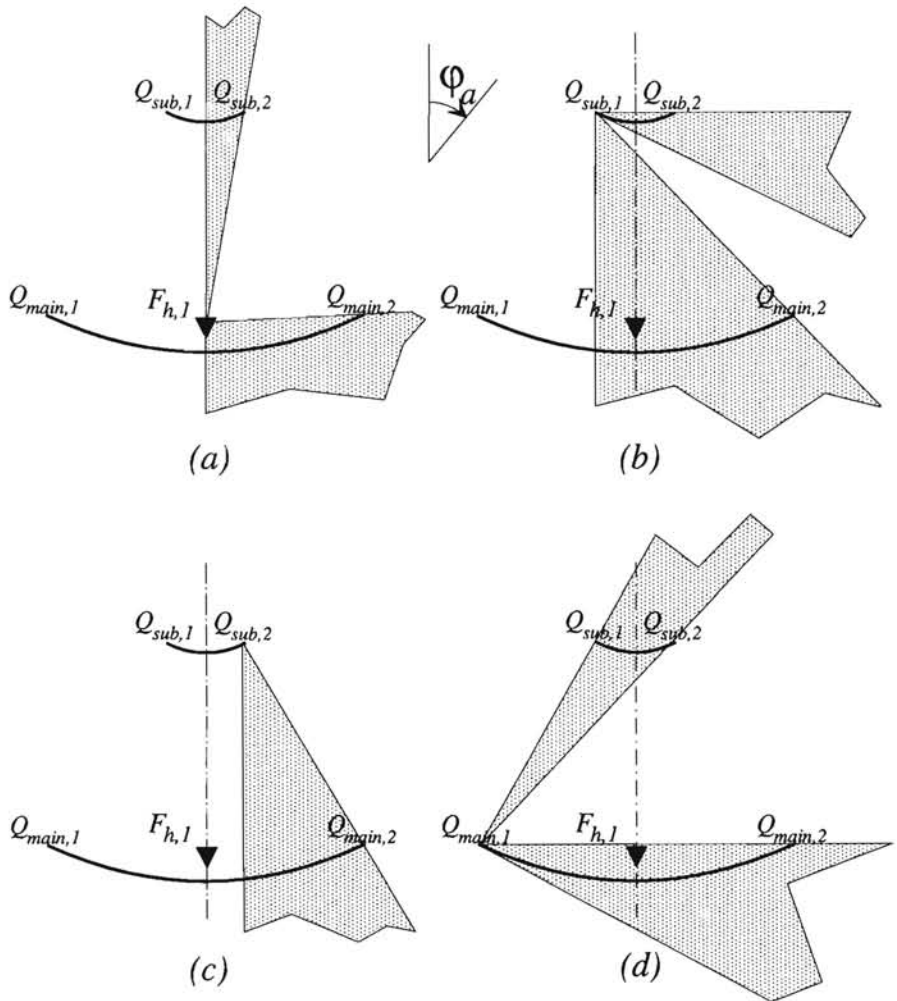


Figure 5.22: Shadow regions for field contributions in a Cassegrain antenna system: shadow region for direct ray (a), for first diffraction point on sub-reflector $Q_{sub,1}$ (b), for second diffraction point on sub-reflector $Q_{sub,2}$ (c), and for first diffraction point on main-reflector $Q_{main,1}$ (d).

3. The second diffraction point $Q_{sub,2}$ on the sub-reflector is blocked by the main-reflector for $\varphi_a > \Psi_2 = \arctan((D_p - D_h)/(2mm_h))$. This is expressed by

$$\epsilon_{sub,2} = \begin{cases} 1, & \text{for } 0 < \varphi_a < \Psi_2, \\ 0, & \text{elsewhere.} \end{cases} \quad (5.58)$$

4. The first diffraction point $Q_{main,1}$ of the main-reflector is blocked by the main-reflector for $\pi/2 < \varphi_a < (\pi + \psi_0)/2$. It is also blocked by the sub-reflector in case the projected shadow of the sub-reflector covers the point $Q_{main,1}$ (Fig. 5.22d). Whether this occurs is determined following a method proposed in [75], and will not be demonstrated here. The shadow indicator for diffraction point $Q_{main,1}$ is defined as

$$\epsilon_{main,1} = \begin{cases} 0, & \text{for } \pi/2 < \varphi_a < (\pi + \psi_0)/2, \\ 0, & \text{if projected shadow of sub-reflector covers } Q_{main,1}, \\ 1, & \text{elsewhere.} \end{cases} \quad (5.59)$$

5. The second diffraction point $Q_{main,2}$ of the main-reflector is never obstructed in our analysis. This is expressed by

$$\epsilon_{main,2} = 1. \quad (5.60)$$

The expression for the total field $E_{V,H}^t$ at the feed is found by weighting each individual diffraction contribution by the polarisation vector $\hat{e}_{polV,polH}$ for the corresponding direction of arrival, and multiplying it with the feed gain $G_f(\Psi)$ for that direction of arrival

$$\begin{aligned} E_{V,H}^t(F_{h,1}) = & \epsilon_{dir} G_f(\psi_{dir}) \hat{e}_{polV,polH}(\Psi_{dir}, \Phi_{dir}) \cdot \vec{E}^{DIR}(F_{h,1}) \\ & + \sum_{i=1}^2 \left[\epsilon_{sub,i} G_f(\alpha_0) \hat{e}_{polV,polH}(\alpha_0, -\varphi_{sub,i}) \cdot \vec{E}_i^S(F_{h,1}) \right. \\ & + \epsilon_{sub,i} G_f(\xi_2) \hat{e}_{polV,polH}(\xi_2, -\varphi_{sub,i}) \cdot \vec{E}_i^{SRR}(F_{h,1}) \\ & + \epsilon_{sub,i} G_f(\alpha_0) \hat{e}_{polV,polH}(\alpha_0, -\varphi_{sub,i} - \pi) \cdot \vec{E}_i^{SS}(F_{h,1}) \\ & + \epsilon_{sub,i} G_f(\chi_0) \hat{e}_{polV,polH}(\chi_0, -\varphi_{sub,i}) \cdot \vec{E}_i^{SM}(F_{h,1}) \\ & + \epsilon_{sub,i} G_f(\xi_2) \hat{e}_{polV,polH}(\xi_2, -\varphi_{sub,i} - \pi) \cdot \vec{E}_i^{SSRR}(F_{h,1}) \\ & + \epsilon_{main,i} G_f(\chi_0) \hat{e}_{polV,polH}(\chi_0, -\varphi_{main,i}) \cdot \vec{E}_i^M(F_{h,1}) \\ & + \epsilon_{main,i} G_f(\alpha_0) \hat{e}_{polV,polH}(\alpha_0, -\varphi_{main,i}) \cdot \vec{E}_i^{MR}(F_{h,1}) \\ & + \epsilon_{main,i} G_f(\chi_0) \hat{e}_{polV,polH}(\chi_0, -\varphi_{main,i} - \pi) \cdot \vec{E}_i^{MM}(F_{h,1}) \\ & + \epsilon_{main,i} G_f(\alpha_0) \hat{e}_{polV,polH}(\alpha_0, -\varphi_{main,i}) \cdot \vec{E}_i^{MS}(F_{h,1}) \\ & \left. + \epsilon_{main,i} G_f(\xi_2) \hat{e}_{polV,polH}(\xi_2, -\varphi_{main,i}) \cdot \vec{E}_i^{MSRR}(F_{h,1}) \right]. \end{aligned} \quad (5.61)$$

where we have introduced the angle Ψ_{dir} and Φ_{dir} according to

$$\Psi_{dir} = \arccos(\hat{s}' \cdot (\hat{e}_0 \times \hat{e}_{\pi/2})), \quad (5.62)$$

and

$$\Phi_{dir} = -\arccos\left(\frac{-\hat{s}' \cdot \hat{e}_0}{\sin \Psi_{dir}}\right). \quad (5.63)$$

The polarisation vector $\hat{e}_{polV,polH}$ is used to determine the co- and cross-polar signals. It is defined in the spherical (r, Ψ, Φ) coordinate system with the origin at $F_{h,1}$

$$\begin{aligned} \hat{e}_{polV} &= (\cos \Psi \cos^2 \Phi + \sin^2 \Phi) \hat{e}_0 - (1 - \cos \Psi) \sin \Phi \cos \Phi \hat{e}_{\pi/2} + \sin \Psi \cos \Phi (\hat{e}_0 \times \hat{e}_{\pi/2}), \\ \hat{e}_{polH} &= (1 - \cos \Psi) \sin \varphi \cos \Phi \hat{e}_0 - (\cos \Psi \sin^2 \Phi + \cos^2 \Phi) \hat{e}_{\pi/2} - \sin \Psi \sin \Phi (\hat{e}_0 \times \hat{e}_{\pi/2}). \end{aligned} \quad (5.64)$$

The minus signs in equation (5.61) in the polarisation vectors are introduced because $\Phi = -\varphi$, where the (ρ, ψ, φ) coordinate system is spherical with its origin at F_p and $\psi = \pi$ is the forward direction of the antenna system.

The power sum $E_{V,H}^P$ is used to obtain some average of the received signal. Note that only the contributions which exhibit an independent phase behaviour may be added on basis of power. This means that all signals that enter the antenna system *via the same point* should still be added on a complex basis. So only five contributions remain:

1. the direct contribution;
2. two sub-reflector contributions that enter the antenna system via $Q_{sub,i}$; each contribution consists of a cluster of five diffraction contributions;
3. two main-reflector contributions that enter the antenna system via $Q_{main,i}$; each contribution consists of a cluster of five diffraction contributions.

The power sum $E_{V,H}^P$ is given by

$$\begin{aligned} E_{V,H}^P(F_{h,1}) &= \left[\left| \epsilon_{dir} G_f(\Psi_{dir}) \hat{e}_{polV,polH}(\Psi_{dir}, \Phi_{dir}) \cdot \vec{E}^{DIR}(F_{h,1}) \right|^2 \right. \\ &+ \sum_{i=1}^2 \left\{ \left| \epsilon_{sub,i} G_f(\alpha_0) \hat{e}_{polV,polH}(\alpha_0, -\varphi_{sub,i}) \cdot \vec{E}_i^S(F_{h,1}) \right. \right. \\ &+ \left| \epsilon_{sub,i} G_f(\xi_2) \hat{e}_{polV,polH}(\xi_2, -\varphi_{sub,i}) \cdot \vec{E}_i^{SRR}(F_{h,1}) \right. \\ &+ \left| \epsilon_{sub,i} G_f(\alpha_0) \hat{e}_{polV,polH}(\alpha_0, -\varphi_{sub,i} - \pi) \cdot \vec{E}_i^{SS}(F_{h,1}) \right. \\ &+ \left| \epsilon_{sub,i} G_f(\chi_0) \hat{e}_{polV,polH}(\chi_0, -\varphi_{sub,i}) \cdot \vec{E}_i^{SM}(F_{h,1}) \right. \\ &+ \left. \left. \left| \epsilon_{sub,i} G_f(\xi_2) \hat{e}_{polV,polH}(\xi_2, -\varphi_{sub,i} - \pi) \cdot \vec{E}_i^{SSRR}(F_{h,1}) \right|^2 \right\} \right. \\ &+ \left| \epsilon_{main,i} G_f(\chi_0) \hat{e}_{polV,polH}(\chi_0, -\varphi_{main,i}) \cdot \vec{E}_i^M(F_{h,1}) \right. \\ &+ \left| \epsilon_{main,i} G_f(\alpha_0) \hat{e}_{polV,polH}(\alpha_0, -\varphi_{main,i}) \cdot \vec{E}_i^{MR}(F_{h,1}) \right. \\ &+ \left| \epsilon_{main,i} G_f(\chi_0) \hat{e}_{polV,polH}(\chi_0, -\varphi_{main,i} - \pi) \cdot \vec{E}_i^{MM}(F_{h,1}) \right. \\ &+ \left| \epsilon_{main,i} G_f(\alpha_0) \hat{e}_{polV,polH}(\alpha_0, -\varphi_{main,i}) \cdot \vec{E}_i^{MS}(F_{h,1}) \right. \\ &+ \left. \left. \left. \left. \left. \left. \epsilon_{main,i} G_f(\xi_2) \hat{e}_{polV,polH}(\xi_2, -\varphi_{main,i}) \cdot \vec{E}_i^{MSRR}(F_{h,1}) \right|^2 \right\} \right]^{1/2}, \end{aligned} \quad (5.65)$$

whereas the polarisation-independent sum E^{PP} , which represents a polarisation average of the power received at the feed, is defined in equation (5.22).

For $\varphi_a = (0, \pi)$, $\varphi_e = 0$, the determination of the diffraction points using Keller's law (eq. (2.40)) breaks down. These directions are the well-known caustic directions [70, 73]. To calculate the received field at the feed in these regions, another method such as equivalent edge currents [71, 72] or physical optics should be used.

5.4.3 Reception properties of a shielded Cassegrain antenna

In this subsection we discuss a method to calculate the reception properties of a Cassegrain reflector antenna shielded by a perfectly-conducting half-plane. We will follow the same procedure as outlined for the unshielded case, and therefore we first focus on the determination of the diffraction points.

If the obstacle is present, the analysis of the receiving properties of the double-reflector antenna changes, because the incident wave at the antenna has a cylindrical wavefront, and its direction of incidence is not uniquely determined. In the E- and H-plane analysis two diametrically opposite diffraction points were found. In the arbitrary case, we have to use a root-finding procedure to find the appropriate diffraction points.

Our analysis follows the analysis set out in [3]; we know that the diffraction point at the horizontal edge Q^h is the projection of a specific point L of the reflector edge onto the obstacle edge, if the arriving wave is propagating parallel to the ground plane into the direction \hat{x} . This means that this diffraction point Q^h is given by

$$\vec{Q}^h = (\vec{L} \cdot \hat{y})\hat{y} + z_{ob}\hat{z}. \quad (5.66)$$

It should be noted that the term in braces is a function of φ , φ_a and φ_e . The projection point Q^h is a diffraction point if, and only if Keller's law of edge diffraction is satisfied at the point L . The location of L is given implicitly as a function of φ . In this special case where the direction of propagation is \hat{x} , Keller's law is automatically satisfied at the half-plane edge.

We obtain diffraction points $Q_{sub,i}$ and $Q_{main,i}$ on the sub- and main-reflector rim that are not diametrically opposite. Once the diffraction points on the reflector edges are found, the wave coming from Q^h is diffracted at the antenna edge and it is directed into the antenna system. From this point on, the analysis is identical to that of the unshielded case.

Within the antenna system, we have at maximum $1 + (4 \cdot 5) = 21$ contributions, as in the unshielded case:

1. the 'direct' wave: this field contribution is diffracted at the point $\vec{Q}_F^h = (\vec{F}_{h,1} \cdot \hat{y})\hat{y} + z_{ob}\hat{z}$ and reaches the feed directly.
2. the waves that enter the antenna system via $Q_{sub,1}$: the wave is diffracted at $\vec{Q}_{sub,1}^h = (\vec{Q}_{sub,1} \cdot \hat{y})\hat{y} + z_{ob}\hat{z}$, and excites a cluster of five diffraction contributions;
3. the waves that enter the antenna system via $Q_{sub,2}$: the wave is diffracted at $\vec{Q}_{sub,2}^h = (\vec{Q}_{sub,2} \cdot \hat{y})\hat{y} + z_{ob}\hat{z}$, and excites a cluster of five diffraction contributions;
4. the waves that enter the antenna system via $Q_{main,1}$: the wave is diffracted at $\vec{Q}_{main,1}^h = (\vec{Q}_{main,1} \cdot \hat{y})\hat{y} + z_{ob}\hat{z}$, and excites a cluster of five diffraction contributions;
5. the waves that enter the antenna system via $Q_{main,2}$: the wave is diffracted at $\vec{Q}_{main,2}^h = (\vec{Q}_{main,2} \cdot \hat{y})\hat{y} + z_{ob}\hat{z}$, and excites a cluster of five diffraction contributions.

The reader is referred to the previous section for the denomination of the individual field contributions that arrive at the feed.

The summation of the field contributions at the feed is similar to that used in the unshielded case. We obtain the total field $E_{V,H}^t$ according to equation (5.61), the power sum $E_{V,H}^P$ according to equation (5.65) and the polarisation independent sum E^{PP} according to equation (5.22). Since the definitions of these quantities is identical to those used in the unshielded case, they will not be repeated here.

We conclude with a remark. By inserting the obstacle into the propagation path, some important parameters in the analysis change. It is obvious that the incident field strength at the Cassegrain antenna is influenced by the diffraction process at the obstacle edge. Apart from a change in amplitude, the diffraction at the edge of the obstacle causes a phase shift due to the longer propagation path. The change in angle of arrival of the wave incident upon the antenna system is more important, however. In the forward region of the antenna ($0 < \Psi < \pi/2$) this may result in a considerable raise in feed gain G_f for the interfering diffracted signal, thereby partly compensating the diffraction loss caused by the obstacle.

5.4.4 Conclusions

In this section we have discussed the ray-tracing which is necessary to calculate the off-axis receiving properties of a Cassegrain reflector antenna. We have presented a list of diffraction contributions within the antenna system. Using this list, higher-order diffractions are identified in the diffraction analysis of the Cassegrain antenna system. It is remarked that

near the forward and rear directions the diffraction analysis of the receiving pattern of the double-reflector antenna breaks down due to the presence of (axial) caustics.

5.5 Off-axis radiation pattern calculation of a Cassegrain antenna system with an application to site shielding

This section² treats the theoretical aspects of the calculations involved in the determination of the site-shielding performance of a Cassegrain reflector system shielded by a perfectly conducting half-plane.

5.5.1 Introduction

Earth-station antennas of the Cassegrain type have been, and still are, frequently used in satellite communications because of their advantageous antenna-noise properties. The placement of these antennas is not performed arbitrarily, and a terrestrial communication system and a satellite-communication system working at the same frequency will be at least separated by the *coordination distance*. The coordination contour around the earth-station antenna divides the space into a region in which coordination is necessary, and in a region in which it is not. For a large time percentage the permissible level of the terrestrial signal at the ground-station site will be below some mutually-agreed threshold. Due to anomalous propagation conditions such as ducting, it is possible that the signal level induced by the terrestrial communication system exceeds this threshold. Often this results in a very strong interfering signal, and the coordination will result in agreements concerning the power radiated by the terrestrial station, and the permissible level of interference at the receiver site as function of the percentage of time. Obviously, this coordination distance is strongly dependent on the propagation mechanism which is most likely to occur in the coordination area. A solution to this interference problem is the use of interference-reduction techniques, of which *site shielding* can be very effective.

Because of the orientation at which the earth-station terminal is mostly being used, interfering signals will couple into the satellite-communication system via the sidelobes

² Note: the major part of this section was already published: G.A.J. van Dooren and H.J.F.G. Govaerts: *Off-axis radiation-pattern calculation of a Cassegrain antenna system with an application to site shielding*, Proceedings of the 8th International Conference on Antennas and Propagation (ICAP), pp. 631-634, Institute of Electrical Engineers (IEE), 1993.

of the antenna radiation pattern. For this reason, knowledge about the off-axis radiation (receiving) pattern of this kind of antenna system is desired, and, more importantly, insight into the influence of the placement of an obstacle on the radiation pattern of the double-reflector system is sought. Few results on the off-axis receiving properties of the Cassegrain reflector antenna were reported in the literature.

This section focuses on the off-axis receiving properties of a Cassegrain reflector antenna. First, the receiving pattern of a double-reflector system is calculated. Subsequently, it is assumed that a hypothetical half-plane is used for shielding the antenna. For analysis purposes, a model is proposed that considers the combined problem of obstacle and antenna diffraction for the determination of the influence of the obstacle on the receiving pattern of the antenna. Note that this combined approach is indeed necessary, because in many cases the obstacle will be located in the near-field of the (large) Cassegrain earth station. In this first analysis strut scattering will be neglected. The section is concluded with an application of the model to an antenna with a prescribed geometry shielded by a half-plane. The effectiveness of the shielding will be analysed as function of the antenna azimuth.

5.5.2 Geometry

The Cassegrain antenna system consists of a hyperboloidal sub-reflector with diameter D_h , a paraboloidal main-reflector with diameter D_p , and a feed. In Figure 5.23 a cross-section of the antenna system is shown. The interrelations between various parameters indicated in this figure can be determined from straightforward geometry [76], and were given in Section 5.4. Points on the sub- and main-reflector rim will be denoted by S and M . The focal distance of the paraboloidal main-reflector is denoted by f_p , while the focal distance of the hyperboloidal sub-reflector is denoted by $2f_h$.

5.5.3 Radiation-pattern calculation

In this section the E- and H-plane receiving patterns are calculated, which correspond to the radiation patterns of the antenna by reciprocity. Geometrical optics (GO) and the uniform theory of diffraction (UTD) are used to describe the interaction of the incident wave with the antenna reflectors and feed.

From GO and UTD it is well-known that reflected waves within the antenna system are of order k^0 with respect to the incident wave of order k^0 , where $k = 2\pi/\lambda$ is the free-space wavenumber and λ is the wavelength. Single-diffracted waves are of order $k^{-1/2}$ out of the transition regions. From this it can be derived that reflection in the antenna system does not attenuate the wave amplitude, while diffraction at the reflector rim will lower it by a factor

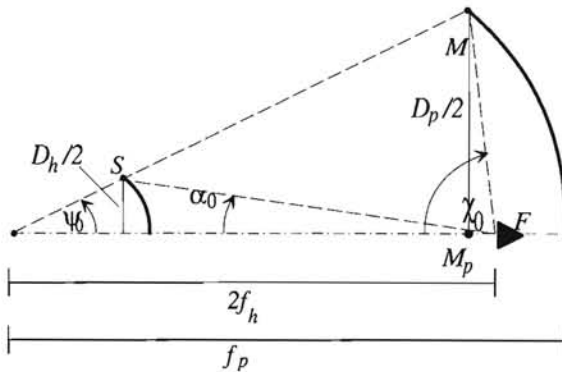


Figure 5.23: Cross-section through a Cassegrain antenna system; only the upper half is shown.

$k^{-1/2}$. For the complexity of the model describing the wave-interaction phenomena within the antenna system it is therefore of importance to know to what order of k contributions should be included. From numerical analyses it was found that it is sufficient to include contributions up to order k^{-1} , resulting in a total number of rays $\mathcal{L} = 21$. In Table 5.1 a list of wave contributions in a descending order of k is given. In this table the source position is indicated by SC , while the diffraction and reflection mechanisms are abbreviated by subscripts \mathcal{D} and \mathcal{R} , respectively. The feed position is denoted by F . Note that the wave contribution corresponding to (double) reflection (1^* in Table 5.1) only reaches the feed if the wave is incident from boresight, which is a caustic direction. Also the backward direction (azimuth angle $\varphi_a = \pi$ and elevation angle $\varphi_e = 0$) is a caustic direction, and both cases are excluded from subsequent analyses because of the primary interest in the off-axis radiation patterns. For satellite communications $\varphi_e > 0$, and therefore the complete radiation patterns from $\varphi_a = 0$ to $\varphi_a = \pi$ in the horizontal plane can be calculated. It was found that, for this particular geometry, it is allowed to neglect the wave contribution corresponding to (single) reflection at the paraboloidal main-reflector (1^{**} in Table 5.1), and for this reason it is not included in the analyses. Depending upon the specific geometry it should be investigated, however, whether this exclusion is appropriate or not.

The ray trajectories of the contributions listed in Table 5.1 are shown in Figure 5.24. Note that the rays numbered 2 to 11 all appear twice: there are also ten rays labelled $2'$ to $11'$ which enter the antenna system at points S' and M' diametrically opposite to S and M within this geometry (Sec. 5.4). By following each ray from its entering point through the antenna system to the feed position F , GO and UTD enable us to compose the total

Table 5.1: Ray contributions in a Cassegrain antenna system.

Number	Order	type	ray path	# rays
1	k^0	direct ray	$SC \rightarrow F$	1
1*		reflected ray	$SC \rightarrow M_R \rightarrow S_R \rightarrow F$	0
1**			$SC \rightarrow M_R \rightarrow F$	0
2	$k^{-1/2}$	diffracted ray	$SC \rightarrow S_D \rightarrow F$	2
3			$SC \rightarrow M_D \rightarrow F$	2
4		diffracted reflected ray	$SC \rightarrow M_D \rightarrow S_R \rightarrow F$	2
5			$SC \rightarrow S_D \rightarrow M_R \rightarrow S_R \rightarrow F$	2
6	k^{-1}	double-diffracted ray	$SC \rightarrow M_D \rightarrow S_D \rightarrow F$	2
7			$SC \rightarrow S_D \rightarrow M_D \rightarrow F$	2
8			$SC \rightarrow S_D \rightarrow S_D \rightarrow F$	2
9			$SC \rightarrow M_D \rightarrow M_D \rightarrow F$	2
10		double-diffracted and	$SC \rightarrow M_D \rightarrow S_D \rightarrow M_R \rightarrow S_R \rightarrow F$	2
11		reflected ray	$SC \rightarrow S_D \rightarrow S_D \rightarrow M_R \rightarrow S_R \rightarrow F$	2
total				21

field at F :

$$\vec{E}^t(F) \propto \sum_{l=1}^{21} \epsilon_l \vec{E}_l(F), \quad (5.67)$$

where \vec{E}_l is the wave contribution reaching the feed via trajectory l , and ϵ_l is a shadow indicator accounting for blockage of the ray path by either the sub- or main-reflector. These blockage effects were included according to a method as described in [75] and they were discussed in Section 5.4. Gain and polarisation of the feed are characterised by the voltage gain function $G_f(\Psi)$ and the unit polarisation vector $\hat{e}_{polV,polH}(\Psi, \Phi)$, where the spherical (r, Ψ, Φ) coordinate system has its origin at F . The signal at the feed is given by (eq. (5.61))

$$E_{V,H}^t(F) = \sum_{l=1}^{21} \epsilon_l G_f(\Psi_l) \vec{E}_l(F) \cdot \hat{e}_{polV,polH}(\Psi_l, \Phi_l). \quad (5.68)$$

The coordinate Ψ_l is given by α_0 for rays arriving from a diffraction point on the sub-reflector, and by χ_0 for rays arriving from a diffraction point on the main-reflector.

A frequently-employed feed is the corrugated horn, of which the gain function G_f is often described by a power of a cosine in the forward angular region, and by a constant in the backward region. This pattern was introduced in equation (5.4). Furthermore, it is assumed that the polarisation properties of the feed can be modelled as that of a Huygens source.

A literature survey revealed that the single reference dealing with the determination of the off-axis radiation properties of a Cassegrain system with a well-defined geometry

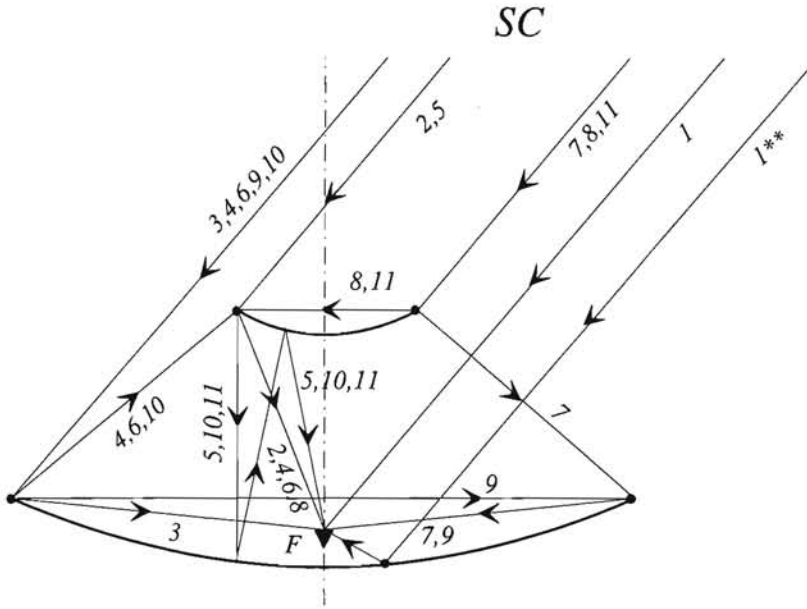


Figure 5.24: Ray trajectories in a double-reflector system.

is [70]. The E- and H-plane patterns of an antenna with the same geometry as in [70] were calculated in receive mode. The geometry considered is: $D_p = 20\lambda$, $f_p/D_p = 0.4$, $D_h/D_p = 0.133$, and $f_h = 2.44\lambda$. For this geometry $\alpha_0 = 17.5^\circ$, $\psi_0 = 64.0^\circ$, and $\chi_0 = \pi/2$. The feed pattern is chosen in such a way that there is a -15 dB edge illumination for the sub-reflector, a forward feed gain of 21.5 dBi, and a relative rear radiation of -50 dB (Fig. 5.3).

In the Figures 5.25 and 5.26 some of the major individual wave contributions in the E-plane pattern calculation that arrive at F are given as function of the azimuth angle. From these figures, the blockage by sub- and main-reflector can clearly be seen. The E- and H-plane patterns of this antenna can be found in Figure 5.27. If the results reported in [70] are compared with ours for the same antenna geometry, it is found that good agreement exists for the E- and H-plane patterns except in the regions for an azimuth φ_a of 70° to 90° . It is believed that this is caused by the incorrect combined ray tracing as performed in [70], while a correct separate tracing of individual rays is performed here.

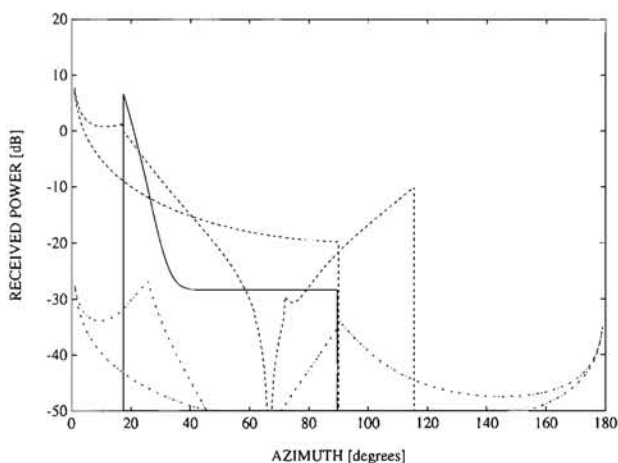


Figure 5.25: Individual contributions as function of azimuth angle φ_a ; shown are the contributions of rays 1 (—), rays 2 (---), and rays 3 (-·-·-·-·).
 Data: $D_p = 20\lambda$, $f_p/D_p = 0.4$, $D_h/D_p = 0.133$, $f_h = 2.44\lambda$, $a = 0.00316$, $m = 37.3$, $\varphi_e = 0$

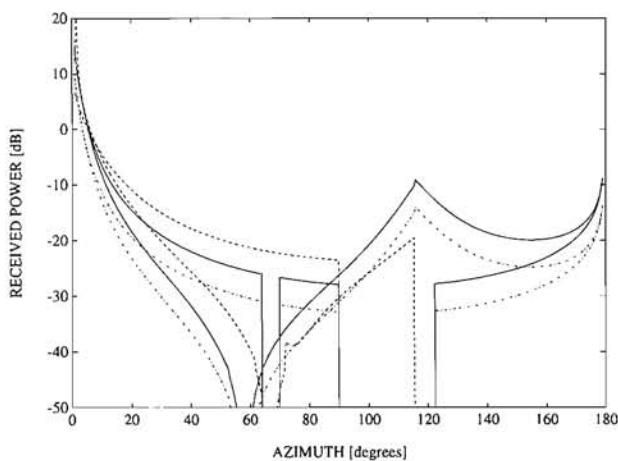


Figure 5.26: Individual contributions as function of azimuth angle φ_a ; shown are the contributions of rays 4 (—), rays 5 (---), and rays 6 (-·-·-·-·).
 Data: $D_p = 20\lambda$, $f_p/D_p = 0.4$, $D_h/D_p = 0.133$, $f_h = 2.44\lambda$, $a = 0.00316$, $m = 37.3$, $\varphi_e = 0$

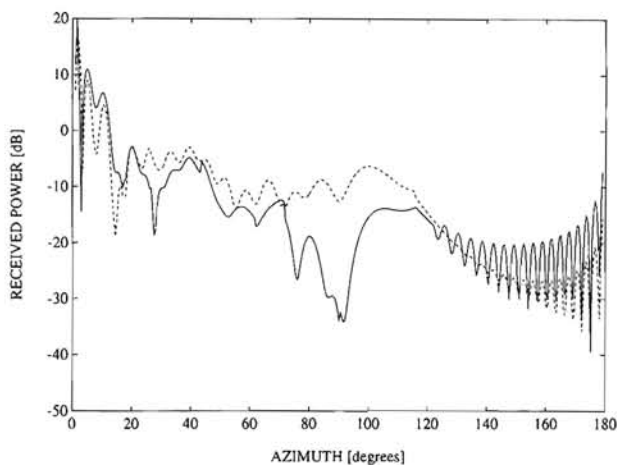


Figure 5.27: Receiving pattern of a Cassegrain reflector antenna as function of the azimuth angle φ_a ; shown are the E-plane (—), and the H-plane (---).
 Data: $D_p = 20\lambda$, $f_p/D_p = 0.4$, $D_h/D_p = 0.133$, $f_h = 2.44\lambda$, $a = 0.00316$,
 $m = 37.3$, $\varphi_e = 0$

5.5.4 Shielded radiation-pattern calculation

The geometry for interference reduction can be found in Figure 5.18, which is nearly identical to the geometry studied in Section 5.1 (Fig. 5.1). The obstacle in the case studied in this section is infinitely wide, and, obviously, the single-reflector antenna is replaced by a Cassegrain antenna.

The incident wave, which propagates into the x -direction, first encounters the half-plane obstacle, and then is incident upon the antenna system which is in the (optical) shadow region for the interfering wave. The half-plane obstacle is defined by $x = 0$, $0 \leq z \leq z_{ob}$. The antenna is positioned in such a way that the wanted signal comes from a direction specified by φ_a and φ_e . Two things are immediately clear. Firstly, the obstacle-diffracted field does not have a plane but a cylindrical wavefront. This causes that the rays arriving at the antenna system are not parallel anymore. Secondly, the direction of incidence at the antenna, and therefore also the positions of the diffraction points within the system, have changed by the placement of the obstacle.

It is very well possible that the obstacle is in the near-field of the Cassegrain antenna. For this reason the diffraction processes at the obstacle edge and antenna system *cannot* be

treated independently. This combined treatment of obstacle and antenna will be referred to as the ‘near-field approach’ (Sec. 5.6). Fortunately, UTD can also be used to treat diffraction at the obstacle, and in this way the obstacle can be seen as just an additional edge where diffraction may take place.

To find some kind of average of the signal response at the feed, the so-called power sum is employed (eq. 5.21). For the present case, this power sum is compactly expressed as (eq. (5.65))

$$E_{V,H}^P(F) = \sqrt{\sum_{l=1}^{\mathcal{M}} \left| \epsilon_l G(\Psi_l) \vec{E}_l(F) \cdot \hat{e}_{polV,polH}(\Psi_l, \Phi_l) \right|^2}, \quad (5.69)$$

where $\mathcal{M} < \mathcal{L} = 21$. Equation (5.69) resembles the calculation of the Euclidean length of a vector in an \mathcal{M} -dimensional space, where the \mathcal{M} coordinates are independent. Note that the contributions which enter the antenna system at the same point do *not* have an independent phase relation, and therefore need to be added on a complex basis. This results in five independent terms to be used in equation (5.69), i.e. $\mathcal{M} = 5$ (Sec. 5.4).

In Figure 5.28 the receiving patterns of a Cassegrain antenna in a shielded and an unshielded geometry can be found. The geometrical parameters of the antenna system are identical to those as used in Figures 5.25 to 5.27, but the elevation is set to $\varphi_e = \pi/9$. The difference in height between the obstacle edge z_{ob} and the aperture centre M_p of the antenna at $(x_M, 0, z_M)$ is $z_{ob} - z_M = 100\lambda$. Furthermore, the distance x_M between obstacle and antenna is $x_M = 1000\lambda$. Results for both a vertically- and horizontally-polarised feed can be found as function of φ_a .

The ratio of the received field in the absence and the presence of the obstacle is a measure for the effectiveness of the shielding, and is called the *site-shielding factor* (SSF). The SSF deduced from Figure 5.28 is shown in Figure 5.29 for both vertical and horizontal polarisation. It is found from this figure that the polarisation, in this specific case, does not strongly influence the SSF as function of the azimuth angle φ_a .

A more extensive treatment of the SSF of a Cassegrain system can be found in Section 5.6, where also a comparison is made with two other methods to calculate the SSF, viz. the ‘far-field method’ and the CCIR-recommended method. The latter methods treat the obstacle and antenna diffraction independently even for small x_M . In Section 5.6 also a comparison between double- and single-reflector antenna shielding is made. The dependence on other antenna parameters has been examined: the dependence on the elevation angle is described in [74], and the influence of the distance between the antenna and the obstacle is discussed in [45].

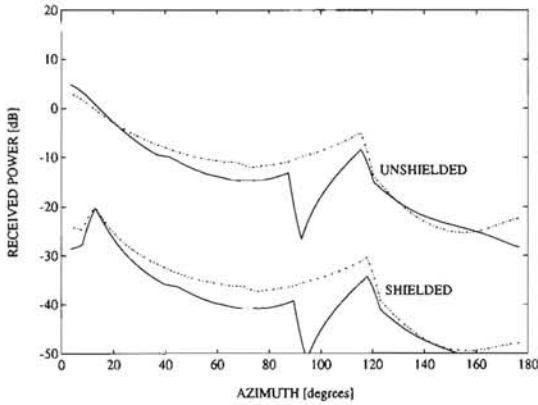


Figure 5.28: Receiving pattern of a Cassegrain reflector antenna as function of the azimuth angle φ_a based on the power sum; shown are the result for horizontal (—), and vertical polarisation (· · · · ·).

Data: $D_p = 20\lambda$, $f_p/D_p = 0.4$, $D_h/D_p = 0.133$, $f_h = 2.44\lambda$, $a = 0.00316$, $m = 37.3$, $\varphi_e = 0$, $x_M = 1000\lambda$, $z_M = 100\lambda$, $z_{ob} = 200\lambda$

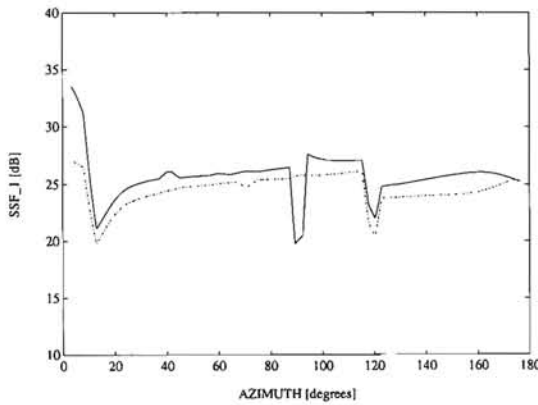


Figure 5.29: SSF of a Cassegrain reflector antenna as function of the azimuth angle φ_a based on the power sum; shown are the result for horizontal (—), and vertical polarisation (· · · · ·).

Data: $D_p = 20\lambda$, $f_p/D_p = 0.4$, $D_h/D_p = 0.133$, $f_h = 2.44\lambda$, $a = 0.00316$, $m = 37.3$, $\varphi_e = 0$, $x_M = 1000\lambda$, $z_M = 100\lambda$, $z_{ob} = 200\lambda$

5.5.5 Conclusions

The off-axis receiving pattern of a Cassegrain reflector antenna with a prescribed geometry as function of antenna azimuth was calculated in the absence as well as in the presence of a half-plane obstacle. The model uses GO and UTD and includes 21 field contributions to calculate the total field at the feed. These contributions are individually followed through the antenna system and are spatially weighted by the feed pattern assumed. The ray analysis revealed that some of the individual contributions can be neglected to simplify the analysis (e.g. rays 3,7,8,9). The model proposed analyses the combined problem of obstacle and antenna diffraction since in many cases the obstacle is in the near field of the earth-station antenna. Results of the additional attenuation caused by the presence of the obstacle on the propagation path of an interference source are given.

5.6 Shielding of single- and double-reflector earth-station antennas: a near- and far-field approach

This section³ describes the off-axis radiation-pattern calculation of a Cassegrain antenna system with prescribed geometrical parameters, in the absence and presence of a (hypothetical) half-plane, located either in the near- or far-field of the antenna. The attenuation of the incident field caused by the obstacle as function of antenna orientation and position is calculated and presented. The results for the half-plane shielding of the double-reflector system are compared with those obtained for a single-reflector antenna system shielded by the same obstacle. Three different, but related, approaches for the calculation of the additional propagation loss for the wave reaching the Cassegrain antenna system are presented and compared. It is found that the proposed near-field approach gives the best results.

5.6.1 Introduction

Frequency sharing in present-day radio-communication systems may lead to mutual interference between satellite and terrestrial links. Also transhorizon propagation of electromagnetic (EM) waves during anomalous propagation conditions such as ducting and elevated-layer reflection may induce signal levels which exceed mutually agreed thresholds. Several interference-reduction techniques are available to raise the carrier-to-interference

³ *Note:* the major part of this section was already published: G.A.J. van Dooren and H.J.F.G. Govaerts: *Shielding of single- and dual-reflector earth-station antennas: a near- and far-field approach*, IEE Proc. Pt. H, vol. 140, pp. 309-314, 1993.

ratio (CIR) for a certain satellite link in the case of interference problems [77, 3]. Besides coding and decoding of the wanted signal, also the principle of interferometric cancellation can be used to suppress the level of the interfering signal. Another method for reducing the interference level at a receiver location is site shielding. This technique tries to introduce an additional propagation loss for the interfering signal, without affecting the level of the desired signal. The additional propagation loss may be, for instance, due to diffraction of the interfering EM wave at some (artificial) object on the propagation path. A figure of merit for the shielding effectiveness is the so-called site-shielding factor (SSF) which was defined in equation (3.2)

The isolated-obstacle problem was treated in Chapter 3 for various type of obstacles. This analysis amounts to the calculation of the field distribution behind an obstacle, and obstacles like the half-plane, the finite-width screen, and the rectangular block were analysed using the UTD. For simplicity the obstacles were assumed to be perfectly conducting, and large in terms of the wavelength λ . The SSFs provided by some scaled obstacles have been experimentally verified as described in Sections 4.3, 4.4, and 4.5, and good agreement between theory and experiments was obtained.

The isolated-obstacle problem can be treated by assuming an antenna with an isotropic radiation pattern at some observation point in the vicinity of the obstacle. In case a non-isotropic radiation pattern is desired, a spatial weight function for the individual wave contributions can be introduced. Note that if the obstacle is in the near field of the antenna, the propagation mechanisms at the obstacle and the antenna cannot be treated independently. Rayleigh's far-field criterion can be used for determining whether a separate treatment of obstacle and antenna is theoretically allowed or not.

In the unshielded case, the far-field receiving properties are calculated, taking into consideration the orientation of the antenna in terms of azimuth (φ_a) and elevation (φ_e) angles.

In this section the emphasis is placed on the receiving properties of a Cassegrain antenna in a shielded and in an unshielded geometry. The shielded geometry corresponds to a Cassegrain antenna shielded by a half-plane of height z_{ob} . In a Cartesian coordinate system, the half-plane is described by $x = 0, 0 \leq z \leq z_{ob}$. The aperture centre M_p of the reflector antenna is at $(x_M, 0, z_M)$. The geometry used is shown in Figure 5.18. Note that, in the shielded configuration, UTD is used to describe the interaction of the incident wave with the obstacle, as well as the interaction of the (diffracted) wave with the reflector-antenna rims. For this reason, the presence of the obstacle is actually the introduction of an additional edge on the propagation path of the interfering wave.

In the following the calculation of the receiving pattern of a Cassegrain reflector system will be briefly discussed. Subsequently, the obstacle is placed, and the (near-field) receiving

pattern of the shielded configuration is determined. Then the receiving properties of a single- and double-reflector antenna shielded by a half-plane are compared. Results of the shielding of a double-reflector system based on a near- and a far-field analysis are given. Conclusions concerning the model, results presented, and the importance of the near-field analysis are drawn.

5.6.2 Radiation-pattern calculation

Despite the fact that the Cassegrain antenna system has been widely used in satellite communications, few results of determining the off-axis radiation pattern of an antenna with a well-defined geometry have been reported in the literature [70, 18]. Furthermore, few details concerning the methods used can be found, or omissions are present. In [70], for instance, a combined-ray approach is used, i.e. the rays are *not* separately traced through the antenna system, while in [18] only main-beam patterns are given.

The following approach has been used in determining which ray contributions should be included in the analysis. As a start, a number of most important ray contributions are selected on the basis of physical insight and asymptotic behaviour of the GO and UTD contributions. These ray contributions are separately traced through the antenna system and each ray is spatially weighted by the receiving pattern of the feed. The individual complex field contributions are then added to give a measure for the received power at the feed position. The received signal at the feed is found according to equation (5.68). Co- and cross-polarised signals can be separated by choosing either horizontal or vertical polarisation. A total of 21 ray contributions is found to be sufficient to describe the receiving properties of the double-reflector system as discussed in Section 5.4.

The feed gain function G_f (see eq. (5.68)) used is the approximation of the radiation pattern of a corrugated horn. In the forward angular region the voltage gain is modelled by a power of a cosine, while in the backward angular region it is given by a constant (eq. (5.4)). In the analyses the feed has the polarisation properties of a Huygens source.

According to UTD, the incident interfering waves can reach the feed only via special ray paths. These paths are determined by the locations of the diffraction points, which can be found using Keller's law of edge diffraction. All propagation paths to and within the antenna system were given in Section 5.4.

Assumptions in the analysis are that the influence of the sub-reflector support structure may be neglected, and that no reflection occurs at the earth's surface. Also it was assumed that the interfering wave arriving at the antenna site is due to a very distant source. Therefore it has a plane wavefront, and for simplicity a unit amplitude is assumed. The

polarisation vector is either \hat{y} or \hat{z} , and the propagation direction is assumed to be \hat{x} as shown in Figure 5.18.

Sub- and main-reflector blockage effects have been included according to a method described in [75]. Throughout the section the following geometrical parameters for the Cassegrain system will be used: main-reflector diameter $D_p = 100\lambda$, sub-reflector to main-reflector diameter ratio $D_h/D_p = 0.15$, sub-reflector eccentricity $e = 1.67$, focal distance to main-reflector diameter ratio $f_p/D_p = 0.4$, main-reflector edge illumination relative to boresight is -20 dB, and relative rear-radiation level of the feed -50 dB. The aperture centre M_p is located at $(x_M, 0, z_M)$, with $z_M = 50\lambda$.

In Figure 5.30 the E-plane pattern based on equation (5.68) is given. Note that for $\varphi_e = 0$ the directions $\varphi_a = 0$ and $\varphi_a = \pi$ are *caustic* directions. Around these directions the UTD cannot be applied, and other methods should be addressed to correctly evaluate the field. It was found that the sidelobes of the calculated pattern lie below the CCIR standard reference sidelobe pattern [78].

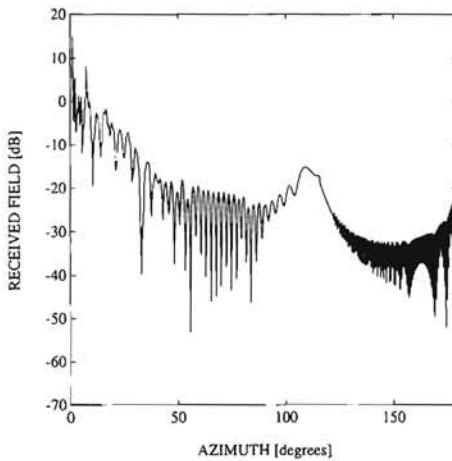


Figure 5.30: E-plane pattern of a Cassegrain reflector antenna as function of the azimuth angle φ_a .

Data: $D_p = 100\lambda$, $f_p/D_p = 0.4$, $D_h/D_p = 0.15$, $e = 1.67$, $a = 0.00316$, $m = 43.2$, $\varphi_e = 0$

5.6.3 Shielded radiation-pattern calculation

If the perfectly-conducting half-plane is present, the analysis of the Cassegrain antenna system remains nearly unchanged. The main difference is that, in the shielded case, the interfering wave is subject to diffraction at the obstacle edge. Therefore the angle of arrival as seen from the antenna has changed. In contrast with the unshielded case, the wave incident upon the antenna system does not have a plane, but a cylindrical wavefront.

In the analysis of the shielded configuration it is assumed that the complete antenna is in the shadow region behind the half-plane obstacle. Furthermore, the elevation angle φ_e of the antenna system is such that the wanted signal from the satellite is not obstructed, i.e. the 'aperture cylinder' is well directed above the obstacle edge. For this reason the elevation angle is chosen to be $\varphi_e = \pi/9$. The distance between antenna and obstacle x_M is chosen to be $x_M = 1000\lambda$, while the obstacle height $z_{ob} = 300\lambda$. The incident interfering field has a \hat{y} polarisation. The receiving patterns for the shielded and unshielded configuration based on equation (5.68) can be found in Figure 5.31. Note that the received field in Figure 5.31 can also be calculated at $\varphi_a = 0$ and $\varphi_a = \pi$, because for $\varphi_e = \pi/9$ these directions are no longer caustic directions. Also shown in Figure 5.31 are the results from the so-called 'power' sum $E_{V,H}^P$ introduced in equation (5.65). This power sum represents some kind of average of the result as given by the phasor sum as introduced in equation (5.61).

Ray contributions which do *not* have an independent phase behaviour are still added on a phasor basis. This means that waves entering the antenna system via the same diffraction point are still added according to equation (5.68). The independent results are added according to equation (5.69), and it is found that five terms remain in the summation (Sec. 5.4). From Figure 5.31 it can be seen that the power-sum result behaves much more smoothly.

The dashed curve in Figure 5.32 gives the SSF of the shielded Cassegrain system for $x_M = 1000\lambda$. It was obtained by subtracting the shielded from the unshielded result in Figure 5.31. The dips in the pattern in this particular curve are caused by the spillover lobes present in the receiving pattern. The SSF as function of azimuth φ_a at different distances x_M to the screen is shown in Figure 5.32. It is seen from this figure that the SSF becomes lower with increasing distance and that the complete curve becomes more smooth. This lowering of the curves can be explained by the fact that for large distances x_M the loss caused by diffraction at the obstacle edge decreases, i.e. the incident wave bends more easily around the screen. That the curves become more smooth with increasing distance is readily explained. For small distances x_M the obstacle-diffracted ray contributions have a large variation in spatial weighting as function of φ_a . If x_M is increased, the individual

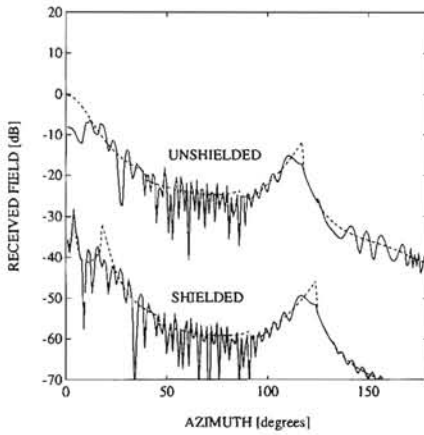


Figure 5.31: Receiving pattern of a Cassegrain reflector antenna as function of the azimuth angle φ_a ; shown are the result for the phasor sum (—), and the power sum (---).

Data: $D_p = 100\lambda$, $f_p/D_p = 0.4$, $D_h/D_p = 0.15$, $e = 1.67$, $a = 0.00316$, $m = 43.2$, $\varphi_e = \pi/9$, $x_M = 1000\lambda$, $z_M = 50\lambda$, $z_{ob} = 300\lambda$

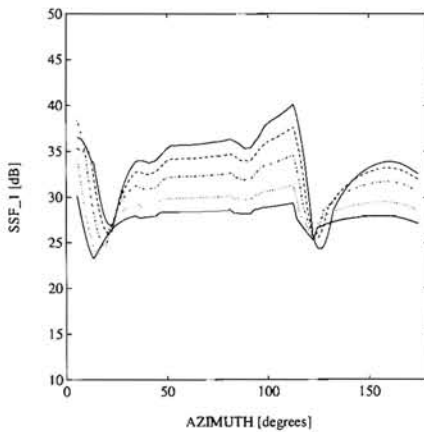


Figure 5.32: SSF of a Cassegrain reflector antenna as function of the azimuth angle φ_a and x_M ; shown are the results for $x_M = 750\lambda$ (upper —), $x_M = 1000\lambda$ (---), $x_M = 1500\lambda$ (- · - · - · - ·), $x_M = 2500\lambda$ (·····), and $x_M = 3500\lambda$ (lower —).

Data: $D_p = 100\lambda$, $f_p/D_p = 0.4$, $D_h/D_p = 0.15$, $e = 1.67$, $a = 0.00316$, $m = 43.2$, $\varphi_e = \pi/9$, $z_M = 50\lambda$, $z_{ob} = 300\lambda$

rays propagate (nearly) parallel and the variation in spatial weighting is decreased. From the analyses it was found that not much difference exists for horizontally (\hat{y}) or vertically (\hat{z}) polarised incident waves. For this reason only results for horizontally-polarised incident waves are given. The fact that the dip in the curve for $x_M = 750\lambda$ is lower than for the other curves is due to the fact that at $x_M = 750\lambda$ there is a strong single-diffraction contribution from a point on the sub-reflector. This particular contribution is obstructed for larger x_M .

5.6.4 Comparison of single- and double-reflector antenna shielding

The analysis of the shielding of a double-reflector antenna raises the question whether the antenna type is of importance in the site-shielding calculations. The calculation of the SSF of a single-reflector antenna shielded by a half-plane was treated in Section 5.5, which is based on work as reported in [3]. Some important results presented in [3] were reproduced [45, 74], and compared to the double-reflector shielding results. The parameters as used in the double-reflector simulations are transformed to the corresponding parameters for a single-reflector antenna using the principle of the equivalent parabola (Sec. 5.4). An identical (main-)reflector diameter, edge illumination, focal distance to reflector-diameter ratio and relative rear-radiation level is used.

Despite the fact that the received levels for the single- and double-reflector antenna show a substantial difference, the deduced SSF curves shown in Figure 5.33 are very similar, except in the feed spillover regions. In Figure 5.33 these regions are given by $20^\circ \leq \varphi_a \leq 30^\circ$ and $100^\circ \leq \varphi_a \leq 110^\circ$. Outside these spillover regions, the SSF results for a single- and double-reflector antenna are nearly identical. This leads to the conclusion that, except for the spillover regions, the antenna type is not of primary importance for the calculation of the SSF *if the antennas have an identical diameter and edge illumination*. This conclusion was also suspected in [3], but was not proven explicitly. The major differences between the results in Figure 5.33 are caused by specific blockage effects of the ray that reaches the feed directly. By the introduction of the obstacle the azimuth angle at which this blockage effect takes place, changes. Hence, the differences between the results for the unshielded and the shielded geometry change.

5.6.5 Near- and far-field antenna shielding

In the foregoing it was mentioned that, if the obstacle is in the near field of the Cassegrain antenna, the diffraction mechanisms at the obstacle and reflector edges cannot be treated independently. In the following, results based on three different methods are presented for

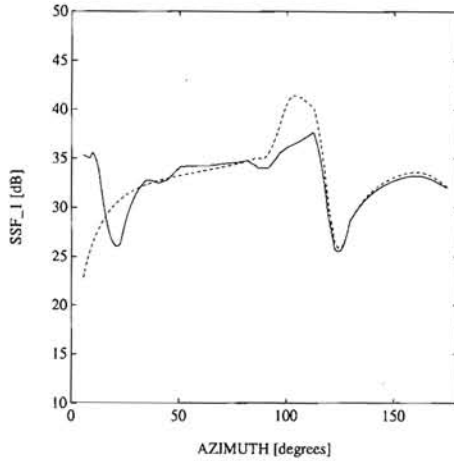


Figure 5.33: Comparison of SSF results as function of azimuth angle φ_a ; shown are the result for a Cassegrain antenna (————), and the result for the single reflector antenna (-----).

Data: $D = 100\lambda$, $f/D = 0.4$, edge illumination of -20 dB, $x_M = 1000\lambda$, $z_M = 50\lambda$, $z_{ob} = 300\lambda$

an antenna orientation $\varphi_a = 0$ and $\varphi_e = \pi/9$. The first method was discussed in an earlier section and is referred to as the 'near-field approach'. The receiving pattern of the antenna is calculated in combination with the obstacle diffraction.

The second method is referred to as the 'far-field approach'. It assumes that the antenna can be treated as a point receiver at the antenna centre, having a receiving pattern equal to the far-field receiving pattern of the Cassegrain antenna system. In the unshielded case, the received field has a level that is determined by the sidelobe attenuation at an angle φ_e . In the shielded case, the interfering wave is diffracted by the obstacle edge, and consequently the angle of arrival at the antenna system has changed. This means that the SSF is found according to

$$SSF = L_{ke} - \Delta G = L_{ke} + G(\varphi_e) - G(\varphi_e - \delta\varphi) \text{ [dB]}, \quad (5.70)$$

where $L_{ke} > 0$ is the knife-edge diffraction loss caused by the obstacle, which can be calculated using equation (3.65). The factors $G(\varphi_e)$ and $G(\varphi_e - \delta\varphi)$ are the antenna sidelobe attenuation factors for the angles of arrival in absence and presence of the obstacle, respectively, not to be confused with the feed gain function G_f . The parameter $\delta\varphi$ is found

from

$$\delta\varphi = \arctan\left(\frac{z_{ob} - z_M}{x_M}\right). \quad (5.71)$$

The near- and far-field for a reflector antenna with diameter D are separated by the Rayleigh distance $R = 2D^2/\lambda$. Theoretically, this far-field approximation can be used for $x_M > R$.

The third method, which is referred to as the 'CCIR approach' [2], is also based on equation (5.70) and assumes the CCIR standard reference sidelobe pattern as given in [78] for the function G . This reference sidelobe pattern is given by

$$G(\varphi) = \begin{cases} 32 - 25 \log \varphi & [\text{dBi}], \text{ for } 1^\circ \leq \varphi \leq 48^\circ, \\ -10 & [\text{dBi}], \text{ for } 48^\circ \leq \varphi \leq 180^\circ, \end{cases} \quad (5.72)$$

and is only valid for $100\lambda \leq D_p \leq 150\lambda$. The application of this method is subject to some stringent conditions that have been discussed in [3] and will not be repeated here. The main restrictions are a limited value of the diffraction angle at the obstacle edge (thereby limiting x_M to some maximum value), and a minimum value of x_M [3].

As a comparison, the SSF based on these three methods was calculated. In Figure 5.34 the three deduced SSF results are shown. Here, the obstacle height $z_{ob} = 200\lambda$. It is seen from Figure 5.34 that even for distances x_M relatively small compared to R the near- and far-field method give quite similar results. Furthermore, the CCIR approach is quite limited in its use, mainly due to the assumptions employed in the knife-edge diffraction term L_{ke} of equation (5.70). The large spikes in this figure are located at distances where in theory nulls appear in the E-plane receiving pattern of the Cassegrain antenna.

The smallest value of x_M used in the calculations is determined by the fact that the aperture cylinder may not be blocked by the obstacle. For this reason also a configuration where the incident (interfering) wave enters the antenna system from the backward angular region was analysed. This corresponds to $\varphi_a = \pi$. Furthermore, the elevation angle was kept constant at $\varphi_e = \pi/9$. In this way, the aperture cylinder is never blocked, even when the terminal is placed very close to the obstacle. In Figure 5.35 the SSFs based on the near-field and the far-field approach are given in case x_M ranges from a minimum value of 25λ to a maximum value of 1000λ , corresponding to normalised distances of respectively $0.001R$ and $0.05R$. For this particular antenna orientation, the CCIR-recommended procedure cannot be used.

From Figure 5.35 it can be seen that there may exist a considerable difference between the results from the near- and far-field approach. Moreover, the difference is not constant as function of x_M . The ripple on both curves is caused by two dominant interfering ray contributions as the antenna moves away from the obstacle. From the figure it is also seen that placing the antenna very close to the obstacle is no guarantee for obtaining a very large

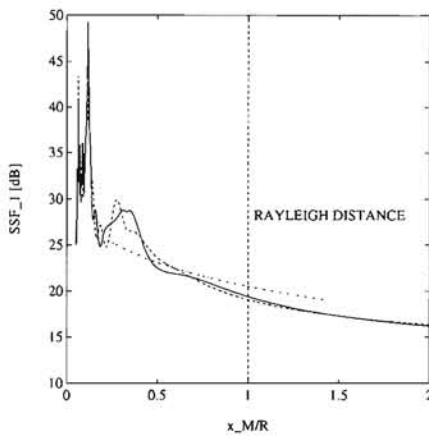


Figure 5.34: SSF of a Cassegrain reflector antenna as function of x_M ; shown are the results for the near-field approach (—), the far-field approach (---), and the CCIR approach (- · - · -).

Data: $D_p = 100\lambda$, $f_p/D_p = 0.4$, $D_h/D_p = 0.15$, $e = 1.67$, $a = 0.00316$, $m = 43.2$, $\varphi_a = 0$, $\varphi_e = \pi/9$, $z_M = 50\lambda$, $z_{ob} = 200\lambda$

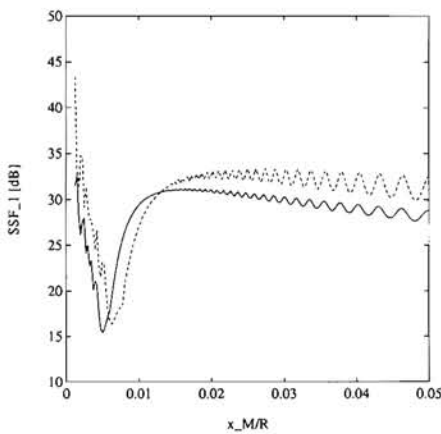


Figure 5.35: SSF of a Cassegrain reflector antenna as function of x_M in the very near field; shown are the results for the near-field approach (—), and the far-field approach (---).

Data: $D_p = 100\lambda$, $f_p/D_p = 0.4$, $D_h/D_p = 0.15$, $e = 1.67$, $a = 0.00316$, $m = 43.2$, $\varphi_a = \pi$, $\varphi_e = \pi/9$, $z_M = 50\lambda$, $z_{ob} = 200\lambda$

SSF. The dip in the near-field curve at $x_M = 0.005R$ is due to the fact that for $x_M > 0.005R$ the ray from the obstacle edge to the sub-reflector is blocked by the main-reflector, while for $x_M < 0.005R$ it is not. The fact that the dip in the far-field result is found at a larger distance x_M is due to the assumption rays that arrive in a parallel way.

From Figures 5.34 and 5.35 it therefore appears that the near-field method as presented in this section is accurate, and that, depending on the relative orientation of the antenna with respect to the obstacle, large differences between the near- and far-field approach can be found. The implication is that the CCIR method is quite unsatisfactory.

5.6.6 Conclusions

The off-axis radiation pattern of a Cassegrain antenna system in the presence as well as in the absence of a half-plane obstacle was calculated. The site-shielding factors obtained are well above 20 dB, even for fairly large distances between antenna and obstacle and small differences in height of the obstacle edge and antenna aperture centre M_p .

For single- and double-reflector antennas with identical diameter and edge illumination, it was shown that the antenna type is not of primary importance in the determination of the SSF, except in the spillover regions. Furthermore, it was shown that the near-field approach provides an accurate result, and, depending on the orientation of the antenna with respect to the obstacle, substantial differences may be found as compared to results given by the far-field method. It was also found that the current CCIR method is very restricted in its use and gives less accurate results than the simple far-field approach. For this reason the use of the far-field approach is recommended in case the antenna and obstacle have a separation larger than $0.25R$. The near-field method, as discussed in this section, should be used in all other cases, especially in situations where the antenna is very close to the obstacle. From the analysis performed in Section 5.3 we know, however, that in many practical cases the far-field approach is the only method tractable for implementation if more than one obstacle edge needs to be considered.

Applications of the shielding model as presented in this section are the evaluation of the shielding of earth stations in (transhorizon) interference problems. The model can also be of primary importance in the determination of the optimal placement of VSAT terminals in urban areas.

Chapter 6

EM field-strength prediction by ray methods

6.1 Introduction

In the last decade, the market for personal telecommunications is growing rapidly. Therefore, paging channels, mobile, broadcast and portable services have more and more the interest of the planners of modern telecommunications systems. Especially Land Mobile Satellite (LMS) systems have a large and continuously increasing interest of system designers and radio-wave propagation engineers. It is obvious that, for planning purposes, it is necessary to investigate whether a certain system will meet the performance criteria required before the system is actually installed. Therefore, a prediction tool from which information regarding the performance of the communications channel can be deduced, is required. Nowadays, most of the LMS field prediction models are based on regression fits to numerical measurement results [79, 80, 81] and fail for some particular urban environments. Furthermore, the theoretical models available are often based on crude approximations and assumptions. So, a more accurate predictive procedure should use a detailed description of the urban environment in order to analyse the channel characteristics for a number of well-defined mobile receiver sites.

In Section 6.2 a deterministic model for field-strength prediction in an urban environment is described, which facilitates the calculation of communication channel parameters such as fading, Doppler shift, and time-delay spread. Different types of multipath wave-propagation phenomena, such as reflection, diffraction, and higher-order combinations of reflection and/or diffraction, are considered. The model is based on the Uniform Theory of Diffraction (UTD) and includes the effects of the non-perfect conductivity of the obstacles and their surface roughness. Moreover, it permits the antenna characteristics of both the transmitter and receiver to be taken into account. Also, the problem of an object in the near-field of the antennas is addressed. Objects with complex shapes are

modelled by a number of standardised objects with suitable dimensions and material properties (Sec. 3.2.4). Particular problems present in conventional prediction methods, such as strong shadowing and reflection, are solved by the new model. In this way, the model extends the region of validity of existing models, and improves the insight into the wave-propagation processes. The major part of this research has been financed by the European Space Agency (ESA).

A simplified model for field strength prediction is proposed in Section 6.3. This model makes use of an advanced ray-tracing scheme, and therefore it is very efficient from a computational point of view. It is believed that, for the derivation of statistical information from the deterministic model, this approach is more useful than the complete deterministic approach because of its efficiency and simplicity. Since in practical situations the communication channel is considered to be reliable only when the relative field strength is above -15 dB relative to the free-space level, the sophisticated prediction model introduced in Section 6.2 can be simplified to include only wave contributions to certain order. This efficient ray-tracing scheme, illustrated by an example, is dealt with in Section 6.3.

The chapter ends with a discussion on the usefulness of the deterministic approach outlined here when applied to other types of telecommunication systems like micro-cellular or terrestrial communication systems (Sec.6.4).

6.2 FiPre: a prediction tool for the planning of mobile and fixed satellite communication services

In this section¹ a ray model for Field Strength Prediction (FiPre) in an urban environment is presented. The model is based on UTD, extended to include effects of non-perfect conductivity and surface roughness of the objects (Sec. 2.6). Through the use of standardised object shapes the user is able to build up the frequency-scaled model of the urban area to be analysed. FiPre is a prediction and planning tool which can be used by system engineers in the design of a mobile or fixed communication service in built-up areas; it delivers accurate information on signal amplitude and phase, time delay and delay-spread profiles, delay-Doppler spectra and so forth. As an example, the results of an analysis carried out with FiPre on a scaled model of the Eindhoven University of Technology (EUT) campus

¹ **Note:** the major part of this section was already published: G.A.J. van Dooren and M. Sforza: *FiPre: a Prediction Tool for the Planning of Mobile and Fixed Satellite Communication Services*, 1st IEEE Symposium on Communications and Vehicular Technology in the Benelux, pp. (6.1-1)-(6.1-8), Delft, The Netherlands, 1993.

are presented.

6.2.1 Introduction

In the last decade, the market demand for conventional mobile and fixed communication services and for new concepts of personal communication networks through hand-held terminals has dramatically increased. Such growing request has spurred the interest of designers and planners and the development of new systems. In this respect, urban and suburban areas are likely to cover a significant niche of such market, hence a thorough understanding of the EM propagation mechanisms and phenomena in these environments is mandatory. To date the analysis of the link impairments and the estimation of their impact on the system performance, especially for the LMS services, has been carried out on the basis of empirical, statistical models. The applicability of these prediction models is generally very limited and often fails to address properly the satellite channel with its inherent characteristics. A deterministic prediction tool not related to a specific urban scenario and based upon canonical and well-known EM laws is therefore strongly needed.

The model, developed at the EUT Telecommunications Division mostly with funding from ESA, is basically a ray model using the well-established UTD approach extended to take into consideration effects due to non perfect conductivity and surface roughness of the objects (Sec. 2.6). The transmit and receive antenna characteristics can also be taken into account by selecting one of the numerous pre-defined radiation patterns available in FiPre. The same approach has led to the parallel development of a similar package, also largely funded by ESA [82].

The user can design his own urban layout with the help of simple standardised block-shaped objects and combinations of them (Sec. 3.2.4). As the position of the observation point can be arbitrarily placed in the urban scaled model, trajectories of vehicles can be simulated at the aim of evaluating the received signal amplitude and phase and the main characteristics of a wide band LMS communication channel: time delay and delay spread, Doppler spectra and delay-Doppler spectrogram. Data are also available for additional narrow-band statistical analyses (not included in the present version of FiPre). Similarly, with a subset of these data FiPre can be also effectively used to solve typical site shielding problems for VSAT networks and fixed broadcasting services (Ch. 5).

In this section the wave-propagation model and the software tool developed are described. Also the processing needed to extract relevant data from the ray-tracer output is discussed. The model will be used to analyse the case of a mobile driving across the EUT campus, and the operating frequencies will be 1.5 and 2.3 GHz. Data will be presented for

the case of strong specular reflection and shadowing effects, the latter usually not modelled in statistical and empirical wave-propagation models. Future improvements for the model are presented, and conclusions are drawn.

6.2.2 Description of prediction model

The wave-propagation model uses Geometrical Optics (GO) complemented with the UTD to account for the bending of EM waves around (sharp) edges. In these theories, the EM wave is assumed to travel along lines in space, which are called rays. In this high-frequency description of EM wave propagation several classes of waves are distinguished, corresponding to the physical propagation mechanisms the waves encounter while propagating from some source S to an observation point Obs . The following classes of EM waves are defined:

1. The direct wave of order k^0 , where k is the free space wavenumber;
2. The reflected wave of order k^0 , where the reflection may either take place at the ground or at an obstacle in the urban environment;
3. The edge-diffracted wave of order $k^{-1/2}$, where the diffraction takes place at a sharp edge of the obstacle;
4. The double-diffracted wave of order k^{-1} , and both diffractions take place at the same obstacle;
5. The corner-diffracted wave of order k^{-1} ;
6. Waves that encounter combinations of the mechanisms just described;
7. Waves that are subject to EM scattering at objects in the vicinity of the observation point. This type of mechanism was included for the modelling of objects that scatter EM energy; it is mainly intended for analysis purposes, and the scatterer is assumed to be a sphere with prescribed equivalent radius.

Some of the wave contributions are shown in Figure 6.1. For analysis purposes also a reference ray was introduced, which is not subject to obstruction. It is identical to the direct wave only in line-of-sight (LOS) conditions. The frequency range for which the model was primarily developed is 1 to 60 GHz. Within this range numerous results have been reported in the literature dealing with the application of the UTD with regard to scattering problems, and data concerning the permittivity of building material is available [49]. Note that for the double-diffraction contribution both diffraction points lie on the

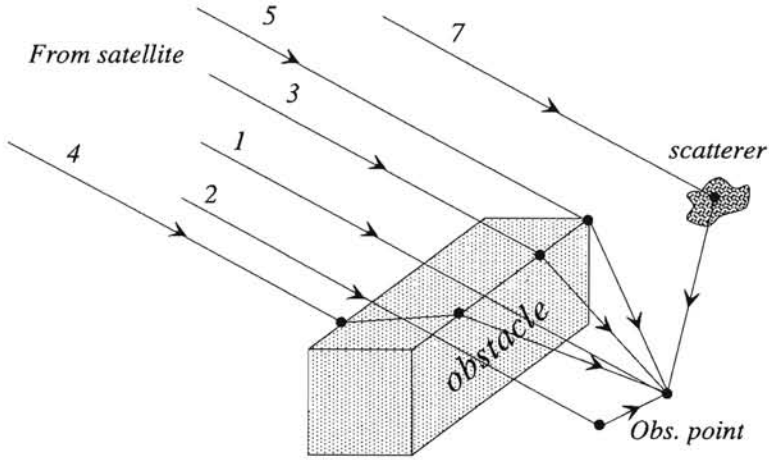


Figure 6.1: An obstacle and various wave contributions included in FiPre.

same obstacle, because the aim is to obtain continuous fields at any arbitrary point in space. It was found that multiple-diffracted contributions from different obstacles need not be incorporated [49, 45].

In general one can say that reflection does not lower the order of the contributions, whereas diffraction lowers it by a factor $k^{-1/2}$. Obviously, only contributions to a certain order of k need to be included in the analysis. In FiPre this order is k^{-1} , corresponding to double and corner diffraction.

In GO, an EM wave is completely described by its polarisation, the amplitude and phase at some reference point, the divergence factor accounting for attenuation as the wave is propagating, and the direction of propagation \hat{k} (Ch. 2). Obviously, all of the aforementioned wave parameters change as the wave interacts with the objects in the environment. The ray-tracer routine of FiPre keeps track of these changes in the wave parameters. As it is assumed that the medium in the urban environment is isotropic and homogeneous, the rays are straight lines in space. This enables the ray-tracer to quickly find reflection and diffraction points using schemes and procedures originally developed for computer graphics [83]. These routines were outlined in Section 3.2.5. In this way also the complex problem of ray obstruction by polygonal obstacles can exactly be solved, and these procedures are very time efficient from a computational point of view.

Because GO and UTD are deterministic methods, S and Obs are well-defined points in space. The wave launched at S interacts with the environment before it reaches Obs and

results in multipath propagation. At the point *Obs* the total electric field \vec{E}^{Obs} is given by

$$\vec{E}^{Obs} \propto \sum_l \vec{E}_l, \quad (6.1)$$

where \vec{E}_l is a wave arriving at *Obs* through one of the propagation phenomena mentioned. At *Obs*, each component \vec{E}_l is weighted in amplitude and polarisation to yield co- and cross-polarised signals at the antenna terminals

$$E^{Obs} = \sum_l G(\vartheta) \vec{E}_l \cdot \hat{e}_{pol,l}(\vartheta) = \sum_l U_l, \quad (6.2)$$

where $\hat{e}_{pol,l}$ is the polarisation vector corresponding to contribution l used to separate the co- or cross-polarised signal. The function G is introduced for spatial weighting of the waves and the angle ϑ is the direction cosine between the boresight direction of the antenna and the direction of arrival \hat{k}_l . If *Obs* is assigned a vectorial velocity, \hat{k}_l is also used to calculate the Doppler signal with magnitude $|U_l|$. Because the waves do not travel along the same propagation path, differences in path length are automatically introduced. Each wave will therefore have its own path length s_l , that, related to the path length of the reference ray s_{ref} , is easily converted to time delays using the speed of light c .

To model the objects in the urban lay-out a standardised obstacle has been used, referred to as the block-shaped obstacle (Sec. 3.2.4). This obstacle is depicted in Figure 6.2 and is specified numerically by its eight corner points, its permittivity and its surface roughness. Note that the edges of the obstacle are straight, and its faces are plane; this considerably simplifies the ray-tracing procedure (Sec. 3.2.5). No further restrictions apply to the obstacle as to the position of its corner points. It is permitted to make logical combinations of the objects, and in this way fairly complex geometries can be assembled. During the study it was found that for this application no circular cylindrical objects are needed in the model [49]. This is caused by the fact that for these types of objects the reflected energy is more important than the diffracted energy as argued in Section 4.6. The reflected waves from the circular-cylindrical structures are replaced by reflected and diffracted contributions from a rectangular cylinder resulting in a slightly modified multipath behaviour. It was found that only in the (small) shadow region behind the object errors are introduced due to this approach [49].

The objects are defined in an Cartesian (x, y, z) coordinate system, of which the xy -plane is assumed to be the ground plane onto which the objects are placed. The number of objects to be analysed is mainly restricted by the CPU time, the number of observation points, and the types of contributions included.

Before the ray-tracer can actually be invoked some input data has to be defined:

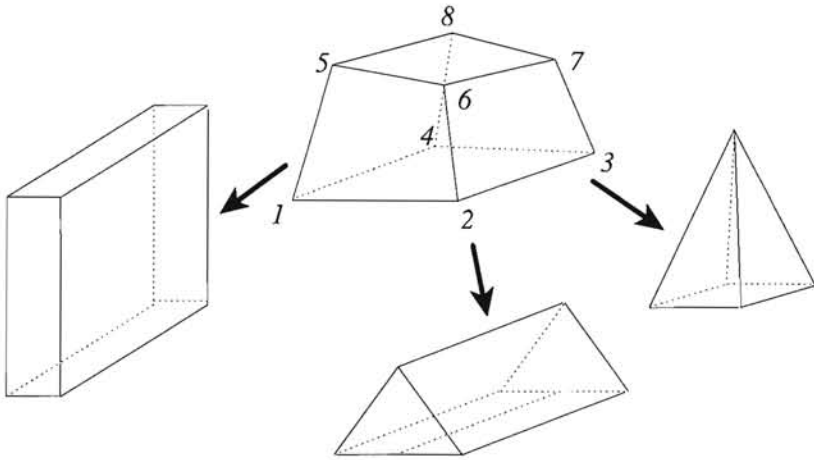


Figure 6.2: The block-shaped obstacle in its various geometries.

1. The source position;
2. The trajectory of the observation point Obs and the number of sample points. In general, this trajectory is a line in space, but also a list with Cartesian coordinates for Obs can be given;
3. The frequency;
4. The source polarisation; included are linear (H/V) and circular (LHC/RHC) polarisation;
5. The types of contributions to be included in the ray-tracer analysis;
6. Optional: a list of scattering points with their equivalent radius;

The ray-tracer algorithm produces a large data file where for each sample point the type of ray (direct, reflected, diffracted, ...), \vec{E}_l , \hat{k}_l and s_l are specified. Using this data file the data postprocessing can be carried out.

6.2.3 Data postprocessing

The types of contributions included in the ray tracer can be individually selected to be taken into account in the data postprocessing. The spatial antenna weight functions G obviously depend on the angle ϑ that the direction of propagation makes with the boresight direction.

The latter is also defined by the user. In the postprocessing routines the following weight functions are implemented:

1. The isotropic pattern;
2. The CCIR reference pattern for small reflector antennas (eq. (5.72));
3. A Bessel pattern derived from a uniformly illuminated circular aperture;
4. A power of a cosine pattern with pedestal (eq. (5.4));
5. The hemi-spherical antenna [49];
6. The toroidal pattern [49];
7. A tabulated antenna pattern defined or measured by the user.

In this section data are presented using the hemi-spherical antenna because the pattern of this antenna type closely resembles the radiation patterns frequently used in mobile communications. The amplitude weight function of this type of antenna is modelled as

$$G(\vartheta) = \begin{cases} \sqrt{2(2n+1)} \cos^n(\vartheta) & , \text{ for } 0 \leq \vartheta \leq \pi/2, \\ 0 & , \text{ for } \pi/2 \leq \vartheta \leq \pi, \end{cases} \quad (6.3)$$

where ϑ is defined as

$$\vartheta = \arccos(-\hat{k}_t \cdot \hat{z}), \quad (6.4)$$

and \hat{z} is the boresight direction of the antenna. This pattern is derived from the cosine pattern of equation (5.4) for $a = 0$. The function $G(\vartheta)$ for some values of n is shown in Figure 6.3 and in this section $n = 5$ was used. Since most of the antenna weight functions are defined analytically within the numerical model, it is very easy to include other functions G if necessary.

6.2.4 Field-strength analysis

By using equation (6.2), the received field at the feed position is readily calculated. An advantage of FiPre is that the same ray-tracer output file can be used more than once, for example, to analyse the impact of excluding some wave contributions in the postprocessing, or to use different antenna weight functions G . Using this postprocessor, blockage effects can be clearly visualised because individual results are available. Note that in the field-strength calculation no attention is paid to the speed of the vehicle and the relative arrival time of the individual waves. Co- and cross-polarised signals are available for all polarisation states defined, and for all types of waves. Currently, only a limited number of them are written to a file in the form of a matrix, but this is straightforward to extend.

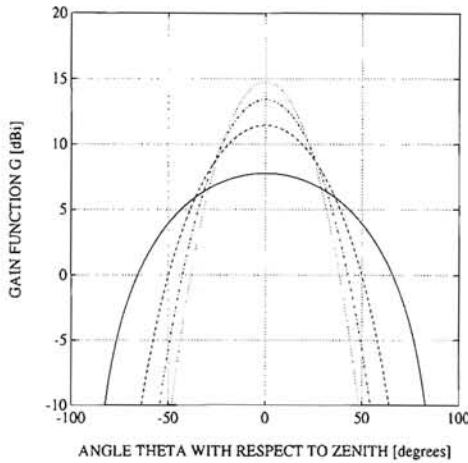


Figure 6.3: Gain function $G(\vartheta)$ for $n = 1$ (————), $n = 3$ (-----), $n = 5$ (- · - · - · - ·), and $n = 7$ (········).

6.2.5 Time-delay analysis

In addition to the direction of propagation \hat{k}_l , in the time delay analysis also attention is paid to the excess path length $\Delta s_l = s_l - s_{ref}$, which yields an excess time delay $\Delta t_l = \Delta s_l/c$. At an observation point *Obs* the time delay response $h(t)$ is given by

$$h(t) = U_0 g(t - \Delta t_0) + \sum_l U_l g(t - \Delta t_l), \quad (6.5)$$

where the subscript 0 indicates the LOS wave and the function $g(t)$ is the channel impulse response. For $g(t) = \delta(t)$ discrete pulses in the time domain are found. For the communications channel having some bandwidth B at carrier frequency ω , the function $g(t)$ is found to be the Fourier transform of the frequency response $H(\omega)$ of the communications channel. From this it is clear that if the reflection and diffraction properties do not change over the bandwidth B , then for the pulse shape function $g(t)$ simply a sinc-function can be used. The requirement that the reflection and diffraction properties do not change over the bandwidth B is usually fulfilled because the relative bandwidth $B/\omega \ll 1$. If this is not the case, the time response should be calculated by performing several frequency analyses to find the frequency response $H(\omega)$. This can elegantly be performed by changing only the individual path lengths in terms of λ , resulting in changing phases as function of frequency. The change in the amplitudes of diffraction and reflection coefficients as function of frequency is neglected. After calculation of $H(\omega)$ the time response $h(t)$ is subsequently

found by applying a Fourier transformation.

The average excess time delay $\bar{\sigma}$ and the time delay spread $\overline{\Delta\sigma}$ can be calculated by using the first and second central moment of $h(t)$. Within the numerical model, these parameters are separately calculated for LOS and optical shadow (OS) regions.

6.2.6 Delay-Doppler analysis

In the delay-Doppler analysis attention is paid to the time delay as well as to the direction of arrival and the vectorial speed \vec{v} of the mobile. The Doppler shift $\Delta\omega_l$ is defined by

$$\Delta\omega_l = -\omega \frac{\vec{v} \cdot \hat{k}_l}{c}. \quad (6.6)$$

The amplitude of the spectral line with Doppler shift $\Delta\omega_l$ obviously is $|U_l|$. The Doppler spectrum $D(\omega)$ is simply the summation of all spectral lines arriving at *Obs*

$$D(\omega) = U_0\delta(\omega - \Delta\omega_0) + \sum_l U_l\delta(\omega - \Delta\omega_l). \quad (6.7)$$

If necessary, also the relative movement of the satellite can be introduced in the Doppler-spectrum calculation.

The delay-Doppler spectrogram is calculated by a two-dimensional mapping of the amplitude terms U_l with respect to the excess time-delay Δt_l and the Doppler shift $\Delta\omega_l$. Using this spectrogram, the time response and Doppler spectrum can be found by projections of the delay-Doppler spectrum along the time and frequency axes, respectively.

6.2.7 Analysis of testcase

As an illustration of the potential and capability of the FiPre model a realistic testcase is analysed. A ray-tracing analysis for two trajectories on the EUT campus has been performed. The trajectories will treat two specific cases frequently encountered in mobile communications, namely LOS propagation with a strong specular reflection, and heavy shadowing. The analysis is carried out at L- and S-band (1.5 and 2.3 GHz) and the signal is assumed to be transmitted from a geostationary satellite at 19W seen from the EUT campus at an elevation of 27°.

The EUT campus as seen from the direction of arrival of the satellite signal is shown in Figure 6.4, while a schematic top-view of the campus is shown in Figure 6.5. In the latter also the two trajectories are depicted. For the trajectory from point 1 to 2 fifteen standardised objects have been included in the ray-tracer analysis, while for the trajectory from 3 to 4 twenty-two objects have been selected. Both trajectories have a length of 200m,

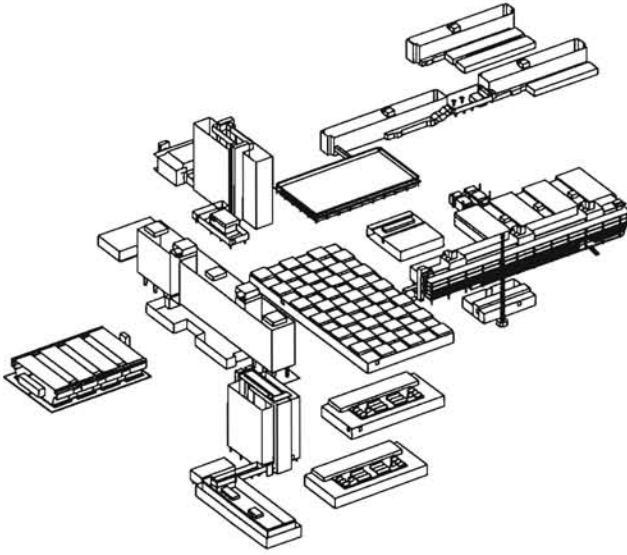


Figure 6.4: The campus of Eindhoven University of Technology as seen from the satellite.

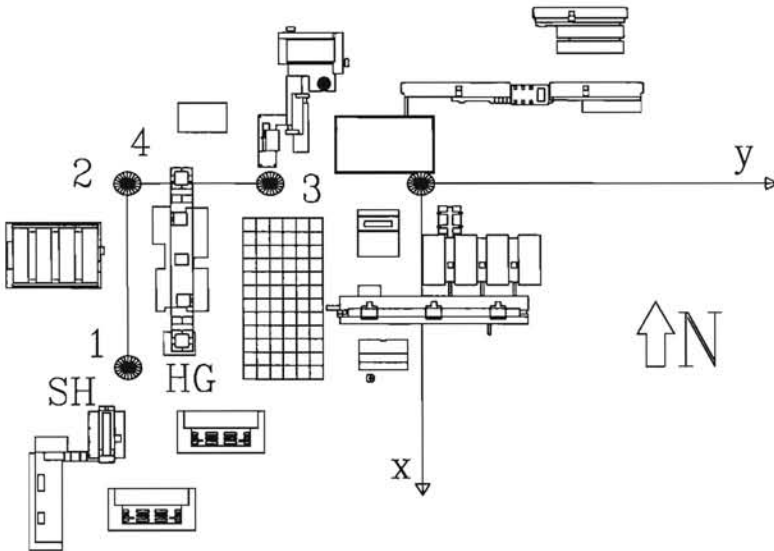


Figure 6.5: Schematic top-view of the EUT campus and trajectories.

and at both frequencies three sample points per wavelength have been used, resulting in 3000 sample points for the analysis at 1.5 GHz, and 4600 for the one at 2.3 GHz. It is assumed that all the buildings are made of brick with a relative humidity of 5%. This results in a complex relative permittivity ϵ_r of $5.3 - 1.25i$ at 1.5 GHz, and $\epsilon_r = 5.3 - 4.1i$ at 2.3 GHz [49].

6.2.8 CPU effort

Obviously, considerable time is needed to perform the analysis. The calculations have been performed on an 486 PC running at a clock speed of 66 MHz. In the following table the CPU time needed can be found for both frequencies and trajectories. For simplicity only the direct, reflection and single-diffraction contributions were included.

Table 6.1: CPU time (in hours:minutes) needed for ray-tracing analysis.

	1 → 2	3 → 4
1.5 GHz (3000)	2:35	4:27
2.3 GHz (4600)	3:56	6:50

The field strength along trajectory 1 → 2 for both frequencies can be found in Figure 6.6. The reflected contribution from building HG for $x < 143m$ can be clearly seen, as well as the shadowing effect at $x = 190m$ from building SH. The fact that the direct incident and reflected field are *in-phase* results in a very strong signal for $x < 143m$. The amplitudes of the reflected fields in Figure 6.6 differ due to the value of ϵ_r at both frequencies.

In Figure 6.7 the received signal along trajectory 3 → 4 for both frequencies is given. In this case strong shadowing from building HG occurs between $x = -210m$ and $x = -120m$. It is found that for the higher frequency the signal level in the deep shadow is lower, while the slope of the received signal near the shadow boundaries, viz. $x = -220$ and $x = -120m$, is higher. This is expected from the theory [5]. For the results presented in Figures 6.6 and 6.7, $\bar{\sigma}$, $\overline{\Delta\sigma}$ and the maximum time delay σ_{max} have been calculated and these values are reported in Table 6.2. Because σ_{max} is a function of the urban environment, it is found that for a fixed geometry the values found are not dependent on the frequency, while $\bar{\sigma}$ and $\overline{\Delta\sigma}$ are also dependent on $|U_l|$ and Δt_l .

Obviously, the most interesting case is the trajectory 3 → 4, where strong shadowing is present. For this trajectory the PDF and CDF of the relative received field were determined and these are reported in Figure 6.8 and 6.9, respectively. The large peaks at a power level of -15 dB are caused by diffraction, while the peaks around 0 dB are caused by reflection

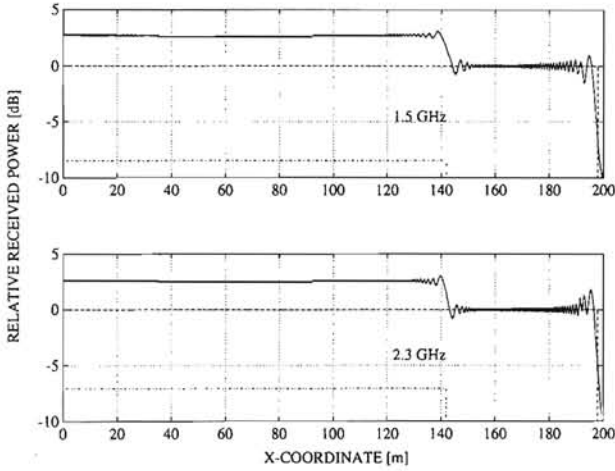


Figure 6.6: Relative received power along trajectory 1 \rightarrow 2 for both frequencies. The total field (—), the direct (---) and reflected field (· · · · ·) are indicated.

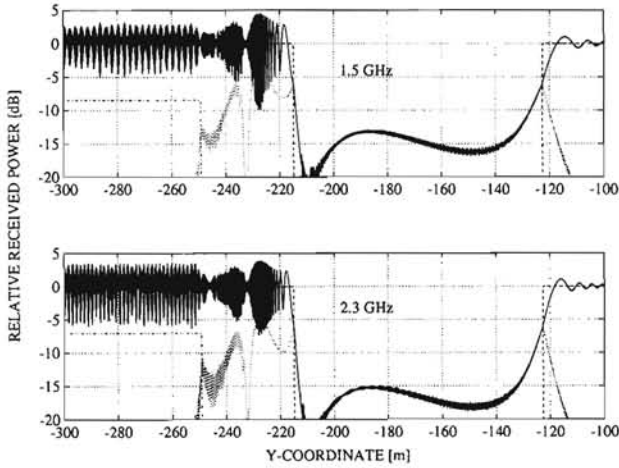


Figure 6.7: Relative received power along trajectory 3 \rightarrow 4 for both frequencies. The total field (—), the direct (---), reflected (· · · · ·) and diffracted field (- · - · - ·) are indicated.

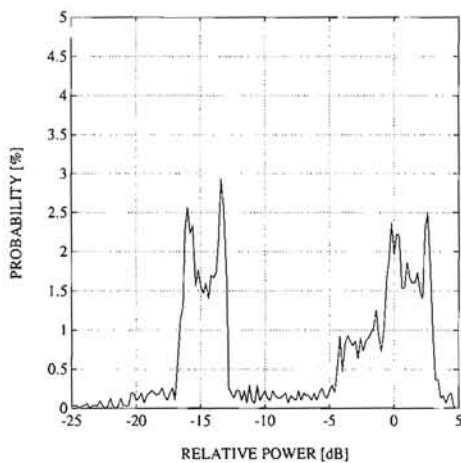


Figure 6.8: Probability density function of relative received power along trajectory 3 \rightarrow 4 at 1.5 GHz.

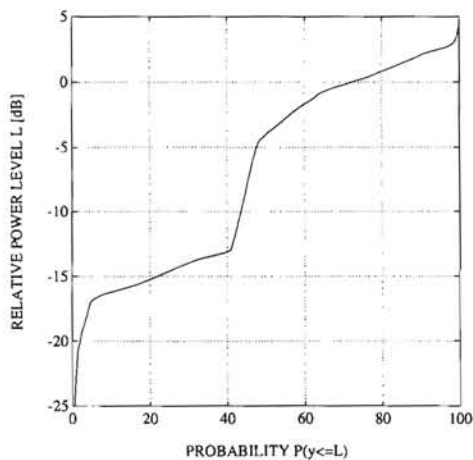


Figure 6.9: Cumulative density function of relative received power along trajectory 3 \rightarrow 4 at 1.5 GHz.

Table 6.2: Excess delay $\bar{\sigma}$, delay spread $\overline{\Delta\sigma}$ and maximum excess delay σ_{max} in LOS and OS regions, in nanoseconds.

	LOS region		OS region		σ_{max}
	$\bar{\sigma}$	$\overline{\Delta\sigma}$	$\bar{\sigma}$	$\overline{\Delta\sigma}$	
1.5 GHz, 1 \rightarrow 2	177	20	9	24	585
1.5 GHz, 3 \rightarrow 4	113	8	19	17	683
2.3 GHz, 1 \rightarrow 2	177	19	7	21	585
2.3 GHz, 3 \rightarrow 4	113	8	19	17	683

and the direct contribution. From this figure it is seen that for 20% of the time the signal level exhibits an attenuation of 15 dB or more, and that for 30% of the time it is higher than the LOS level.

The Doppler spectrum for a mobile travelling at a speed of 50 km/h along trajectory 3 \rightarrow 4 at 1.5 GHz is given in Figure 6.10. For this case the maximum Doppler shift is

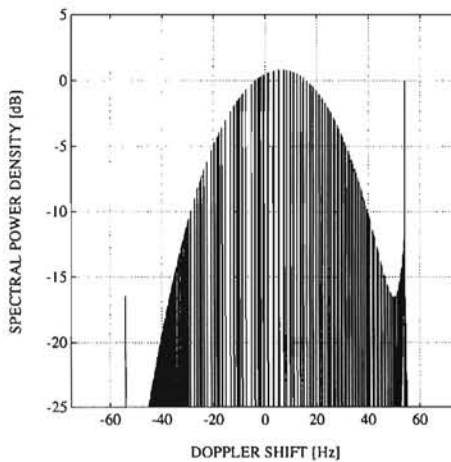


Figure 6.10: Doppler spectrum along trajectory 3 \rightarrow 4 at 1.5 GHz for a mobile at a speed of 50 km/h.

± 55 Hz. Because the mobile is moving towards the source, the maximum of the Doppler spectrum occurs at a positive Doppler shift. The delay-Doppler spectrogram is shown in Figure 6.11. The time response and the Doppler spectrum can be found using the delay-Doppler spectrogram by projections of the data onto both side planes.

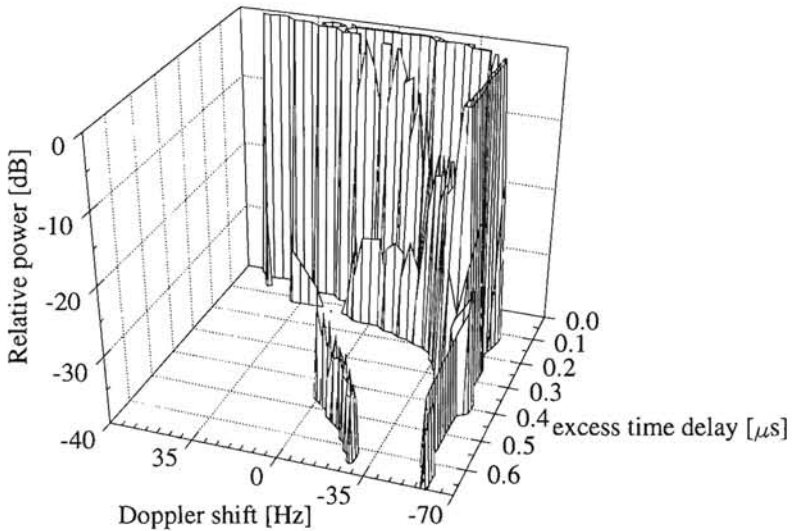


Figure 6.11: Delay-Doppler spectrogram along trajectory 3 \rightarrow 4 at 1.5 GHz.

6.2.9 Future improvements

The FiPre prediction model is still under development and future improvements will include obstacle transmittivity, improved ray-racing procedures and a moving source for simulation of non-geostationary satellites. Also scattering from vegetation is intended to be included. Currently, the statistical methods need to be invoked using external procedures. A more elegant way is to do this inside the FiPre postprocessor. Also other types of contributions (multiple-reflected and diffracted) will be implemented.

6.2.10 Conclusions

In this section the major features of a prediction tool originally developed for the simulation of the most significant parameters of an LMS communication channel have been presented and discussed. This simulation package is particularly suited for the study of the narrow and wide band channel characteristics of any LMS system serving built-up areas. Significant results of some of the available functions of the postprocessor have been given, showing the potential of such LMS prediction tool. Due to its inherent capabilities and the large use of well-established UTD routines, the simulation tool is also very effective for the planning of fixed communication systems in urban environments such as broadcasting services and site shielding for VSAT networks (Ch. 5).

6.3 An efficient model for field-strength prediction

In practice, system engineers consider the satellite-communication channel to be reliable only when the field strength relative to the free-space level is above some threshold. Practical values of this threshold are -15 and -16 dB. This level can easily be reached, for example in regions where heavy shadowing occurs, as shown in Figure 6.7. This indicates that below this threshold the channel cannot be used, and hence there is no need for calculating the field strength in a very accurate way.

If the prediction model is used to derive statistical information like level crossing rates and fading statistics, a more advanced ray tracing scheme can prove to be very helpful. Based on the FiPre model described in the previous section such a scheme is fairly easy to derive [55]. Instead of finding all wave contributions at every observation point, a selective search is made, where attention is paid only to the highest-order contribution present for that observation point. This is schematically visualised in Figure 6.12. The ray-tracing

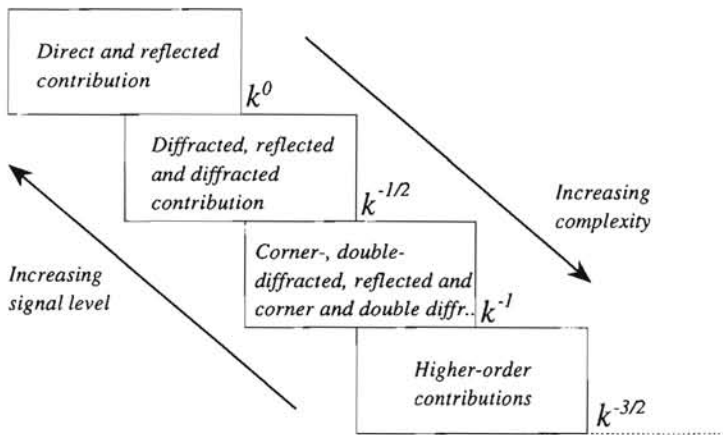


Figure 6.12: Schematic flow-diagram for modified ray-tracing scheme.

procedure is started by determining whether the direct and reflection contributions exist. If so, the ray-tracing analysis is finished and the signal level at the observation point is calculated based on the field contributions found. If not, the search for higher-order field contributions continues, e.g. edge-diffracted, and combinations of reflection and diffraction. If these contributions exist, the procedure is halted and the signal level is calculated. If not, the search continues. This simplified approach proves to be very time efficient, as will be demonstrated in the following.

The 'highest-order' calculation scheme is applied to the same configuration as used in

Figure 3.12 of Section 3.2.4. The SSF on the observation line defined is shown in figure 6.13. The left side of this figure shows the SSF when taking into consideration all the wave contributions that are present, as in Figure 3.12. Since the SSF curve is symmetric with respect to the line $y_p = 0$, the result on the right side gives the result obtained using the highest-order contribution scheme. For $y_p > 116m$ only the direct wave of order k^0 is used. For $43m < y_p < 116m$ a single diffraction contribution of order $k^{-1/2}$ is the highest, and behind the screen only double-diffraction contributions of order k^{-1} are present. Obviously this approach does not result in continuous fields when traversing shadow boundaries. The major differences between the left and right part of Figure 6.13 appear around the shadow boundaries. From a calculation point of view, however, the ‘highest-order’ approach has the advantage that it asks for very little CPU time as compared to the conventional approach. Using this reduction scheme, a very efficient ray tracing procedure for simulations can be developed, obviously at the expense of accuracy.

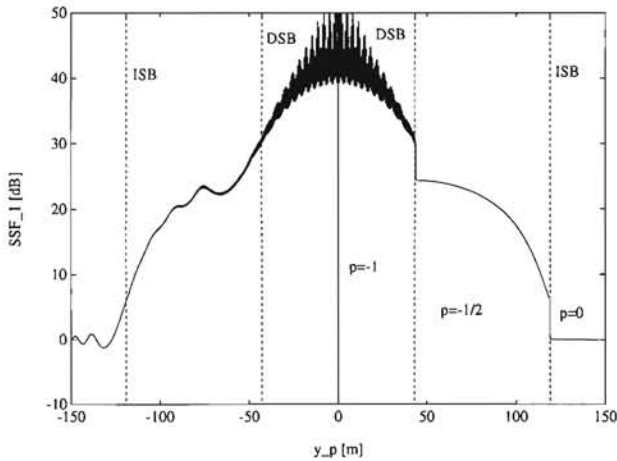


Figure 6.13: SSF behind the rectangular block as function of y_p : the result including all wave contributions is shown on the left side of the figure, while the result of the ‘highest-order’ approach is shown on the right side. The shadow boundaries are indicated and the order of contributions are given as k^p .

Data: $x_p = 250m$, $z_p = 1.5m$, $d \times h \times z_{ob} = 20m \times 86m \times 68m$, $\lambda = 0.3m$

6.4 Discussion

It should be noted that in the previous section attention has been paid to an LMS system only. This has been done on purpose, because it is believed that the accurate UTD field-strength prediction model is needed only for a limited number of situations. This is explained using Figure 6.14.

The LMS application studied here is shown in Figure 6.14a. In this geometry only a limited number of objects surrounding the mobile is of importance in the determination of the field strength at the mobile receiver location. This can be understood by the fact that the receiver only 'sees' a limited number of buildings, because the others are obstructed by the visible ones. To first order, only the visible objects need to be taken into account in the field strength analysis, as shown schematically by the dashed semi-circle in Figure 6.14a.

An identical argumentation holds for the case of micro-cellular systems (Fig. 6.14b). In this application the transmitter is usually placed at a fairly high position, and the coverage area per transmitter is relatively small. In this pseudo-LMS geometry, there is also a visible region associated with the receiver. It is expected that the model proposed here can also be applied to micro-cellular systems as long as the transmitter is placed fairly high, i.e. the angle of arrival is quite large. If the antenna is placed low, for example to reduce the size of the coverage cell, modifications have to be introduced to the ray-tracing algorithm, possible in the form of higher-order diffraction contributions.

The geometry encountered in the terrestrial application, shown in Figure 6.14c, is rather different. Here the distance between the transmitter and the mobile receiver is usually quite large, and the angle of arrival with the groundplane at the receiver consequently is very small. Hence a visible region around the receiver as well as around the transmitter is identified. Also the area in between transmitter and receiver automatically becomes important, because it influences the EM field arriving at the receiver.

So for applications where the angle of arrival with respect to the ground plane is quite large, as in the LMS and the micro-cellular applications, the GO/UTD model can be used because the interaction of the wave arriving at the receiver with the environment is restricted to the 'visible' region just identified. For the terrestrial application sketched in Figure 6.14c it is concluded, however, that the use of the deterministic model is too intensive from a computational point of view. More important, it is not needed because, for large transmitter-receiver separation, the variability of the field is quite low due to the settling of the field. The average amplitude is nearly constant, and its standard deviation is quite small because the influences of the side edges and faces of the buildings can be neglected due to obstruction. In this case, a statistical analysis can prove to be more advantageous

than the deterministic one proposed here. Up to know, the point where the results from the deterministic and statistical models meet is unknown. A statistical approach using deterministic wave-propagation models could consist of varying the properties of the field incident upon the region close to the receiver. In this case, the field strength at the receiver is calculated taking into account only this region, as performed in the LMS geometry. The incident field, however, would have a statistical part in its wave parameters, e.g. the angle of arrival or its amplitude. Actually this is some kind of spectral approach, and it is known from the literature that transhorizon-propagating fields due to ducting have a very narrow spectrum of the angle of arrival around zero, which is the direction of propagation parallel to the earth's surface. The average and the variance of the field strength at the receiver can be calculated by assigning to each spectral line, i.e. angle of arrival, an amplitude and phase according to some statistical distribution. In this case the problem of finding the ray paths in a three-dimensional geometry is transferred to the problem of finding the appropriate statistical distributions of the angular spectrum. Also this alternative would be very time consuming from a computational point of view.

In the deterministic model the CPU effort can be made smaller by taking cross sections through the urban environment and effectively taking into account a two-dimensional geometry instead of the original three-dimensional one. Effects of scatter and diffraction out of the great circle plane are accounted for by effective scatterers, as proposed in [63, 64]. Using this approach, however, few accurate results have been obtained yet, and hence the usefulness of this approach should be doubted. It seems as if too few details concerning the actual geometry are taken into account. This conclusion is supported by the results reported in [84, 85], where an upper bound for the path length for the applicability of their GTD model is found as function of the difference in the transmitter and receiver height. The applicability of the GTD model is extended as the difference in transmitter-receiver height is increased. This confirms the usefulness of the 'visibility' regions close to the receiver as performed in this dissertation.

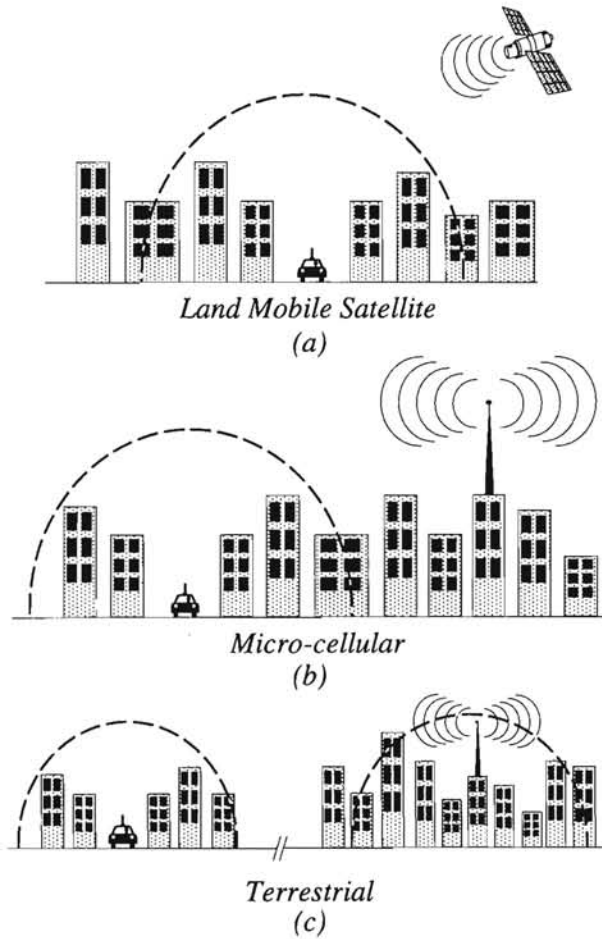


Figure 6.14: Regions close to the transmitter and mobile receiver in various communications systems: a Land Mobile Satellite system (a), a micro cellular system (b), and a terrestrial system (c).

Chapter 7

Summary and conclusions

Currently available statistical field-strength prediction models for urban environments are in most cases based on measurement results and are therefore suitable for one generalised geometry only. The effects of strong shadowing by buildings and strong specular reflections are usually not adequately modelled. To overcome this deficiency, a deterministic field-strength prediction model can be used which accepts a detailed description of the urban environment. In this thesis such a model is applied to two practical problems frequently encountered in telecommunications engineering, viz. the determination of the signal strength at the terminals of a reflector antenna placed behind an isolated obstacle, and the prediction of the field strength from a satellite signal in a mobile that travels through an urban environment. Geometrical Optics (GO) complemented with the Uniform Theory of Diffraction (UTD) are used to compose a reliable and accurate wave propagation model.

In *Chapter 2* the high-frequency representation of electromagnetic (EM) waves was discussed. Several propagation mechanisms such as line-of-sight propagation, reflection, edge diffraction, and higher-order diffractions were reviewed and theoretically analysed. The (heuristic) extension of UTD to account for non-perfect conductivity and surface roughness of the obstacle was also examined. Furthermore, an approximate theory for the inclusion of edge-irregularity effects was presented. Also, the UTD for reflection and diffraction by a convex body was reviewed, and a formal treatment of EM wave propagation in terms of wave parameters, e.g. principal directions and associated principal radii of curvature and direction of propagation, was presented.

The theory for EM wave propagation discussed in *Chapter 2* was used in *Chapter 3* to formulate a model for the calculation of the field strength in the surroundings of an obstacle with a predetermined shape. The method of site shielding was introduced, and a new consistent definition of the site shielding factor (SSF) correctly incorporating the effect of the obstacle placement on the unwanted as well as the wanted signal, was given. Theoretical results for the SSF of the half-plane, the finite-width screen, the metallic cylinder and the block-shaped obstacle were presented. The use of the latter type of obstacle proved to be

very efficient because it can easily be specified numerically and may therefore take many different shapes, because it has plane faces that simplify the ray-tracing procedures, and because it can be used to 'build up' nearly any urban environment.

An efficient ray-tracing scheme to be used in conjunction with the block-shaped obstacle was presented. Also an engineering approach for site shielding calculations incorporating the finite-width screen was derived from the GO/UTD model in order to extend the currently available SSF prediction models provided by the CCIR. Results on the average and minimum SSF were presented. The CCIR models cover only very simple geometries, and therefore have a limited range of applicability. In the framework of the collaboration within the COST 235 project, comparisons between results from three different field-strength prediction models (GO/UTD, Fresnel surface integral and parabolic equation method) were performed for the half-plane obstacle, the finite-width screen and the rectangular block. In all cases considered good agreement between results was obtained, and it was found that, for isolated obstacles, all three methods can be used to predict or analyse the SSF. Each of these methods was found to have its own specific advantages and disadvantages. We believe that GO/UTD is the most versatile model and that it gives the best insight. The parabolic equation method, on the other hand, is very adequate to analyse complex geometries, obviously at the expense of CPU time.

In *Chapter 4* practical verifications of the models discussed in *Chapter 3* were presented. The measurements were performed using scaled obstacles at a frequency of 50 GHz using a vector network analyser. A novel calibration scheme was necessary in order to carry out the measurements in an ordinary room, and data processing techniques were needed to suppress undesired reflections from nearby objects and walls. The calibration procedure as well as some measurement results were presented in *Section 4.2*. Comparisons between theoretical and measured results for diffraction by a finite-width screen (*Sec. 4.3*), the metallic block-shaped obstacle (*Sec. 4.4*), a dielectric block-shaped obstacle (*Sec. 4.5*), and single and multiple cylinders (*Sec. 4.6*) were presented. Not only results as function of probe position, but also time-domain measurements showed excellent agreement with theoretically predicted results. The theory presented in *Chapter 2* concerning double, slope and corner diffraction by a pair of joined dielectric wedges was verified and proved to be sufficiently accurate for the applications studied here. It was found that the theory presented in *Chapter 2* can very well be used for field-strength prediction behind obstacles.

The postulate of GO and UTD that waves propagate independently in space was confirmed by time-domain measurements, and the polarisation dependence of the diffracted fields was verified in the frequency domain as well as in the time domain. It was found that the polarisation dependence of the field strength behind a dielectric obstacle is small,

as was predicted by the extended theory.

In addition, the lower limit of applicability of the UTD for convex bodies was theoretically and experimentally assessed. Also for the measurements incorporating cylindrical objects the correspondence between theory and experiment was very good.

Chapter 5 focused on the so-called near-field problem for reflector antennas, which corresponds to a combined treatment of obstacle-edge and antenna-rim diffraction. In most popular ray-based field-strength prediction models the antenna spatial filtering is accounted for by the introduction of antenna weight functions. In many cases, however, the antenna is placed very close to the obstacle (within the Rayleigh distance) and consequently this combined analysis is not permitted. In this thesis we have concentrated on single- and double-reflector antennas shielded by a (hypothetical) half-plane. For both antenna types the off-axis receiving properties were discussed, and the SSF as function of antenna-obstacle separation and antenna orientation were presented. It was found that outside the spillover regions the antenna type is not of primary importance in the evaluation of the SSF, provided that the antennas have identical diameter and edge illumination. For half-plane shielding of the antenna it was found that the far-field method, i.e. a separate treatment of obstacle and antenna diffraction, also gives reasonable results, even if the obstacle-antenna separation d is smaller than the Rayleigh distance R . A lower limit for the applicability of the far-field method was found to be $d = R/4$, although this value in a small measure depends on the antenna geometry in terms of edge illumination and orientation. The model provided by the CCIR for the antenna shielding problem proved to be very restricted in its use.

From the discussion concerning the introduction of antenna weight functions it was concluded that for finite-width screen shielding of a parabolic reflector antenna the near-field method needs to be used up to a very large separation between obstacle and antenna, viz. $d > 6R$. This indicates that, for obstacles of finite extent, the Rayleigh distance is an unreliable parameter for deciding on what method to use. A broadband analysis revealed that if an averaging of the received signal over a frequency band is allowed, as is performed in a radio receiver, the results predicted by the far-field method considerably deviate from those predicted by the near-field model. Implications of using the far-field approach instead of the near-field approach for other antenna configurations were identified. Results predicted by a field-strength prediction model based on far-field antenna weighting should be used with caution. In many practical cases, however, the far-field method is the only one amenable for implementation in a numerical wave-propagation model.

In *Chapter 6* the GO/UTD model was used to predict the field strength in an urban environment schematically represented as a collection of appropriately-dimensioned block-

shaped obstacles. The prediction tool developed was used to derive communication parameters such as field strength, time-delay profile, Doppler spectrum and secondary statistics of these parameters for a mobile travelling through the urban scenery. As a test case, the field strength along two trajectories at the EUT campus was determined for signals at a frequency of 1.5 and 2.3 GHz, which are the frequencies to be used for future mobile communication systems. Parameters such as the probability density function and the cumulative distribution of the field strength were presented. Together with digital databases of urban areas, the model proposed is expected to be a powerful tool for analysis and prediction purposes; its validity was already demonstrated in Chapter 4. It should, however, not be considered as a replacement of current statistical field-strength prediction models, but rather as a complement. In many situations insufficient information on the environment to be analysed is available for a deterministic model to be used, in which case one should resort to the use of statistical models. It is expected that in the near future, when most of the urban-area information has been digitised, the model will reveal itself as a calculation tool capable of predicting the field strength in a very accurate way. The model can possibly be extended to also include statistical effects such as atmospheric attenuation, scattering from passing vehicles, trees and foliage, so that *statistical* information of the communications channel can be extracted from the *deterministic* model proposed in this dissertation.

Note that attention has been paid to Land Mobile Satellite (LMS) applications only, because it is believed that for terrestrial applications, i.e. when the transmitter and receiver are both placed close to the earth's surface, the current model has only a limited applicability. Reasons for this are the large amount of time needed to perform the higher-order diffraction calculations, and the fact that the average amplitude in a terrestrial communication system can be predicted by statistical methods in a fairly accurate way. Nevertheless, the deterministic model can be used to analyse 'problem areas' where the statistical methods fail, e.g. regions with reflection and strong shadowing.

In conclusion, it is believed that a deterministic wave-propagation model as developed, described and verified in this dissertation can effectively be used for field-strength prediction, with applications such as site shielding and other obstacle-diffraction problems. Although other methods exist to describe the interaction process of EM wave and obstacle, a ray-based method offers a considerable insight and proves to be more than sufficiently accurate for the applications studied in this thesis. The models developed here are expected to be the basis for a complement to and an extension of currently available models for field-strength

prediction, that in many cases have a statistical character. Communication engineers may benefit from the results predicted by the deterministic models in the planning stages of new telecommunications services and in the analysis of operational systems.

References

- [1] International Telecommunications Union, CCIR Recommendations 1992, "Propagation by diffraction", *Recommendations of the CCIR*, Studygroup 5, Rec. 526-2, Geneva, 1992.
- [2] CCIR, Plenary Assembly, "Earth-station antennas for the fixed satellite service", *Recommendations and Reports of the CCIR*, vol. IV-1, Rep. 390-5, Geneva, 1986.
- [3] P.M.J. Scheeren, "Reduction of transhorizon radio interference in satellite earth stations", Ph.D. thesis, Eindhoven University of Technology, 1988.
- [4] J.B. Keller, "Geometrical Theory of Diffraction", *Journ. Opt. Soc. Am.*, vol. 52, no. 2, pp. 116-130, 1962.
- [5] R.G. Kouyoumjian and P.H. Pathak, "A Uniform Geometrical Theory of Diffraction for an edge in a perfectly conducting surface", *Proc. IEEE*, vol. 62, no. 11, pp. 1448-1462, 1974.
- [6] D.S. Ahluwalia, R.M. Lewis, and J. Boersma, "Uniform Asymptotic Theory of Diffraction by a plane screen", *SIAM Journ. Appl. Math.*, vol. 16, no. 4, pp. 783-807, 1968.
- [7] S.W. Lee and G.A. Deschamps, "A Uniform Asymptotic Theory of Edge diffraction", *IEEE Trans. Ant. Prop.*, vol. AP-24, no. 1, pp. 25-34, 1976.
- [8] E. Yazgan and M. Safak, "Comparison of UTD and UAT in axially symmetric reflectors", *IEEE Trans. Ant. Prop.*, vol. AP-35, no. 1, pp. 113-116, 1987.
- [9] J.W. Wallenburg, "Diffractie aan een 'finite-width screen' volgens de ILDC methode en GTD", Report of Training Work (in Dutch), Eindhoven University of Technology, Faculty of Electrical Engineering, Telecommunications Division, 1992.
- [10] I. Kay and J.B. Keller, "Asymptotic evaluation of the field at a caustic", *J. Appl. Physic.*, vol. 25, pp. 876-883, 1954.
- [11] D.A. McNamara, C.W.I. Pistorius, and J.A.G. Malherbe, "Introduction to the Uniform Geometrical Theory of Diffraction", Artech House, Boston, 1990.
- [12] J. Boersma, "Computation of Fresnel integrals", *Math. Comp.*, vol. 14, p. 380, 1960.
- [13] P.M.J. Scheeren, Dutch PTT, private communications, 1990.
- [14] W.D. Burnside, M.C. Gilreath, B.M. Kent, and G.L. Clerici, "Curved edge modification of compact range reflectors", *IEEE Trans. Ant. Prop.*, vol. AP-35, no. 2, pp. 176-182, 1987.

- [15] R.G. Kouyoumjian, "The geometrical theory of diffraction and its applications", in R. Mittra, editor, *Numerical and asymptotic techniques in electromagnetics*, Springer-Verlag, Berlin, 1975.
- [16] J.M. van Houten, P.J.I. de Maagt, M.H.A.J. Herben, and G. Brussaard, "The second order diffracted field of a symmetrical parabolic reflector antenna", *Proceedings of the 1993 international symposium on radio propagation (ISR/P '93)*, pp. 654-657, CIE Radio Propagation Society, 1993.
- [17] F.A. Sikta, W.D. Burnside, T.T. Chu, and L.J. Peters Jr., "First order equivalent current and corner diffraction scattering from flat plate structures", *IEEE Trans. Ant. Prop.*, vol. AP-31, no. 4, pp. 584-589, 1983.
- [18] Y.T. Lo and S.W. Lee, *Antenna Handbook*, Van Nostrand Reinhold Company, New York, 1988.
- [19] N.D. Taket and R.E. Burge, "A Physical optics version of the Geometrical Theory of Diffraction", *IEEE Trans. Ant. Prop.*, vol. AP-39, no. 6, pp. 719-731, 1991.
- [20] T. van Mierlo, "On the use of the PO-GTD formulation", Report of Training Work, Eindhoven University of Technology, Faculty of Electrical Engineering, Telecommunications Division, 1993.
- [21] S.W. Lee, Y. Rahmat-Samii, and R.C. Menendez, "GTD, ray field, and comments on two papers", *IEEE Trans. Ant. Prop.*, vol. AP-26, no. 2, pp. 352-354, 1978.
- [22] R. Tiberio and R.G. Kouyoumjian, "A uniform GTD solution for the diffraction by strips illuminated at grazing incidence", *Radio Science*, vol. 14, no. 6, pp. 933-941, 1979.
- [23] R. Tiberio and R.G. Kouyoumjian, "An analysis of diffraction at edges illuminated by transition region fields", *Radio Science*, vol. 17, no. 2, pp. 323-336, 1982.
- [24] R. Tiberio and R.G. Kouyoumjian, "Calculation of the high-frequency diffraction by two nearby edges illuminated at grazing incidence", *IEEE Trans. Ant. Prop.*, vol. AP-32, no. 11, pp. 1186-1196, 1984.
- [25] M. Schneider and R.J. Luebbers, "A general, uniform double wedge diffraction coefficient", *IEEE Trans. Ant. Prop.*, vol. AP-39, no. 1, pp. 8-14, 1991.
- [26] K.A. Chamberlin and R.J. Luebbers, "An evaluation of Longley-Rice and GTD propagation models", *IEEE Trans. Ant. Prop.*, vol. AP-30, no. 6, pp. 1093-1098, 1982.
- [27] R.J. Luebbers, "Finite conductivity uniform GTD versus knife edge diffraction in prediction of propagation path loss", *IEEE Trans. Ant. Prop.*, vol. AP-32, no. 1, pp. 70-76, 1984.
- [28] P. Beckman and A. Spizzichino, *The scattering of electromagnetic waves from rough surfaces*, Pergamon Press, Oxford, 1963.

- [29] S-Y. Kim, J-W. Ra, and S-Y. Shin, "Diffraction by an arbitrary-angled dielectric wedge: part I - Physical optics approximation", *IEEE Trans. Ant. Prop.*, vol. AP-39, no. 9, pp. 1272-1281, 1991.
- [30] S-Y. Kim, J-W. Ra, and S-Y. Shin, "Diffraction by an arbitrary-angled dielectric wedge: part II - Correction to physical optics solution", *IEEE Trans. Ant. Prop.*, vol. AP-39, no. 9, pp. 1282-1292, 1991.
- [31] R.J. Luebbers, "A heuristic slope diffraction coefficient for rough lossy wedges", *IEEE Trans. Ant. Prop.*, vol. AP-37, no. 2, pp. 206-211, 1989.
- [32] B.B. Baker and E.T. Copson, "*The mathematical theory of Huygens' principle*", Oxford University Press, Oxford, 2nd edition, 1950.
- [33] R.J. Luebbers, "Comparison of lossy wedge diffraction coefficients with application to mixed path propagation loss prediction", *IEEE Trans. Ant. Prop.*, vol. AP-36, no. 7, pp. 1031-1034, 1988.
- [34] G.D. Maliuzhinets, "Excitation, reflection and emission of surface waves from a wedge with given impedance faces", *Sov. Phys. Dokl.*, vol. 3, pp. 752-755, 1958.
- [35] J. Dijk, A. v.d. Vorst, L. Wijdemans, F.M. Boumans, and W.T.E. Vaessen, "Microgolfdemping bij bouwmaterialen t.b.v. het stoorniveau in computerruimtes", Report, Eindhoven University of Technology, Faculty of Electrical Engineering, Telecommunications Division, 1988.
- [36] Y.I. Leshchanskii and N.V. Ul'yanychev, "Computation of dielectric characteristics for brick and concrete with varying moisture content", *Defektoskopiya*, vol. 1, no. 7, pp. 34-39, 1980.
- [37] A. Michaeli, "Equivalent edge currents for arbitrary aspects of observation", *IEEE Trans. Ant. Prop.*, vol. AP-32, no. 3, pp. 252-258, 1984.
- [38] P.H. Pathak, W.D. Burnside, and R.J. Marhefka, "A uniform GTD analysis of the diffraction of electromagnetic waves by a smooth convex surface", *IEEE Trans. Ant. Prop.*, vol. AP-28, no. 5, pp. 631-642, 1980.
- [39] COST 235 Management Committee, "A note on the definition of the site shielding factor", *COST 235 internal communications*, vol. CP68, 1992.
- [40] C. Vyncke and A. Vander Vorst, "Site shielding evaluation of a ground-based antenna as a function of frequency", *JINA 1992 Antenna Symposium*, pp. 649-652, Journées Internationales de Nice sur les Antennes, 1992.
- [41] A. Sommerfeld, "Mathematische Theorie der Diffraktion", *Mathematische Annalen*, vol. 47, no. 1, pp. 317-373, 1895.
- [42] Z. Wu, T.S.M. Maclean, M.J. Mehler, and D.J. Bagwell, "Radio wave propagation in presence of finite width knife edges", *Radio Science*, vol. 24, no. 3, pp. 361-368, 1989.

- [43] M.G.J.J. Klaassen, "Theoretical modelling and practical verification of the Site Shielding Factor of a finite-width screen with knife edges", M.Sc. thesis, Eindhoven University of Technology, Faculty of Electrical Engineering, Telecommunications Division, 1992.
- [44] H.J.F.G. Govaerts, "Electromagnetic-wave scattering by a circular cylinder of arbitrary radius", M.Sc. thesis, Eindhoven University of Technology, Faculty of Electrical Engineering, Telecommunications Division, 1993.
- [45] G.A.J. van Dooren, "Electromagnetic diffraction models for the shielding of single- and dual-reflector antennas by obstacles with simple shapes", Report ISBN 90-5282-162-3, Eindhoven University of Technology, 1991.
- [46] S.W. Lee, P. Cramer, K. Woo, and Y. Rahmat-Samii, "Diffraction by an arbitrary subreflector: GTD solution", *IEEE Trans. Ant. Prop.*, vol. AP-27, no. 3, pp. 305-315, 1979.
- [47] W.V.T. Rusch and O. Sørensen, "On determining if a specular point exists", *IEEE Trans. Ant. Prop.*, vol. AP-27, no. 1, pp. 99-101, 1979.
- [48] S.W. Lee, "Differential geometry for GTD applications", Report no. 77-21, Electromagnetics Laboratory, University of Illinois at Urbana-Champaign, 1977.
- [49] G.A.J. van Dooren, "Electromagnetic field strength prediction model for urban environments", Final report for ESA/ESTEC contract PO 123078, Eindhoven University of Technology, Faculty of Electrical Engineering, Telecommunications Division, 1993.
- [50] M.P.M. Hall, chairman COST 235, "COST project 235 activities on radiowave propagation effects on next generation fixed-service terrestrial telecommunications systems", *Proc. of the 8th Int. Conf. Ant. Prop. (ICAP), Edinburgh*, vol. 2, pp. 655-659, Institute of Electrical Engineers (IEE), 1993.
- [51] J.H. Whitteker, "Diffraction over a flat-topped terrain obstacle", *IEE Proceedings Pt. H*, vol. 137, no. 2, pp. 113-116, 1990.
- [52] M. F. Levy, "Parabolic equation modelling of propagation over irregular terrain", *Electron. Lett.*, vol. 26, pp. 1153-1155, 1990.
- [53] C.J. Haslett, "Multiple path diffraction by rectangular buildings", *Electron. Lett.*, vol. 29, no. 6, pp. 539-540, 1993.
- [54] M. F. Levy, "Diffraction studies for microcellular applications", *Proc. of the 8th Int. Conf. Ant. Prop. (ICAP), Edinburgh*, vol. 1, pp. 76-79, Institute of Electrical Engineers (IEE), 1993.
- [55] G.A.J. van Dooren and M.H.A.J. Herben, "Electromagnetic wave diffraction by obstacles with application to field strength prediction and interference reduction", *accepted for publication in Journal of Electromagnetic Waves and Applications*, 1993.

- [56] CCIR, Plenary Assembly, "Characteristics of antennas at earth stations in the fixed-satellite service", *Questions and Study Programmes, Resolutions, Opinions and Decisions of the CCIR*, vol. XV-4, Question 42/4, Geneva, 1990.
- [57] CCIR, Plenary Assembly, "Preferred technical characteristics and selection of sites for earth stations in the fixed-satellite service to facilitate sharing with services", *Questions and Study Programmes, Resolutions, Opinions and Decisions of the CCIR*, vol. XV-4, Question 57/4, Geneva, 1990.
- [58] CCIR, Plenary Assembly, "Interference reduction and cancellation techniques for the earth stations in the fixed-satellite service", *Questions and Study Programmes, Resolutions, Opinions and Decisions of the CCIR*, vol. XV-4, Question 58/4, Geneva, 1990.
- [59] COST 235 Management Committee, "Memorandum of Understanding for the implementation of a european research project on radio propagation effects on next-generation fixed-service terrestrial telecommunication systems (COST project 235)", *COST 235 internal communications*, committee paper 2, 1991.
- [60] C. Loo, "A statistical model for land mobile satellite link", *IEEE Trans. Veh. Technol.*, vol. VT-34, no. 3, pp. 122-127, 1985.
- [61] R.M. Barts, W.L. Stutzman, W.T. Smith, R.S. Schmier, and C.W. Bostian, "Land mobile satellite propagation modeling", *Conf. Rcd. IEEE-AP Symp.*, vol. 2, pp. 20-23, IEEE Antennas and Propagation Society, 1987.
- [62] H. Suzuki, "A statistical model for urban radio propagation", *IEEE Trans. Commun.*, vol. COM-25, no. 7, pp. 673-680, 1977.
- [63] M. Leberherz and T. Kurner, "A UTD wave propagation model for microcell planning purposes", *Proceedings of the 21st European Microwave Conference*, vol. 1, pp. 379-384, Microwave Exhibitions and Publishers ltd., 1991.
- [64] M. Leberherz, W. Wiesbeck, and W. Krank, "A versatile wave propagation model for the VHF/UHF range considering three-dimensional terrain", *IEEE Trans. Ant. Prop.*, vol. AP-40, no. 10, pp. 1121-1131, 1992.
- [65] R.J. Luebbers, "Propagation prediction for hilly terrain using GTD wedge diffraction", *IEEE Trans. Ant. Prop.*, vol. AP-32, no. 9, pp. 951-955, 1984.
- [66] J. Musil and F. Zacek, "Microwave measurements of complex permittivity by free space methods and their applications", Elsevier, Amsterdam, 1986.
- [67] G.A.J. van Dooren, M.H.A.J. Herben, G. Brussaard, M. Sforza, and J.P.V. Poiaries-Baptista, "Electromagnetic field strength prediction in an urban environment: a useful tool for the planning of LMSS", *Proc. of the International conference on Mobile-Satellite Communications (IMSC '93), Pasadena, California*, pp. 343-348, N.A.S.A./J.P.L./C.R.C., 1993.

- [68] A.Z. Elsherbeni and A.A. Kishk, "Modeling of cylindrical objects by circular dielectric and conducting cylinders", *IEEE Trans. Ant. Prop.*, vol. AP-40, no. 1, pp. 96-99, 1992.
- [69] M.A.J. van de Griendt, "Site shielding of a parabolic reflector antenna by a finite-width screen", Report of Training Work, Eindhoven University of Technology, Faculty of Electrical Engineering, Telecommunications Division, 1993.
- [70] C.A. Mentzer and L.J. Peters Jr., "A GTD analysis of the far out sidelobes of Cassegrain antennas", *IEEE Trans. Ant. Prop.*, vol. AP-23, no. 9, pp. 702-709, 1975.
- [71] C.E. Ryan and L.J. Peters Jr., "Evaluation of edge-diffracted fields including equivalent currents for the caustic regions", *IEEE Trans. Ant. Prop.*, vol. AP-17, no. 5, pp. 292-299, 1969.
- [72] G.L. James and V. Kermemelidis, "Reflector antenna radiation pattern analysis by equivalent edge currents", *IEEE Trans. Ant. Prop.*, vol. AP-21, no. 1, pp. 19-24, 1973.
- [73] J. Chen, P.J.I. de Maagt, and M.H.A.J. Herben, "Wide-angle radiation pattern calculation of paraboloidal reflector antennas: a comparative study.", Report EUT 91-E-252, Eindhoven University of Technology, 1991.
- [74] H.J.F.G. Govaerts, "Half plane shielding of a Cassegrain antenna system", Report of Training Work, Eindhoven University of Technology, Faculty of Electrical Engineering, Telecommunications Division, 1991.
- [75] W.V.T. Rusch, L.R. Welch, and G.E. Mires, "Observation-point-dependent blocking shadows on a reflector antenna", *IEEE Trans. Ant. Prop.*, vol. AP-37, no. 6, pp. 690-697, 1989.
- [76] P.W. Hannan, "Microwave antennas derived from the Cassegrain telescope", *IRE Trans. Ant. and Propag.*, vol. AP-9, no. 3, pp. 140-153, 1961.
- [77] E. Ballabio, editor, "COST 210, Influence of the atmosphere on interference between radio communications systems at frequencies above 1 GHz", vol. EUR 13407 EN of *Information Technologies and Sciences*, Commission of the European Communities, Brussels, 1991.
- [78] CCIR Plenary assembly, "Radiation diagrams for use as design objectives for antennas of earth stations operating with geostationary satellites", *Recommendations and Reports of the CCIR*, vol. IV-1, Rep. 580-1, Geneva, 1986.
- [79] Y. Okumura, E. Ohmori, T. Kawano, and K. Fukuda, "Field strength prediction and its variability in VHF and UHF land-mobile radio service", *Rev. Elec. Commun. Lab.*, vol. 16, no. 5, pp. 825-873, 1968.
- [80] D.O. Reudink, "Properties of mobile radio propagation above 400 MHz", *IEEE Trans. Veh. Technol.*, vol. VT-23, no. 11, pp. 143-159, 1974.

-
- [81] D.C. Cox, "Multipath delay spread and path loss correlation for 910 MHz urban mobile radio propagation", *IEEE Trans. Veh. Technol.*, vol. VT-26, no. 11, pp. 340-344, 1977.
- [82] Space Engineering (Rome) and Ingegneria dei Sistemi (Pisa), "Propagation Model for the Land Mobile Satellite Radio Channel in Urban Environments", Report of ESA Contract 9788/92/NL/LC, 1993.
- [83] D.F Rogers, "*Procedural elements of computer graphics*", McGraw-Hill Book company, New York, 1985.
- [84] M.J. Neve and G.B. Rowe, "Assessment of GTD for mobile radio propagation prediction", *Electron. Lett.*, vol. 29, no. 7, pp. 618-620, 1993.
- [85] M.J. Neve and G.B. Rowe, "Estimation of cellular mobile radio planning parameters using a GTD-based model", *Electron. Lett.*, vol. 29, no. 15, pp. 1372-1374, 1993.

Korte samenvatting

Dit proefschrift behandelt de ontwikkeling van een deterministisch model voor de voorspelling van de elektromagnetische (EM) veldsterkte in stedelijke gebieden. Het model gebruikt de geometrische optica (GO) aangevuld met verschillende bijdragen die berekend zijn op basis van de uniforme theorie van diffractie (UTD) om de interactie van de EM golf met obstakels in een stedelijke omgeving te beschrijven. Twee toepassingen van dit model worden besproken in deze dissertatie.

De eerste is de bepaling van de doeltreffendheid van het plaatsen van een obstakel op het propagatiepad van een stoorsignaal. Resultaten van deze opzettelijke signaalblokkering worden gepresenteerd voor verschillende types obstakels en posities van de ontvangantenne. Ook een geometrie waarbij de antenne heel dicht bij het obstakel is geplaatst wordt bestudeerd. In dit geval is een afzonderlijke beschouwing van diffractie aan de antenne en het obstakel niet meer geoorloofd en dient een gecombineerde analyse te worden uitgevoerd. Dit is gedaan voor twee soorten parabolische reflectorantennes, en resultaten voor het afscherpende effect van een halfvlak worden gepresenteerd en vergeleken. Ook de introductie van antenne-weegfuncties in modellen voor veldsterktevoorspelling gebaseerd op een stralenbeschouwing van het EM veld wordt behandeld.

De tweede toepassing van het besproken model is de bepaling van de EM veldsterkte van een door een satelliet uitgezonden radiosignaal in een bebouwde omgeving. Door zijn deterministisch karakter is het ontwikkelde model in staat effecten zoals reflectie en schaduwvorming te analyseren. Deze effecten worden niet meegenomen in gebruikelijke, statistische modellen voor de voorspelling van de veldsterkte. Omdat het GO/UTD model gebruik maakt van een gedetailleerde beschrijving van de stedelijke omgeving is het toepasbaar op een willekeurige omgeving. Dit staat in tegenstelling tot de conventionele statistische modellen die normaal gesproken slechts voor een beperkt aantal gegeneraliseerde geometrieën te gebruiken zijn. De kracht van het model wordt gedemonstreerd aan de hand van de theoretische bepaling van de veldsterkte langs twee trajecten door de campus van de TU Eindhoven. Niet alleen de veldsterkte, maar ook het Dopplerspectrum, de impulsresponsie en het impuls-Dopplerspectrogram worden bepaald. Het deterministische model kan een waardevolle aanvulling zijn van reeds bestaande statistische modellen voor veldsterktevoorspelling, vooral als een digitale beschrijving van de gebouwen in steden en dorpen voorhanden is.

Toelichting

In dit proefschrift zijn resultaten beschreven die ten dele behaald zijn door bijdragen van anderen. Deze bijdragen worden hieronder nader omschreven.

- *Comparison of three field-strength prediction models (par. 3.3).*

Deze paragraaf is het resultaat van een nauwe samenwerking tussen dr. Mireille Levy van Rutherford Appleton Laboratory (UK), dr. Chris Haslett van de University of Glamorgan (UK) en de auteur van dit proefschrift in het kader van het Europese project COST 235. Dr. C. Haslett was verantwoordelijk voor de berekeningen met de Fresnel-integralen en dr. M. Levy heeft de berekeningen met de parabolische vergelijking uitgevoerd.

- *Large-bandwidth diffraction measurements at 54 GHz using both time-domain filtering and frequency smoothing (par. 4.2).*

Ir. M.G.J.J. Klaassen ontwikkelde en realiseerde in het kader van zijn afstudeerwerk in de vakgroep Telecommunicatie van de Technische Universiteit Eindhoven de meetopstelling voor het verrichten van de diffractie- en site shielding metingen. De ontwikkeling van de calibratie procedure en de meetresultaten in par. 4.2 en 4.3 zijn aan dit afstudeerwerk ontleend. De auteur van dit proefschrift en dr.ir. M.H.A.J. Herben hebben ir. Klaassen bij zijn afstudeerwerk begeleid.

- *Comparison between measurements and UTD simulations of EM-wave scattering by circular cylinders (par. 4.6).*

Ir. H.J.F.G. Govaerts analyseerde het probleem van diffractie aan een metalen cilinder in het kader van zijn afstudeerwerk in de vakgroep Telecommunicatie. De auteur van dit proefschrift en dr.ir. M.H.A.J. Herben en hebben ir. Govaerts tijdens het afstudeerwerk begeleid, waarbij opgemerkt dient te worden dat de auteur van dit proefschrift de veldsterktemetingen in de cilindergeometrie uitgevoerd heeft.

Verder zijn in de dissertatie resultaten verwerkt die verkregen zijn uit het werk van een aantal stagiairs die hun werk uitgevoerd hebben onder begeleiding van de auteur van dit proefschrift.

Acknowledgments

This thesis could not have been completed without the physical and moral support of various people.

The cooperation with the colleagues of the COST 235 project has been pleasant, fruitful and enlightening. I am particularly indebted to Mireille Levy from the Rutherford Appleton Laboratory, and Chris Haslett and Miqdad Al-Nuaimi from the University of Glamorgan, for the stimulating discussions during many of the meetings.

Furthermore, I would like to thank Mario Sforza and Pedro Poiares-Baptista of the European Space Agency for the collaboration and discussions on the topic of field-strength prediction related to mobile communications.

The work in this thesis has been performed during my stay at the Telecommunications Division of the Eindhoven University of Technology. I am very grateful to all members of this group, particularly to Marc Klaassen and Rico Govaerts who both did a huge amount of work during their temporary stay in room EH 11-10.

I also would like to thank Matti 'pitcher' Herben for the discussions on diffraction and antenna theory and the launching of small 'balls', especially during Friday afternoons, and Gert Brussaard for reading and commenting on the numerous manuscripts produced during the Ph.D. study. I am also grateful to Leo Ligthart for his constructive comments on the draft version of my thesis.

I thank my father, Gerard van Dooren, for convincing me that, if you really want, you can achieve (nearly) everything.

Finally, I thank my wife Kitty, for being so patient during the last four years, when yet another weekend was used for working on my dissertation.

Curriculum vitae

De auteur van dit proefschrift werd op 19 april 1967 geboren te Roosendaal en Nispen. Na het doorlopen van de lagere school volgde hij van 1979 tot 1985 de middelbare-schoolopleiding (VWO) aan de Katholieke Scholengemeenschap Etten-Leur te Etten-Leur.

In 1985 begon hij met de studie Elektrotechniek aan de Technische Hogeschool Eindhoven (thans TUE). Het afstudeerwerk betrof de analyse van een optische (de)multiplexer voor elektromagnetische golven, met behulp van gaussische bundels, en werd uitgevoerd bij de European Space Agency (ESA/ESTEC) in opdracht van de vakgroep Telecommunicatie. In 1989 werd het ingenieursdiploma behaald. Tijdens de studie werd tevens de radio-amateurmachtiging A behaald onder de roepnaam PA3EWA.

Aansluitend op de eerste-fasestudie werd begonnen met een tweede-faseopleiding met als onderwerp het opstellen van een site-shieldingmodel voor een dubbelreflector-antennesysteem. Het diploma van het instituut vervolgopleidingen (IVO) van de TUE werd in 1991 behaald. Besloten werd de tweede fase opleiding uit te bouwen tot een promotiestudie, die geleid heeft tot het schrijven van dit proefschrift.

Vanaf 1991 was hij de Nederlandse vertegenwoordiger in werkgroep 3 van het Europese COST 210 project, en aansluitend in het COST 235 project. In het laatste project was hij coördinator in werkgroep 3 voor het onderdeel diffractietheorie.

The author of this dissertation was born in Roosendaal en Nispen on April 19, 1967. From the Katholieke Scholengemeenschap Etten-Leur e.o. he obtained the school-leaving certificate in 1985. In the same year he started studying Electrical Engineering at the Eindhoven University of Technology (EUT). He graduated in 1989, and his master's thesis described the analysis of a multi-reflector demultiplex circuit with gaussian beams. The work was carried out at the European Space Agency (ESA/ESTEC) as an external graduate student of the Telecommunications Division of EUT. During the study he also obtained the radio-amateur license A with call-sign PA3EWA.

In 1989, he started a second-phase designers course on Information and Communication Technology. The study programme concerned the formulation of a site shielding model for a Cassegrain antenna shielded by a half-plane. The research programme was extended, and the results were recorded in this dissertation.

From 1991, he is the Dutch representative in working group 3 of the European project COST 210 and then in the COST 235 project. In the latter project he is coordinator in working group 3 concerning diffraction theory.

Stellingen bij het proefschrift

A Deterministic Approach to the Modelling
of Electromagnetic Wave Propagation
in Urban Environments

door

Gerardus Adrianus Johannes van Dooren

St. Willebrord, 29 maart 1994

-
- 1 Tuovinen gaat in zijn beschouwing over de gaussische bundel geheel voorbij aan het feit dat het fasefront alleen sferisch verondersteld mag worden nabij de as van de bundel. Dit verklaart waarom grote verschillen gevonden worden tussen de fase van de gaussische bundel en die van een resultaat verkregen via apertuurintegratie.
 - J. Tuovinen, 'Accuracy of a Gaussian Beam', IEEE Transactions on Antennas and Propagation, vol. AP-40, no. 4, pp. 391–398, 1992.

 - 2 Voor het ontbinden van een *willekeurig* apertuurveld in gaussische modi zijn behalve radiale ook hoekafhankelijke (azimuthale) modi nodig.
 - G.A.J. van Dooren en C.G.M. van't Klooster, 'Analysis of a Reflector Antenna with Quasi-optical Front-end using Gaussian Beams', Proceedings of Journées Internationales de Nice sur les Antennes (JINA), pp. 201–205, 1990.

 - 3 In de definitie van de slechtste maand is het begrip jaar voor verschillende uitleg vatbaar. Door gebruik te maken van een lopend gemiddelde met de duur van een jaar wordt een betrouwbaardere dempingsstatistiek voor de slechtste maand verkregen.
 - G.A.J. van Dooren, 'Electromagnetic Diffraction Models for the Shielding of Single- and Dual-Reflector Antennas by Obstacles with Simple Shapes', IVO-rapport, T.U. Eindhoven, 1991.

 - 4 Het examen morsecode-opnemen en -seinen ter verkrijging van de zendmachtiging A en B voor radioamateurs moet eerder gezien worden als een proeve van mentale bekwaamheid dan als een proeve van theoretische of fysieke bekwaamheid.

 - 5 AIO-promovendi en verpleegkundigen beoefenen hun werk uitsluitend uit liefde voor hun vak.

-
- 6 Voor het bepalen van de afschermende werking van een obstakel bij niet-uniforme belichting kan de UTD niet algemeen gebruikt worden. Een spectrale aanpak is dan een betere oplossing.
- 7 Het drie-stralen-model ter bepaling van de stralingseigenschappen van een symmetrische parabolantenne zou op basis van fysische gronden uitgebreid moeten worden met een oneindig aantal andere bijdragen.
- 8 Het in rekening brengen van de invloed van een obstakel op zowel het gewenste als het ongewenste signaal in de berekening van de site shielding factor (SSF), zoals voorgesteld door Vyncke en Vander Vorst, leidt tot een schijnbaar frequentieafhankelijke SSF.
- C. Vyncke en A. Vander Vorst, 'Effect of Obstacles on Interference between Slant Paths and Terrestrial Links, as a Function of Frequency', *Proceedings of the International Conference on Antennas and Propagation (ICAP)*, pp. 1003-1006, 1993.
 - Dit proefschrift, par. 3.2.
- 9 Ondanks het feit dat de Cassegrain-reflectorantenne al geruime tijd gebruikt wordt in de satellietcommunicatie is er slechts weinig bekend over de berekening van de ver van de antenne-as gelegen zijlussen.
- Dit proefschrift, par. 5.3.
- 10 De keuze van een geschikte basisvorm ter modellering van obstakels in een deterministisch model voor veldsterktevoorspelling is bepalend voor de praktische bruikbaarheid.
- Dit proefschrift, par. 6.2.
